NUMERICAL MODELING OF GRAVITATIONAL WAVES

A Dissertation

Presented to the Faculty of the Graduate School

of Cornell University

in Partial Fulfillment of the Requirements for the Degree of

Doctor of Philosophy

by

Abdul Hussein Kamel Mroué

August 2009

NUMERICAL MODELING OF GRAVITATIONAL WAVES

Abdul Hussein Kamel Mroué, Ph.D.

Cornell University 2009

Gravitational wave detectors such as LIGO are poised to detect signals from coalescing binary black hole systems. Such a detection would allow for the first time a test of general relativity in the strong-field regime. We discuss a number of related problems that must be solved in order to carry out this program successfully. First, we present a numerical simulation of a 15-orbit quasicircular equal mass nonspinning binary black hole system. Different uncertainties in the phase of the extracted and extrapolated gravitational waveforms are discussed. The phase and the amplitude of analytical post-Newtonian approximations of the gravitational waveforms are compared to the phase and amplitude of the numerical gravitational waveforms extrapolated to infinity. The comparison establishes the regime where post-Newtonian theory is accurate, and suggests ways to improving the wave templates used in searches. Padé resummation techniques have been used by the community in constructing templates. We study this technique and show its limitations. Finally, we study how to generalize the concept of eccentricity to the relativistic case. We estimate the precession of a binary system and compare various post-Newtonian precession formula.

BIOGRAPHICAL SKETCH

Abdul Hussein Mroué was born in Beirut, Lebanon on April 16, 1981. He graduated in 1999 from his high school, Collège Notre Dame des Sœurs Antonines, and he entered the American University of Beirut. He graduated in June 2002 with a B.S., majoring in physics and minoring in Math. In his senior year, he started working with professor Jihad Touma on non-linear dynamics, and he pursued a Master's program under his supervision at the same institution until he graduated again in June 2004. Looking for a different experience, Abdul applied for graduate school in the US. He was accepted at Cornell where he joined the physics PhD program, which is a great place to do physics. Living in Ithaca with all the fascinating and peaceful landscape around it and acquiring precious scientific knowledge was worth the long journey. For the next five years, he worked under the supervision of Saul Teukolsky on various topics in numerical relativity, mainly the two-body problem, until he graduated on August 2009.

For my parents.

ACKNOWLEDGEMENTS

I would like to thank all my colleagues and friends at Cornell for their support and help over the many years at Cornell. In particular, I would like to thank my advisor, Saul Teukolsky, to whom I am very much in debt. Without his great support, patience, guidance and insightful advice, I would certainly not have been able to have accomplish my work. I am as well in debt to Lawrence Kidder for his help, advice and patience in teaching me details of the Caltech-Cornell numerical relativity code and for many productive discussions. I would like also to thank him for his guidance to accomplish some of the projects not included in this dissertation.

I would like also to thank Harald Pfeiffer and Mark Scheel for helpful discussions and advice on many of the projects included in this dissertation. Also, I would like to thank all of my collaborators on the projects in this dissertation, without whom this work would not have been accomplished. I am grateful also to my group members at Cornell Micheal Boyle, Francois Foucart, Geoffrey Lovelace, Robert Owen and Nicholas Taylor for helpful discussions.

The research presented in this thesis was supported in part by by the Sherman Fairchild Foundation; by the NSF grants PHY-0652952, DMS-0553677, PHY-0652929 and by NASA grants NNG05GG51G, NNX09AF96G to Cornell.

I would like to thank David Chernoff and Richard Galik who served on my special committee, and I am also grateful to Lawrence Gibbons for serving as a proxy on my B exam.

It is also a pleasure to thank Jihad Touma for his continuous support, encouragement, and for being a mentor and a friend since my early days at the American University of Beirut.

Finally, I thank my family especially my parents, Kamel and Wafika, my brother Mohamad, my sister Fatima and my brother-in-law Ayman for their love and great support over the many adventurous years of my life. Without them I would have never accomplished many things in my life. I am also grateful to many of my relatives and Lebanese friends for their support and encouragement.

TABLE OF CONTENTS

LIST OF TABLES

LIST OF FIGURES

CHAPTER 1

INTRODUCTION

For centuries, scientists believed that gravity was governed by Newton's laws, as it explained the motions of planets and stars as well as the motion of a falling object on Earth. Our view to gravity did not change until 1915 when Albert Einstein put forward his theory of general relativity. His theory revolutionized our understanding of space and time and presented fascinating new physics to explore in the universe.

Black holes are among many remarkable consequences of general relativity, some of which are still being unraveled. General relativity also predicts the emission of gravitational waves by a binary system. The waves carry away energy, causing the orbit to decay until the system finally merges. An observable example of such indirect detection of gravitational waves is the Hulse-Taylor pulsar. The observed decay of the orbit provides very good consistency between the theory and the experimental data.

Inspiralling binary systems of compact objects eventually merge and form a remnant compact object that is usually a single spinning black hole. Their coalescence is one of the most promising sources of gravitational radiation in the strong field limit, and a direct measurement of gravitational waves from such a source would validate general relativity in this regime. With this aim, many ground-based interferometric detectors such as LIGO were constructed in the last decade, and they are currently attempting to make a direct measurement of the first gravitational wave signal. With successful detection of gravitational waves, these laser interferometers would open a new window to our universe.

Because of the complexity of Einstein's equations, the simplest two-body problem in general relativity does not have an analytical solution. To detect gravitational waves from a coalescing binary, large banks of templates that model these theoretical waveforms are needed. Templates based on post-Newtonian approximations have been developed, and they are used in various searches for gravitational waves. These approximations are known to be valid only when the black holes are sufficiently far apart. Therefore, it is urgent to independently check the validity of these post-Newtonian models in the strong field regime.

Fortunately, recent breakthroughs over the past few years in numerical relativity have made it possible to successfully simulate the late inspiral and merger phase of binary black hole coalescence. Full waveforms including the merger can be modeled completely using numerical relativity. This thesis presents the numerical evolution of a nonspinning equal mass quasi-circular binary black hole system, and it compares the numerically extracted gravitational waveforms to the post-Newtonian analytical description of the expected gravitational wave signal approximations. This comparison is essential in verifying the validity and the robustness of the analytical templates.

In this thesis, I consider a number of problems related to the quest to carry out the confrontation of general relativity with observed gravitational wave data from a binary black hole system.

In chapter 2, numerical simulations of 15 orbits of an equal-mass binary black hole system are presented. Gravitational waveforms from these simulations, covering more than 30 cycles and ending about 1.5 cycles before merger, are compared with those from quasi-circular zero-spin post-Newtonian (PN)

formulae. The cumulative phase uncertainty of these comparisons is about 0.05 radians, dominated by effects arising from the small residual spins of the initial black holes and the small residual orbital eccentricity in the simulations. Matching numerical results to PN waveforms early in the run yields excellent agreement (within 0.05 radians) over the first $\sim$ 15 cycles, thus validating the numerical simulation and establishing a regime where PN theory is accurate. In the last 15 cycles to merger, however, generic PN Taylor approximants build up phase differences of several radians, casting doubt on their utility in gravitational wave searches.

Gravitational-wave *amplitude* comparisons are also done between numerical simulations and post-Newtonian approximations, and the agreement depends on the post-Newtonian order of the amplitude expansion: the amplitude difference is about 6–7% for zeroth order and becomes smaller for increasing order. A newly derived 3.0PN amplitude correction improves agreement significantly ($<$ 1% amplitude difference throughout most of the run, increasing to 4% near merger) over the previously known 2.5PN amplitude terms.

In chapter 3, we test the resummation techniques used in developing Padé and effective one body (EOB) waveforms for gravitational wave detection. Convergence tests show that Padé approximants of the gravitational wave energy flux do not accelerate the convergence of the standard Taylor approximants even in the test mass limit, and there is no reason why Padé transformations should help in estimating parameters better in data analysis. Moreover, adding a pole to the flux seems unnecessary in the construction of these Padé-approximated flux formulas. Padé approximants may be useful in suggesting the form of fitting formulas. We compare a 15-orbit numerical waveform of the

Caltech-Cornell group to the suggested Padé waveforms of Damour et al. in the equal mass, nonspinning quasicircular case. The comparison suggests that the Padé waveforms do not agree better with the numerical waveform than the standard Taylor based waveforms. Based on this result, we design a simple EOB model by modifiying the ET EOB model of Buonanno et al., using the Taylor series of the flux with an unknown parameter at the fourth post-Newtonian order that we fit for. This simple EOB model generates a waveform having a phase difference of only 0.002 radians with the numerical waveform, much smaller than 0.04 radians the phase uncertainty in the numerical data itself. An EOB Hamiltonian can make use of a Padé transformation in its construction, but this is the only place Padé transformations seem useful.

Chapter 4 deals with expressions for the gravitational wave (GW) energy flux and center-of-mass energy of a compact binary, which are integral building blocks of post-Newtonian (PN) waveforms. In this chapter, we compute the GW energy flux and GW frequency derivative from a highly accurate numerical simulation of an equal-mass, non-spinning black hole binary. We also estimate the (time derivative of the) center-of-mass energy from the simulation by assuming energy balance. We compare these quantities with the predictions of various PN approximants (adiabatic Taylor and Padé models; non-adiabatic effective-one-body (EOB) models). We find that Padé summation of the energy flux does not accelerate the convergence of the flux series despite claims to the contrary in the literature; nevertheless, the Padé flux is markedly closer to the numerical result for the whole range of the simulation (about 30 GW cycles). Taylor and Padé models overestimate the increase in flux and frequency derivative close to merger, whereas EOB models reproduce more faithfully the shape of and are closer to the numerical flux, frequency derivative and derivative of energy. We

also compare the GW phase of the numerical simulation with Padé and EOB models. Matching numerical and untuned 3.5 PN order waveforms, we find that the phase difference accumulated until $M\omega = 0.1$ is -0.12 radians for Padé approximants, and 0.50 (0.45) radians for an EOB approximant with Keplerian (non-Keplerian) flux. We fit free parameters within the EOB models to minimize the phase difference, and confirm the presence of degeneracies among these parameters. By tuning the pseudo 4PN order coefficients in the radial potential or in the flux, or, if present, the location of the pole in the flux, we find that the accumulated phase difference at $M\omega = 0.1$ can be reduced—if desired—to much less than the estimated numerical phase error (0.02 radians). For comparison, Lindblom et al. [178] have estimated that Advanced LIGO requires template phase errors less than about 0.07 for maximum detection efficiency, and less than about 0.007 for optimum parameter estimation. The parameter estimation requirements for the proposed space-based detector LISA are even more stringent.

In chapter 5, two complementary techniques are developed for obtaining the asymptotic form of gravitational-wave data at large radii from numerical simulations, in the form of easily implemented algorithms. Numerical simulation allows the extraction of waveforms at finite radii, because the simulation is carried out on a finite domain. It is shown that, without extrapolation, near-field effects produce errors in extracted waveforms that can significantly affect LIGO data analysis. The extrapolation techniques are discussed in the context of Newman–Penrose data applied to extrapolation of waveforms from an equal-mass, nonspinning black-hole binary simulation. The results of the two methods are shown to agree within error estimates. The various benefits and deficiencies of the methods are discussed.

Finally in chapter 6, we compute the eccentricity of a quasi-circular binary black hole system using different methods based on the orbital variables and gravitational wave phase and frequency. Orbital eccentricity is well-defined only in the Newtonian limit. Different definitions of the eccentricity incorporating post-Newtonian effects are compared. We find that an eccentricity definition based on the phase of the waveform seems to work best in practice. Using the proper horizon separation and the wave phase and frequency, we measure the decay of the eccentricity and the periastron advance, and we compare them to post-Newtonian approximations.

CHAPTER 2

HIGH-ACCURACY COMPARISON OF NUMERICAL RELATIVITY SIMULATIONS WITH POST-NEWTONIAN EXPANSIONS

2.1 Introduction

[1] The last two years have witnessed tremendous progress in simulations of black hole binaries, starting with the first stable simulation of orbiting and merging black holes [204, 206], development of the moving puncture method [72, 14] and rapid progress by other groups [74, 143, 118, 212, 215, 57, 182, 121, 217]. Since then, an enormous amount of work has been done on the late inspiral and merger of black hole binaries, among them studies of the universality of the merger waveforms [13, 12], investigations into black hole kicks [15, 136, 171, 78, 135, 144, 214, 82, 77, 56, 11, 145, 143, 213] and spin dynamics [76, 75, 73], comparisons to post-Newtonian models [64, 5, 24], and applications to gravitational wave data analysis [192, 67, 20].

Compared to the intense activity focusing on simulations close to merger, there have been relatively few simulations covering the inspiral phase. To date, only three simulations [17, 16, 197, 141, 151] cover more than five orbits. Long inspiral simulations are challenging for a variety of reasons: First, the orbital period increases rapidly with separation, so that simulations must cover a significantly longer evolution time. In addition, the gravitational waveform must be extracted at larger radius (and the simulation must therefore cover a larger spatial volume) because the gravitational wavelength is longer. Furthermore,

[1] This chapter is extracted from Ref. [51] which was written in collaboration with Micheal Boyle, Duncan A. Brown, Lawrence E. Kidder, Abdul H. Mroué, Harald P. Pfeiffer, Mark A. Scheel, Gregory B. Cook, and Saul A. Teukolsky, and published in 2007.

gravitational wave data analysis requires small *absolute* accumulated phase uncertainties in the waveform, so the relative phase uncertainty of the simulation must be smaller.

Gravitational wave detectors provide a major driving force for numerical relativity (NR). The first generation interferometric gravitational wave detectors, such as LIGO [19, 228], GEO600 [147] and VIRGO [117, 3], are now operating at or near their design sensitivities. Furthermore, the advanced generation of detectors are entering their construction phases. This new generation of interferometers will improve detector sensitivity by a factor of ~ 10 and hence increase expected event rates by a factor of ~ 1000 [132]. One of the most promising sources for these detectors is the inspiral and merger of binary black holes (BBHs) with masses $m_1 \sim m_2 \sim 10$–$20\,M_\odot$ [126]. These systems are expected to have circularized long before their gravitational waves enter the sensitive frequency band of ground-based detectors [194].

A detailed and accurate understanding of the gravitational waves radiated as the black holes spiral towards each other will be crucial not only to the initial detection of such sources, but also to maximize the information that can be obtained from signals once they are observed. When the black holes are far apart, the gravitational waveform can be accurately computed using a post-Newtonian (PN) expansion. As the holes approach each other and their velocities increase, the post-Newtonian expansion is expected to diverge from the true waveform. It is important to quantify any differences between theoretical waveforms and the true signals, as discrepancies will cause a reduction of search sensitivity. Several techniques have been proposed to address the problem of the breakdown of the post-Newtonian approximation [98, 65, 62], but

ultimately, the accuracy of the post-Newtonian waveforms used in binary black hole gravitational wave searches can only be established through comparisons with full numerical simulations.

Unfortunately, comparing post-Newtonian approximations to numerical simulations is not straightforward, the most obvious problem being the difficulty of producing long and sufficiently accurate numerical simulations as explained above. In addition, post-Newtonian waveforms typically assume circular orbits, and most astrophysical binaries are expected to be on circular orbits late in their inspiral, so the orbital eccentricity within the numerical simulation must be sufficiently small[2]. Another factor that complicates comparisons is the variety of post-Newtonian approximants available, from several straightforward Taylor expansions to more sophisticated Padé resummation techniques and the effective one-body approach (see e.g. [100, 101, 98, 65, 66, 105, 94, 97, 60], as well as Section 2.3.5 below). While all post-Newtonian approximants of the same order should agree sufficiently early in the inspiral (when neglected higher-order terms are small), they begin to disagree with each other during the late inspiral when the post-Newtonian approximation starts to break down—exactly the regime in which NR waveforms are becoming available.

Finally, agreement (or disagreement) between NR and PN waveforms will also depend very sensitively on the precise protocol used to compare the waveforms. Are PN and NR waveforms matched early or late in the inspiral? Is the matching done at a particular time, or is a least-squares fit performed over part (or all) of the waveform? Does one compare frequencies $\omega(t)$ or phases $\phi(t)$? Are comparisons presented as functions of time or of frequency? Up to which cutoff

[2]Unfortunately, this circularization occurs on extremely long time scales [194], thousands of orbits, making it impossible to run the numerical simulation long enough to radiate the eccentricity away.

frequency does one compare PN with NR?

Despite these difficulties, several comparisons between NR and PN have been done for the last few orbits of an equal-mass, non-spinning black hole binary. The first such study was done by Buonanno *et al* [64] based on simulations performed by Pretorius [204] lasting somewhat more than 4 orbits ($\sim$ 8 gravitational wave cycles). This comparison performs a least-squares fit over the full waveform, finds agreement between the numerical evolution and a particular post-Newtonian approximant (in our language TaylorT3 3.0/0.0[3]) and notes that another approximant (TaylorT4 3.5/0.0) will give similarly good agreement. However, as the authors note, this study is severely limited by numerical resolution, sizable initial eccentricity ($\sim$ 0.015), close initial separation of the black holes, and coordinate artifacts; for these reasons, the authors do not quantify the level of agreement.

More recently, Baker et al. [17, 16] performed simulations covering the last $\sim$ 14 cycles before merger. These simulations have an orbital eccentricity ~ 0.008 [17], forcing the authors to use a fitted smooth ("de-eccentrized") gravitational wave phase to obtain a monotonically increasing gravitational wave frequency. Comparing to TaylorT4 3.5/2.5, they find agreement between numerical and post-Newtonian gravitational wave phase to within their numerical errors, which are about 2 radians. The authors also indicate that other post-Newtonian approximants do not match their simulation as well as TaylorT4, but unfortunately, they do not mention whether any disagreement is significant (i.e., exceeding their numerical errors). Pan *et. al* [192] performed a more com-

[3]We identify post-Newtonian approximants with three pieces of information: the label introduced by [100] for how the orbital phase is evolved; the PN order to which the orbital phase is computed; and the PN order that the amplitude of the waveform is computed. See Sec. 2.3.5 for more details.

prehensive analysis of the numerical waveforms computed by Pretorius [64] and the Goddard group [17, 16], confirming that TaylorT4 3.5/0.0 matches the numerical results best.

The most accurate inspiral simulation to date was performed by the Jena group and presented in Husa et al. [151] and Hannam et al. [141]. This simulation covers 18 cycles before merger and has an orbital eccentricity of $\sim$ 0.0018 [152]. Discarding the first two cycles which are contaminated by numerical noise, and terminating the comparison at a gravitational-wave frequency $m\omega = 0.1$ (see Eq. (3.24) for the precise definition) their comparison extends over 13 cycles. We discuss the results of Ref. [141] in more detail in Sec. 2.6.1.

This paper presents a new inspiral simulation of a non-spinning equal mass black hole binary. This new simulation more than doubles the evolution time of the simulations in Refs. [17, 16, 141, 151], resulting in a waveform with 30 gravitational wave cycles, ending $\sim$ 1.5 cycles before merger, and improves numerical truncation errors by one to two orders of magnitude over those in Refs. [17, 16, 141, 151]. The orbital eccentricity of our simulations is $\sim 6 \times 10^{-5}$; this low eccentricity is achieved using refinements of techniques described in [197]. We present a detailed analysis of various effects which might influence our comparisons to post-Newtonian waveforms for non-spinning black hole binaries on circular orbits. These effects result in an uncertainty of ~ 0.05 radians out of the accumulated ~ 200 radians. Perhaps surprisingly, the largest uncertainty arises from the residual orbital eccentricity, despite its tiny value. The second largest effect arises due to a potential residual spin on the black holes, which we bound by $|S|/M_{\rm irr}^2 < 5 \times 10^{-4}$.

We compare the numerical waveforms with four different time-domain post-

Newtonian Taylor-approximants [100, 101, 62] and we match PN and NR waveforms at a specific time during the inspiral. We explore the effects of varying this matching time. When matching ~ 9 cycles after the start of our evolution, all post-Newtonian approximants of 3.0PN and 3.5PN order in orbital phase agree with our simulation to within ~ 0.03 radians over the first 15 cycles. This agreement is better than the combined uncertainties of the comparison, thus validating our simulations in a regime where the 3.5PN truncation error of post-Newtonian theory is comparable to the accuracy of our simulations. Lower order post-Newtonian approximants (2.0PN and 2.5PN order), however, accumulate a significant phase difference of ~ 0.2 radians over this region.

Extending the comparison toward merger (as well as when matching closer to merger), we find, not surprisingly, that the agreement between PN and NR at late times depends strongly on exactly what post-Newtonian approximant we use [100, 101]. Typical accumulated phase differences are on the order of radians at frequency $m\omega = 0.1$. One particular post-Newtonian approximant, TaylorT4 at 3.5PN order in phase, agrees with our NR waveforms far better than the other approximants, the agreement being within the phase uncertainty of the comparison (0.05 radians) until after the gravitational wave frequency passes $m\omega = 0.1$ (about 3.5 cycles before merger). It remains to be seen whether this agreement is fundamental or accidental, and whether it applies to more complicated situations (e.g. unequal masses, nontrivial spins).

We also compare the post-Newtonian gravitational wave amplitude to the numerical amplitude, where we estimate the uncertainty of this comparison to be about 0.5%. Restricted waveforms (i.e., 0PN order in the amplitude expansion) are found to disagree with the numerical amplitudes by 6–7%. An am-

plitude expansion of order 2PN shows significantly better agreement than the expansion at order 2.5PN. A newly derived 3PN amplitude [164] is found to give much better agreement than the 2.0PN amplitude.

This paper is organized as follows: Section 2.2 discusses our numerical techniques. In particular, we describe how we construct binary black hole initial data, evolve these data for 15 orbits, extract gravitational wave information from the evolution, and produce a gravitational waveform as seen by an observer at infinity. Section 2.3 details the generation of post-Newtonian waveforms, including details of how we produce the four approximants that we compare against NR. We describe our procedure for comparing NR and PN waveforms in Sec. 2.4, and present a detailed study of various sources of uncertainty in Sec. 2.5. The comparisons between NR and PN are presented in Section 2.6. This section is split into two parts: First, we compare each PN approximant separately with the numerical simulation. Subsequently, we show some additional figures which facilitate cross-comparisons between the different PN approximants. Finally, we present some concluding remarks in Section 6.5. The impatient reader primarily interested in NR-PN comparisons may wish to proceed directly to Table 2.3 summarizing the uncertainties of our comparisons, and then continue to Sec. 2.6, starting with Fig. 2.15.

2.2 Generation of numerical waveforms

In order to do a quantitative comparison between numerical and post-Newtonian waveforms, it is important to have a code capable of starting the black holes far enough apart to be in a regime where we strongly believe the

post-Newtonian approximation is valid, track the orbital phase extremely accurately, and do so efficiently so the simulation can be completed in a reasonable amount of time. Furthermore, the gravitational waves from such a simulation must be extracted in such a manner that preserves the accuracy of the simulation and predicts the waveform as seen by a distant observer, so a comparison with the post-Newtonian waveform can be made. In this section we describe the techniques we use to do this, as well as the results of a simulation starting more than 15 orbits prior to merger.

When discussing numerical solutions of Einstein's equations, we write all dimensioned quantities in terms of some mass scale m, which we choose to be the sum of the irreducible masses of the two black holes in the initial data:

$$m = M_{\mathrm{irr},1} + M_{\mathrm{irr},2}. \tag{2.1}$$

The irreducible mass of a single hole is defined as

$$M_{\mathrm{irr}} \equiv \sqrt{A/16\pi}, \tag{2.2}$$

where A is the surface area of the event horizon; in practice we take A to be the surface area of the apparent horizon. More generally, it is more appropriate to use the Christodoulou mass of each black hole,

$$M_{\mathrm{BH}}^2 = M_{\mathrm{irr}}^2 + \frac{S^2}{4M_{\mathrm{irr}}^2}, \tag{2.3}$$

instead of the irreducible mass. Here S is the spin of the hole. However, for the case considered in this paper, the spins are sufficiently small that there is little difference between M_{BH} and M_{irr}.

2.2.1 Initial data

Initial data are constructed within the conformal thin sandwich formalism [234, 199] using a pseudo-spectral elliptic solver [196]. We employ quasi-equilibrium boundary conditions [84, 85] on spherical excision boundaries, choose conformal flatness and maximal slicing, and use Eq. (33a) of Ref. [79] as the lapse boundary condition. The spins of the black holes are made very small via an appropriate choice of the tangential shift at the excision surfaces, as described in [79].

As the most accurate post-Newtonian waveforms available assume adiabatic inspiral of quasi-circular orbits, it is desirable to reduce the eccentricity of the numerical data as much as possible. Using techniques developed in [197], each black hole is allowed to have a nonzero initial velocity component towards the other hole. This small velocity component v_r and the initial orbital angular velocity Ω_0 are then fine-tuned in order to produce an orbit with very small orbital eccentricity[4]. We have improved our eccentricity-reduction procedure since the version described in [197], so we summarize our new iterative procedure here:

We start with a quasi-circular (i.e., $v_r = 0$) initial data set at coordinate separation $d = 30$, where Ω_0 is determined by equating Komar mass with Arnowitt-Deser-Misner (ADM) mass [79]. We then evolve these data for about 1.5 orbits, corresponding to a time $t/m \approx 600$. From this short evolution, we measure the proper separation s between the horizons by integration along the coordinate axis connecting the centers of the black holes. We fit the time derivative ds/dt in

[4] An alternative method of producing low-eccentricity initial data, based on post-Newtonian ideas, is developed in [152]. While that technique is computationally more efficient than ours, it merely reduces orbital eccentricity by a factor of ~ 5 relative to quasi-circular initial data, which is insufficient for the comparisons presented here. (cf. Sec. 2.5.5).

Table 2.1: Summary of the initial data sets used in this paper. The first block of numbers (d, Ω_0, f_r, and v_r) represent raw parameters entering the construction of the initial data. The second block gives some properties of each initial data set: m denotes the sum of the irreducible masses, $M_{\rm ADM}$ and $J_{\rm ADM}$ the ADM energy and angular momentum, and s_0 the initial proper separation between the horizons. The last column lists the eccentricity computed from Eq. (2.7). The initial data set 30c is used for all evolutions (except for consistency checks) described in this paper.

Name	d	Ω_0	f_r	$v_r \times 10^4$	$m\Omega_0$	$M_{\rm ADM}/m$	$J_{\rm ADM}/m^2$	s_0/m	$e_{ds/dt}$
30a	30	0.0080108	0.939561	0.00	0.01664793	0.992333	1.0857	17.37	1.0×10^{-2}
30b	30	0.0080389	0.939561	-4.90	0.0167054	0.992400	1.0897	17.37	6.5×10^{-4}
30c	**30**	**0.0080401**	**0.939561**	**-4.26**	**0.0167081**	**0.992402**	**1.0898**	**17.37**	$\mathbf{5 \times 10^{-5}}$
24a	24	0.0110496	0.92373	-8.29	0.0231947	0.990759	1.0045	14.15	1.1×10^{-3}
24b	24	0.0110506	0.923739	-8.44	0.0231967	0.990767	1.0049	14.15	1.5×10^{-4}

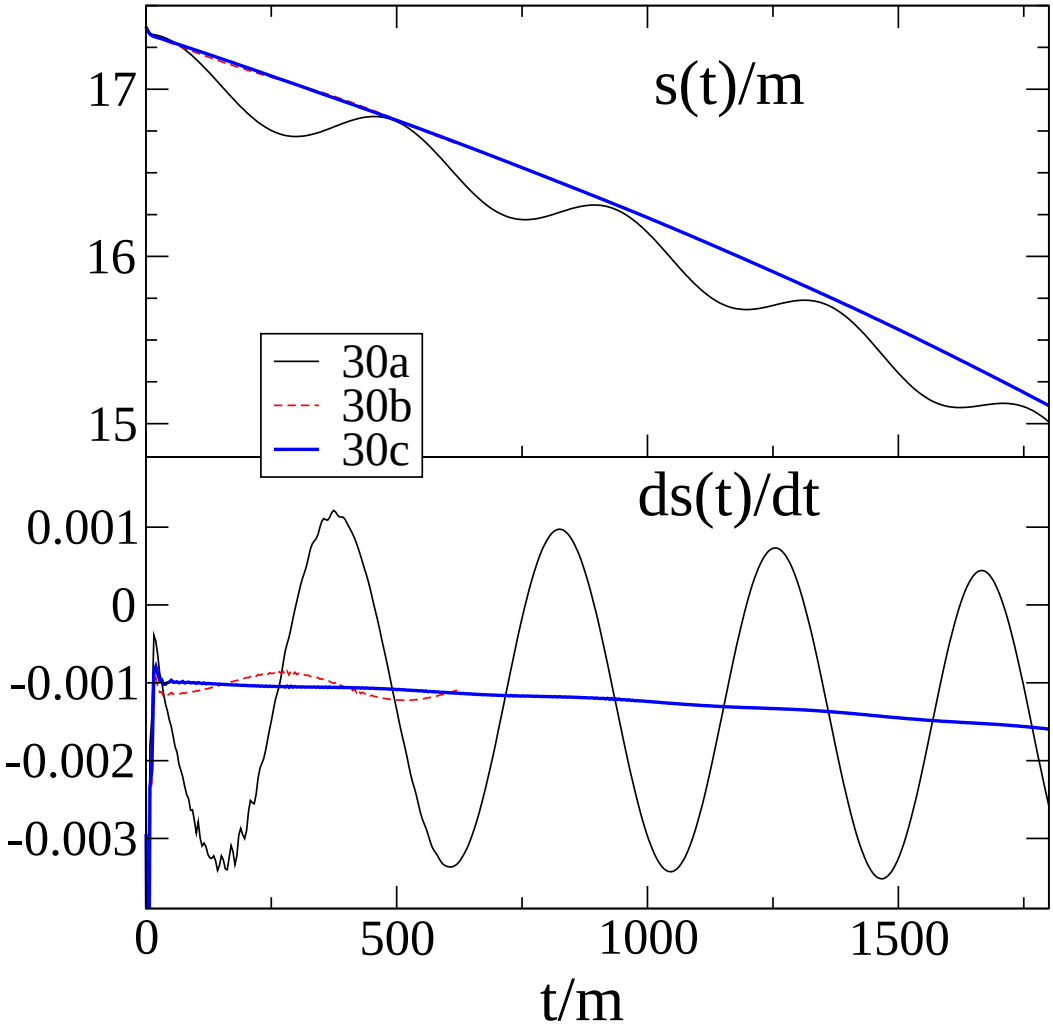

Figure 2.1: Proper separation (top panel) and its time derivative (lower panel) versus time for short evolutions of the $d = 30$ initial data sets 30a, 30b, and 30c (see Table 2.1). These three data sets represent zero through two iterations of our eccentricity-reduction procedure. The orbital eccentricity is reduced significantly by each iteration.

the interval $100 \lesssim t/m \lesssim 600$ to the function

$$\frac{ds}{dt} = A_0 + A_1 t + B\cos(\omega t + \varphi), \tag{2.4}$$

where we vary all five parameters A_0, A_1, B, ω and φ to achieve the best fit. The desired smooth inspiral is represented by the part $A_0 + A_1 t$; the term $B\cos(\omega t + \varphi)$ corresponds to oscillations caused by orbital eccentricity.

For a *Newtonian* orbit with radial velocity $B\cos(\omega t + \varphi)$ at initial separation s_0, it is straightforward to determine the changes to the orbital frequency and the radial velocity which make the orbit perfectly circular, namely

$$\Omega_0 \to \Omega_0 + \frac{B\sin\varphi}{2s_0}, \tag{2.5}$$

$$v_r \to v_r - \frac{B\cos\varphi}{2}. \tag{2.6}$$

For Newtonian gravity, Eq. (2.6) will of course result in a circular orbit with $v_r = 0$. In *General Relativity*, Ω_0 and v_r will be different from their Newtonian values, for instance $v_r < 0$ to account for the inspiral of the two black holes. Nevertheless, we assume that small perturbations around the zero-eccentricity inspiral trajectory behave similarly to small perturbations around a Newtonian circular orbit. Therefore, we apply the same formulae, Eqs. (2.5) and (2.6), to obtain improved values for Ω_0 and v_r for the black hole binary, where s_0 is the initial proper separation between the horizons. We then use the new values of Ω_0 and v_r to construct a new initial data set, again evolve for two orbits, fit to Eq. (2.4), and update Ω_0 and v_r. We continue iterating this procedure until the eccentricity is sufficiently small.

We estimate the eccentricity for each iteration from the fit to Eq. (2.4) using the formula

$$e_{ds/dt} = \frac{B}{s_0\omega}, \tag{2.7}$$

which is valid in Newtonian gravity for small eccentricities. Successive iterations of this procedure are illustrated in Fig. 2.1 and yield the initial data sets 30a, 30b, and 30c summarized in Table 2.1. Eccentricity decreases by roughly a factor of 10 in each iteration, with 30c having $e_{ds/dt} \approx 5 \times 10^{-5}$. The evolutions used during eccentricity reduction need not be very accurate and need to run only for a short time, $t \sim 600m$. One iteration of this procedure at our second lowest resolution requires about 250 CPU-hours. For completeness, Table 2.1 also lists parameters for initial data at smaller separation; these data will be used for consistency checks below. Apart from these consistency checks, the remainder of this paper will focus exclusively on evolutions of the low-eccentricity initial data set 30c.

2.2.2 Evolution of the inspiral phase

The Einstein evolution equations are solved with the pseudo-spectral evolution code described in Ref. [212]. This code evolves a first-order representation [179] of the generalized harmonic system [130, 134, 205]. We handle the singularities by excising the black hole interiors from our grid. Our outer boundary conditions [179, 207, 208] are designed to prevent the influx of unphysical constraint violations [216, 131, 18, 218, 70, 219, 168] and undesired incoming gravitational radiation [58], while allowing the outgoing gravitational radiation to pass freely through the boundary.

The code uses a fairly complicated domain decomposition to achieve maximum efficiency. Each black hole is surrounded by several (typically six) concentric spherical shells, with the inner boundary of the innermost shell (the excision

boundary) just inside the horizon. A structure of touching cylinders (typically 34 of them) surrounds these shells, with axes along the line between the two black holes. The outermost shell around each black hole overlaps the cylinders. The outermost cylinders overlap a set of outer spherical shells, centered at the origin, which extend to large outer radius. External boundary conditions are imposed only on the outer surface of the largest outer spherical shell. We vary the location of the outer boundary by adding more shells at the outer edge. Since all outer shells have the same angular resolution, the cost of placing the outer boundary farther away (at full resolution) increases only linearly with the radius of the boundary. External boundary conditions are enforced using the method of Bjorhus [27], while inter-domain boundary conditions are enforced with a penalty method [138, 146].

We employ the dual-frame method described in Ref. [212]: we solve the equations in an 'inertial frame' that is asymptotically Minkowski, but our domain decomposition is fixed in a 'comoving frame' that rotates with respect to the inertial frame and also shrinks with respect to the inertial frame as the holes approach each other. The positions of the holes are fixed in the comoving frame; we account for the motion of the holes by dynamically adjusting the coordinate mapping between the two frames. Note that the comoving frame is referenced only internally in the code as a means of treating moving holes with a fixed domain. Therefore all coordinate quantities (e.g. black hole trajectories, wave-extraction radii) mentioned in this paper are inertial-frame values unless explicitly stated otherwise.

One side effect of our dual frame system is that the outer boundary of our domain (which is fixed in the comoving frame) moves inward with time as ob-

served in the inertial frame. This is because the comoving frame shrinks with respect to the inertial frame to follow the motion of the holes. In Refs. [212, 197] the inertial frame coordinate radius r (with respect to the center of mass) and the comoving coordinate radius r' are related by a simple scaling

$$r = a(t)r'. \tag{2.8}$$

The expansion parameter $a(t)$ is initially set to unity and decreases dynamically as the holes approach each other, so that the comoving-frame coordinate distance between the holes remains constant. The outer boundary of the computational grid is at a fixed comoving radius $R'_{\rm bdry}$, which is mapped to the inertial coordinate radius $R_{\rm bdry}(t) = a(t)R'_{\rm bdry}$. Because we wish to accurately compute the gravitational radiation as measured far from the holes, it is desirable to have a moderately large outer boundary ($R_{\rm bdry}(t) \gtrsim 200m$) throughout the run. For the linear mapping, Eq. (2.8), this requires a very distant outer boundary early in the run, $R_{\rm bdry}(0) \simeq 1000m$. Computationally this is not very expensive. However, the initial junk radiation contaminates the evolutions for a time interval proportional to the light-crossing time to the outer boundary, and for $R_{\rm bdry}(0) \simeq 1000m$ it would be necessary to discard a significant portion of the evolution.

We therefore use the mapping

$$r = \left[a(t) + (1 - a(t))\,\frac{r'^2}{R'^2_0}\right] r', \tag{2.9}$$

for some constant R'_0 which is chosen to be roughly the radius of the outer boundary in comoving coordinates. This mapping has the following properties: (1) At the initial time $t = 0$, the map reduces to the identity map because $a(0) = 1$. Thus we do not need to re-map our initial data before evolving. (2) For small radii (i.e., at the locations of the black holes), the map reduces to the linear map, $r = a(t)r' + O(r'^3)$. This allows use of the control system without

Table 2.2: Overview of low-eccentricity simulations discussed in this paper. $R_{\rm bdry}$ is the initial coordinate radius of the outer boundary; this radius changes during the evolution according to the choice of "radial map" between inertial and comoving coordinates. The last column lists the different resolutions run for each evolution, N6 being highest resolution. Evolution 30c-1/N6 forms the basis of our post-Newtonian comparisons, and is used in all figures unless noted otherwise.

Name	ID	$N_{\rm orbits}$	$R_{\rm bdry}$	radial map	resolutions
30c-1	**30c**	**15.6**	**462*m***	**Eq. (2.9)**	**N1, N2, . . . , N6**
30c-2	30c	15.6	722*m*	Eq. (2.8)	N2, N4, N6
30c-3	30c	15.6	202*m*	Eq. (2.8)	N2, N3, . . . , N6
24b-1	24b	8.3	160*m*	Eq. (2.8)	N2, N3, N4

modifications. (3) The moving radius $r' = R'_0$ is mapped to a *constant* inertial radius: $r(R'_0) = R'_0$. This allows us to keep the inertial radius of the outer boundary constant (or nearly constant[5]) in time rather than shrinking rapidly.

In total, we have run three evolutions of the 30c initial data set; these use different combinations of outer boundary radius and radial mapping between inertial and moving coordinates. Some properties of these evolutions are summarized in Table 2.2. We also performed extensive convergence testing, running the same evolution on up to six distinct resolutions, N1 to N6. The coarsest resolution 30c-1/N1 uses approximately 41^3 grid points (summing all grid points in all the subdomains), while the most accurate evolution, 30c-1/N6, uses about 67^3 grid points. The run 30c-1/N2 required about 2,500 CPU-hours and run 30c-1/N6 about 19,000, where our simulations do not take advantage of symmetries. The distance to the outer boundary is adjusted by adding or removing outer spherical shells to an otherwise unmodified domain-decomposition. Run 30c-1 has 20 such outer spherical shells, while 30c-2 utilizes 32 and 30c-3 only 8.

[5]In practice, we choose R'_0 somewhat larger than the outer boundary, so that the outer boundary of the computational domain slowly contracts in inertial coordinates. This makes the zero-speed characteristic fields *outgoing* there, avoiding the need to impose boundary conditions on those fields.

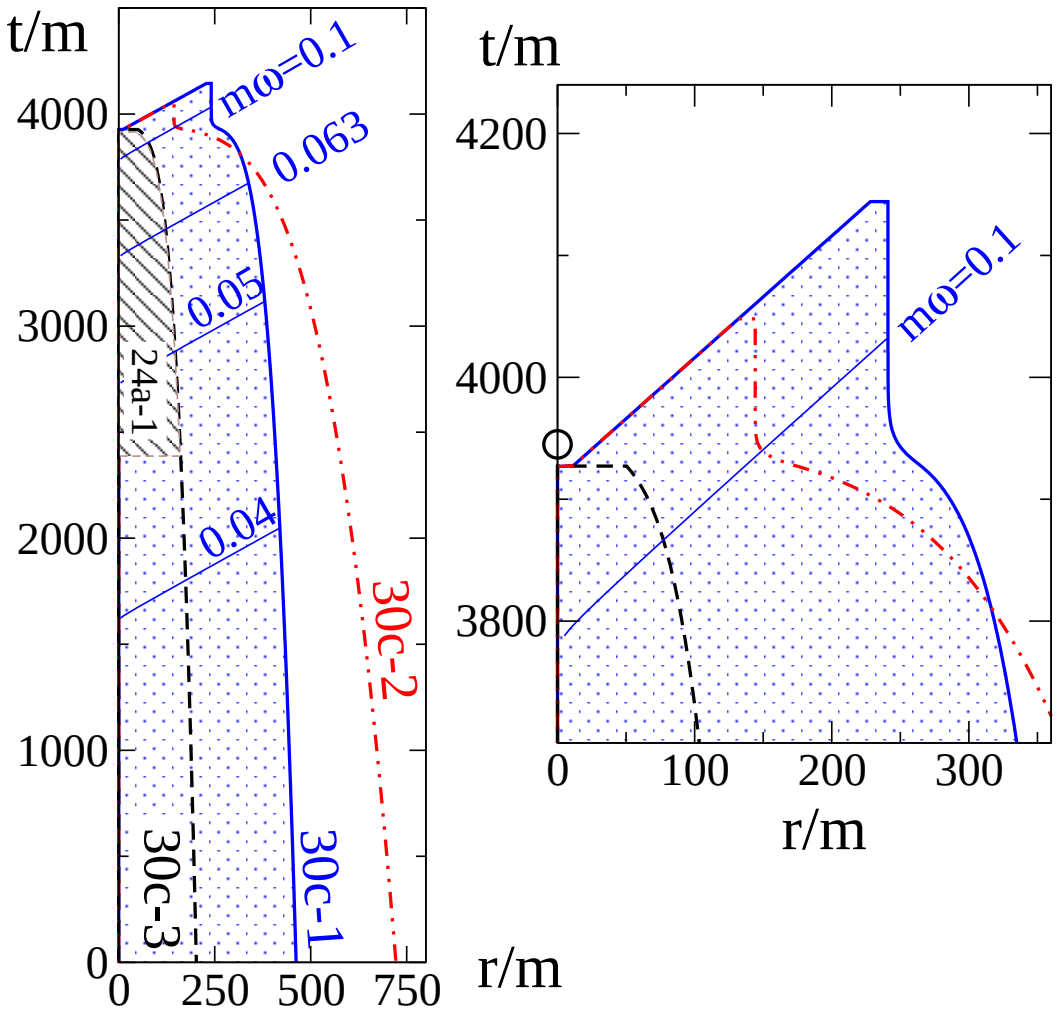

Figure 2.2: Spacetime diagram showing the spacetime volume simulated by the numerical evolutions listed in Tab. 2.2. The magnified view in the right panel shows how the gravitational waves are escorted to our extraction radii (see Sec. 2.2.3) after the simulation in the center has already crashed at $t \sim 3930m$, and after the estimated time of the black hole merger, which is indicated by the circle. The thin diagonal lines are lines of constant $t - r^*$; each corresponds to a retarded time at which the gravitational wave frequency ω at infinity assumes a particular value.

Thus, the total number of grid points varies slightly between runs, e.g. about 71^3 for 30c-2/N6. Figure 2.2 indicates the different behavior of the outer boundary location for these three evolutions.

For all of the evolutions 30c-1/2/3, the coordinate trajectories of the centers of the apparent horizons appear as in Fig. 2.3. The regular inspiral pattern without noticeable oscillations once again indicates that our evolutions indeed have very low eccentricity.

Figure 2.4 demonstrates the convergence of the black hole mass $m(t)$ with spatial resolution for run 30c-1. The mass $m(t)$ is computed as the sum of the irreducible masses of both black holes, as defined in Eq. (2.2). At the highest resolution, $m(t)$ deviates by only a few parts in 10^6 from its initial value m.

Our apparent horizon finder works by expanding the radius of the apparent horizon as a series in spherical harmonics up to some order L. We utilize the fast flow methods developed by Gundlach [139] to determine the expansion coefficients; these are significantly faster than our earlier minimization algorithms [21, 198]. The apparent horizon is almost spherical during the inspiral, so that the expansion in L converges exceedingly fast: $L = 8$ results in a relative error of the irreducible mass of better than 10^{-8}. The distortion of the horizons becomes more pronounced toward the end of the evolution when the black holes approach each other rapidly. This results in an error of 10^{-6} in the $L = 8$ apparent horizon expansion for the last $10m$ of the evolution.

We also measure the quasi-local spin using coordinate rotation vectors projected into the apparent horizon surfaces [55, 7, 8]. Only the z-component of the spin is non-zero (i.e., the spins are aligned with the orbital angular momentum).

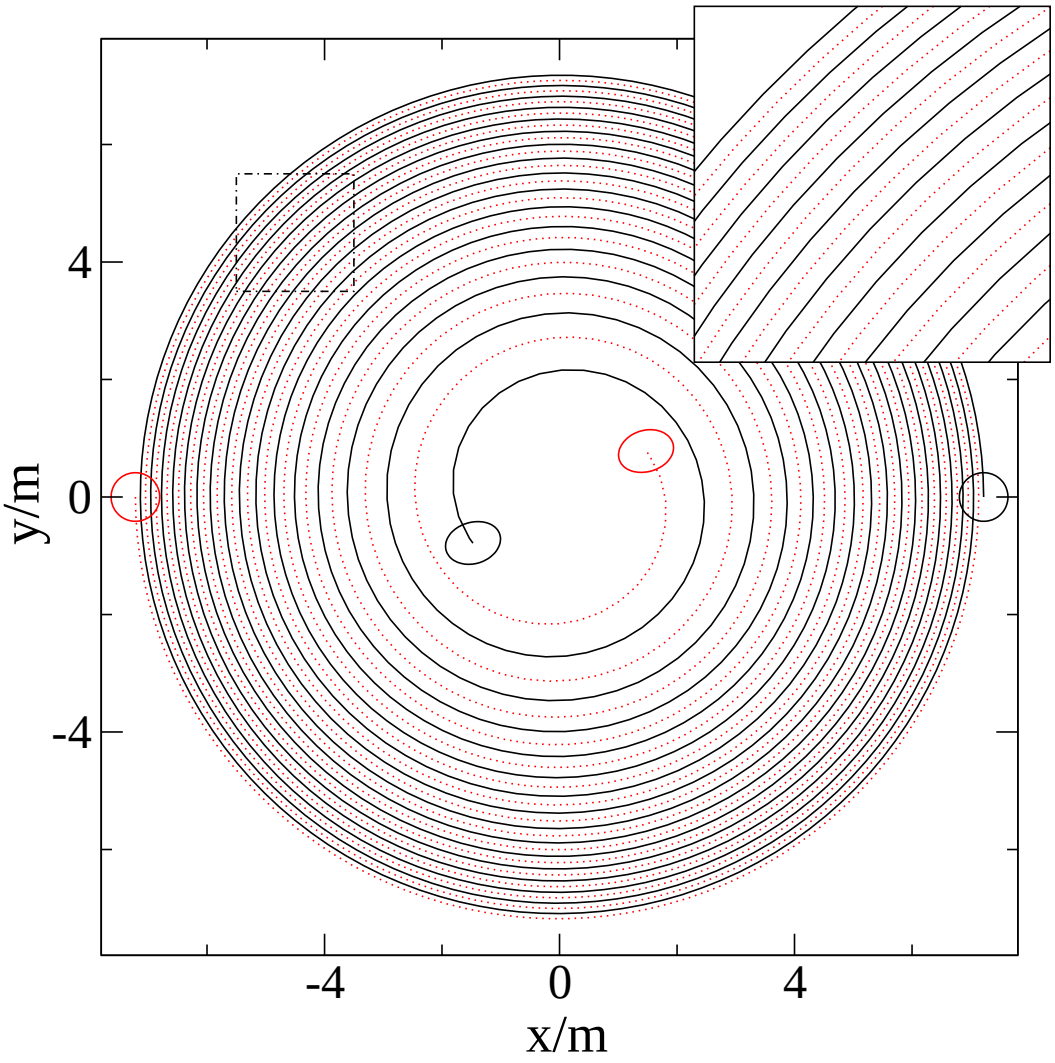

Figure 2.3: Coordinate trajectories of the centers of the black holes. The small circles/ellipsoids show the apparent horizons at the initial time and at the time when the simulation ends and wave escorting begins. The inset shows an enlargement of the dashed box.

The spin starts at $S_z/M_{\rm irr}^2 \approx -6 \times 10^{-5}$ and increases slowly to -5×10^{-4} during the evolution, where the minus sign indicates that the black hole spin is anti-aligned with the orbital angular momentum. Thus it appears the black hole's spins move further away from the corotational state. We believe this effect is caused by the use of coordinate rotation vectors when calculating the quasi-local spin, rather than more sophisticated approximate Killing vectors [119, 86, 191]. Preliminary results with approximate Killing vectors find the initial spin to be less than 10^{-6}, and slowly increasing during the evolution to a final value of 2×10^{-5} at the end of the comparison interval to post-Newtonian theory. Given the preliminary character of these results, we will take here the conservative bound $|\mathbf{S}|/M_{\rm irr}^2 \leq 5 \times 10^{-4}$ obtained from coordinate rotation vectors.

2.2.3 Escorting gravitational waves

The simulation presented in Fig. 2.3 stops when the horizons of the black holes become too distorted just before merger. At this time, most of the domain (all regions except for the immediate vicinity of the two holes) is still well resolved, and the spacetime contains gravitational radiation that has not yet propagated out to the large radii where we perform wave extraction. So instead of losing this information, which consists of several gravitational-wave cycles, we evolve only the outer portions of our grid beyond the time at which the code crashes in the center, effectively 'escorting' the radiation out to the extraction radii.

To do this, we first stop the evolution shortly before it crashes, and we introduce a new spherical excision boundary that surrounds both black holes and has a radius of roughly three times the black hole separation. This new exci-

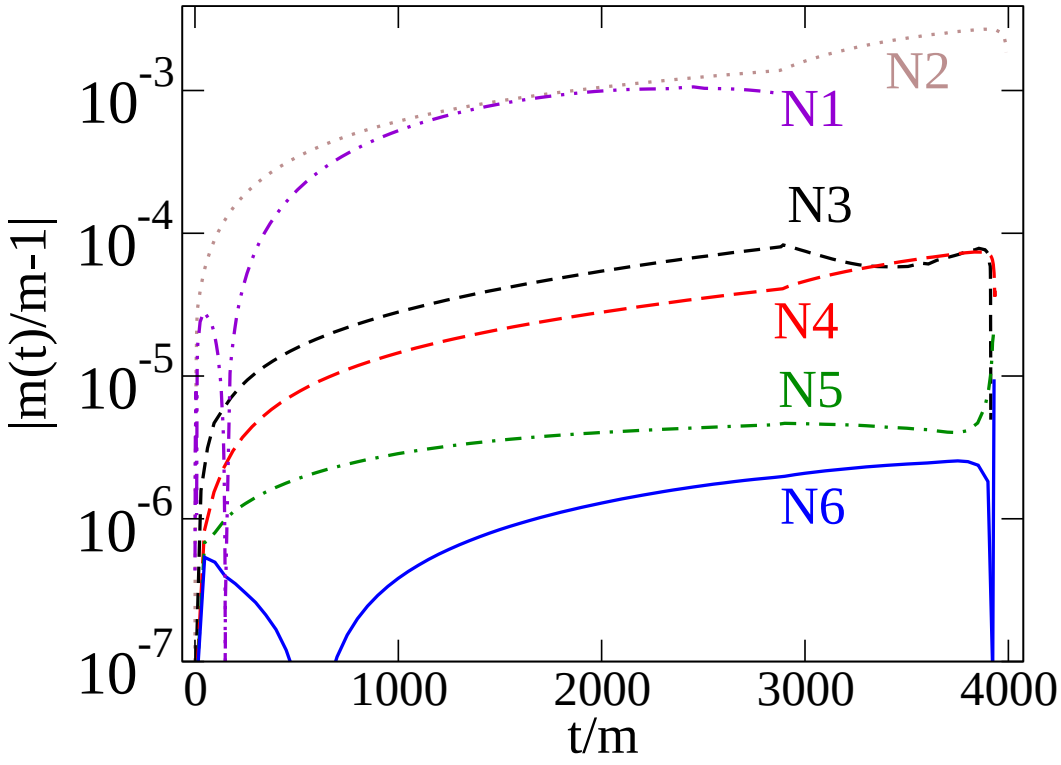

Figure 2.4: Deviation of total irreducible mass $m(t) = 2M_{\rm irr}(t)$ from its value in the initial data. Plotted are the six different resolutions of run 30a-1.

sion boundary moves radially outward at slightly faster than the speed of light so that it is causally disconnected from the interior region where the code is crashing, and so that no boundary conditions are required on this boundary. We then continue the evolution on the truncated spherical-shell domain that extends from the new excision boundary to the outer boundary. To move both boundaries appropriately, we employ a new radial coordinate mapping

$$r = A(t)r(r') + B(t), \tag{2.10}$$

where $r(r')$ is given by Eq. (2.9). The functions $A(t)$ and $B(t)$ are chosen to satisfy three criteria: First, the inner boundary of the spherical shell moves outward with coordinate speed of unity, which turns out to be slightly superluminal. Second, the outer boundary location $R_{\rm bdry}(t)$ has continuous first and second time derivatives at the time we transition to the truncated domain. And finally, the outer boundary location $R_{\rm bdry}(t)$ approaches some fixed value at late times. The right panel of Fig. 2.2 shows the motion of the inner and outer radii for evolutions 30c-1 and 30c-2 (we did not perform wave escorting for 30c-3). For 30c-1, wave escorting extends the evolution for an additional time $220m$ beyond the point at which the simulation stops in the center.

Figure 2.5 shows the gravitational waveform extracted at inertial coordinate radius $R = 240m$ for the run 30c-1. The brown vertical line indicates the time when wave escorting starts. Wave escorting allows us to extract another 4 cycles of gravitational waves. When computing the gravitational wave strain $h(t)$ from the Newman-Penrose scalar Ψ_4 (see Eq. (2.11) below), one must choose integration constants during the time integration. These integration constants were chosen such that $h(t)$ has zero average and first moment [197], which is is sufficiently accurate for the illustrative Fig. 2.5. To avoid errors caused by the choice of integration constants, the comparison to post-Newtonian waveforms

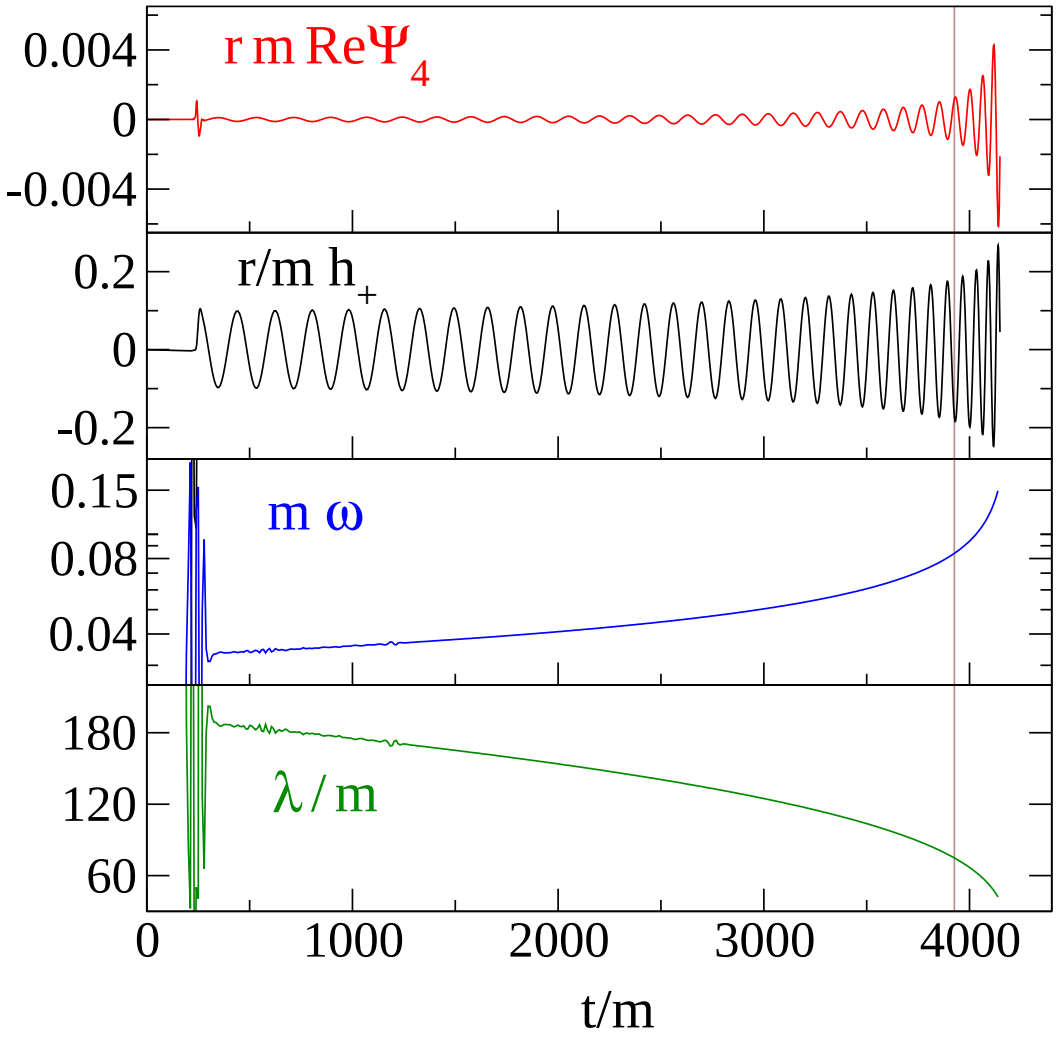

Figure 2.5: Gravitational waveform extracted at $r = 240m$. From top panel to bottom: The real part of the $(2, 2)$ component of $r\Psi_4$; the gravitational wave strain, obtained by two time integrals of $\mathrm{Re}(r\Psi_4)$; the frequency of the gravitational wave, Eq. (3.24); the gravitational wavelength, $\lambda = 2\pi/\omega$. The vertical brown line at $t \approx 3930m$ indicates the time when "wave escorting" starts.

below is based entirely on Ψ_4.

In the lower two panels of Fig. 2.5 there is a significant amount of noise near the beginning of the run, at $t < 250m$. This noise is barely evident in the top panel of Fig. 2.5 as well. The noise is a manifestation of 'junk radiation', a pulse of radiation often seen at the beginning of numerical relativity simulations, and is caused by the initial data not being precisely a snapshot of an evolution that has been running for a long time. Among the effects that produce junk radiation are incorrect initial distortions of the individual holes, so that each hole radiates as it relaxes to its correct quasi-equilibrium shape.

Our evolution code does not explicitly enforce either the Einstein constraints or the secondary constraints that arise from writing the system in first-order form. Therefore, examining how well these constraints are satisfied provides a useful consistency check. Figure 2.6 shows the constraint violations for run 30c-1. The top panel shows the L^2 norm of all the constraint fields of our first order generalized harmonic system, normalized by the L^2 norm of the spatial gradients of the dynamical fields (see Eq. (71) of Ref. [179]). The bottom panel shows the same quantity, but without the normalization factor (*i.e.*, just the numerator of Eq. (71) of Ref. [179]). The L^2 norms are taken over the entire computational volume that lies outside of apparent horizons. At early times, $t < 500m$, the constraints converge rather slowly with resolution because the junk radiation contains high frequencies. Convergence is more rapid during the smooth inspiral phase, after the junk radiation has exited through the outer boundary. The constraints increase around $t \sim 3900m$ as the code begins to fail near the two merging holes, but then the constraints decrease again after the failing region is excised for wave escorting. The normalized constraint violations are less than

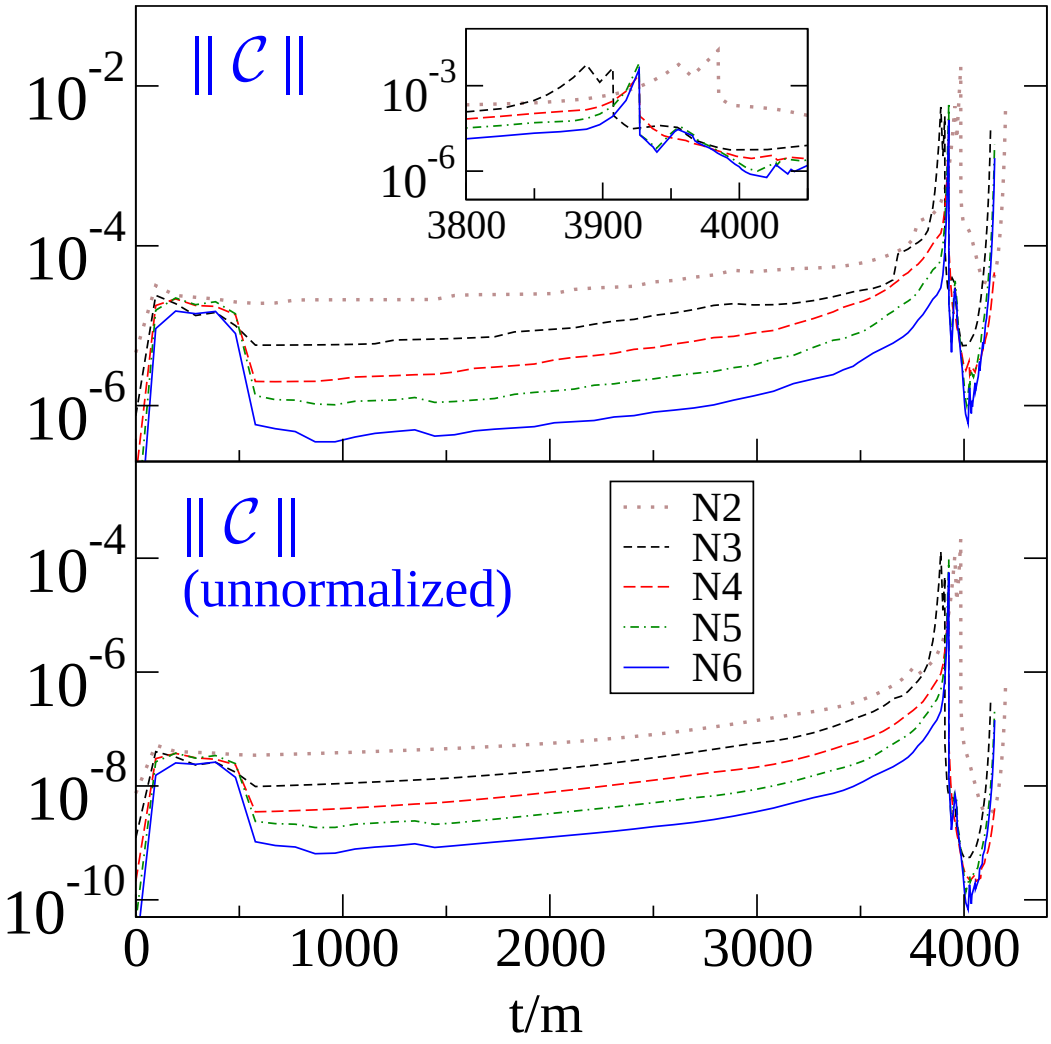

Figure 2.6: Constraint violations of run 30c-1. The top panel shows the L^2 norm of all constraints, normalized by the L^2 norm of the spatial gradients of all dynamical fields. The bottom panel shows the same data, but without the normalization factor. Norms are taken only in the regions outside apparent horizons.

10^{-4} until just before the peak (which occurs at $t = 3930m$ for all but the lowest resolutions). The size of the peak causes some concern that the waveforms at late times may be contaminated by constraint violations to a non-negligible degree. However, near the peak, the constraint violations are large only in the inner regions of the domain near the black holes (note that the curves in Fig. 2.6 decrease by two orders of magnitude immediately after these inner regions are excised at $t = 3930m$). Because all constraint quantities propagate at the speed of light or slower for the formulation of Einstein's equations that we use, any influence that the constraint peak has on the extracted waveform occurs after the constraint violations have had time to propagate out to the wave extraction zone. This is very late in the waveform, well after the gravitational wave frequency reaches $m\omega = 0.1$, as can be seen from the right panel of the spacetime diagram in Fig. 2.2.

2.2.4 Waveform extraction

Gravitational waves are extracted using the Newman-Penrose scalar Ψ_4, using the same procedure as in [197]. To summarize, given a spatial hypersurface with timelike unit normal n^μ, and given a spatial unit vector r^μ in the direction of wave propagation, the standard definition of Ψ_4 is the following component of the Weyl curvature tensor,

$$\Psi_4 = -C_{\alpha\mu\beta\nu}\ell^\mu\ell^\nu\bar{m}^\alpha\bar{m}^\beta, \tag{2.11}$$

where $\ell^\mu \equiv \frac{1}{\sqrt{2}}(n^\mu - r^\mu)$, and m^μ is a complex null vector (satisfying $m^\mu\bar{m}_\mu = 1$) that is orthogonal to r^μ and n^μ. Here an overbar denotes complex conjugation.

For (perturbations of) flat spacetime, Ψ_4 is typically evaluated on coordinate

spheres, and in this case the usual choices for n^μ, r^μ and m^μ are

$$n^\mu = \left(\frac{\partial}{\partial t}\right)^\mu, \tag{2.12a}$$

$$r^\mu = \left(\frac{\partial}{\partial r}\right)^\mu, \tag{2.12b}$$

$$m^\mu = \frac{1}{\sqrt{2}r}\left(\frac{\partial}{\partial \theta} + i\frac{1}{\sin\theta}\frac{\partial}{\partial \phi}\right)^\mu, \tag{2.12c}$$

where (r, θ, ϕ) denote the standard spherical coordinates. With this choice, Ψ_4 can be expanded in terms of spin-weighted spherical harmonics of weight -2:

$$\Psi_4(t, r, \theta, \phi) = \sum_{lm} \Psi_4^{lm}(t, r)\, {}_{-2}Y_{lm}(\theta, \phi), \tag{2.13}$$

where the Ψ_4^{lm} are expansion coefficients defined by this equation.

For curved spacetime, there is considerable freedom in the choice of the vectors r^μ and m^μ, and different researchers have made different choices [64, 125, 22, 189, 69, 71, 57] that are all equivalent in the $r \to \infty$ limit. We choose these vectors by first picking an extraction two-surface $\mathcal{E}$ that is a coordinate sphere ($r^2 = x^2 + y^2 + z^2$ using the global asymptotically Cartesian coordinates employed in our code) centered on the center of mass of the binary system, i.e. the point of symmetry. We choose r^μ to be the outward-pointing spatial unit normal to $\mathcal{E}$ (that is, we choose r_i proportional to $\nabla_i r$ and raise the index with the spatial metric). Then we choose m^μ according to Eq. (2.12c), using the standard spherical coordinates θ and ϕ defined on these coordinate spheres. Finally we use Eqs. (2.11) and (2.13) to define the Ψ_4^{lm} coefficients.

Note that the m^μ vector used here is not exactly null nor exactly of unit magnitude at finite r. The resulting Ψ_4^{lm} at finite r will disagree with the waveforms observed at infinity. Our definition does, however, agree with the standard definition given in Eqs. (2.11)–(2.13) as $r \to \infty$. Because we extrapolate the extracted waves to find the asymptotic radiation field (see Section 2.2.6), these

effects should not play a role in our PN comparisons: Relative errors in Ψ_4^{lm} introduced by using the simple coordinate tetrad fall off like $1/r$, and thus should vanish after extrapolating to obtain the asymptotic behavior. While more careful treatment of the extraction method—such as those discussed in [190, 193, 176]—may improve the quality of extrapolation and would be interesting to explore in the future, the naive choice made here should be sufficient to ensure that the waveform after extrapolation is correct to the accuracy needed for these simulations.

In this paper, we focus on the $(l, m) = (2, 2)$ mode. Following common practice (see e.g. [13, 57]), we split the extracted waveform into real phase ϕ and real amplitude A, defined by

$$\Psi_4^{22}(r, t) = A(r, t)e^{-i\phi(r,t)}. \tag{2.14}$$

The gravitational-wave frequency is given by

$$\omega = \frac{d\phi}{dt} \tag{2.15}$$

The minus sign in the definition of ϕ is chosen so that the phase increases in time and ω is positive. Equation (3.23) defines ϕ only up to multiples of 2π. These multiples of 2π are chosen to make ϕ continuous through each evolution, still leaving an overall multiple of 2π undetermined. We will consider only phase differences in this paper, so the choice of this overall phase offset is irrelevant.

2.2.5 Convergence of extracted waveforms

In this section we examine the convergence of the gravitational waveforms extracted at fixed radius, without extrapolation to infinity. This allows us to study

the behavior of our code without the complications of extrapolation. The extrapolation process and the resulting extrapolated waveforms are discussed in Sec. 2.2.6.

The top panel of Fig. 2.7 shows the convergence of the gravitational wave phase ϕ with numerical resolution for the run 30c-1. For this plot, the waveform is extracted at a fixed radius $R = 77m$. Each line shows the difference between ϕ computed at some particular resolution and ϕ computed from our highest-resolution run 30c-1/N6. When subtracting results at different resolutions, no time or phase adjustment has been performed. The difference in ϕ between the two highest-resolution runs is smaller than 0.03 radians throughout the run, and it is smaller than 0.02 radians between $t = 1000m$ and the point at which $m\omega = 0.1$.

At times before $1000m$, the phase convergence of our simulation is limited to about 0.05 radians because of effects of junk radiation (described at the end of Section 2.2.3). The sharp pulse of junk radiation has comparatively large numerical truncation error, and excites all characteristic modes at truncation-error level, including waves that propagate back toward the origin. Generation of these secondary waves stops when the pulse of junk radiation leaves through the outer boundary (*i.e.*, after one light-crossing time). Because we use the improved outer boundary conditions of Rinne et al. [208], there are no significant reflections when the junk radiation passes through the outer boundary. However, the waves produced before the junk radiation leaves remain in the computational domain for two additional light-crossing times, until they eventually leave through the outer boundary.

The bottom panel of Fig. 2.7 shows phase comparisons between different

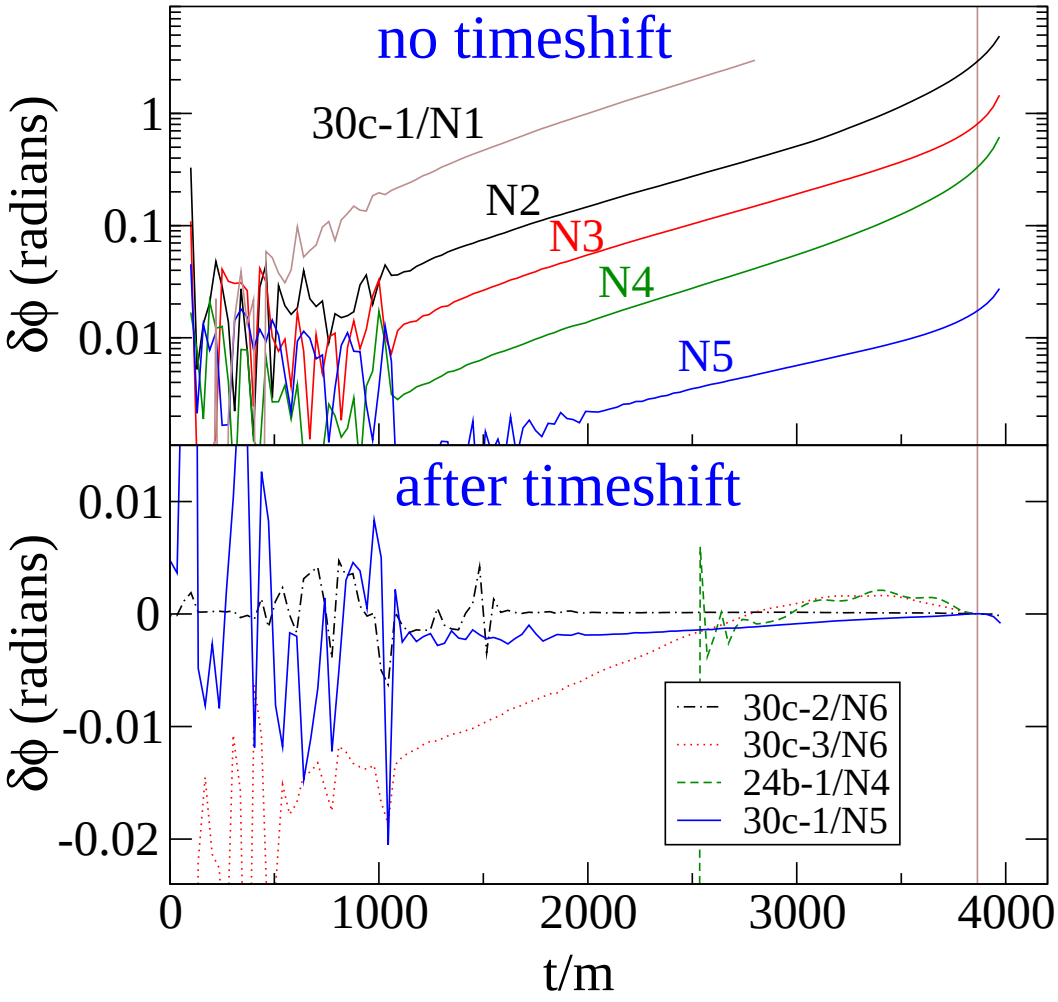

Figure 2.7: Convergence of the gravitational wave phase extracted at radius $R = 77m$. All lines show differences with respect to our highest resolution run, 30c-1/N6. The top panel shows different resolutions of the same run 30c-1; no time or phase shifts have been performed. The bottom panel compares different runs, aligning the runs at $m\omega = 0.1$ by a time and phase shift. The thin vertical line indicates the time at which $m\omega = 0.1$ for 30c-1/N6.

waveforms after we perform a time shift and phase shift so that the waveforms agree at $m\omega = 0.1$. Our procedure for time shifting and phase shifting is the same as the shifting procedure we use to compare NR with PN waveforms (see Sec. 4.6.1), so that the error estimates we extract from the bottom panel of Fig. 2.7 are relevant for our later NR-PN comparison.

There are three different types of comparisons shown in the bottom panel of Fig. 2.7: Phase differences between runs with the same initial data but with different outer boundary locations, phase differences between runs with different initial data, and phase differences between different numerical resolutions of the same run (this last comparison is the same as what is shown in the top panel, except in the bottom panel the waveforms are time and phase shifted). We will discuss all three of these in turn.

First, we compare the phase difference of 30c-1/N6 with runs that have different outer boundary locations. Run 30c-2 (with more distant outer boundary) agrees to within 0.002 radians with run 30c-1, but run 30c-3 (with closer outer boundary), has a much larger phase difference with 30c-1. We believe that this is because run 30c-3 has a very small ratio of outer boundary location to gravitational wavelength: R/λ is about 1.1 for the first two-thirds of the run, and remains less than 2 for the entire run.

We can explain the order of magnitude of these phase differences using the analysis of Buchman & Sarbach [58]. Our outer boundary conditions are not perfectly absorbing, but instead they reflect some fraction of the outgoing radiation.[6] The ratio of the amplitude of curvature perturbations (i.e. Ψ_4) of the

[6]However, in a comparison of various boundary conditions [208], the boundary conditions we use produced smaller reflections than other boundary conditions commonly used in numerical relativity.

reflected wave to that of the outgoing wave is

$$q \approx \frac{3}{2(2\pi)^4}\left(\frac{\lambda}{R}\right)^4. \tag{2.16}$$

The incoming reflected waves grow like $1/r$ as they travel inward just like the outgoing waves decrease by $1/r$ as they propagate outward. Therefore, the ratio of amplitudes of incoming and outgoing waves will have approximately the same value, q, at smaller radii, and we assume for the sake of this rough argument that this ratio remains equal to q even in the vicinity of the black holes (where it is no longer technically meaningful to talk about 'radiation'). Now consider the second time derivative of the gravitational wave phase, $\ddot{\phi}$; this is nonzero only because of gravitational wave emission, so $\ddot{\phi}$ is proportional to some power of the outgoing wave amplitude. To get the correct power, we can use Eq. (2.45) to find $\dot{x} \sim x^5$, so Eq. (2.36) yields $\ddot{\phi} \sim x^{11/2}$ (we assume gravitational wave phase is twice the orbital phase). The amplitude of Ψ_4 scales like x^4, so $\ddot{\phi} \sim A^{11/8}$. Let us assume for the sake of this rough error estimate that the change in $\ddot{\phi}$ due to the *ingoing* reflected wave scales similarly with amplitude, $\ddot{\phi} \sim \bar{A}^{11/8}$, where $\bar{A} = qA$ is the amplitude of the reflected ingoing wave. Therefore the unphysical gravitational-wave force acting back on the system due to boundary reflections will cause fractional errors in the second derivative of the phase of about $q^{11/8}$. That is, the error $\delta\phi$ caused by the improper boundary condition will be given by

$$\frac{d^2\delta\phi}{dt^2} = q^{11/8}\frac{d^2\phi}{dt^2}. \tag{2.17}$$

Integrating this yields $\delta\phi = q^{11/8}\phi$, where ϕ is the total gravitational wave phase accumulated during the evolution. For 30c-3, $\lambda/R \sim 0.9$, so $q \sim 6 \times 10^{-4}$, which yields $\delta\phi \sim 0.08$ radians for an accumulated gravitational wave phase of about 200 radians. This rough estimate agrees in order of magnitude with the phase difference between 30c-3 and 30c-1 as shown in the bottom panel of Figure 2.7.

The run 30c-1 has an outer boundary about 2.5 farther away, reducing the reflection coefficient by a factor $2.5^4 \approx 40$, so for 30c-1 this estimate of the phase error gives $\delta\phi = 5 \times 10^{-4}$ radians. Therefore, we expect reflection of the outgoing radiation at the outer boundary to be insignificant for 30c-1. This is confirmed by the excellent agreement between runs 30c-1 and 30c-2 (the latter having even larger outer boundary).

The second comparison shown in the lower panel of Fig. 2.7 is the phase difference between 30c-1/N6 and 24b-1/N4, a shorter 8-orbit evolution started from a separate initial data set (set 24b in Table 2.1) with a separate eccentricity-reduction procedure. The phase agreement between these two runs (including an overall time shift and phase shift) is better than 0.01 radians for a total accumulated phase of ~ 100 radians of the 8-orbit run, i.e. better than one part in 10^4. Run 24b-1 has a similar outer boundary location as run 30c-3, and indeed both of these runs show similar phase differences from 30c-1.

Finally, the third comparison shown in the lower panel of Fig. 2.7 is the phase difference between the two highest resolutions of the run 30c-1 when a time shift is applied. For $t \gtrsim 1000m$ the agreement is much better than without the time shift (see upper panel), indicating that the dominant error is a small difference in the overall evolution time. For the post-Newtonian comparisons we perform in the second part of this paper, waveforms are always aligned at specific frequencies by applying time and phase shifts. Therefore, the time-shifted phase difference as displayed in the lower panel is the most appropriate measure of numerical truncation error for these PN comparisons. This difference is less than 0.003 radians after $t = 1000m$ but is larger, about 0.02 radians, at early times where the waveforms are noisy because of junk radiation.

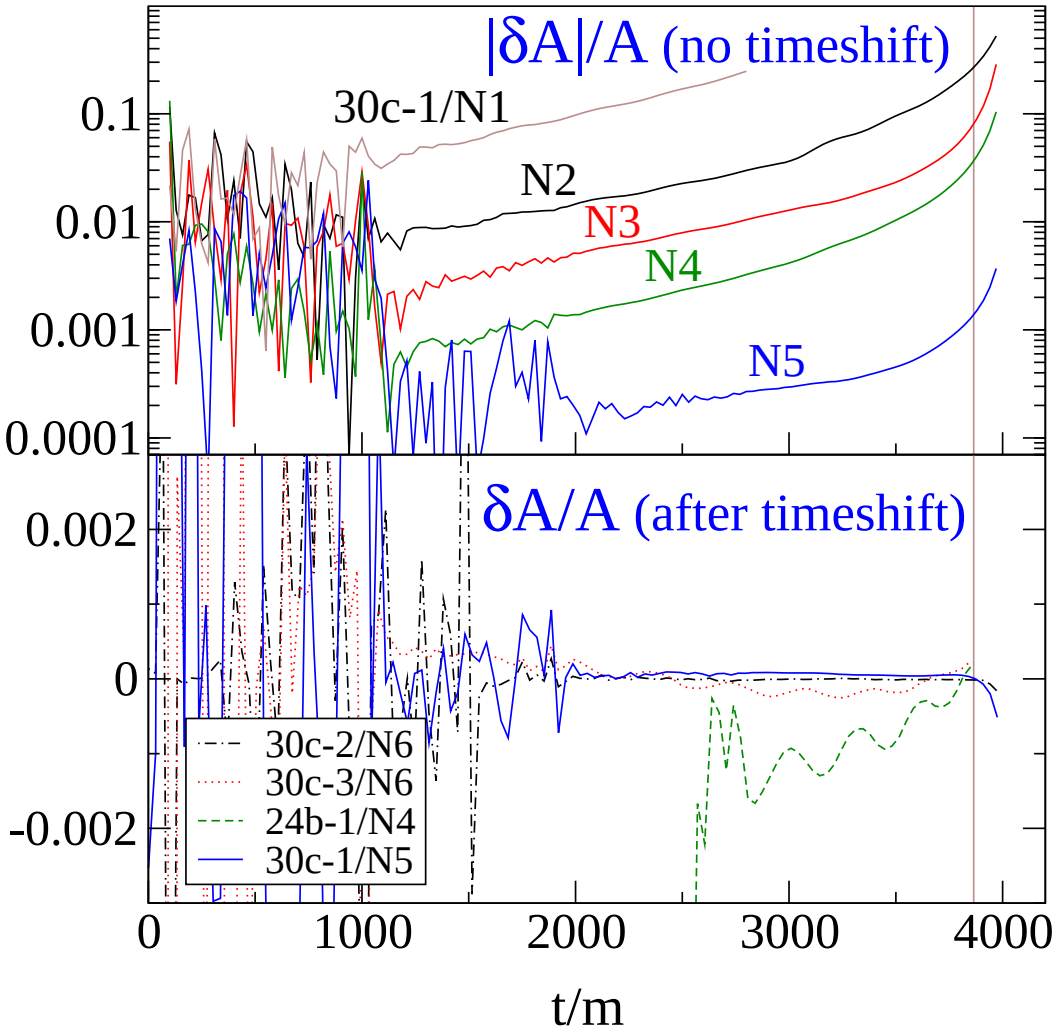

Figure 2.8: Convergence of the gravitational wave amplitude extracted at radius $R = 77m$. This plot corresponds to Fig. (2.7), except that relative amplitude differences are shown. The thin vertical line indicates the time at which $m\omega = 0.1$ for 30c-1/N6.

We now compare the gravitational wave amplitudes of different runs in the same manner as we compared the gravitational wave phases. Figure 2.8 presents convergence data for the amplitude of the gravitational waves for the same runs as shown in Fig. 2.7. Spatial truncation error for the amplitude is less then 0.1 percent for $t/m > 1000$, and earlier than this it is limited by residual noise from the junk radiation. Differences (including time shifts) between runs of different lengths are shown in the lower panel of Fig. 2.8. These differences are even smaller, but because of their small size, they are dominated by noise for about the first half of the run. The oscillations apparent in the comparison to 24b-1 are caused by the larger orbital eccentricity of 24b-1 (cf. Tab. 2.1).

2.2.6 Extrapolation to infinity

The quantity of interest to gravitational wave detectors is the gravitational waveform as seen by an observer effectively infinitely far from the source. Our numerical simulations, in contrast, cover only a region of finite volume around the source, and our numerical waveforms are extracted at a finite radius. Waveforms extracted at a finite radius can differ from those extracted at infinity because of effects discussed in Section 2.2.4; these effects can lead to phase errors of several tenths of a radian and relative amplitude errors of several percent. To avoid such errors we extrapolate to infinite extraction radius as follows.

We extract data for Ψ_4 on coordinate spheres of coordinate radii $r/m = 75, 80, 85, \ldots, 240$, as described in Section 2.2.4. These extracted waveforms are shifted in time relative to one another because of the finite light-travel time between these extraction surfaces. We correct for this by shifting each waveform

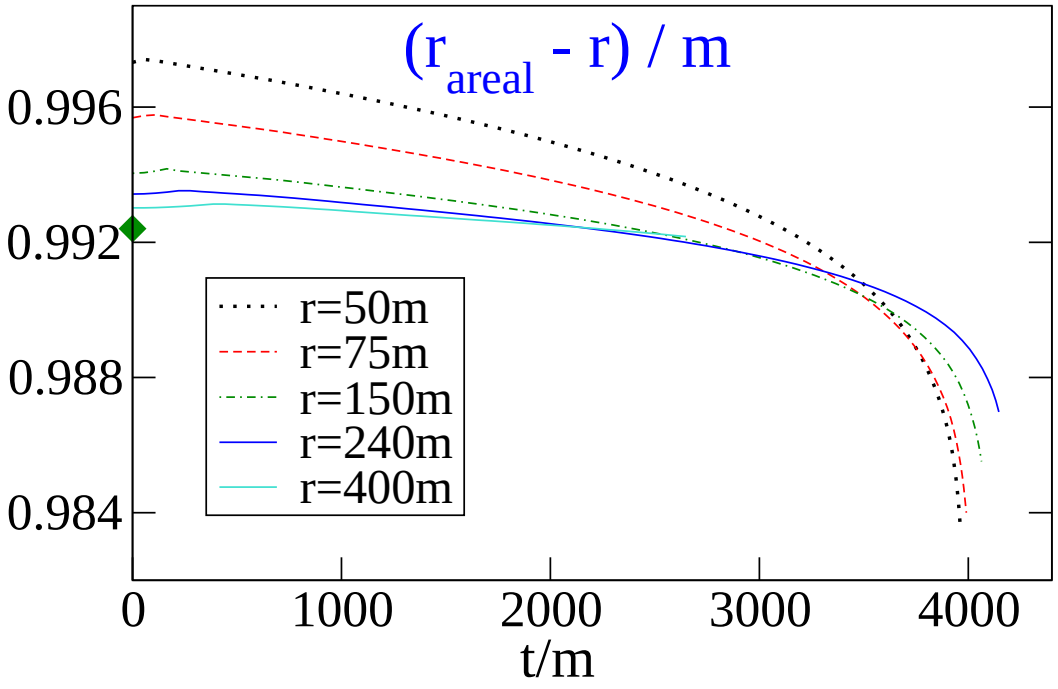

Figure 2.9: Difference between areal radius r_{areal} and coordinate radius r of selected extraction surfaces. r_{areal} remains constant to within $0.01m$ during the evolution. The diamond indicates M_{ADM}/m of the initial data.

by the tortoise-coordinate radius at that extraction point [125]

$$r^* = r_{\rm areal} + 2M_{\rm ADM} \ln\left(\frac{r_{\rm areal}}{2M_{\rm ADM}} - 1\right). \tag{2.18}$$

Here $M_{\rm ADM}$ is the ADM mass of the initial data, and $r_{\rm areal} = \sqrt{A/4\pi}$, where A is the area of the extraction sphere. This is not the only possible choice for the retarded time—for example, the waveforms could be shifted so that the maxima of the amplitude align [141]. It has also been suggested [169] that the time shift should change with the amount of radiated energy—essentially, that the factor of $M_{\rm ADM}$ should be replaced by the amount of mass interior to the extraction radius at each time. We leave investigation of other choices of retarded time for future work.

Figure 2.9 presents the areal radius during the evolution at several typical extraction radii. The areal radius of these extraction surfaces is constant to within about $0.01m$, and to the same precision, $r_{\rm areal} = r + M_{\rm ADM}$. This relationship is not surprising, because the initial data is conformally flat, so that for coordinate spheres $r_{\rm areal} = r + M_{\rm ADM} + O(M_{\rm ADM}/r)$. For convenience, we simply set $r_{\rm areal} = r + M_{\rm ADM}$ in Eq. (2.18), rather than explicitly integrating to find the area of each extraction sphere.

After the time shift, each waveform is a function of retarded time, $t - r^*$. At a given value of retarded time, we have a series of data points—one for each extraction radius. We fit phase and amplitude of these data separately to a polynomial in $1/r$,

$$\phi(t - r^*, r) = \phi_{(0)}(t - r^*) + \sum_{k=1}^{n} \frac{\phi_{(k)}(t - r^*)}{r^k}, \tag{2.19}$$

$$rA(t - r^*, r) = A_{(0)}(t - r^*) + \sum_{k=1}^{n} \frac{A_{(k)}(t - r^*)}{r^k}. \tag{2.20}$$

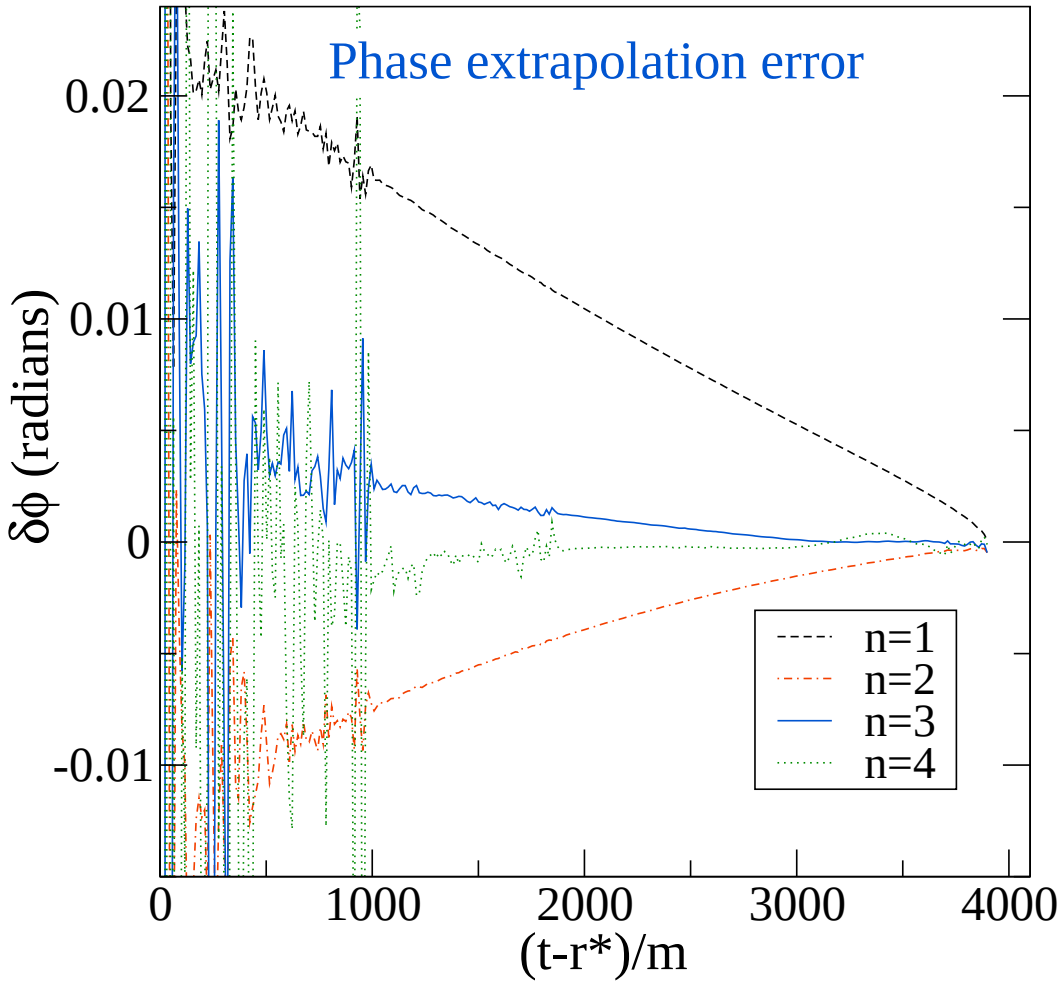

Figure 2.10: Error of phase extrapolation to infinity for extrapolation of order n, cf. Eq. (2.19). Plotted are absolute differences between extrapolation with order n and $n + 1$. Increasing the order of the polynomial increases accuracy, but also amplifies noise.

The leading-order term of each polynomial, as a function of retarded time, is then the desired asymptotic waveform:

$$\phi(t - r^*) = \phi_{(0)}(t - r^*), \tag{2.21}$$

$$rA(t - r^*) = A_{(0)}(t - r^*). \tag{2.22}$$

We find good convergence of this method as we increase the order n of the extrapolating polynomial. Figure 2.10 shows the difference in phase between waveforms extrapolated using successively higher-order polynomials. We see a broad improvement in the accuracy of the phase with increasing order, but unfortunately, higher order extrapolations tend to amplify the noise. Our preferred choice is $n = 3$ extrapolation, resulting in extrapolation errors of $\lesssim 0.003$ radians for $t - r^* \gtrsim 1000m$.

Figure 2.11 is analogous to Fig. 2.10, except that it shows relative differences in the extrapolated amplitudes. The basic picture agrees with the phase extrapolation: Higher order extrapolation reduces the errors, but amplifies noise. Our preferred choice $n = 3$ gives a relative amplitude error of $\lesssim 0.002$ for $t - r^* \gtrsim 1000m$, dropping to less than 0.001 for $t - r^* \gtrsim 2000m$.

Phase and amplitude extrapolation become increasingly more accurate at late times. The main obstacle to accuracy seems to be near-zone effects scaling with powers of (λ/r), where λ is the wavelength of the gravitational wave. The wavelength is quite large at the beginning of the simulation ($\lambda \approx 180m$, cf. Fig. 2.5), but becomes shorter during the evolution, so that even low-order extrapolation is quite accurate at late times. Alternatively, near-zone effects can be mitigated by using data extracted at large values of r. It is precisely because of these near-zone effects that we have chosen to ignore data extracted at $r < 75m$

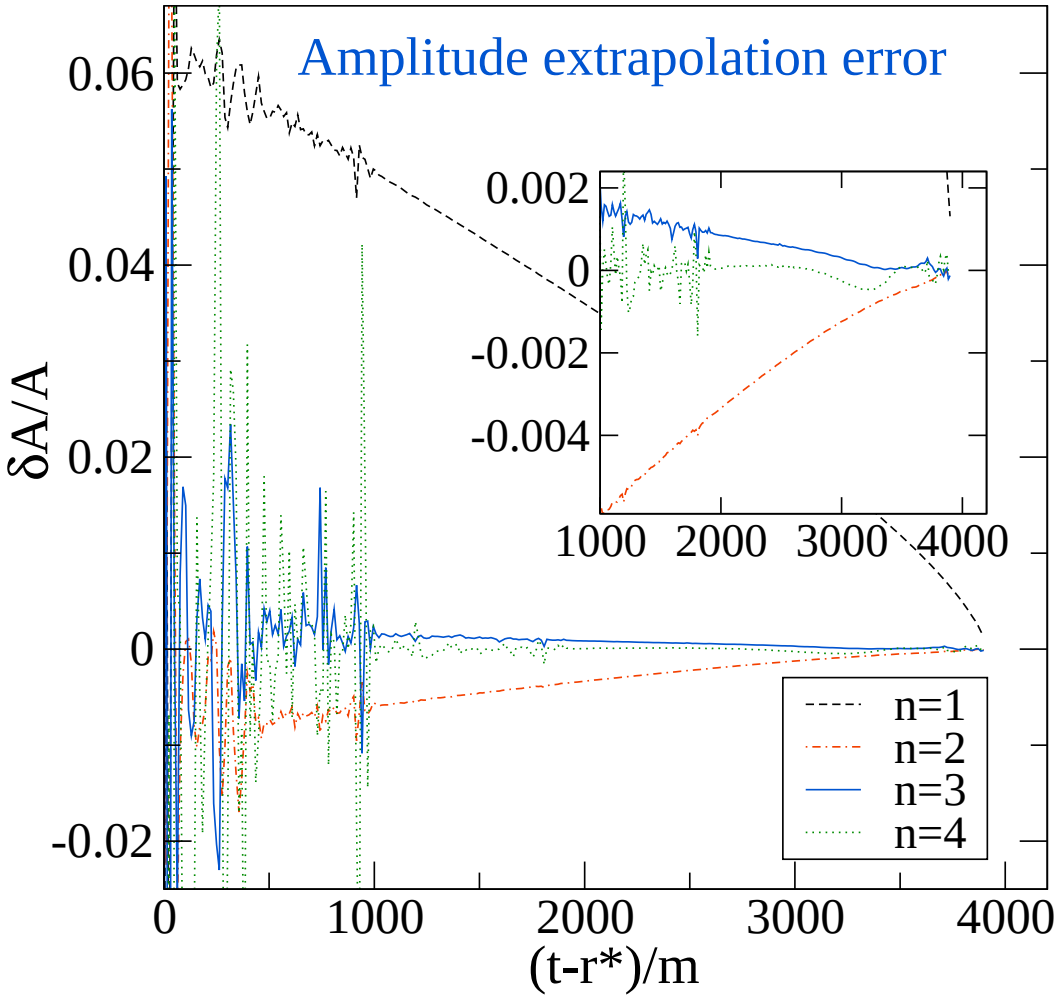

Figure 2.11: Error of amplitude extrapolation to infinity for extrapolation with order n, cf. Eq. (2.20). Plotted are relative amplitude differences between extrapolation with orders n and $n+1$. The inset is an enlargement for $t - r^* \geq 1000m$.

when we extrapolate to infinity.

In Figs. 2.12 and 2.13, we show the effects of extrapolation using different ranges of extracted data. Using data extracted every $5m$ in the range $r = 50m$–$90m$ results in noticeable differences early in the run—though it is adequate later in the run. For ranges at higher radii (e.g. $[75m, 150m]$ or $[150m, 240m]$), the accuracy is not highly variable, though we find that noise is increased when using data from such a smaller range of extraction radii.

To estimate the errors generated by not extrapolating waveforms to infinity at all, Fig. 2.12 contains also the phase difference between wave extraction at two finite radii ($90m$ and $240m$) and our preferred extrapolated phase at infinity. The dotted lines show such phase differences when only a time shift by the tortoise-coordinate radius of the extraction sphere is applied. The errors are dramatic, tenths of radians or more, even very late in the run. When matching to post-Newtonian waveforms, we are free to add an overall time and phase shift (cf. Section 4.6.1). Therefore, the dashed lines in Fig. 2.12 show phase differences with the same unextrapolated waveforms as shown by the dotted lines, except that a phase and time shift has been applied so that the ϕ and $\dot{\phi}$ agree with those of the extrapolated waveform late in the run (where $m\omega = 0.1$), where the wavelengths are shortest and wave extraction is expected to work best. Even with such an adjustment, the gravitational wave phase extracted at $r = 90m$ differs by about 0.1 radian at $t \sim 1000m$ before coalescence, with this difference growing to 0.3 radians at the start of our simulation.

Figure 2.13 makes the same comparison for the gravitational wave amplitude. Wave extraction at $r = 90m$ results in relative amplitude errors of up to 8 per cent, and of about 2 per cent even in the last $1000m$ of our simulation. We

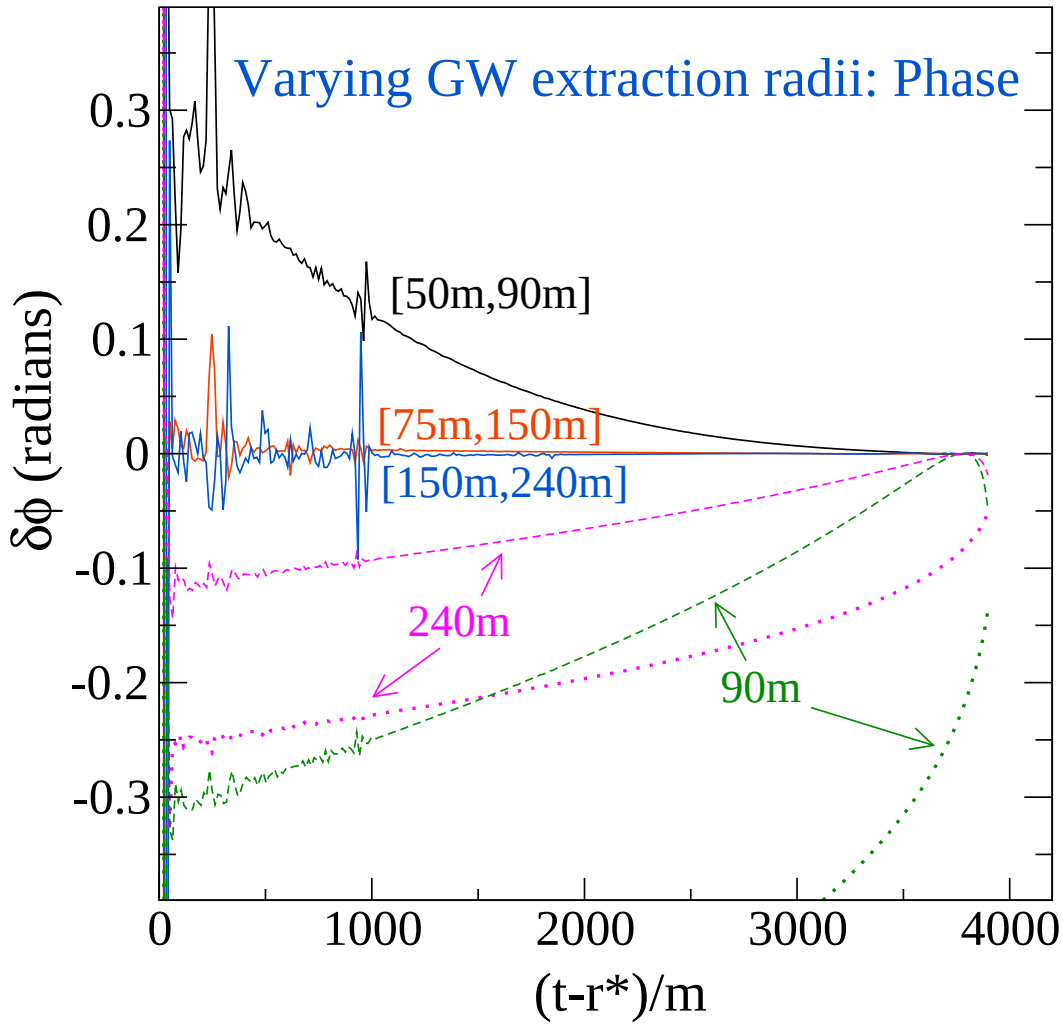

Figure 2.12: Effect of wave extraction radii on extrapolated phase. Each curve represents the difference from our preferred wave extrapolation using $r \in [75m, 240m]$. The three solid curves represent extrapolation from different intervals of extraction radii. The curves labeled "240m" and "90m" represent differences from waves extracted at these two radii, without any extrapolation, for two cases: time and phase shifted so that ϕ and $\dot{\phi}$ match at $m\omega = 0.1$ (dashed), and without these shifts (dotted).

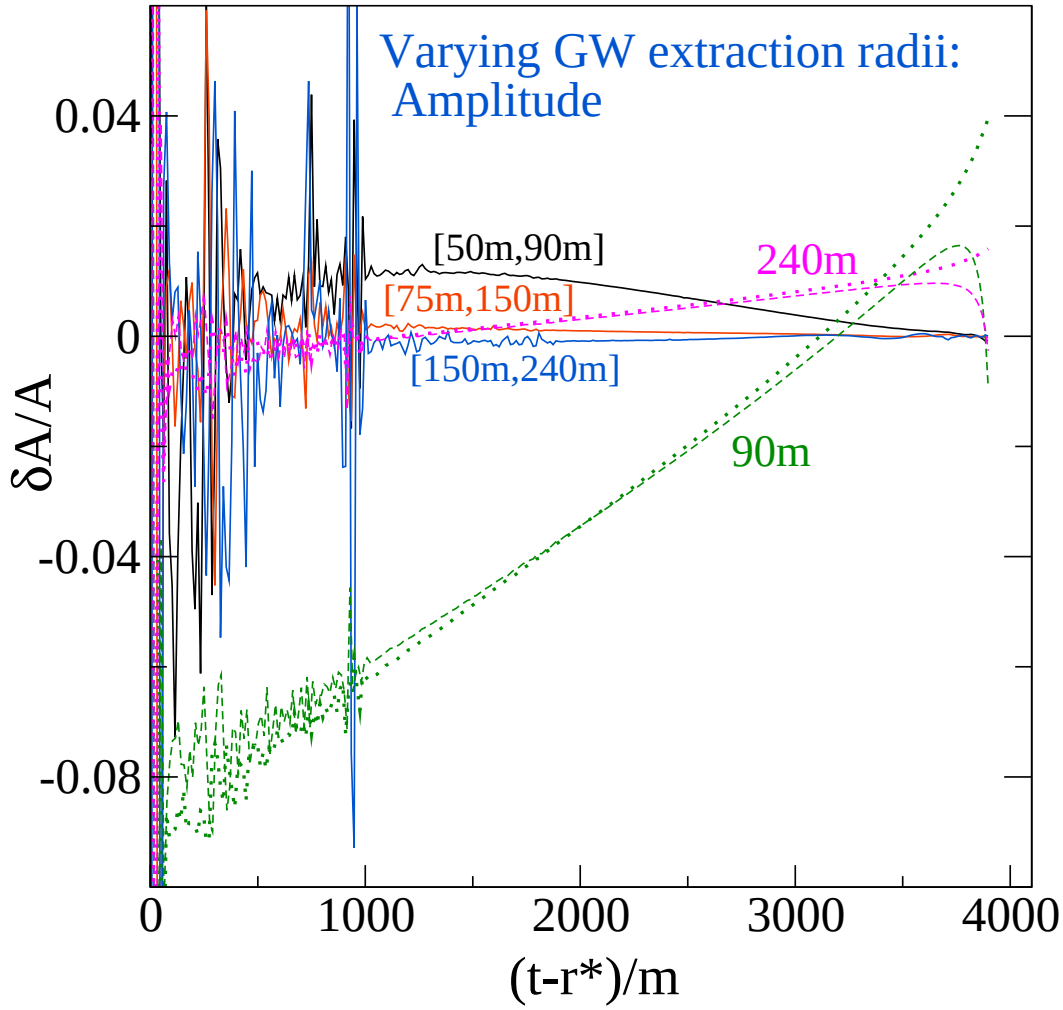

Figure 2.13: Effect of choice of wave extraction radii on extrapolated amplitude. Each curve represents the (relative) amplitude difference to our preferred wave extrapolation using $r \in [75m, 240m]$. The three solid curves represent extrapolation from different intervals of extraction radii. The curves labeled "240m" and "90m" represent differences from waves extracted at these two radii, without any extrapolation, for two cases: time and phase shifted so that ϕ and $\dot{\phi}$ match at $m\omega = 0.1$ (dashed), and without these shifts (dotted).

also point out that the errors due to finite extraction radius decay approximately as the inverse of the extraction radius: For waves extracted at $r = 240m$ the errors are smaller than for waves extracted at $r = 90m$ by about a factor of three, as can be seen in Figs. 2.12 and 2.13; for wave extraction at $r = 45m$, the errors would be approximately twice as large as the $r = 90m$ case. The errors introduced by using a finite extraction radius are significantly larger than our truncation error (even at extraction radius $240m$). Therefore extrapolation to infinity is essential to realize the full accuracy of our simulations.

2.2.7 Estimated time of merger

Since we have not yet been successful with simulating the merger, we do not precisely know when merger occurs. However, by comparing the orbital and gravitational wave frequencies to already published results, we can nevertheless estimate the time of merger.

The simulation presented in Fig. 2.3 stops at time $t = 3929m$ when the horizons of the black holes become too distorted just before merger. At that point, the proper separation between the horizons is $\sim 4.0m$, and the orbital frequency has reached $m\Omega_{\rm orbit} = 0.125$; comparison with [64] suggests this is about $15m$ before formation of a common apparent horizon, i.e. the common horizon should form in our simulations at $t_{\rm CAH} \approx 3945m$.

The waveform extrapolated to infinity ends at $t - r^* = 3897m$ at a gravitational wave frequency of $m\omega \approx 0.16$. This places the end of the waveform at about $50m$ (or ~ 1.5 cycles) before formation of a common apparent horizon[7] (judged by

[7]The waveform ends somewhat further from merger than the orbital trajectory, because the

comparison with [64]). Thus, we estimate the formation of a common horizon to correspond to a retarded time of approximately $(t - r^*)_{\rm CAH} \approx 3950m$.

2.3 Generation of post-Newtonian waveforms

It is not our intention to review all of post-Newtonian (PN) theory, but to summarize the important points that go into the construction of the post-Newtonian waveforms that we will compare to our numerical simulation. For a complete review of post-Newtonian methods applied to inspiralling compact binaries, see the review article by Blanchet[35].

The post-Newtonian approximation is a slow-motion, weak-field approximation to general relativity with an expansion parameter $\epsilon \sim (v/c)^2 \sim (Gm/rc^2)$. For a binary system of two point masses m_1 and m_2, v is the magnitude of the relative velocity, m is the total mass, and r is the separation. In order to produce a post-Newtonian waveform, it is necessary to solve both the post-Newtonian equations of motion describing the binary, and the post-Newtonian equations describing the generation of gravitational waves.

Solving the equations of motion yields explicit expressions for the accelerations of each body in terms of the positions and velocities of the two bodies[158, 159, 107, 109, 41, 42, 108, 38, 155, 154, 153]. The two-body equations of motion can then be reduced to relative equations of motion in the center-of-mass frame in terms of the relative position and velocity[45]. The relative acceleration is currently known through 3.5PN order, where 0PN order for the

artificial boundary is placed initially at a radius $\sim 15m$, and then moves outward somewhat faster than the speed of light, thus overtaking the very last part of the waveform as it travels to the wave-extraction radii.

equations of motion corresponds to Newtonian gravity. The effects of radiation reaction (due to the emission of gravitational waves) enters the relative acceleration starting at 2.5PN order. The relativistic corrections to the relative acceleration at 1PN, 2PN and 3PN order (ignoring the radiation reaction terms at 2.5PN and 3.5PN order) admit a conserved center of mass binding energy through 3PN order[115]. There is no 2.5PN or 3.5PN order contribution to the energy.

Solving the post-Newtonian wave generation problem yields expressions for the gravitational waveform h_{ij} and gravitational wave flux $\mathcal{L}$ in terms of radiative multipole moments[225]. These radiative multipole moments are in turn related to the source multipole moments, which can be given in terms of the relative position and relative velocity of the binary[32]. For the gravitational wave generation problem, PN orders are named with respect to the leading order waveform and flux, which are given by the quadrupole formalism. Thus, for example, 1.5PN order in the wave generation problem represents terms of order $(v/c)^3$ beyond quadrupole. Higher order effects enter both through post-Newtonian corrections to the mass quadrupole, as well as effects due to higher multipole moments. Starting at 1.5PN order the radiative multipole moments include non-linear and non-instantaneous (i.e. depend upon the past history of the binary) interactions among the source multipole moments (e.g. gravitational wave tails)[32, 37, 33, 31].

It was recognized early that simply plugging in the orbital evolution predicted by the equations of motion into the expressions for the waveform would not generate templates accurate enough for matched filtering in detecting gravitational waves[87]. This is because radiation reaction enters the equations of

motion only at the 2.5PN order; hence computing a waveform to k PN order beyond the quadrupole formalism would require $2.5 + k$ PN orders in the equations of motion. In order to obtain as accurate a post-Newtonian waveform as possible it is thus necessary to introduce the assumption of an adiabatic inspiral of a quasi-circular orbit, as well as the assumption of energy balance between the orbital binding energy and the energy emitted by the gravitational waves.

2.3.1 Adiabatic inspiral of quasi-circular orbits

The emission of gravitational radiation causes the orbits of an isolated binary system to circularize [194]. Thus it is a reasonable assumption to model the orbital evolution of the binary as a slow adiabatic inspiral of a quasi-circular orbit. With this assumption, post-Newtonian expressions for the orbital energy E and gravitational energy flux $\mathcal{L}$ are currently known through 3.5PN order [47, 43, 46, 39, 40]. These expressions can be given in terms of a parameter related to either the harmonic coordinate separation r, or to the orbital frequency Ω. We choose to use the expressions given in terms of a frequency-related parameter

$$x \equiv \left(\frac{Gm\Omega}{c^3}\right)^{2/3} \tag{2.23}$$

rather than a coordinate-related parameter, because the coordinate relationship between the numerical simulation and the harmonic coordinates used in post-Newtonian approximations is unknown. The orbital energy for an equal mass system is given by[35]

$$E = -\frac{mc^2}{8}x\left[1 - \frac{37}{48}x - \frac{1069}{384}x^2 + \left(\frac{1427365}{331776} - \frac{205}{384}\pi^2\right)x^3\right], \tag{2.24}$$

and the gravitational wave flux for an equal mass system is given by [35]

$$\begin{aligned}\mathcal{L} &= \frac{2c^5}{5G}x^5\left\{1-\frac{373}{84}x+4\pi x^{3/2}-\frac{59}{567}x^2-\frac{767}{42}\pi x^{5/2}\right.\\ &\quad+\left[\frac{18608019757}{209563200}+\frac{355}{64}\pi^2-\frac{1712}{105}\gamma\right.\\ &\quad\left.\left.-\frac{856}{105}\ln(16x)\right]x^3+\frac{16655}{6048}\pi x^{7/2}\right\},\end{aligned} \tag{2.25}$$

where $\gamma = 0.577216\ldots$ is Euler's constant.

2.3.2 Polarization Waveforms

The gravitational polarization waveforms for a quasi-circular orbit in the $x-y$ plane, as measured by an observer at spherical coordinates $(R, \hat{\theta}, \hat{\phi})$, are given by

$$h_+ = \frac{2G\mu}{c^2R}x\left\{-(1+\cos\hat{\theta})\cos 2(\Phi-\hat{\phi})+\cdots\right\} \tag{2.26}$$

$$h_\times = \frac{2G\mu}{c^2R}x\left\{-2\cos\hat{\theta}\sin 2(\Phi-\hat{\phi})+\cdots\right\}, \tag{2.27}$$

where Φ is the orbital phase (measured from the x-axis) and $\mu = m_1m_2/m$ is the reduced mass. The polarization waveforms are currently known through 2.5PN order[6, 165].

Optimally oriented observer

For an equal-mass binary the polarization waveforms along the z-axis (i.e. the optimally oriented observer along the normal to the orbital plane) are given by

[6, 165]

$$h_+^{(z)} = \frac{Gm}{2c^2R}x\Bigg(\cos 2\Phi\left\{-2+\frac{17}{4}x-4\pi x^{3/2}+\frac{15917}{2880}x^2+9\pi x^{5/2}\right\} + \sin 2\Phi\left\{-12\ln\left(\frac{x}{x_0}\right)x^{3/2}+\left[\frac{59}{5}+27\ln\left(\frac{x}{x_0}\right)\right]x^{5/2}\right\}\Bigg) \quad (2.28)$$

$$h_\times^{(z)} = \frac{Gm}{2c^2R}x\Bigg(\sin 2\Phi\left\{-2+\frac{17}{4}x-4\pi x^{3/2}+\frac{15917}{2880}x^2+9\pi x^{5/2}\right\} + \cos 2\Phi\left\{12\ln\left(\frac{x}{x_0}\right)x^{3/2}-\left[\frac{59}{5}+27\ln\left(\frac{x}{x_0}\right)\right]x^{5/2}\right\}\Bigg), \quad (2.29)$$

where

$$\ln x_0 \equiv \frac{11}{18}-\frac{2}{3}\gamma+\frac{2}{3}\ln\left(\frac{Gm}{4bc^3}\right) \quad (2.30)$$

is a constant frequency scale that depends upon the constant time scale b entering the gravitational wave tail contribution to the polarization waveforms [233, 49]. The freely-specifiable constant b corresponds to a choice of the origin of radiative time T with respect to harmonic time t, and enters the relation between the retarded time $T_R = T - R/c$ in radiative coordinates (the coordinates in which the waveform is given) and the retarded time $t - r/c$ in harmonic coordinates (the coordinates in which the equations of motion are given) [233, 49]:

$$T_R = t - \frac{r}{c} - \frac{2GM_{\rm ADM}}{c^3}\ln\left(\frac{r}{bc}\right). \quad (2.31)$$

Here $M_{\rm ADM}$ is the ADM mass (mass monopole) of the binary system.

The (2,2) mode

When comparing a post-Newtonian waveform with data from a physical gravitational wave detector, it is necessary to compare waves emitted in a certain direction $(\hat{\theta}, \hat{\phi})$ with respect to the source. However, comparing waveforms between PN and numerical simulations can be done in all directions simultaneously by decomposing the waveforms in terms of spherical harmonics and then

comparing different spherical harmonic modes. Since the power in each spherical harmonic mode decreases rapidly with spherical harmonic index, with the $(2,2)$ mode dominating (for an equal-mass non-spinning binary), it is possible to do a very accurate comparison that is valid for all angles by using only a few modes. In addition, as pointed out by Kidder [164], the dominant (2,2) mode can be computed to 3PN order. For an equal-mass binary, the (2,2) mode is

$$\begin{aligned} h_{(2,2)} &= -2\sqrt{\frac{\pi}{5}}\frac{Gm}{c^2R}e^{-2i\Phi}x\left\{1-\frac{373}{168}x+\left[2\pi+6i\ln\left(\frac{x}{x_0}\right)\right]x^{3/2}-\frac{62653}{24192}x^2\right. \\ &\quad -\left[\frac{197}{42}\pi+\frac{197i}{14}\ln\left(\frac{x}{x_0}\right)+6i\right]x^{5/2} \\ &\quad +\left[\frac{43876092677}{1117670400}+\frac{99}{128}\pi^2-\frac{428}{105}\ln x-\frac{856}{105}\gamma\right. \\ &\quad \left.\left.-\frac{1712}{105}\ln 2-18\left[\ln\left(\frac{x}{x_0}\right)\right]^2+\frac{428}{105}i\pi+12i\pi\ln\left(\frac{x}{x_0}\right)\right]x^3\right\}. \end{aligned} \tag{2.32}$$

Since the (2,2) mode of the numerical waveforms is less noisy than the waveform measured along the z-axis, and since we have access to the 3PN amplitude correction of the (2,2) mode, we will use the (2,2) waveforms rather than the z-axis waveforms for our comparisons between NR and PN in Sec. 2.6. We have verified (for all comparisons using post-Newtonian waveforms of $\leq$ 2.5PN order in amplitude) that our results do not change significantly when we use z-axis waveforms instead of (2,2) waveforms.

2.3.3 Absorbing amplitude terms into a redefinition of the phase

The logarithms of the orbital frequency parameter x (as well as the constant frequency scale x_0) that appear in the amplitude expressions (2.28), (2.29),

and (2.32) can be absorbed into a redefinition of the phase by introducing an auxiliary phase variable $\Psi = \Phi + \delta$. Noting that the $\ln x$ terms first enter at 1.5 PN order, it is straightforward to show that choosing [29, 6, 164]

$$\delta = -3\frac{M_{\rm ADM}}{m}x^{3/2}\ln\left(\frac{x}{x_0}\right), \tag{2.33}$$

where $M_{\rm ADM}/m = 1 - x/8 + O(x^2)$ for an equal mass system, will eliminate the $\ln x$ terms from both the (2,2) mode as well as for the polarization waveforms. This follows from

$$\begin{aligned} h_{(2,2)} &= Ae^{-2i\Psi} \\ &= Ae^{-2i\Phi}e^{-2i\delta} \\ &= Ae^{-2i\Phi}(1 - 2i\delta - 2\delta^2 + O(x^{9/2})), \end{aligned}$$

and similarly for the polarization waveforms. Furthermore, since the orbital phase as a function of frequency goes as $x^{-5/2}$ at leading order (see Eq. (2.40) below), the $\ln x$ terms, which were 1.5PN, 2.5PN, and 3PN order in the original amplitude expressions, now appear as phase corrections at relative order 4PN, 5PN, and 5.5PN. As these terms are beyond the order to which the orbital phase evolution is known (3.5PN order), it can be argued that these terms can be ignored. Note that the choices of x_0 in Eq. (2.30) and δ in Eq. (2.33) are not unique; they were made to gather all logarithmic terms into one term, as well as to simplify the waveform [29].

2.3.4 Energy balance

The second assumption that goes into making as accurate a post-Newtonian waveform as possible is that of energy balance. It is assumed that the energy

carried away by the emission of gravitational waves is balanced by the change in the orbital binding energy of the binary,

$$\frac{dE}{dt} = -\mathcal{L}. \tag{2.34}$$

While this is extremely plausible, it has only been confirmed through 1.5 PN order[30].

Given the above expressions for the energy, flux, and waveform amplitude, there is still a set of choices that must be made in order to produce a post-Newtonian waveform that can be compared to our numerical waveform. These include

1. The PN order through which terms in the orbital energy and luminosity are retained.
2. The procedure by which the energy balance equation is used to obtain $x(t)$ and $\Phi(t)$.
3. The PN order through which terms in the waveform amplitude are kept.
4. The treatment of the $\ln x$ terms. These terms can be included in the amplitude or included in the orbital phase via the auxiliary phase $\Psi \equiv \Phi + \delta$. If the latter is chosen, these terms can be retained or ignored; ignoring them can be justified because they occur at higher order than all known terms in the orbital phase.

We always expand energy and luminosity to the same order, which may be different from the order of the amplitude expansion; both of these expansion orders are indicated explicitly in each of our comparisons. We ignore the $\ln(x/x_0)$ terms in the amplitude by absorbing them into the phase and dropping them

because of their high PN order. In the next section we describe several choices for obtaining $x(t)$ and $\Phi(t)$ from the energy balance equation.

2.3.5 Taylor approximants: Computing $\Phi(t)$

In this section we describe how to obtain the orbital phase as a function of time, $\Phi(t)$, using the energy balance equation (3.21). Different methods of doing this exist; here we follow the naming convention of [100]. These methods, and variations of them, are called Taylor approximants, and all formally agree to a given PN order but differ in how higher-order terms are truncated. We discuss four time-domain approximants here, but more can be defined.

TaylorT1

The TaylorT1 approximant is obtained by numerically integrating the ODEs

$$\frac{dx}{dt} = -\frac{\mathcal{L}}{(dE/dx)} \tag{2.35}$$

$$\frac{d\Phi}{dt} = \frac{c^3}{Gm}x^{3/2}, \tag{2.36}$$

to produce $\Phi(t)$. The fraction on the right side of Eq (2.35) is retained as a ratio of post-Newtonian expansions, and is not expanded further before numerical integration. This is the approximant used in the NR-PN comparisons in [141, 192].

TaylorT2

The TaylorT2 approximant is obtained by starting with the parametric solution of the energy balance equation:

$$t(x) = t_0 + \int_x^{x_0} dx \frac{(dE/dx)}{\mathcal{L}} \tag{2.37}$$

$$\Phi(x) = \Phi_0 + \int_x^{x_0} dx \frac{x^{3/2}c^3}{Gm} \frac{(dE/dx)}{\mathcal{L}}. \tag{2.38}$$

The integrand of each expression is re-expanded as a single post-Newtonian expansion in x and truncated at the appropriate PN-order; these integrals are then evaluated analytically to obtain for an equal-mass binary [100, 101]:

$$\begin{aligned} t &= t_0 - \frac{5Gm}{64c^3} x^{-4} \left\{ 1 + \frac{487}{126} x - \frac{32}{5} \pi x^{3/2} + \frac{2349439}{254016} x^2 \right. \\ &\quad - \frac{1864}{63} \pi x^{5/2} + \left[- \frac{999777207379}{5867769600} + \frac{1597}{48} \pi^2 \right. \\ &\quad \left. \left. + \frac{6848}{105} \gamma + \frac{3424}{105} \ln(16x) \right] x^3 - \frac{571496}{3969} \pi x^{7/2} \right\} \end{aligned} \tag{2.39}$$

$$\begin{aligned} \Phi &= \Phi_0 - \frac{1}{8} x^{-5/2} \left\{ 1 + \frac{2435}{504} x - 10 \pi x^{3/2} + \frac{11747195}{508032} x^2 \right. \\ &\quad + \frac{1165}{42} \pi x^{5/2} \ln x + \left[\frac{1573812724819}{4694215680} - \frac{7985}{192} \pi^2 \right. \\ &\quad \left. \left. - \frac{1712}{21} \gamma - \frac{856}{21} \ln(16x) \right] x^3 + \frac{357185}{7938} \pi x^{7/2} \right\}. \end{aligned} \tag{2.40}$$

TaylorT3

The TaylorT3 approximant is closely related to TaylorT2. It is obtained by introducing the dimensionless time variable

$$\tau \equiv \frac{\nu c^3}{5Gm}(t_0 - t), \tag{2.41}$$

where $\nu = m_1 m_2/m^2$ and $\tau^{-1/4} = O(\epsilon)$. The TaylorT2 expression $t(x)$ is inverted to obtain $x(\tau)$, and truncated at the desired PN order. Then $x(\tau)$ is integrated to obtain

$$\Phi(\tau) = \Phi_0 - \int_{\tau_0}^{\tau} d\tau \frac{5x^{3/2}}{\nu}. \tag{2.42}$$

This procedure yields for an equal-mass binary [35]:

$$\begin{aligned} x &= \frac{1}{4}\tau^{-1/4}\left\{1 + \frac{487}{2016}\tau^{-1/4} - \frac{1}{5}\pi\tau^{-3/8}\right. \\ &+ \frac{1875101}{16257024}\tau^{-1/2} - \frac{1391}{6720}\pi\tau^{-5/8} \\ &+ \left[-\frac{999777207379}{1502149017600} + \frac{1597}{12288}\pi^2 + \frac{107}{420}\gamma\right. \\ &- \left.\left.\frac{107}{3360}\ln\left(\frac{\tau}{256}\right)\right]\tau^{-3/4} - \frac{88451}{282240}\pi\tau^{-7/8}\right\} \end{aligned} \tag{2.43}$$

$$\begin{aligned} \Phi &= \Phi_0 - 4\tau^{5/8}\left\{1 + \frac{2435}{4032}\tau^{-1/4} - \frac{3}{4}\pi\tau^{-3/8}\right. \\ &+ \frac{1760225}{1806336}\tau^{-1/2} - \frac{1165}{5376}\pi\tau^{-5/8}\ln\tau \\ &+ \left[\frac{24523613019127}{3605157642240} - \frac{42997}{40960}\pi^2 - \frac{107}{56}\gamma\right. \\ &+ \left.\left.\frac{107}{448}\ln\left(\frac{\tau}{256}\right)\right]\tau^{-3/4} + \frac{28325105}{21676032}\pi\tau^{-7/8}\right\} \end{aligned} \tag{2.44}$$

This is the post-Newtonian approximant used in visual comparisons by [64] and in the NR-PN comparisons in [141] at 3PN order in phase.

TaylorT4

In addition to simply numerically integrating the flux-energy equation (2.35), as is done for TaylorT1, one may instead re-expand the right side of (2.35) as a single series and truncate at the appropriate PN order before doing the integration. The phase evolution $\Phi(t)$ can thus be obtained by numerically integrating

the ODEs

$$\begin{aligned}
\frac{dx}{dt} &= \frac{16c^3}{5Gm}x^5\left\{1 - \frac{487}{168}x + 4\pi x^{3/2} + \frac{274229}{72576}x^2\right. \\
&- \frac{254}{21}\pi x^{5/2} + \left[\frac{178384023737}{3353011200} + \frac{1475}{192}\pi^2 - \frac{1712}{105}\gamma\right. \\
&- \left.\left.\frac{856}{105}\ln(16x)\right]x^3 + \frac{3310}{189}\pi x^{7/2}\right\} \qquad (2.45)\\
\frac{d\Phi}{dt} &= \frac{x^{3/2}c^3}{Gm}. \qquad (2.46)
\end{aligned}$$

This approximant was not considered in [100], however for consistency with their notation, we call it TaylorT4. TaylorT4 is the primary approximant used in the NR-PN comparisons in [17, 16], and one of the several approximants considered in the NR-PN comparisons in [192]. Ref.[64] pointed out that TaylorT4 at 3.5PN order in phase is close to TaylorT3 at 3PN order in phase, and therefore should give similar agreement with numerical results.

2.4 PN-NR Comparison Procedure

2.4.1 What to compare?

There are many ways to compare numerical relativity and post-Newtonian results. For example, the post-Newtonian orbital phase $\Phi(t)$ could be compared with the coordinate phase of the black hole trajectories. However, this and many other comparisons are difficult to make in a coordinate-independent manner without expending significant effort to understand the relationship between the gauge choices used in post-Newtonian theory and in the NR simulations. Therefore, in order to obtain the most meaningful comparison possible, we attempt to minimize gauge effects by comparing gravitational waveforms as seen

by an observer at infinity. The waveform quantity most easily obtained from the numerical relativity code is the Newman-Penrose quantity Ψ_4, and we will compare its $(2,2)$ component [cf. Eq. (2.13)], split into phase ϕ and amplitude A according to Eq. (3.23) and extrapolated to infinite extraction radius.

The post-Newtonian formulae in Section 2.3 yield the metric perturbation components h_+ and $h_\times$, which—for a gravitational wave at infinity—are related to Ψ_4 by

$$\Psi_4(t) = \frac{\partial^2}{\partial t^2}\left(h_+(t) - i h_\times(t)\right). \tag{2.47}$$

We numerically differentiate the post-Newtonian expressions for $h_+(t)$ and $h_\times(t)$ twice before computing amplitude and phase using Eq. (3.23). Note that $\phi(t)$ will differ slightly from the phase computed from the metric perturbation directly, as $\tan^{-1}(h_\times/h_+)$, because both the amplitude and phase of the metric perturbation are time dependent. For the same reason, $\phi(t)$ is not precisely equal to twice the orbital phase.

As in Ref. [141], we compare Ψ_4 rather than $h_{+,\times}$ to avoid difficulties arising with fixing the integration constants when integrating the numerically obtained Ψ_4 (see [197] for more details). Both Ψ_4 and $h_{+,\times}$ contain the same information, so differences between both procedures should be minimal.

2.4.2 Matching procedure

Each of the post-Newtonian waveforms has an arbitrary time offset t_0 and an arbitrary phase offset ϕ_0. These constants can be thought of as representing the absolute time of merger and the orientation of the binary at merger, and we are free to adjust them in order to match NR and PN waveforms. Following [17,

141], we choose these constants by demanding that the PN and NR gravitational wave phase and gravitational wave frequency agree at some fiducial frequency ω_m. Specifically, we proceed as follows: We start with a NR waveform $\Psi_4^{\rm NR}(t)$ and an unshifted PN waveform $\Psi_4^{\rm PN'}(t)$ that has an arbitrary time and phase shift. After selecting the matching frequency ω_m, we can find (to essentially unlimited accuracy) the time t_c such that the derivative of the PN phase satisfies $\dot{\phi}_{\rm PN'}(t_c) = \omega_m$, where $\phi_{\rm PN'}(t)$ is the phase associated with $\Psi_4^{\rm PN'}(t)$. Similarly, we find the time t_m such that $\dot{\phi}_{\rm NR}(t_m) = \omega_m$. The time t_m cannot be found to unlimited accuracy, and the uncertainty in t_m is due mainly to residual eccentricity of the NR waveform, as discussed in Section 2.5.5. Once we have t_m and t_c, we leave the NR waveform untouched, but we construct a new, shifted, PN waveform

$$\Psi_4^{\rm PN}(t) = \Psi_4^{\rm PN'}(t + t_c - t_m) e^{i\left(\phi_{\rm PN'}(t_c) - \phi_{\rm NR}(t_m)\right)}. \tag{2.48}$$

The phase of this new PN waveform is therefore

$$\phi_{\rm PN}(t) = \phi_{\rm PN'}(t + t_c - t_m) - \phi_{\rm PN'}(t_c) + \phi_{\rm NR}(t_m), \tag{2.49}$$

which satisfies $\phi_{\rm PN}(t_m) = \phi_{\rm NR}(t_m)$ and $\dot{\phi}_{\rm PN}(t_m) = \omega_m$ as desired. All our comparisons are then made using the new shifted waveform $\Psi_4^{\rm PN}(t)$ rather than the unshifted waveform $\Psi_4^{\rm PN'}(t)$.

2.4.3 Choice of Masses

The post-Newtonian expressions as written in Section 2.3 involve the total mass m, which corresponds to the the sum of the bare masses of the point particles in post-Newtonian theory. When comparing PN to NR, the question then arises as to which of the many definitions of the mass of a numerically-generated binary

black hole solution should correspond to the post-Newtonian parameter m. For non-spinning black holes at very large separation, m reduces to the sum of the irreducible masses of the two holes. Neglecting tidal heating, the irreducible masses should be conserved during the inspiral, so that we identify m with the sum of the irreducible masses of the initial data 30c. As discussed in Sec. 2.5 the black hole spins are sufficiently small so that there is no discernible difference between irreducible mass of the black holes and the Christodoulou mass, Eq. (2.3). Of course, the latter would be more appropriate for spinning black holes.

2.5 Estimation of uncertainties

To make precise statements about agreement or disagreement between numerical and post-Newtonian waveforms, it is essential to know the size of the uncertainties in this comparison. When discussing these uncertainties, we must strive to include all effects that may cause our numerical waveform to differ from the post-Newtonian waveforms we compare to. For instance, in addition to considering effects such as numerical truncation error, we also account for the fact that NR and PN waveforms correspond to slightly different physical scenarios: The PN waveforms have identically zero spin and eccentricity, whereas the numerical simulations have some small residual spin and eccentricity. Table 2.3 lists all effects we have considered; we discuss these in detail below starting in Sec. 2.5.1. All uncertainties are quoted in terms of phase and amplitude differences, and apply to waveform comparisons via matching at a fixed ω_m according to the procedure in Sec. 4.6.1.

Table 2.3: Summary of uncertainties in the comparison between numerical relativity and post-Newtonian expansions. Quoted error estimates ignore the junk-radiation noise at $t \lesssim 1000m$ and apply to times before the numerical waveform reaches gravitational wave frequency $m\omega = 0.1$. Uncertainties apply to waveform comparisons via matching at a fixed ω_m according to the procedure in Sec. 4.6.1, and represent the maximum values for all four different matching frequencies ω_m that we consider, unless noted otherwise.

Effect	$\delta\phi$ (radians)	$\delta A/A$
Numerical truncation error	0.003	0.001
Finite outer boundary	0.005	0.002
Extrapolation $r \to \infty$	0.005	0.002
Wave extraction at $r_{\rm areal}$=const?	0.002	10^{-4}
Drift of mass m	0.002	10^{-4}
Coordinate time = proper time?	0.002	10^{-4}
Lapse spherically symmetric?	0.01	4×10^{-4}
residual eccentricity	0.02[8]	0.004
residual spins	0.03	0.001
root-mean-square sum	**0.04**[1]	**0.005**

Most of the effects responsible for our uncertainties are time dependent, so that it is difficult to arrive at a single number describing each effect. For simplicity, the error bounds in Table 2.3 ignore the junk-radiation noise that occurs in the numerical waveform for $t - r^* \lesssim 1000m$. The extent to which this noise affects the PN-NR comparisons presented below in Sections 2.6.1 and 2.6.2 will be evident from the noise in the graphs in these sections. Note that all four matching frequencies ω_m occur after the noise disappears at $t - r^* \sim 1000m$. Furthermore, the post-Newtonian waveforms end at different times depending on the PN order and on which particular post-Newtonian approximant is used. Therefore, in order to produce a single number for each effect listed in Table 2.3, we consider only the part of the waveform prior to some cutoff time, which we choose to be the time at which the numerical waveform reaches gravitational wave frequency $m\omega = 0.1$.

2.5.1 Errors in numerical approximations

The first three error sources listed in Table 2.3 have already been discussed in detail in Section 2.2. We estimate numerical truncation error using the difference between the two highest resolution runs after the waveforms have been shifted to agree at some matching frequency ω_m. For $m\omega_m = 0.1$ this difference is shown as the curves labeled '30c-1/N5' in the lower panels of Figs. 2.7 and 2.8, and corresponds to a phase difference of 0.003 radians and a relative amplitude difference of 0.001. For other values of ω_m the differences are similar. The effect of the outer boundary is estimated by the difference between the runs 30c-1/N6 and 30c-2/N6, which for $m\omega_m = 0.1$ is shown as the curves labeled '30c-2/N6' in the lower panels of Figs. 2.7 and 2.8, and amount to phase differences of 0.005 radians and relative amplitude differences of 0.002. Errors associated with extrapolation to infinity have been discussed in detail in Figs. 2.10 and 2.12. Specifically, Fig. 2.10 shows that increasing the extrapolation order between 3 and 4 changes the extrapolated phase by less than 0.005 radians, and Fig. 2.12 confirms that the extrapolated result is robust under changes of extraction radii.

2.5.2 Constancy of extraction radii

If the physical locations of the coordinate-stationary extraction radii happen to change during the evolution, then the extracted gravitational waves will accrue a timing error equal to the light-travel time between the original location and the final location. From Fig. 2.9, we see that the drift in areal radius is less than $0.02m$, resulting in a time uncertainty of $\delta t = 0.02m$. This time uncertainty

translates into a phase uncertainty via

$$\delta\phi = m\omega \times (\delta t/m) \tag{2.50}$$

which yields $\delta\phi \approx 0.002$, when $m\omega = 0.1$ (the value at the end of the PN comparison) was used.

To estimate the effect of this time uncertainty on the amplitude, we first note that to lowest order in the post-Newtonian parameter x (defined in Eq. (2.23)), the wave amplitude of Ψ_4 scales like x^4. Also, from Eq. (2.45), we have $dx/dt = 16/(5m)x^5$. Therefore,

$$\frac{\delta A}{A} \sim \frac{d\ln A}{dx}\frac{dx}{dt}\delta t \sim \frac{64}{5}(m\omega/2)^{8/3}\frac{\delta t}{m}, \tag{2.51}$$

where we have used the fact that the gravitational wave frequency ω is approximately twice the orbital frequency. For a time uncertainty $\delta t = 0.02m$, Eq. (2.51) gives $\delta A/A \approx 10^{-4}$ for $m\omega = 0.1$.

2.5.3 Constancy of mass

Our comparisons with post-Newtonian formulae assume a constant post-Newtonian mass parameter m, which we set equal to the total irreducible mass of the black holes in the numerical simulation. If the total mass of the numerical simulation is not constant, this will lead to errors in the comparison. For example, changes in t/m caused by a changing mass will lead to phase differences. Figure 2.4 demonstrates that the irreducible mass is conserved to a fractional accuracy of about $\delta m/m \approx 5 \times 10^{-6}$.

This change in irreducible mass could be caused by numerical errors, or by a physical increase of the mass of each black hole through tidal heating. For

our simulations, $m(t)$ *decreases* during the run (this is not apparent from Fig. 2.4 which plots absolute values), thus contradicting the second law of black hole thermodynamics. Moreover, the increase in $m(t)$ through tidal heating is much smaller than the observed variations in $m(t)$ (see, e.g. [202]). Therefore, the variations in $m(t)$ are numerical errors, and we need to bound the influence of these errors on the comparison to post-Newtonian expansions.

Over an evolution time of $t/m = 4000$, the observed mass uncertainty of $\delta m/m \approx 5 \times 10^{-6}$ results in an uncertainty in the overall time interval of $\delta(t/m) = (t/m) \times (\delta m/m) \approx 0.02$. This time uncertainty translates into a phase uncertainty of $\delta\phi \approx 0.002$, using Eq. (2.50) for $m\omega = 0.1$. Note that the effect of the black-hole spins on the mass is negligible relative to the numerical drift of 5×10^{-6}. This is because the spins of the holes are bounded by $S/M_{\rm irr} < 2 \times 10^{-4}$ and the spin enters quadratically into the Christodoulou formula (2.3). The error in the gravitational wave amplitude caused by time uncertainties due to varying mass is $\delta A/A \approx 10^{-4}$ using Eq. (2.51) for $m\omega = 0.1$. An error in the mass will affect the amplitude not only via a time offset, but also because the amplitude is proportional to $(\omega m/2)^{8/3}$ (to lowest PN order). However, this additional error is very small, $\delta A/A \approx (8/3)\delta m/m \approx 10^{-5}$.

2.5.4 Time coordinate ambiguity

We now turn to two possible sources of error that have not yet been discussed, both of which are related to ambiguity in the time coordinate. The basic issue is that the time variable t in post-Newtonian expansions corresponds to proper time in the asymptotically flat region, but the time t in numerical simulations

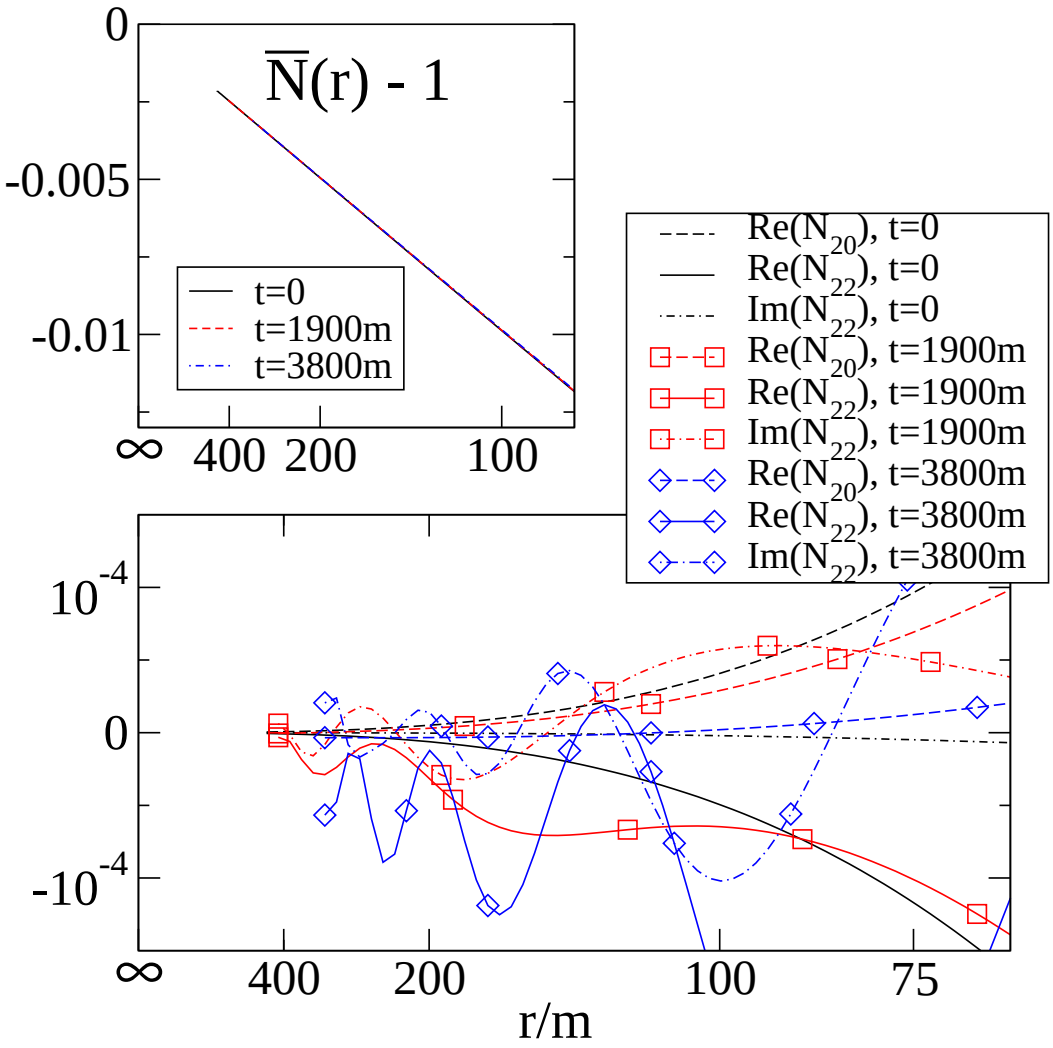

Figure 2.14: Asymptotic behavior of the lapse at large radii for times $t/m = 0, 1900, 3800$. The top figure displays the angular average of the lapse as a function of radius at $t = 0, 1900m, 7800m$. The bottom figure shows the dominant higher multipole moments of the lapse. Both horizontal axes are spaced in $1/r$.

is coordinate time. These two quantities agree only if the lapse function N approaches unity at large distances. To verify this, we decompose N in spherical harmonics centered on the center of mass of the system,

$$N(r,\theta,\varphi) = \sum_{l=0}^{\infty} \sum_{m=-l}^{l} N_{lm}(r) Y_{lm}(\theta,\varphi). \tag{2.52}$$

The angular average of the lapse function, $\bar{N}(r) \equiv \sqrt{4\pi} N_{00}(r)$ should then approach unity for $r \to \infty$, and all other modes $N_{lm}(r)$ should decay to zero. The top panel of Fig. 2.14 plots $\bar{N}(r)-1$ vs. m/r for three different evolution times. Fitting $\bar{N}(r) - 1$ for $r > 100m$ to a polynomial in m/r gives a y-intercept of $< 5 \times 10^{-6}$ for all three times, and for polynomial orders of two through five. Therefore, the coordinate time of the evolution agrees with proper time at infinity to better than $\delta t/m = t/m \times 5 \times 10^{-6} \approx 0.02$, which induces a phase error of at most $\delta\phi \approx 0.002$ and an amplitude error of $\delta A/A \approx 10^{-4}$ [cf. Eqs. (2.50) and (2.51)].

The second source of error related to the lapse is shown in the lower panel of Fig. 2.14, which presents the three dominant higher order moments $N_{lm}(r)$. All these modes decay to zero as $r \to \infty$, except, perhaps, the real part of the N_{22} mode at $t/m = 3800$. This mode seems to approach a value of about 5×10^{-5}. At $t = 1900m$, this mode still decays nicely to zero, hence the maximum time uncertainty introduced by this effect at late times is $\delta t = 1900m \times 5 \times 10^{-5} \approx 0.1m$, resulting in a potential phase uncertainty of $\delta\phi \approx 0.01$ and a potential amplitude uncertainty of $\delta A/A \approx 4 \times 10^{-4}$.

2.5.5 Eccentricity

We estimated the eccentricity during the numerical simulation with several of the methods described in [64, 197, 152], and have found consistently $e \lesssim 6{\times}10^{-5}$.

This eccentricity can affect our comparison to a post-Newtonian waveform of a quasi-circular (i.e. zero eccentricity) inspiral in three ways.

Change in rate of inspiral

The first effect arises because an eccentric binary has a different inspiral rate than a non-eccentric binary; physically, this can be understood by noting that the gravitational flux and orbital energy depend upon the eccentricity, and therefore modify the rate at which the orbital frequency evolves assuming energy balance. Reference [173] has derived the first-order correction in the phase of the gravitational wave due to this effect. Converting their result to our notation and restricting to the equal mass case yields

$$\frac{1}{(dx/dt)} = \frac{5Gm}{16c^3x^5}\left(1 - \frac{157}{24}e_i^2\left(\frac{x_i}{x}\right)^{19/6}\right), \tag{2.53}$$

where e_i is the initial eccentricity and x_i is the initial value of the orbital frequency parameter. Substituting this into Eq. (2.38) yields

$$\Phi = \Phi_0 - \frac{1}{8}x^{-5/2} + \frac{785}{2176}e_i^2 x_i^{19/6} x^{-17/3}. \tag{2.54}$$

Using $e_i = 6 \times 10^{-5}$ and integrating over the frequency range from the start of our simulation to the matching frequency of $m\omega = 0.1$ yields a phase shift of $\sim -2\times10^{-6}$, which is dwarfed by many other error sources, such as the uncertainty in the numerical mass m, cf. Sec. 2.5.3.

Uncertainty in matching time

The second way in which eccentricity affects our comparison is by introducing errors in our procedure for matching the PN and NR waveforms. Recall that

our matching procedure involves determining the time t_m at which the gravitational wave frequency ω takes a certain value $m\omega_m$; eccentricity modulates the instantaneous gravitational wave frequency $\omega(t)$ via

$$\omega(t) = \bar{\omega}(t)[1 + 2e\cos(\Omega_r t)], \tag{2.55}$$

where $\bar{\omega}(t)$ represents the averaged "non-eccentric" evolution of the gravitational wave frequency, and Ω_r is the frequency of radial oscillations, which is approximately equal to the orbital frequency. We see that ω can differ from $\bar{\omega}$ by as much as $2e\bar{\omega} \approx 2e\omega$. This could induce an error in the determination of t_m by as much as

$$|\delta t_m| = \frac{|\delta\omega|}{\dot{\omega}} \approx \frac{2e\omega}{\dot{\omega}} \tag{2.56}$$

We can simplify this expression by using Eq. (2.45) to lowest order, and by noting that the gravitational wave frequency is approximately twice the orbital frequency. We find

$$|\delta t_m| \leq e\frac{5m}{12}\left(\frac{m\omega}{2}\right)^{-8/3}. \tag{2.57}$$

This uncertainty is largest at *small* frequencies, because the frequency changes much more slowly. For $m\omega = 0.04$, we find $|\delta t_m| \lesssim 0.9m$, and for $m\omega = 0.1$, we find $|\delta t_m| \lesssim 0.1m$.

To determine how uncertainties in t_m translate into phase differences, recall that in the matching procedure described in Section 4.6.1, t_m enters into the phase of the shifted PN waveform according to Eq. (2.49). Therefore the phase difference that we compute between the PN and NR waveforms is

$$\begin{aligned}\Delta\phi(t) &= \phi_{\rm PN}(t) - \phi_{\rm NR}(t) \\ &= \phi_{\rm PN'}(t+t_c-t_m) - \phi_{\rm NR}(t) + \phi_{\rm NR}(t_m) - \phi_{\rm PN'}(t_c).\end{aligned} \tag{2.58}$$

Then the error in $\Delta\phi$ is found by Taylor expanding Eq. (2.58):

$$\begin{aligned}\delta\phi \equiv \delta(\Delta\phi(t)) &= \left(\dot{\phi}_{\mathrm{PN}'}(t + t_c - t_m) - \dot{\phi}_{\mathrm{NR}}(t_m)\right)\delta t_m \\ &= \left(\dot{\phi}_{\mathrm{PN}}(t) - \omega_m\right)\delta t_m. \end{aligned} \tag{2.59}$$

Our simulations (and therefore the comparisons to post-Newtonian theory) start at $m\omega \approx 0.033$, so that the maximal error $\delta\phi$ within our comparison at times *before* the matching frequency will be

$$|\delta\phi_{\mathrm{before}}| \leq |0.033 - \omega_m|\,|\delta t_m| \tag{2.60}$$

Combining Eqs. (2.60) and (2.56), and using $e \approx 6 \times 10^{-5}$, we find that $\delta\phi_{\mathrm{before}} < 0.01$ radians for all four of our matching frequencies $m\omega_m = 0.04, 0.05, 0.063, 0.1$. The maximum error $\delta\phi$ within our comparison at times *after* the matching frequency is

$$|\delta\phi_{\mathrm{after}}| \leq |0.1 - \omega_m|\,|\delta t_m|, \tag{2.61}$$

because we end our comparisons to post-Newtonian theory at $m\omega = 0.1$. Eq. (2.61) evaluates to 0.05 radians for $m\omega_m = 0.04$, and is less than about 0.02 radians for the three higher matching frequencies.

The error in the gravitational wave amplitude caused by an error in t_m can be estimated by Eq. (2.51). A conservative estimate using $\delta t = 0.9m$ still gives a small error, $\delta A/A \approx 0.004$.

Note that the bounds on $\delta\phi_{\mathrm{before}}$ and $\delta\phi_{\mathrm{after}}$ are proportional to the eccentricity of the numerical simulation. Even with eccentricity as low as 6×10^{-5}, this effect is one of our largest sources or error for the PN-NR comparison. (cf. Table 2.3). This is the reason why the simpler eccentricity removal procedure of Husa *et al.* [152] (resulting in $e = 0.0016$) is not adequate for our purposes.

Periodic modulation of phase and amplitude

The third effect of orbital eccentricity is a periodic modulation of the gravitational wave phase and amplitude. If we assume that $\bar{\omega}(t)$ varies on much longer time scales than $1/\Omega_r$ (which is true at large separation) then time integration of Eq. (2.55) yields

$$\phi(t) = \bar{\phi}(t) + 2e\frac{\bar{\omega}}{\Omega_r}\sin(\Omega_r t). \tag{2.62}$$

Because $\Omega_r \approx \Omega \approx \bar{\omega}/2$, we therefore find that the gravitational wave phase consists of the sum of the desired "circular" phase, $\bar{\phi}(t)$, plus an oscillatory component with amplitude $4e \approx 2 \times 10^{-4}$. This oscillatory component, however, is much smaller than other uncertainties of the comparison, for instance the uncertainty in determination of t_m.

Residual eccentricity will also cause a modulation of the gravitational wave amplitude in a manner similar to that of the phase. This is because eccentricity explicitly enters the post-Newtonian amplitude formula at 0PN order [227]. This term is proportional to e, and since $e \lesssim 6 \times 10^{-5}$ its contribution to the amplitude error is small compared to the effect due to uncertainty in t_m.

While oscillations in phase and amplitude due to eccentricity are tiny and dwarfed by other uncertainties in the PN-NR comparison, their characteristic oscillatory behavior makes them nevertheless visible on some of the graphs we present below, for instance, both panels of Fig. 2.19.

2.5.6 Spin

We now turn our attention to effects of the small residual spins of the black holes. References [122, 36] compute spin-orbit coupling up to 2.5 post-Newtonian order, and find that the orbital phase, Eq. (2.40), acquires the following spin contributions

$$\begin{aligned}\Phi_S(x) = -\frac{1}{32\nu}\sum_{i=1,2}\chi_i\Bigg\{&\left(\frac{565}{24}\frac{m_i^2}{m^2}+\frac{125\nu}{8}\right)x^{-1}\\ &-\Bigg[\left(\frac{681145}{4032}+\frac{965\nu}{28}\right)\frac{m_i^2}{m^2}\\ &\quad+\frac{37265\nu}{448}+\frac{1735\nu^2}{56}\Bigg]\ln x\Bigg\},\end{aligned} \tag{2.63}$$

where $\chi_i = \mathbf{S}_i \cdot \hat{\mathbf{L}}/m_i^2$ is the projection of the dimensionless spin of the i-th hole onto the orbital angular momentum. For equal-mass binaries with spins $\chi_1 = \chi_2 \equiv \chi$, this reduces to

$$\Phi_S(x) = -\chi\left(\frac{235}{96}x^{-1} - \frac{270625}{16128}\ln x\right). \tag{2.64}$$

Our comparisons to post-Newtonian theory are performed over the orbital frequency range of $0.0167 \leq m\Omega \leq 0.05$, corresponding to $0.065 \leq x \leq 0.136$. The gravitational wave phase is approximately twice the orbital phase, so that the spin-orbit coupling contributes

$$\delta\phi_S = 2\big[\Phi_S(0.065) - \Phi_S(0.136)\big] \approx -64\chi \tag{2.65}$$

to the gravitational wave phase. In Sec. 2.2.2 we estimated $|\mathbf{S}|/M_{\rm irr}^2 < 5\times10^{-4}$, where $M_{\rm irr}$ is the irreducible mass of either black hole. Because $\chi \leq |\mathbf{S}|/M_{\rm irr}^2 \approx 5\times10^{-4}$, the residual black hole spins contribute less than 0.03 radians to the overall gravitational wave phase.

We now turn to errors in the amplitude comparison caused by residual spin.

From Eq. (2.64) we can compute the error in orbital frequency as

$$\delta\Omega = \dot{\Phi}_s = \chi \frac{\dot{x}}{x}\left(\frac{235}{96}x^{-1} + \frac{270625}{16128}\right)$$
$$= \chi x^4 \frac{16}{5m}\left(\frac{235}{96}x^{-1} + \frac{270625}{16128}\right), \tag{2.66}$$

where we have used Eq. (2.45). Because the amplitude of Ψ_4 scales like $\Omega^{8/3}$, we arrive at

$$\frac{\delta A}{A} = \frac{8}{3}\frac{\delta\Omega}{\Omega} = \chi x^{5/2}\frac{128}{15}\left(\frac{235}{96}x^{-1} + \frac{270625}{16128}\right), \tag{2.67}$$

which for $m\omega_m = 0.1$ (i.e. $x = 0.136$) gives $\delta A/A = 2.0\chi \sim 1.0 \times 10^{-3}$.

Spin-orbit terms also contribute directly to the amplitude [166, 231]. The leading order contribution (for an equal-mass binary with equal spins) contributes a term $\delta A/A \sim (4/3)\chi x^{3/2}$, which is the same order of magnitude as the previous error, 10^{-3}.

2.6 Results

2.6.1 Comparison with individual post-Newtonian approximants

We compare our simulations with four different post-Newtonian approximants: the TaylorT1, TaylorT2, TaylorT3, and TaylorT4 waveforms. These four waveforms agree with each other up to their respective post-Newtonian expansion orders, but they differ in the way that the uncontrolled higher order terms enter. We start with the comparison to TaylorT1.

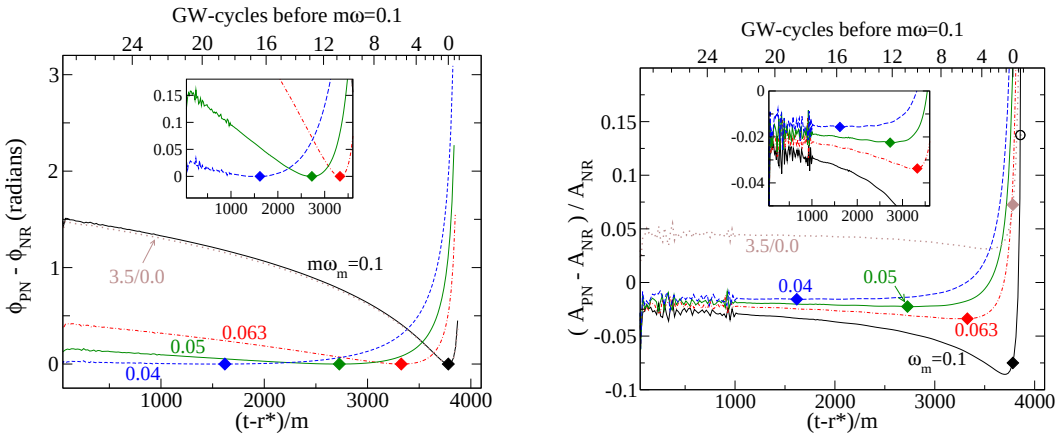

Figure 2.15: Comparison of numerical simulation with **TaylorT1 3.5/2.5** waveforms. Left: Difference in gravitational wave phase. Right: Relative amplitude difference. Plotted are comparisons for four values of ω_m. The filled diamond on each curve shows the point at which $\dot{\phi} = \omega_m$. The insets show enlargements for small differences and early times. Also shown is the difference between the numerical and restricted (i.e. 3.5PN phase, 0PN amplitude) Taylor T1 for $m\omega_m = 0.1$.

TaylorT1 (3.5PN phase, 2.5PN amplitude)

Figure 2.15 compares the numerical simulation to TaylorT1 3.5/2.5 waveforms (i.e. expansion order 3.5PN in phase and 2.5PN in amplitude, the highest expansion orders currently available for generic direction, cf. 2.3.2). The left panel shows the phase difference, where we find differences of more than a radian for all four matching frequencies we consider: $\omega_m = 0.04$, 0.05, 0.063, and 0.01.

For our largest matching frequency, $m\omega_m = 0.1$, the phase differences are small toward the end of the run by construction. Nevertheless, a phase difference of more than 0.5 radians builds up in the ~ 1.5 cycles after the matching point before the TaylorT1 template generation fails. Recall that $m\omega_m = 0.1$ occurs about 2.2 gravitational wave cycles before our simulations fail, which is still about 1.5 cycles before merger. However, the largest phase disagreement for $m\omega_m = 0.1$ builds up at early times, reaching 1.5 radians at the beginning of our simulation, about 28 cycles before the matching (~ 30 cycles before the end of the simulation), and still showing no sign of flattening even at the start of our simulation.

To achieve phase coherence with the early inspiral waveform, it is therefore necessary to match earlier than $m\omega_m = 0.1$. The left panel of Fig. 2.15 clearly shows that phase differences at earlier times become smaller when the matching point itself is moved to earlier time. For instance, $m\omega_m = 0.063$ (about eight gravitational wave cycles before the end of our simulation), results in phase differences less than 0.5 radians during the 22 earlier cycles of our evolution. However, the phase difference $\phi_{\rm PN} - \phi_{\rm NR}$ does not level off at early times within the length of our simulation, so it seems quite possible that the phase difference may grow to a full radian or more if the numerical simulations could cover

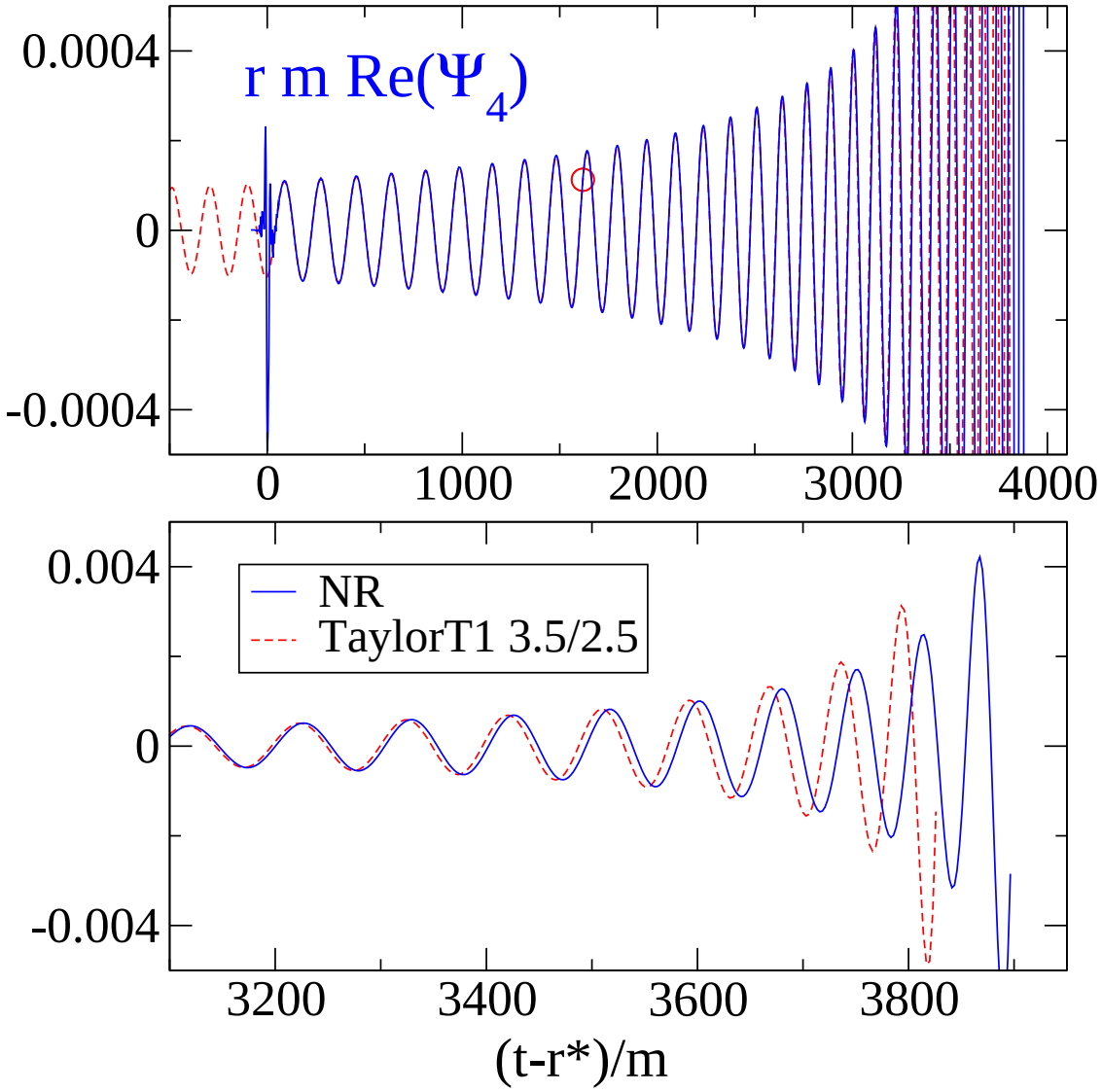

Figure 2.16: Numerical and **TaylorT1 3.5/2.5** waveforms. The PN waveform is matched to the numerical one at $m\omega_m = 0.04$, indicated by the small circle. The lower panel shows a detailed view of the last 10 gravitational wave cycles.

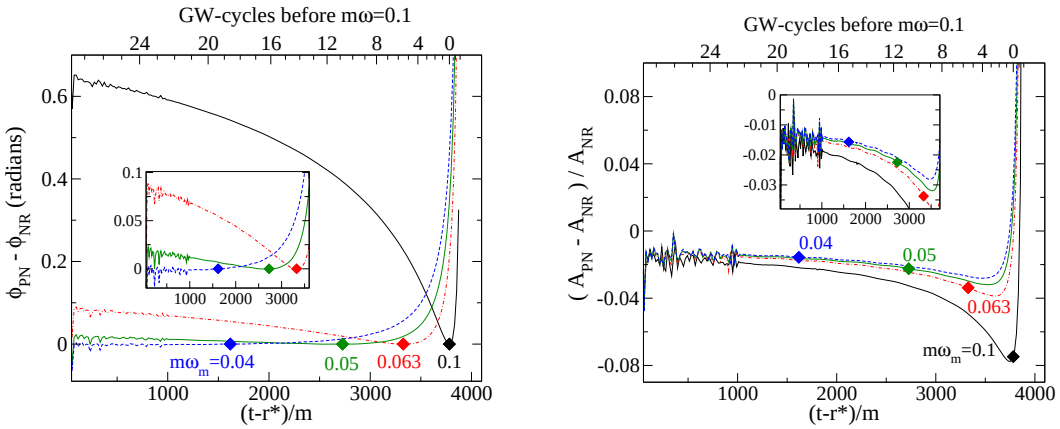

Figure 2.17: Comparison of numerical simulation with **TaylorT2 3.5/2.5** waveforms. Left: Difference in gravitational wave phase. Right: Relative amplitude difference. Plotted are comparisons for four values of ω_m. The filled diamond on each curve shows the point at which $\dot{\phi} = \omega_m$. The insets show enlargements for small differences and early times.

many more cycles. We thus estimate that for TaylorT1, to achieve 1-radian phase coherence with the early inspiral may require matching more than 10 cycles before merger. To achieve more stringent error bounds in phase coherence will require matching even earlier: for instance it appears one needs to use $m\omega_m = 0.04$ (about 20 cycles before the end of our simulation) for a phase error of less than $\lesssim 0.1$ radians.

While matching at small ω_m yields good phase coherence early in the run, it produces much larger phase differences late in the run. For example, matching at $m\omega_m = 0.04$ results in a phase difference of almost 2 radians at frequency $m\omega = 0.1$. This rather dramatic disagreement is illustrated in Fig. 2.16, which plots both the numerical and the TaylorT1 waveform, matched at $m\omega_m = 0.04$.

The left panel of Fig. 2.15 also includes a comparison to the so-called restricted TaylorT1 template, where only the leading order amplitude terms are used (*i.e.* 0PN in amplitude). The reason that higher-order amplitude terms affect the phase differences at all is because we are plotting gravitational-wave phase, not orbital phase. However, we see that the effect of these higher-order amplitude terms on the phase difference is small.

We now turn our attention to comparing the amplitudes of the post-Newtonian and numerical waveforms. The right panel of Fig. 2.15 shows relative amplitude differences between TaylorT1 3.5/2.5 and the numerical waveforms. At early times, the amplitudes agree to within 2 or 3 per cent, the agreement being somewhat better when the matching is performed at early times. At late times, the amplitudes disagree dramatically; a large fraction of this disagreement lies probably in the fact the post-Newtonian point of merger (i.e. the point at which the amplitude diverges) occurs at a different time than the nu-

merical point of merger. We also plot the amplitude of the restricted TaylorT1 template. The disagreement between restricted TaylorT1 and the numerical result is much larger, about 5 per cent.

Hannam et al. [141] performed a similar comparison, matching their waveforms with a restricted TaylorT1 waveform (i.e. 3.5/0.0) generated using the LIGO Algorithm Library (LAL) [83]. The phase difference they observe for waveforms matched at $m\omega = 0.1$ is consistent with our results within numerical errors. When matching TaylorT1 3.5/0.0 early in their simulation (at $m\omega = 0.0455$), however, Hannam et al. find a cumulative phase difference of 0.6 radians at $m\omega = 0.1$. From Fig. 2.15 we find a quite different value of 1.5 radians for our simulation. This disagreement might be caused by the use of the finite extraction radius $R = 90m$ for the gravitational wave phase in Hannam et. al.: Figure 2.10 shows that extracting at a finite radius leads to a systematic phase error, which will induce a systematic error in determination of the matching time of Hannam et al. This error is amplified by the increasing gravitational wave frequency toward merger.

TaylorT2 (3.5PN phase, 2.5PN amplitude)

Figure 2.17 presents the comparison between the numerical waveform and the TaylorT2 approximant. The overall trends are very similar to the TaylorT1 comparison of Fig. 2.15, however, the phase differences are smaller by about a factor of 2 when matching at $m\omega_m = 0.1$, and smaller by a factor of 3 to 4 when matching earlier. To our knowledge TaylorT2 has never been compared to a numerical simulation; we include it here mainly for completeness.

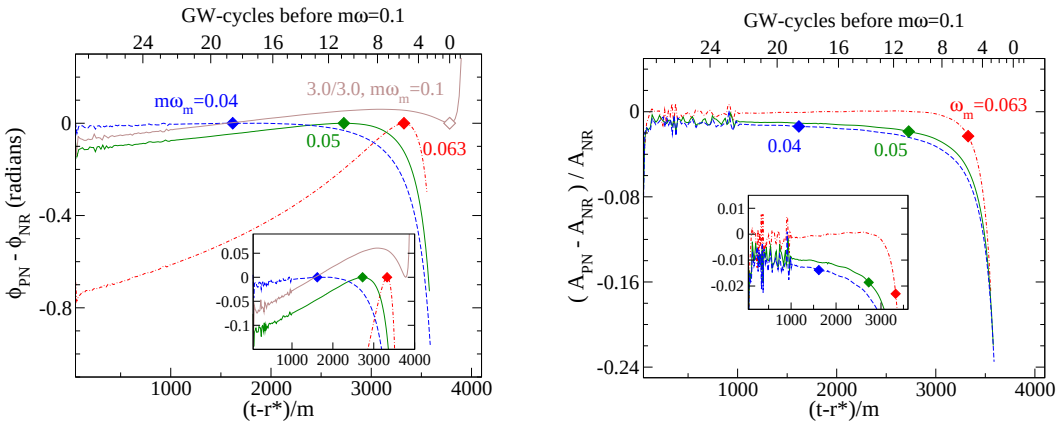

Figure 2.18: Comparison of numerical simulation with **TaylorT3 3.5/2.5** waveforms. Left: Difference in gravitational wave phase. Right: Relative amplitude difference. Plotted are comparisons for three values ω_m. The filled diamond on each curve shows the point at which $\dot{\phi} = \omega_m$. The lines end when the frequency of the TaylorT3 waveform reaches its maximum, which happens before $m\omega = 0.1$, so that the matching frequency $m\omega_m = 0.1$ is absent. The left plot also contains TaylorT3 3.0/3.0, matched at $m\omega_m = 0.1$. The insets show enlargements for small differences.

TaylorT3 (3.5PN and 3.0PN phase, 2.5PN amplitude)

Figure 2.18 is the same as Fig.2.15 except it compares numerical simulations to the TaylorT3 family of waveforms. Two differences between TaylorT1 and TaylorT3 are readily apparent from comparing these two figures. The first is that we do not match TaylorT3 3.5/2.5 waveforms at $m\omega_m = 0.1$. This is because the frequency of TaylorT3 3.5/2.5 waveforms reaches a maximum shortly before the formal coalescence time of the post-Newtonian template, and then *decreases*. The maximal frequency is less than 0.1, so that matching at $m\omega_m = 0.1$ is not possible. For this reason, we have also shown in Fig. 2.18 a comparison with a TaylorT3 3.0/3.0 waveform matched at $m\omega_m = 0.1$. The other major difference between the TaylorT3 3.5/2.5 and TaylorT1 3.5/2.5 comparison is that the phase difference, $\phi_{\rm PN} - \phi_{\rm NR}$, has a different sign. While TaylorT1 3.5/2.5 spirals in *more rapidly* than the numerical simulation, TaylorT3 3.5/2.5 *lags behind*. Interestingly, the phase differences from the numerical simulation for both TaylorT1 3.5/2.5 and TaylorT3 3.5/2.5 are of about equal magnitude (but opposite sign). The TaylorT3 3.0/3.0 comparison matched at $m\omega_m = 0.1$ has smaller phase differences than does the TaylorT3 3.5/2.5 comparison, but the slope of the 3.0/3.0 curve in Fig. 2.18 is nonzero at early times, so it appears that Taylor T3 3.0/3.0 will accumulate significant phase differences at even earlier times, prior to the start of our simulation. In Fig. 2.22 it can be seen that matching TaylorT3 3.0/3.0 at $m\omega_m = 0.04$ leads to a good match early, but leads to a phase difference of 0.6 radians by $m\omega = 0.1$.

Hannam et al. [141] match a TaylorT3 3.0/0.0 waveform at $m\omega_m = 0.1$ and $m\omega_m = 0.0455$. Matching at $m\omega_m = 0.1$ again gives phase differences consistent with our results within numerical errors. Matching at $m\omega_m = 0.0455$, Hannam

et al. find a phase difference of 0.9 radians, while we find a smaller value of 0.5 radians. Again, this difference could be due to the finite extraction radius used by Hannam et al.

TaylorT4 (3.5PN phase, 2.5PN amplitude)

Figure 2.19 is the same as Figs. 2.15 and 2.18 except it compares numerical simulations to the TaylorT4 PN waveforms. The agreement between TaylorT4 waveforms and the numerical results is astonishingly good, far better than the agreement between NR and either TaylorT1 or TaylorT3. The gravitational wave phase difference lies within our error bounds for the entire comparison region $m\omega \leq 0.1$, agreeing to 0.05 radians or better over 29 of 30 gravitational wave cycles. Ref. [17] found agreement between TaylorT4 and their numerical simulation to the level of their numerical accuracy (~ 2 radians), agreeing to roughly 0.5 radians in the gravitational frequency range of $0.054 \leq m\omega \leq 0.1$. Ref. [192] found that NR agrees better with TaylorT4 than with TaylorT1, but the larger systematic and numerical errors of the numerical waveforms used in these studies did not allow them to see the surprising degree to which NR and TaylorT4 agree. The gravitational wave amplitude of TaylorT4 agrees with the NR waveform to about 1–2 percent at early times, and 8 percent at late times. In Fig. 2.20 we plot the NR and TaylorT4 waveforms; the two waveforms are visually indistinguishable on the plot, except for small amplitude differences in the final cycles.

On the left panel of Fig. 2.19 we also show phase comparisons using PN waveforms computed to 3.5PN order in phase but to 0PN and 3.0PN orders in amplitude, for the case $m\omega_m = 0.1$. The PN order of the amplitude expansion af-

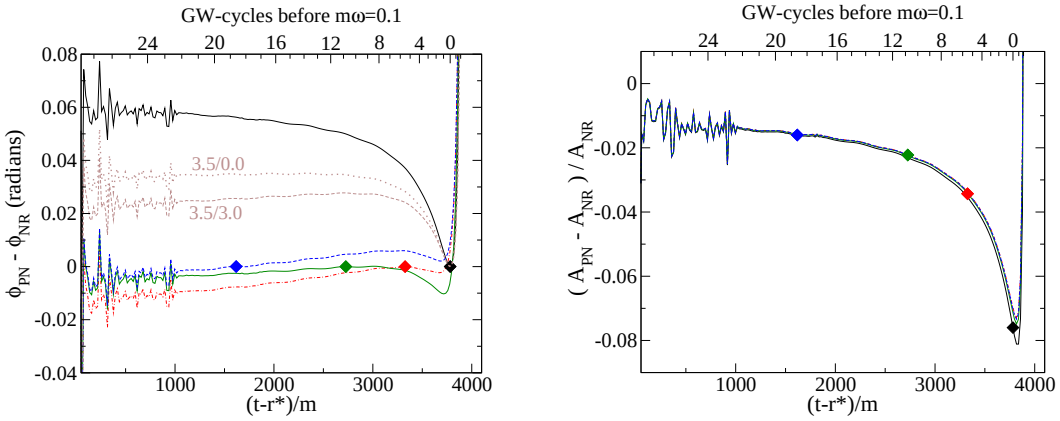

Figure 2.19: Comparison of numerical simulation with **TaylorT4 3.5/2.5** waveforms. Left: Difference in gravitational wave phase. Right: Relative amplitude difference. Plotted are comparisons for four values of ω_m. The filled diamond on each curve shows the point at which $\dot{\phi} = \omega_m$. The left plot also includes two phase comparisons with expansions of different PN order in amplitude, as labeled, for $m\omega_m = 0.1$.

fects the phase comparison because we are plotting differences in gravitational-wave phase and not orbital phase. The differences between using 0PN, 2.5PN, and 3.0PN amplitude expansions are evident on the scale of the graph, but because these differences are smaller than our estimated uncertainties (see Table 2.3), we cannot reliably conclude which of these most closely agrees with the true waveform.

Figure 2.21 presents amplitude differences between NR and TaylorT4 as the post-Newtonian order of the amplitude expansion is varied, but the phase expansion remains at 3.5PN. The 2.5PN amplitude curve was already included in the right panel of Fig. 2.19. We see clearly that higher order amplitude corrections generally result in smaller differences. The 3PN amplitude correction to the $(2,2)$ mode recently derived by Kidder [164] improves agreement dramatically over the widely known 2.5PN amplitude formulae. Unfortunately, the 3PN amplitude correction to the entire waveform, including all Y_{lm} modes, is not known.[9]

2.6.2 Comparing different post-Newtonian approximants

The previous section presented detailed comparisons of our numerical waveforms with four different post-Newtonian approximants. We now turn our attention to some comparisons between these approximants. In this section we also explore further how the post-Newtonian order influences agreement between numerical and post-Newtonian waveforms.

[9] To get the complete waveform to 3PN order, only the $(2,2)$ mode must be known to 3PN order; other modes must be known to smaller PN orders. For an equal mass, non-spinning binary, all modes except the $(3,2)$ mode are currently known to sufficient order to get a complete 3PN waveform [164].

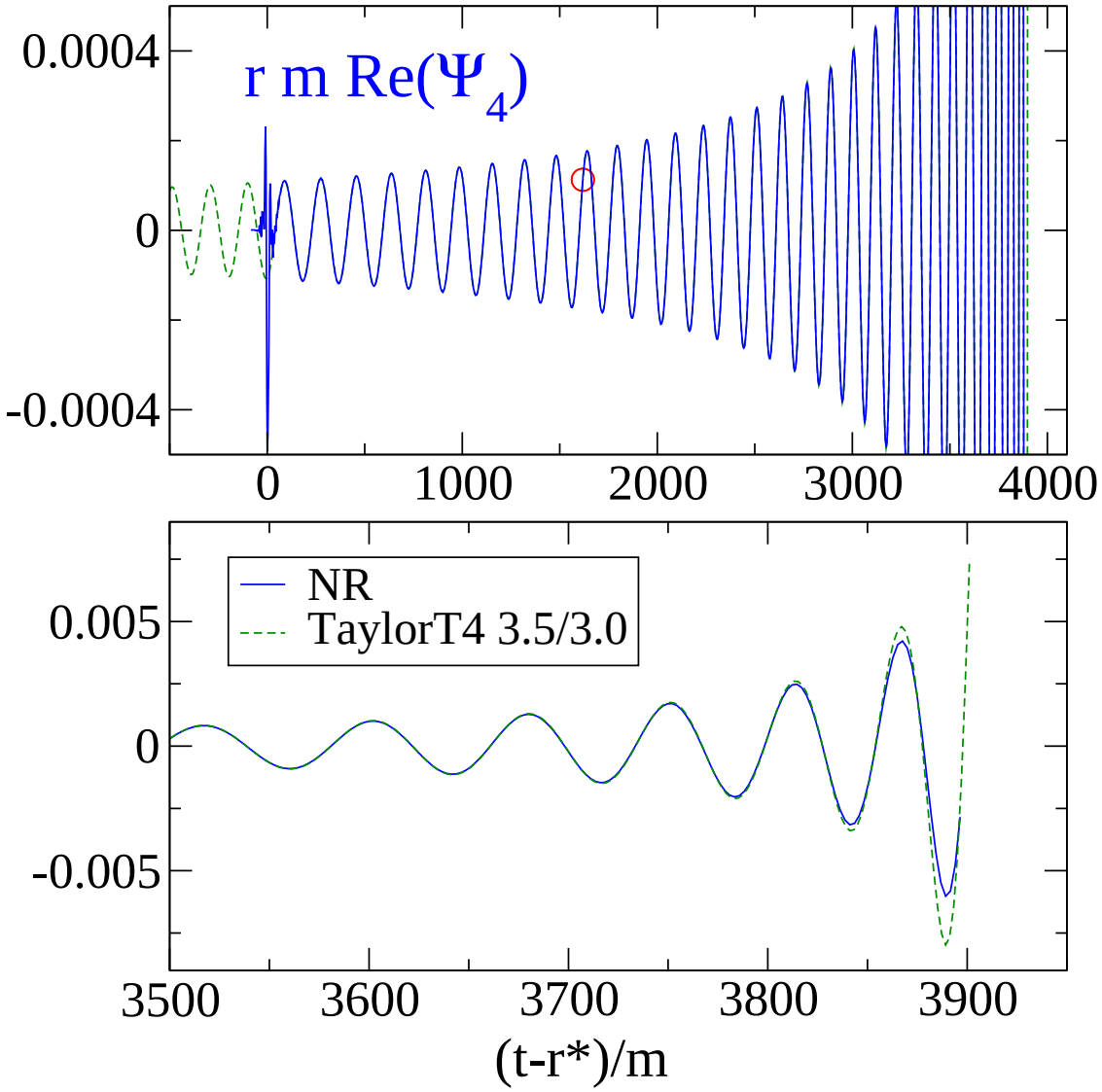

Figure 2.20: Numerical and **TaylorT4 3.5/3.0** waveforms. The PN waveform is matched to the numerical one at $m\omega_m = 0.04$, indicated by the small circle. The lower panel shows a detailed view of the end of the waveform.

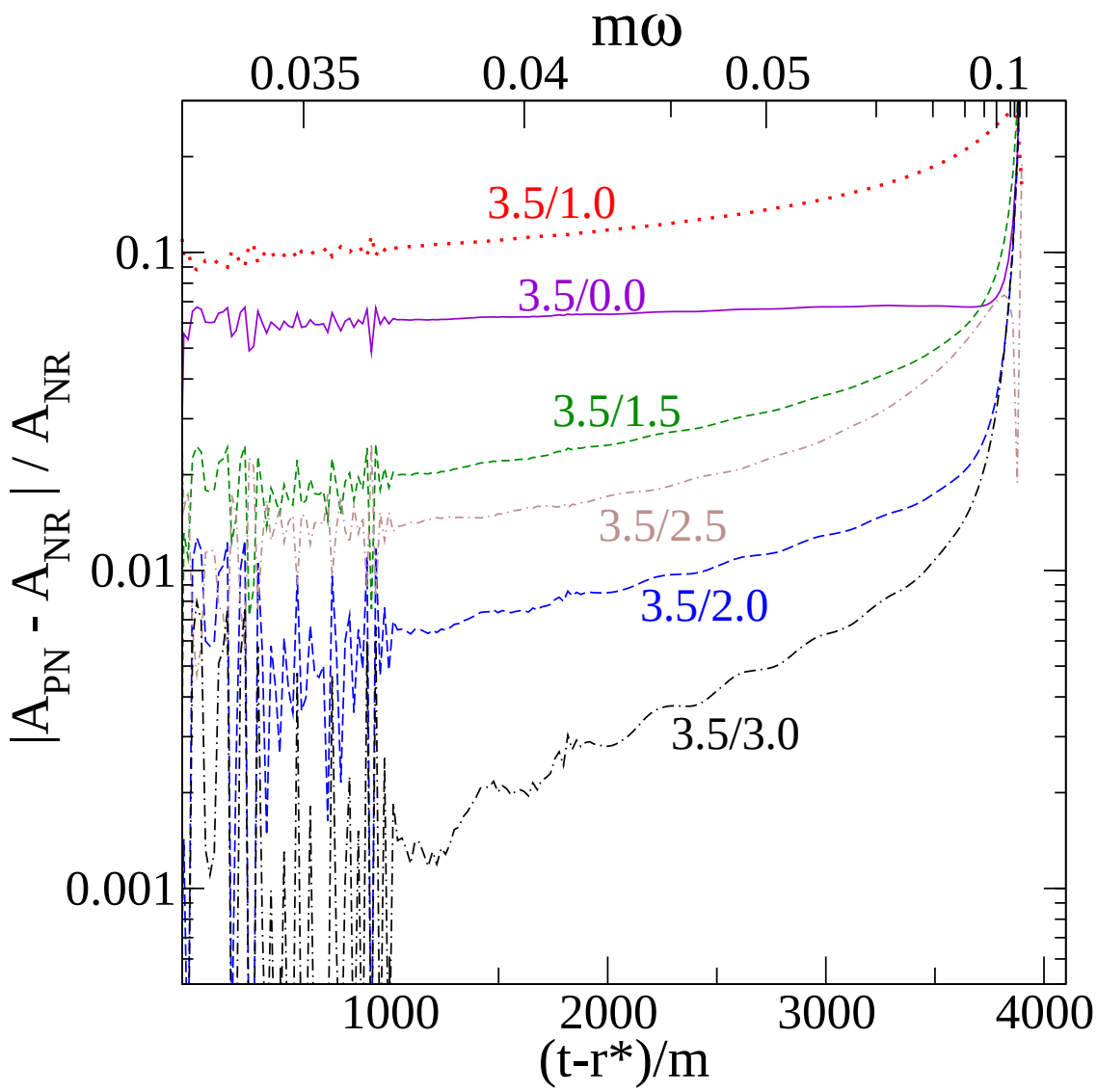

Figure 2.21: **TaylorT4** amplitude comparison for different PN orders. Shown is the relative difference in gravitational wave amplitude between TaylorT4 and numerical Y_{22} waveforms as a function of time. Matching is performed at $m\omega_m$ = 0.04. All curves use 3.5PN order in phase but different PN orders (as labeled) in the amplitude expansion.

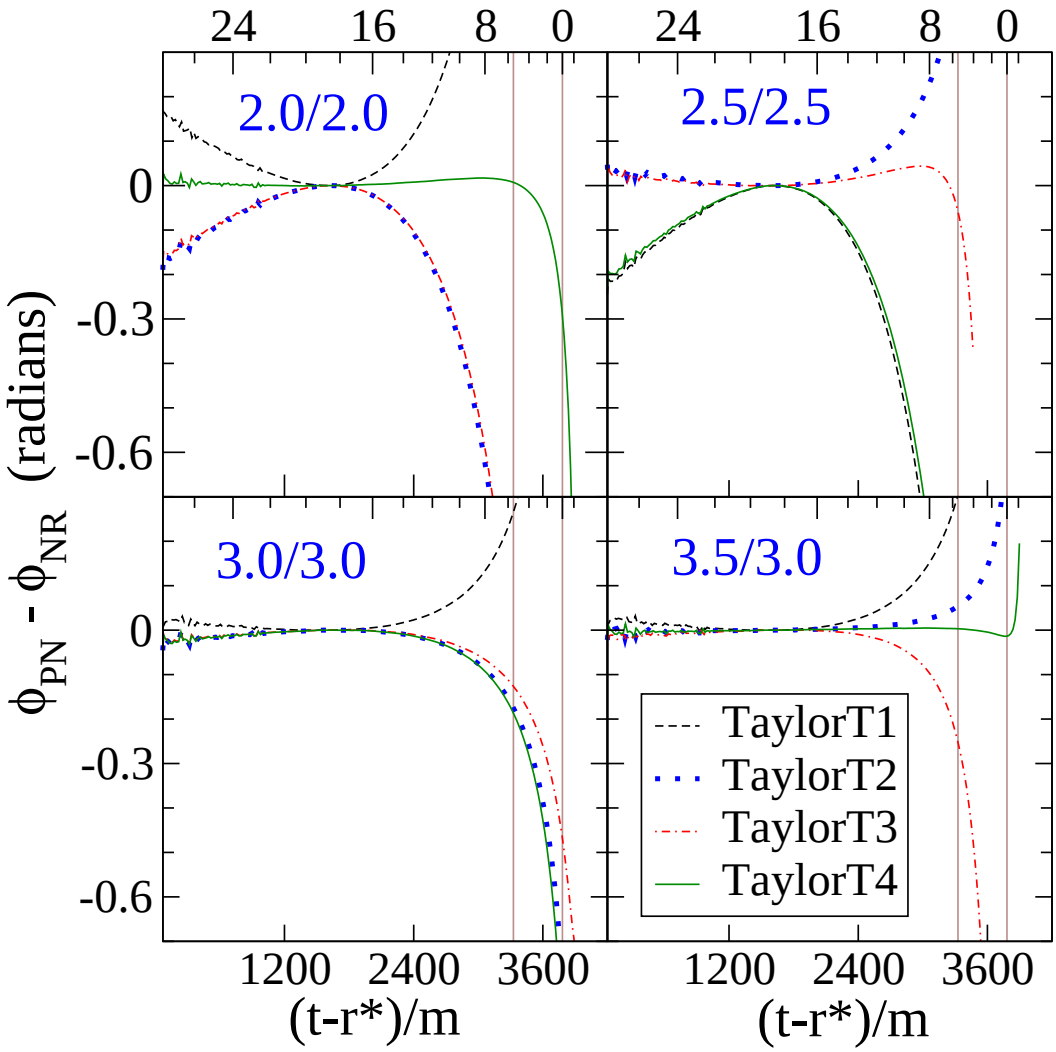

Figure 2.22: Phase comparison for different PN approximants at different PN orders, matched at $m\omega_m = 0.04$. Shown is the difference in gravitational wave phase between each post-Newtonian approximant and the numerical Y_{22} waveforms as a function of time. The two vertical brown lines indicate when the numerical simulation reaches $m\omega = 0.063$ and 0.1, respectively; the labels along the top horizontal axes give the number of gravitational-wave cycles before $m\omega = 0.1$.

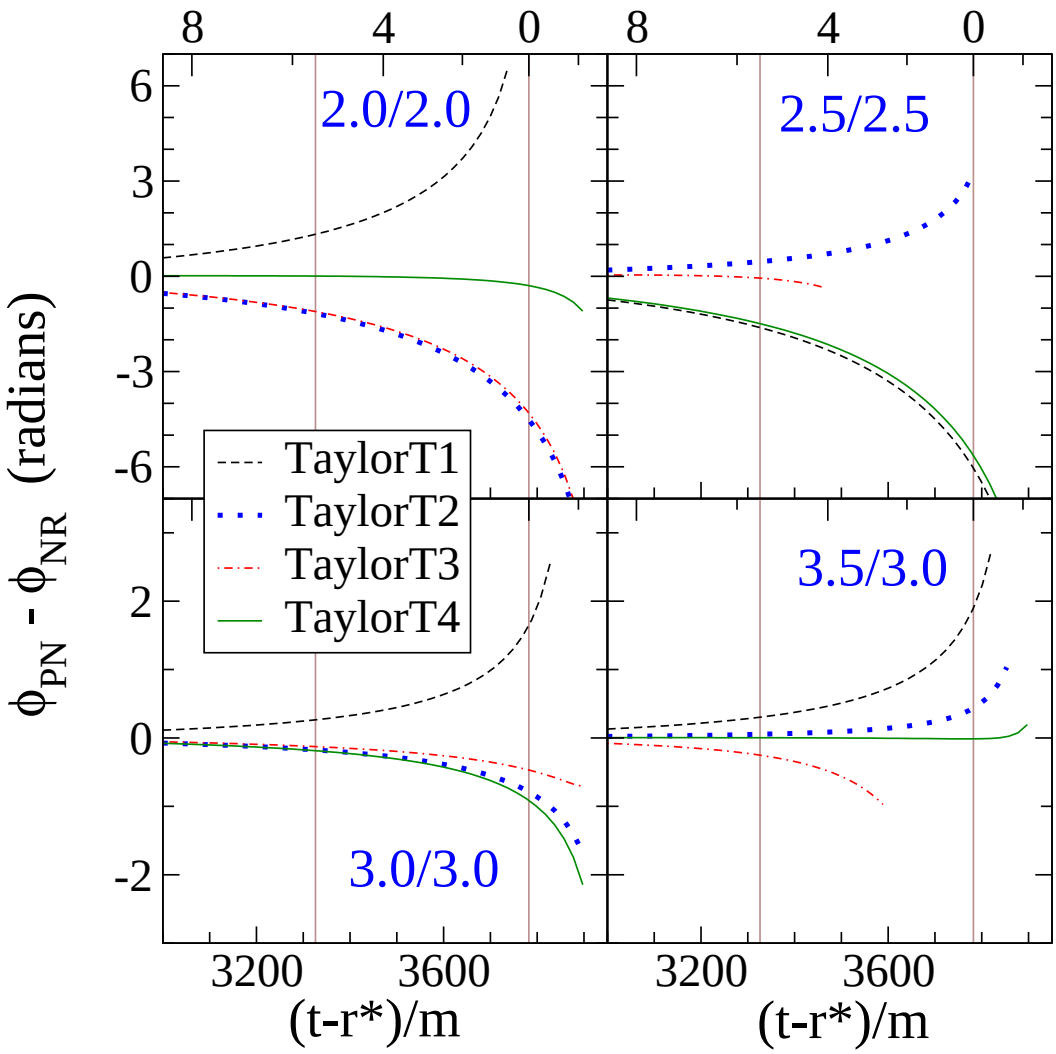

Figure 2.23: Same as Fig. 2.22, but showing only the last stage of the inspiral. The horizontal axis ends at the estimated time of merger, $(t - r^*)_{\rm CAH} = 3950m$, cf. Sec 2.2.7. The top and bottom panels use different vertical scales.

Figure 2.22 presents phase differences as a function of time for all four PN approximants we consider here and for different PN orders. The post-Newtonian and numerical waveforms are matched at $m\omega_m = 0.04$, about 9 cycles after the beginning of the numerical waveform, and about 21 cycles before its end. We find that some PN approximants at some particular orders agree exceedingly well with the numerical results. The best match is easily TaylorT4 at 3.5PN order, and the next best match is TaylorT4 at 2.0PN order. Some approximants behave significantly worse, such as the TaylorT1 and TaylorT4 waveforms at 2.5PN order. The 2.5PN and 3PN TaylorT3 waveforms agree very well with the numerical waveform at early times, but at late times they accumulate a large phase difference; the 2.5PN TaylorT3 waveform ends even before the numerical waveform reaches $m\omega = 0.1$ (the rightmost vertical brown line in Fig. 2.22).

We also find that all four PN approximants, when computed to 3PN order or higher, match the numerical waveform (and each other) quite closely at early times, when all PN approximants are expected to be accurate. However, at late times, $t - r^* > 2500m$, the four PN approximants begin to diverge, indicating that PN is beginning to break down.

Figure 2.23 is an enlargement of Fig. 2.22 for the last 10 gravitational wave cycles before merger. This figure shows in more detail how the different PN approximants behave near merger.

Figure 2.24 presents similar results in a different format. We compute the phase differences between the numerical waveform and the various post-Newtonian approximants at the times when the numerical waveform reaches gravitational wave frequencies $m\omega = 0.063$ and $m\omega = 0.1$ (the times corresponding to these frequencies are also indicated by brown lines in Fig. 2.22).

We then plot these phase differences as a function of the post-Newtonian order (using equal order in phase and amplitude, except for 3.5PN order, where we use 3.0PN in amplitude). Three PN approximants end before $t_{0.1}$: TaylorT1 2.0/2.0, TaylorT3 2.5/2.5, TaylorT3 3.5/3.0. These data points therefore cannot be included in the right panel of Fig. 2.24.

The general trend seen in Fig. 2.24 is that the phase difference decreases with increasing PN order. However, this convergence is not monotonic, and the scatter in Fig. 2.24 can be larger than the phase differences themselves. For example, the 0PN waveforms are about as good as the 2.5PN waveforms for TaylorT1 and TaylorT4, and the 2PN TaylorT4 waveform agrees with the numerical results much better than do either the 2.5PN or 3PN TaylorT4 waveforms. Considering Fig. 2.24, it seems difficult to make statements about the convergence with PN order for any particular PN approximant, or statements about which PN orders are generally "good". Given that at fixed PN order the different approximants differ merely by the treatment of uncontrolled higher-order terms, the scatter in Fig. 2.24 in some sense represents the truncation error at each PN order. While some PN approximants at certain orders may show better agreement with the numerical simulation, we are not aware of any means to predict this besides direct comparisons to numerical simulations (as is done here). In particular, Fig. 2.24 suggests that the remarkable agreement between our numerical results and the 3.5PN TaylorT4 approximant may be simply due to luck; clearly, more PN-NR comparisons are needed, with different mass ratios and spins, to see if this is the case.

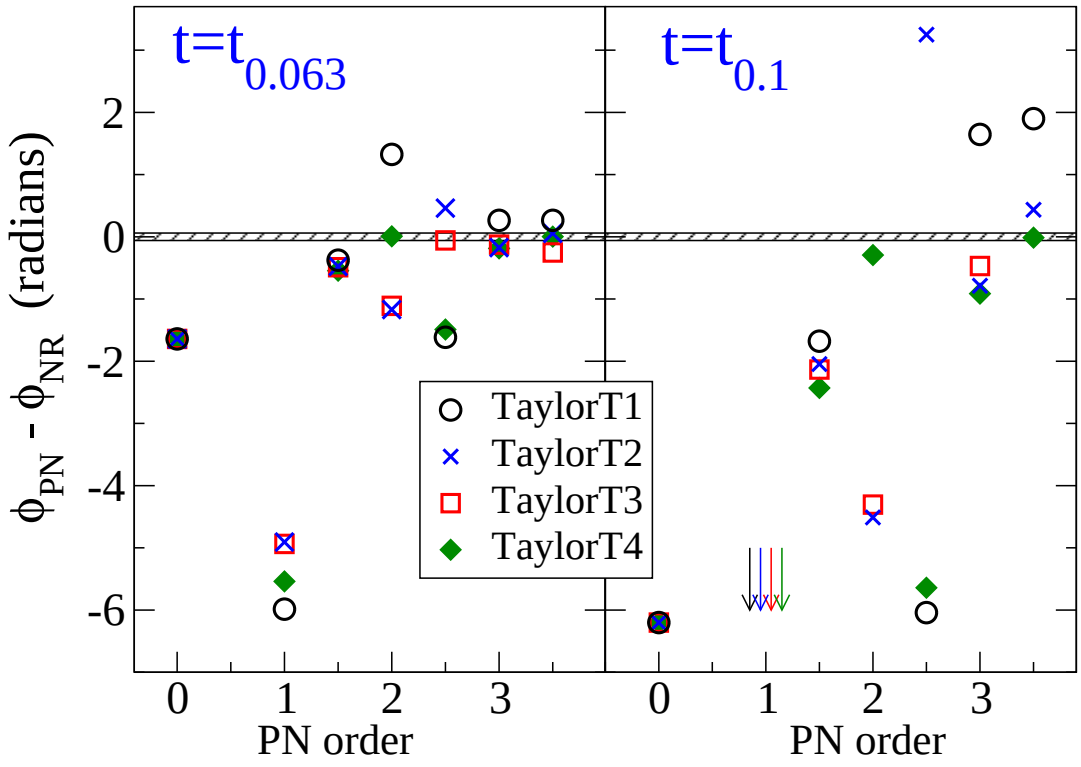

Figure 2.24: Phase differences between numerical and post-Newtonian waveforms at two selected times close to merger. Waveforms are matched at $m\omega_m$ = 0.04, and phase differences are computed at the time when the numerical simulation reaches $m\omega$ = 0.063 (left panel) and $m\omega$ = 0.1 (right panel). Differences are plotted versus PN order (equal order in phase and amplitude, except the '3.5 PN' points are 3.5/3.0). On the right plot, the 1PN data points are off scale, clustering at −15 radians. The thin black bands indicate upper bounds on the uncertainty of the comparison as discussed in Sec. 2.5.1.

2.7 Conclusions

We have described numerical simulations of an equal mass, non-spinning binary black hole spacetime covering 15 orbits of inspiral just prior to the merger of the two black holes. Using a multi-domain pseudospectral method we are able to extract the gravitational wave content measured by a distant observer with a phase accuracy of better than 0.02 radians over the roughly 30 cycles of gravitational radiation observed. We demonstrate that in order to achieve this accuracy it is necessary to accurately extrapolate the waveform from data obtained at extraction surfaces sufficiently far from the center of mass of the system. When comparing to zero-spin, zero-eccentricity PN formulae, our phase uncertainty increases to 0.05 radians because the numerical simulation has a small but nonzero orbital eccentricity and small but nonzero spins on the holes.

Judging from the case in which we match at $m\omega_m = 0.04$, our numerical simulations are consistent (within our estimated phase uncertainty) with all PN approximants (at the highest PN order) from the beginning of our inspiral until about 15 gravitational wave cycles prior to the merger of the binary. This agreement provides an important validation of our numerical simulation. It also establishes a regime in which the 3.5-th order post-Newtonian waveforms are accurate to this level, at least for an equal mass, non-spinning black hole binary. After this point, the various PN approximants begin to diverge, suggesting that the approximation is beginning to break down. Since there are many different PN approximants (including Padé [100] and effective-one-body [65, 94, 97, 67] which were not discussed in this paper) it may be possible to find a clever way to push the PN expansion beyond its breaking point.

Indeed, we find that one approximant, TaylorT4 at 3.5PN in phase, works astonishingly well, agreeing with our numerical waveforms for almost the entire 30-cycle length of our runs. Given the wide scatter plot of predictions by various PN approximants, it is likely that TaylorT4 3.5/3.0 simply got lucky for the equal mass non-spinning black hole binary. In fact, the assumption of adiabaticity (*i.e.*, circular orbits) is known to lead to much larger phase differences relative to a non-adiabatic inspiral (see Fig. 4 of [66] and [183]) than the phase differences between NR and TaylorT4 we find in Fig. 2.19. Thus it seems that the uncontrolled higher order terms of TaylorT4 3.5/3.0 balance the error introduced by the adiabaticity assumption to a remarkable degree. It remains to be determined whether similar cancellations occur when the black hole masses are unequal or when the holes have nonzero spin.

Regardless of the robustness of TaylorT4, it seems evident that numerical simulations are needed in order to know which, if any, PN approximant yields the correct waveform after the various approximants begin to diverge. For there is no *a priori* reason why TaylorT4 should be a better choice than TaylorT1 as they differ only in whether the ratio of gravitational wave flux to the derivative of the orbital energy with respect to frequency is left as a ratio of post-Newtonian expansions or re-expanded as a single post-Newtonian expansion.

The surprising accuracy of TaylorT4 3.5/3.0 in the gravitational frequency range from $m\omega = 0.035$ through $m\omega = 0.15$, for the equal mass, non-spinning inspiral of two black holes, in principle could form a basis for evaluating the errors of numerical simulations. Instead of worrying about errors due to different formulations, initial data, boundary conditions, extraction methods, etc., perhaps a long inspiral simulation could be compared with TaylorT4 3.5/3.0 in

order to get a direct estimate of the phase error. Similarly, because of its good agreement, TaylorT4 3.5/3.0 could also be used to address questions that require much longer waveforms than currently available, for instance the question of when lower order post-Newtonian waveforms become unreliable.

We find that the 3PN contributions to the amplitude of the $(2, 2)$ modes improve their accuracy with respect to the numerical waveforms. This suggests that for accurate parameter estimation, it may be desirable to compute the full 3PN amplitude for the polarization waveforms. Despite the formidable nature of the calculation required, it would also be interesting to see how the inclusion of 4PN order corrections to the phasing would affect our comparisons.

Much work still needs to be done to improve the comparison between NR and PN. Our primary goal is to push our simulations through merger and ringdown so that we may compare various resummed PN approximants and the effective-one-body approximants during the last cycle of inspiral and merger, as well as test TaylorT4 3.5/3.0 closer to merger. We also intend to do long inspirals with arbitrary masses and spins in order to test the robustness of PN over a range of these parameters.

Furthermore we wish to improve our initial data. There is a large amount of 'junk radiation' present in the initial data that limits how early we can match PN and NR waveforms. Reduction of this junk radiation [180] would improve the accuracy of our simulations as well.

Finally, we have done just a simple comparison between NR and PN, without including any treatment of effects that are important for real gravitational wave detectors such as limited bandwidth and detector noise. In order to more

directly address the suitability of PN formulae for analyzing data from gravitational wave detectors, it will be necessary to fold in the properties of the detector, to consider specific values for the total mass of the binary, and to fit for the mass from the waveforms rather than assuming that the PN and NR waveforms correspond to the same mass. We leave this for future work.

CHAPTER 3

INEFFECTIVENESS OF PADÉ RESUMMATION TECHNIQUES IN POST-NEWTONIAN APPROXIMATIONS

3.1 Introduction

[1] Even though general relativity was developed at the beginning of the twentieth century, no analytical solution is known for the two-body problem. Until recently, attempts to find a numerical solution failed because of the complexity of the mathematical equations and the instabilities inherent in the analytical formulations being used. In the past few years, breakthroughs in numerical relativity [204, 206, 72, 14] allowed a system of two inspiraling black holes to be evolved through merger and the ringdown of the remnant black hole [74, 143, 118, 212, 215, 57, 182, 121, 217].

Studying the late dynamical evolution of these inspiraling compact binaries is important because they are among the most promising source of gravitational waves for the network of laser interferometric detectors such as LIGO and VIRGO. The detection of these gravitational waveforms (GW) is important for testing general relativity in the strong field limit. Moreover, these detectors can extract from the waves physical data about these sources such as the component masses and spins and the orbital eccentricity. For an unbiased extraction of these parameters, a large bank of accurate waveforms needs to be constructed. Numerical relativity alone cannot compute all the waveforms needed because of the computational cost. Instead, the waveforms are based on post-Newtonian

[1] This chapter is extracted from Ref. [186] which was written in collaboration with Lawrence E. Kidder, and Saul A. Teukolsky, and published in 2008.

(PN) approximations [38, 35].

The post-Newtonian approximation is a slow-motion, weak-field approximation to general relativity. In order to produce a post-Newtonian waveform, the PN equations of motion of the binary are solved to yield explicit expressions for the accelerations of each body in terms of the binary's orbital frequency Ω [158, 159, 107, 109, 41, 42, 108, 38, 155, 154, 153]. Then solving the post-Newtonian wave generation problem yields expressions for the gravitational waveform h and the gravitational wave flux F in terms of radiative multipole moments [225]. These radiative multipole moments are in turn related to the source multipole moments, which can be given in terms of the relative position and relative velocity of the binary [32]. Instead of comparing the post-Newtonian waveform with a numerical waveform along a certain direction with respect to the source, the comparison can be done in all directions by decomposing the waveform in terms of spherical harmonic modes. For an equal-mass nonspinning binary, the $(2,2)$ mode h_{22} [164, 162, 163, 28] is often used to compare numerical and post-Newtonian waveforms, because it is the dominant mode. Its time derivative $\dot{h}_{22}$ is used to compute the gravitational wave flux. The resulting expressions for the orbital energy E, the gravitational energy flux F, and the amplitude h_{22} are given as Taylor series of the frequency-related parameter

$$x = (M\Omega)^{2/3}\,, \tag{3.1}$$

where M is the total mass of the binary and $G = c = 1$. The invariantly defined "velocity"

$$v = x^{1/2}\,, \tag{3.2}$$

another dimensionless parameter, is often used in writing these Taylor series.

Computing PN series to high order is difficult and time consuming. Since the various PN expressions are given as slowly convergent Taylor series, the Padé transformation [23, 232] was suggested in Ref. [98] to accelerate the convergence of these series. The Padé transformation, P_n^m, consists of writing a Taylor series, T_k, of order k as the ratio of two polynomials, one of order m in the numerator, and another of order n in the denominator, such that $m + n \leq k$. If well behaved, this method accelerates the convergence of a Taylor series as the order of the Padé transformation, $m + n$, is increased. For example, in Table 3.1 we compare the convergence of the Taylor expansion of the exponential function $\mathrm{Exp}_n(v)(\equiv e^v)$ at order n to its Padé approximant $\mathrm{Exp}_m^{m+\epsilon}(v) = P_m^{m+\epsilon}[\mathrm{Exp}_n(v)]$ along the diagonal, where $m = \lfloor n/2 \rfloor$ and $\epsilon = 0$ or 1. After 12 terms ($n = 11$), the last two partial sums of the Taylor expansion converge to 4 significant figures. However, the last two Padé approximants $\mathrm{Exp}_5^5(v)$ and $\mathrm{Exp}_5^6(v)$ converge to 6 significant figures. The error between the exact value of the exponential, 7.46331734, and the Padé approximant $\mathrm{Exp}_5^6(v = 2.01)$ is 6×10^{-8}, while the error between the 11th order partial sum and the exact value is 10^{-5}. Figure 3.1 shows the convergence of the Taylor expansion of the exponential function and its Padé approximant.

The hope of accelerating the convergence of the post-Newtonian Taylor series of the energy and flux motivated the use of their Padé approximants to construct Padé approximant waveforms [98, 100, 101, 105, 111, 113, 62, 66, 60, 67, 65, 220, 120]. If these resummation techniques accelerate the convergence of the Taylor series in PN approximations, the range of validity of PN approximations suggested by Ref [188] could be extended. Moreover, the work of Refs. [200, 88] in the test mass limit motivated the addition of a simple pole to the flux F of a binary system as the bodies approach the light ring orbit. By mathematical

Table 3.1: Convergence of the Taylor expansion, $\mathrm{Exp}_n = \sum_{k=0}^{n} v^k/k!$ of the exponential function $\mathrm{Exp}(v)$ and its Padé approximant $\mathrm{Exp}_m^{m+\epsilon}$ at $v = 2.01$, $m = \lfloor n/2 \rfloor$. The Padé approximant converges to six significant figures while the Taylor series converges to four significant figures at $v = 2.01$. The error between the exact value of the exponential, 7.46331734, and the Padé approximant $\mathrm{Exp}_5^6(v = 2.01)$ is 6×10^{-8}, while the error between the Taylor approximant $\mathrm{Exp}_{11}(v = 2.01)$ and the exact value is 10^{-5}.

n	$\mathrm{Exp}_n(v)$	$P_m^{m+\epsilon}[\mathrm{Exp}_n(v)]$
0	1.0000000	1.0000000
1	3.0099999	3.0099999
2	5.0300499	-401.0000
3	6.3834834	9.1313636
4	**7**.0635838	**7**.0601492
5	**7**.3369841	**7.4**053299
6	**7.4**285732	**7.4**747817
7	**7.4**548724	**7.46**45660
8	**7.46**14801	**7.463**1404
9	**7.46**29558	**7.4633**014
10	**7.463**2524	**7.46331**91
11	**7.463**3066	**7.46331**74

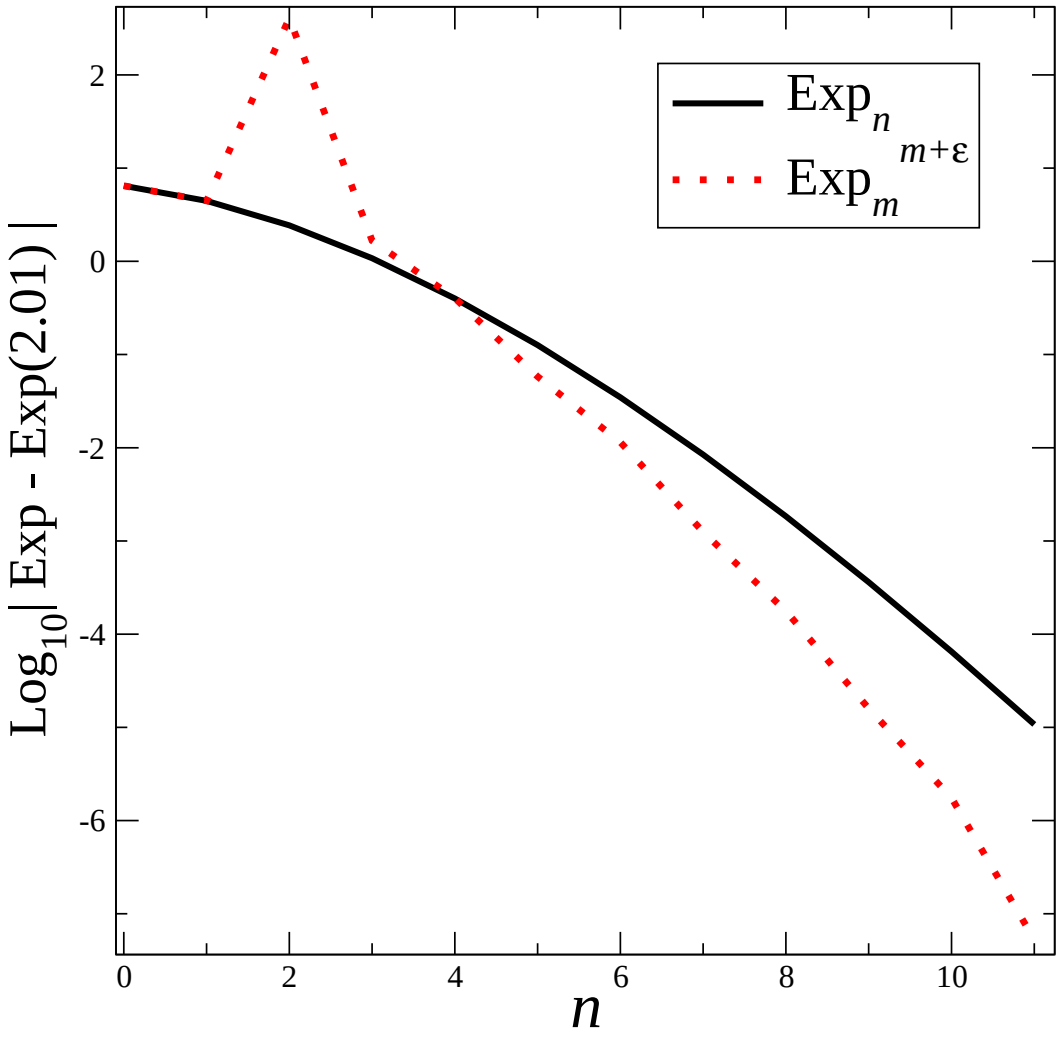

Figure 3.1: Convergence of the Taylor expansion, $\mathrm{Exp}_n = \sum_{k=0}^{n} v^k/k!$ of the exponential function $\mathrm{Exp}(v)$ and its Padé approximant $\mathrm{Exp}_m^{m+\epsilon}$ at $v = 2.01$, $m = \lfloor n/2 \rfloor$. The Padé approximant converges faster than the Taylor series.

continuity, the existence of a pole in the equal mass case was anticipated [98].

More recently, waveforms are constructed by including these ideas in effective one body (EOB) models. The EOB approach [66, 60, 67, 65, 62, 61, 94, 101, 97, 100, 90, 112, 222, 111, 113, 95, 114] aims at providing an accurate analytical description of the motion and radiation of coalescing binary black holes. The approach consists of three separate ingredients: 1) a description of the conservative Hamiltonian part of the dynamics $\hat{H}$, 2) a formulation of the radiation reaction force $\mathcal{F}$ from the radiated flux F and 3) an expression of the GW waveform amplitude emitted by the coalescing binary system (i.e h_{22}).

The flux plays an important role in approximating the radiation reaction force $\mathcal{F}$ in the EOB models [156, 157, 66]. The leading-order radiation reaction force $\mathcal{F}$ [221, 89, 133] enters the equations of motion at 2.5PN order. Since the equations of motion are known only to 3.5PN order, one has to rely on the assumed balance between energy loss in the system and radiated flux at infinity [175, 30] to generate an approximate expression of the radiation reaction force at 3.5PN order beyond the leading term.

Ref. [53] computes the GW energy flux and GW frequency derivative from a highly accurate numerical simulation of an equal-mass, nonspinning black hole binary. By assuming energy balance, the (derivative of the) center-of-mass energy is estimated. These quantities are then compared with the numerical values using various Taylor, Padé, and EOB models. The main goal of Ref. [53] is taking a set of well-established proposals in the literature for approximating waveforms and seeing how well they work in practice. Another goal of Ref. [53] is to examine some modifications of those proposals. The main goal of this paper, by contrast, is to show that a key ingredient in those proposals does not

appear to be necessary.

In Ref. [174], Blanchet gave an argument that Padé and EOB resummations are unjustified because for two comparable-mass bodies there is no equivalent of the Schwarzschild light-ring orbit at the radius $r = 3M$. His argument is based on the PN coefficients of the binary's energy and their relation to predicting the innermost circular orbit. He finds that the radius of convergence of the PN series, which is related to the radius of the light-ring orbit, is around 1 (instead of 1/3 as for Schwarzschild). Blanchet concluded that Taylor series converge well for equal masses and that templates based on Padé/EOB are not justified, because the dynamics of two bodies in general relativity does not appear as a small "deformation" of the motion of a test particle in Schwarzschild. This paper arrives at similar conclusions but not by considering the innermost circular orbit, which is not precisely defined in the full nonlinear case. Instead, we compare Padé approximants of the flux and Padé/EOB waveforms to the numerical data of Refs. [201, 51].

In this paper, we focus on testing two main techniques involved in building EOB models: the systematic use of Padé approximants, and the addition of a pole to the flux. The goal is to simplify these models by removing any unnecessary procedures in designing waveforms that provide good agreement with numerical waveforms.

Damour et al. [98, 100] first suggested techniques for resumming the Taylor expansions of the energy and flux functions. Starting from the PN expansions of the energy E and the flux F, they proposed a new class of waveforms called P approximants, based on three essential ingredients. The first step is the introduction of new energy-type [Eq. 3.4] and flux type [Eq. 3.16] functions, called

$e(v)$ and $f(v)$, respectively. The second step is to Padé approximate the Taylor expansion of these functions. The third step is to use these Padé transforms in the definition of the energy E [Eq. 3.6] and Padé-approximated flux [Eq. 3.20]. The last step is to construct either the Padé-approximated waveform as in Sec. 3.4 or the EOB waveform as in Sec. 3.5. Schematically, the suggested procedure is summarized by the following map:

$$\left[E_n, F_n\right] \to \left[e_n, f_n\right] \to \left[e_n^m, f_n^m\right] \to \left[E(e_n^m), F(f_n^m)\right] \to h\,. \tag{3.3}$$

Our notation is to denote by $T_n^m(x)$ the Padé approximant of a k-th order Taylor series $T_k(x)$ with an m-th order polynomial in the numerator and an n-th order polynomial in the denominator such that $m + n \leq k$, i.e. the Padé approximant of $e_k(x)$ is $e_n^m(x)$.

In Sec. 3.2, we compare the 3PN Taylor series of the energy function to its possible Padé approximants using the intermediate energy function $e(x)$, as suggested by Damour et al. [98]. We compute the last stable orbit frequency, defined as the frequency for which the energy reaches a minimum as a function of frequency, and also the poles of the energy in the complex plane corresponding to each possible Padé approximant. The large variation of last stable orbit frequency and poles does not suggest good convergence of the Padé-approximated intermediate energy function $e(x)$. The energy function $E(x)$ is strongly dependent on the choice of the Padé approximant of $e(x)$. Accordingly, the Padé waveform will also be strongly dependent on the choice of the Padé approximant.

In Sec. 3.3, we present two possible methods for calculating the Padé approximant of the flux function. The first method simply takes the Padé approximant

of the Taylor series treating the logarithmic contribution as constant. Following [98], the second method adds a pole to the Taylor series, factors out the logarithmic contribution to the series, and then computes the Padé approximant of the resulting Taylor series. We test the convergence of the Padé approximant for both methods versus their Taylor series. We find that the Padé approximants of the flux do not converge any faster than their Taylor counterpart.

A simple example that illustrates the problem is shown in Table 3.2. There we compare the partial sums of the Taylor series for the flux with the corresponding Padé approximants in the test mass limit. The four flux functions $\overline{F}_n$, $\overline{F}_m^{m+\epsilon}$, F_n, and $F_m^{m+\epsilon}$ are given in Eqs. 3.14, 3.15, 3.18 and 3.20 respectively. Even for a relatively small value of x, namely $x = 0.04$ ($v = 0.2$), the Taylor series is converging very slowly. After 12 terms, only about 4 or 5 significant digits seem reliable. Moreover, the Padé resummation shows very similar behavior; there is no improvement in the convergence. We will return to this example in Fig. 3.3.

In Sec. 3.4, we generate all the possible Padé waveforms as suggested by Damour et al. [98] corresponding to 3 and 3.5 PN order. The waveform approximation requires the choice of a pole. We use the only physical pole, found from the 2PN Padé-approximated energy E_1^1. We also use the last stable orbit from the 3PN energy Taylor series E_3. The results are not very sensitive to this choice. We compare the Padé waveforms to a 15-orbit numerical waveform in the equal mass, nonspinning quasicircular case [51]. The phase difference in these comparisons ranges between 0.05 and a few radians for well-defined Padé approximants (not having a pole in the frequency domain of interest) when the matching of the numerical and Padé waveforms is done at the gravitational wave frequency $M\omega = 0.1$ [51]. None of the Padé waveforms agrees with the

Table 3.2: Convergence of the Taylor series and its Padé aprroximants of the flux in the test particle limit at $v = 0.2$ ($x = 0.04$). The four flux functions $\overline{F}_n$, $\overline{F}_m^{m+\epsilon}$, F_n, and $F_m^{m+\epsilon}$ are given in Eqs. 3.14, 3.15, 3.18, and 3.20 respectively. Even in the test mass limit, the Padé approximant of the flux fails to converge faster that its 5.5 PN Taylor series at a relatively small value of $v = 0.2$. After 12 terms, only about 4 or 5 significant digits seem reliable for the Taylor expansions and their Padé approximants. The lack of improvement in the convergence of the Padé approximants should be contrasted with the example in Table 3.1.

PN order	$\overline{F}_n$	$\overline{F}_m^{m+\epsilon}$	F_n	$F_m^{m+\epsilon}$
0.0	1.000000	1.000000	1.530011	1.530011
0.5	1.000000	1.000000	1.000000	1.000000
1.0	0.851547	1.000000	0.772866	0.602534
1.5	**0.9**52078	**0.9**11487	1.005361	0.887757
2.0	**0.9**44193	**0.9**28720	**0.9**40013	**0.93**7227
2.5	**0.9**31939	**0.93**6461	**0.9**25444	**0.93**8929
3.0	**0.9**41025	**0.939**366	**0.9**45405	**0.93**9502
3.5	**0.939**726	**0.939**399	**0.93**8991	**0.93**8082
4.0	**0.939**208	**0.939**363	**0.939**048	**0.939**471
4.5	**0.939**745	**0.939**719	**0.939**979	**0.939**516
5.0	**0.93960**1	**0.93965**3	**0.939**526	**0.93968**4
5.5	**0.93960**5	**0.93962**3	**0.939**616	**0.93962**1

numerical waveform better than the Taylor series T4-3.5/3.0PN, which has an error of 0.02 radians. (We identify post-Newtonian approximants with three pieces of information: the label introduced by [100] for how the orbital phase is evolved; the PN order to which the orbital phase is computed; and the PN order at which the amplitude of the waveform is computed. See Ref. [51] for more details.) Our conclusion is that the Padé approximant might be helpful in suggesting fitting formulas but it does not provide a more rapidly convergent method. Note that the Padé transform also fails to accelerate the convergence of the T2, T3, and h_{22} Taylor series (see Refs. [51, 100] for the definition of these Taylor series).

In Sec. 3.5, based on the results of the previous sections, we design a simple EOB model (closely related to the ET EOB model of Ref. [62]) using the Taylor series of the flux. We add one unknown 4PN term that we fit for by maximizing the agreement between the EOB model waveform and the numerical waveform. The model does not require adding a pole to the flux, nor an *a priori* knowledge of the last stable orbit from the energy function. This simple EOB model, with only one parameter to fit for, agrees with the numerical waveform to within 0.002 radians (3×10^{-4} cycles). (This is 6 times smaller than the claimed numerical accuracy of [113], smaller by an even larger factor than the claimed numerical accuracy of [220], and 25 times smaller than the gravitational wave phase uncertainty of the numerical waveform. See Table III in Ref [51] for more details.) This model agrees with the numerical waveform better than any previously suggested Taylor, Padé, or EOB waveform.

3.2 Energy Function

Damour et al. [98] introduced a new energy-type function $e(x)$, where x is the PN frequency related parameter. This assumed more "basic" energy function $e(x)$ is constructed out of the total relativistic energy $E_{\rm tot}(x)$ of the binary system. Explicitly

$$e(x) \equiv \left(\frac{E_{\rm tot}^2 - m_1^2 - m_2^2}{2 m_1 m_2} \right)^2 - 1 \,, \tag{3.4}$$

where m_1, m_2 are the masses of the bodies. The total relativistic energy function $E_{\rm tot}$ is related to the post-Newtonian energy function $E(x)$ through

$$E_{\rm tot}(x) = M \left[1 + E(x) \right] \,, \tag{3.5}$$

where M is the total mass ($M = m_1 + m_2$). Solving for $E(x)$ in terms of $e(x)$ using Eqs. (3.4) and (3.5), we get[98]

$$E(x) = \left\{ 1 + 2\nu \left[\sqrt{1 + e(x)} - 1 \right] \right\}^{1/2} - 1 \,, \tag{3.6}$$

where the symmetric mass ratio is $\nu = m_1 m_2 / M^2$. The orbital energy function $E(x)$ is known as a Taylor series E_k up to 3PN order as a function of x and ν [35]

$$\begin{aligned} E_{\rm 3PN}(x) = -\frac{1}{2}\,\nu\, x \Big\{ 1 - \frac{1}{12}\,(9+\nu)\, x - \frac{1}{8}\,(27 - 19\nu + \frac{1}{3}\nu^2)\, x^2 \\ + \Big[-\frac{675}{64} + \left(\frac{34445}{576} - \frac{205}{96}\pi^2 \right) \nu \\ - \frac{155}{96}\nu^2 - \frac{35}{5184}\nu^3 \Big]\, x^3 \Big\} \,. \end{aligned} \tag{3.7}$$

Using the above equations, we compute the Taylor series expansion, $e_k(x)$, of $e(x)$ up to 3PN order:

$$\begin{aligned} e_{\rm 3PN}(x) = -\, x \Big\{ 1 - (1 + \frac{1}{3}\nu) x - (3 - \frac{35}{12}\nu) x^2 \\ - \Big[9 + \frac{1}{288} \left(-17236 + 615\pi^2 \right) \nu \\ + \frac{103}{36}\nu^2 - \frac{1}{81}\nu^3 \Big]\, x^3 \Big\} \,. \end{aligned} \tag{3.8}$$

In the test mass limit ($\nu \to 0$), the exact function $e(x)$ coincides with the Padé approximant $P^1_1(x)$ of its Taylor expansion in Eq. (3.8)

$$e(x; \nu \to 0) = -x\frac{1-4x}{1-3x}\,. \tag{3.9}$$

This quantity has a pole at $x_{\rm pole} = 1/3$. The orbital energy is then

$$E(x; \nu \to 0) = \nu\left(\sqrt{1 - x\frac{1-4x}{1-3x}} - 1\right), \tag{3.10}$$

and it derivative is

$$\frac{dE(x; \nu \to 0)}{dx} = -\nu\frac{1-6x}{2(1-3x)^{3/2}}\,. \tag{3.11}$$

The last stable orbit occurs where

$$\frac{dE}{dx} = 0\,, \tag{3.12}$$

so in the limit $\nu \to 0$ the last stable orbit is at exactly $x_{\rm lso} = 1/6$. On the grounds of mathematical continuity between the test mass limit $\nu \to 0$ and the finite mass ratio case, Damour et al. [98] argued that the exact function $e(x)$ should be meromorphically extendable in at least part of the complex plane and should have a simple pole on the real axis. They suggested that Padé approximants would be excellent tools for giving accurate representations of functions having such poles.

Once we know the Taylor series of the new energy function $e_k(x)$, we compute its Padé approximant $e^m_n(x)$, with $m+n \leq k$. The Padé-approximated energy $E^m_n(x)$ is obtained by replacing $e(x)$ in Eq. (3.6) with $e^m_n(x)$. In the equal mass case ($\nu = 1/4$), we can define several Padé approximants of $e_k(x)$. The most interesting Padé approximants have a maximal sum of their indices, since they should be closest to the unknown exact function if the Padé resummation is converging. In Fig. 3.2, we show a plot of the PN energy function $E_{\rm 3PN}(x)$ and its Padé approximants E^1_1, E^2_1, E^1_2, E^0_3, and E^3_0 as a function of x.

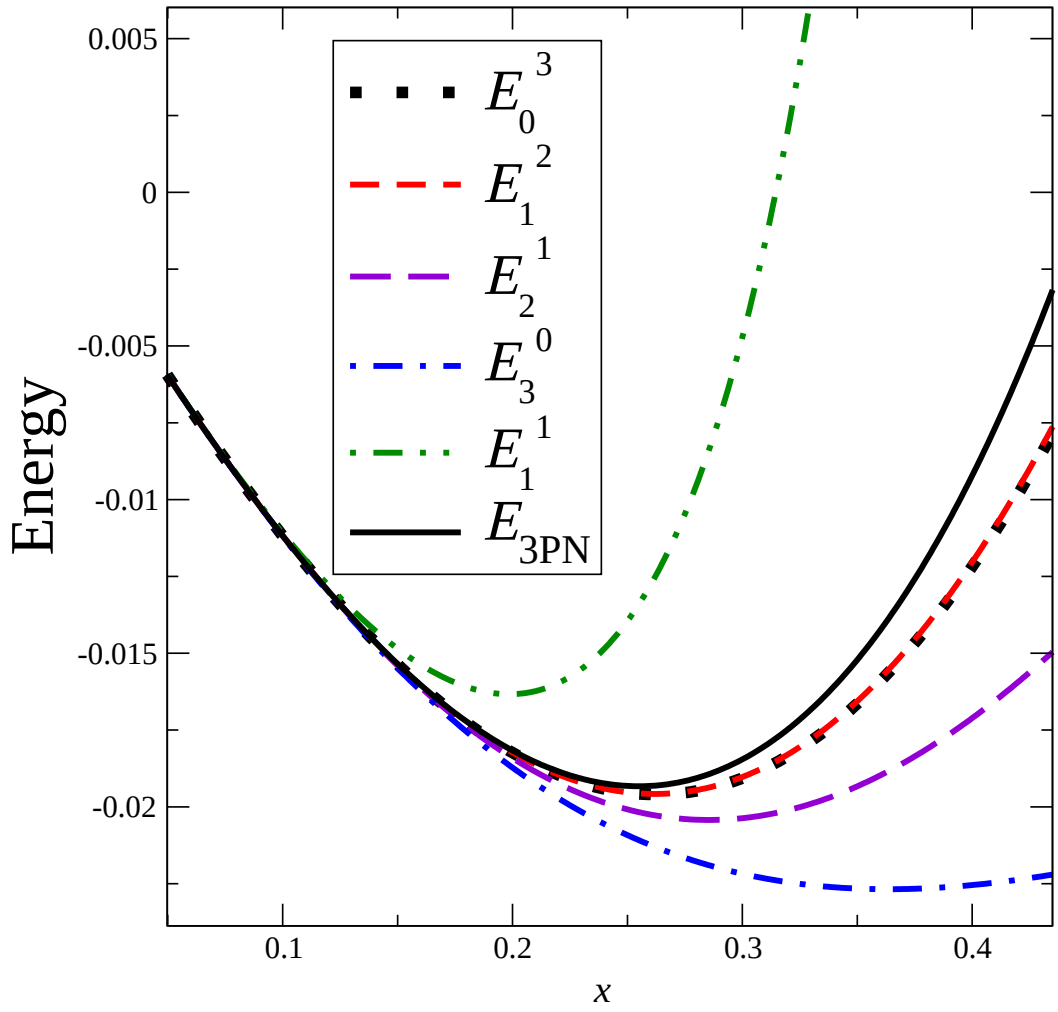

Figure 3.2: Post-Newtonian Energy at 3PN and its Padé approximants for the case $\nu = 1/4$. The plot includes the high value of $x_{\rm lso} = 0.36$, the numerical data available is at $x = 0.16$. The plots of E_0^3, E_1^2, E_2^1, and E_3^0 vary significantly, although they all correspond to the 3PN Taylor series of the energy function. E_1^1 is very different from the other functions, which suggests a poorly convergent Padé approximant.

Although the Padé approximants of the energy are of maximal order, they differ significantly. Good convergence of the Padé approximants requires good agreement between approximants of the same order $n + m$, if there is no pole in the region of interest ($0 < x \lesssim 0.4$). For example, there is no *a priori* reason why one should prefer either E_1^2 or E_2^1. Although both have the same order and are equally close to the diagonal, the difference between these functions is quite large.

In Table 3.3, we compute the locations of the poles and the last stable orbits for all of these Padé approximants. The ill convergence of the Padé transform is again seen by looking at the variation of the last stable orbit positions. In Table 3.3, for example, $x_{\rm lso}$ of E_1^2 differs by about 8% from $x_{\rm lso}$ of E_2^1. Moreover, for finite ν, the poles are all complex or not in the interval $[0, 1]$ except for the case $x_{\rm pole} = 52/109$, corresponding to the Padé-approximated energy E_1^1. There is no reason why this should be the "exact" pole that should be used in the formalism, since none of the third-order Padé approximants of the 3PN energy has a physical pole.

In summary, using Padé approximants for the energy function in the equal mass case does not seem to provide any benefit. The differences between the various Padé approximants of the energy are large. The quantities $x_{\rm pole}$ and $x_{\rm lso}$ do not show any regular behavior that could be a sign of a physical pole that could be found by using the Padé transform.

3.3 Flux Function

The general form of the PN flux at order N is

$$F(v) = \frac{32}{5}\nu^2 v^{10} \times \overline{F}_N \,, \tag{3.13}$$

where the normalized flux $\overline{F}$ is a Taylor expansion in v with logarithmic terms

$$\overline{F}_N(v) = \sum_{k=0}^{2N} A_k v^k + \left(\sum_{k=6}^{2N} B_k v^k \right) \log v \,, \tag{3.14}$$

where the post-Newtonian coefficients A_i and B_i are functions of the mass ratio parameter ν. They are given in the test mass limit in Ref. [223] and in the equal mass quasicircular case in Ref. [35]. The flux series has a logarithmic contribution starting at 3PN. Padé approximants, however, are well defined only for pure polynomials. Two possible methods are therefore used to compute the Padé approximant of the flux. The first method simply treats the logarithmic terms as constants and resums the series as a pure polynomial such that the Padé-approximated flux $\overline{F}_n^m$ is

$$\overline{F}_n^m(v) = P_n^m \left[\overline{F}_N(v) \right] . \tag{3.15}$$

The second method, suggested by Ref. [98], defines a new flux function f by adding a pole, factoring the logarithmic terms from the series, and finally computing the Padé approximant of the pure polynomial. Since we would like to check the convergence of the Padé-approximated flux versus its Taylor series, we sketch the definitions of the various functions involved. According to Ref. [98], two ideas are needed for a good representation of the analytic structure of the flux. First, since in the test mass limit F is thought to have a simple pole at the light ring [88], one might expect it by continuity to have a pole in the

Table 3.3: Values of the poles and last stable orbit (lso) of the energy for the case $\nu = 1/4$. The poles $x_{\rm pole}$ and last stable orbit frequency of the function $E_n^m(x)$ depend significantly on which Padé approximant is constructed from the Taylor series $e_k(x)$. The only physical pole is $x_{\rm pole} = 52/109$, which is at a larger value than the pole in the test mass limit. The position of the last stable orbit also varies significantly.

Energy	$x_{\rm pole}$	$x_{\rm lso}$
$E_{\rm 3PN}$	–	0.254
E_1^1	$52/109 = 0.477$	0.199
E_0^3	–	0.262
E_1^2	-4.41	0.261
E_2^1	$0.170 \pm 0.757i$	0.285
E_3^0	$0.044 \pm 0.501i, -0.696$	0.363

comparable mass case. This motivates the introduction of the following factored flux function, $f(v;\nu)$:

$$f(v;\nu) \equiv \left(1 - \frac{v}{v_{\rm pole}(\nu)}\right) F(v;\nu)\,, \tag{3.16}$$

where $v_{\rm pole}$ is the pole of the Padé-approximanted energy function used.

Second, the logarithmic term that appears in the flux function needs to be factored out so we can use the standard Padé transformation. After factoring the logarithmic terms out, the flux function f becomes

$$f_n(v;\nu) \;=\; \left[1 + \log\frac{v}{v_{\rm lso}}\left(\sum_{k=6}^{2N} \ell_k v^k\right)\right] \times \left(\sum_{k=0}^{2N} f_k v^k\right), \tag{3.17}$$

where the coefficients l_k and f_k are given in Ref. [98], and $v_{\rm lso}$ is the velocity of the last stable orbit of the Padé-approximated energy. Then the Taylor series of the flux with a pole is defined as

$$F_n(v;\nu) \equiv \frac{f_n(v;\nu)}{1 - v/v_{\rm pole}(\nu)}\,. \tag{3.18}$$

The Padé approximant of the intermediate flux function $f(v)$ is defined as

$$f_n^m(v) \;\equiv\; \left[1 + \log\frac{v}{v_{\rm lso}(e_n^m;\nu)}\left(\sum_{k=6}^{2N} \ell_k v^k\right)\right] \times P_n^m\left[\sum_{k=0}^{2N} f_k\, v^k\right], \tag{3.19}$$

where $v_{\rm lso}(e_n^m; \nu)$ denotes the last stable orbit velocity for the Padé approximant $P_n^m[e(x)]$. Finally, the corresponding Padé approximant of the flux $F(v)$ is given by

$$F_n^m(v; \nu) \equiv \frac{f_n^m(v; \nu)}{1 - v/v_{\rm pole}(e_n^m; \nu)}\,, \tag{3.20}$$

where $v_{\rm pole}(e_n^m; \nu)$ denotes the pole velocity defined by $e_n^m(x)$.

3.3.1 Flux for the test mass case

The exact gravitational wave luminosity F is not known analytically in the test particle limit. It has been computed numerically by Poisson [201]. The post-Newtonian expansion of the flux is known in the test mass limit to 5.5PN order [223]. This allows us to test the rate of convergence of the Taylor series of the normalized flux $\overline{F}_n$ [Eq. 3.14] and its Padé-approximant $\overline{F}_n^m$ constructed treating the logarithmic term as a constant [Eq. 3.14]. We also test the convergence of the flux function F_n [Eq. 3.18] and its Padé approximant F_n^m [Eq. 3.20]. These convergence tests use the known values $v_{\rm pole} = 1/\sqrt{3}$ and $v_{\rm lso} = 1/\sqrt{6}$ for the test mass limit as discussed in Sec. 3.2.

In Fig. 3.3, we test the convergence of the various flux functions at the velocity value $v = 0.2$. The four flux functions $\overline{F}_n$, $\overline{F}_m^{m+\epsilon}$, F_n, and $F_m^{m+\epsilon}$ are given in Eqs. 3.14, 3.15, 3.18 and 3.20 respectively. We use the Padé approximant along the diagonal $P_m^{m+\epsilon}$, where $\epsilon = 0$ or 1. The rates of convergence of the Taylor expansion and its Padé approximant are nearly equal for the two methods, whether or not we include a pole. As the PN order increases, the Taylor series and its Padé approximant alternate in which provides a better fit to the numerical data for the flux. For example, at 2PN order the Taylor flux with a

pole [Eq. 3.18] fits the numerical data the best. At 2.5 and 3 PN order the Padé approximant of the flux F_n^m [Eq. 3.20] fits the numerical data the best, while at 3.5 and 5PN order the Taylor series of the flux [Eq. 3.14] is the best. At 5.5PN the Padé approximant of the flux [Eq. 3.20] gives the best agreement. The results are similar for other values of v. No method has the best convergence rate.

According to Padé theory, the convergence of the Padé approximant is best along the diagonal, but it is equally good along the off-diagonal terms if no pole exists in the region of interest (i.e. no zeroes appear in the denominator of the Padé approximant.) For this reason, we show the error between all the possible maximal Padé-approximated fluxes $\overline{F}_n^{11-n}$ [Eq. 3.14] and the numerical flux for three values of v (= 0.2, 0.25, 0.35) (x = 0.04, 0.06, 0.12) in Fig. 3.4. The 5.5PN Taylor series, denoted by $\overline{F}_0^{11}$, fits the exact numerical data better than the Padé approximants $\overline{F}_1^{10}, \overline{F}_6^5, \overline{F}_8^3, \overline{F}_9^2$. In the other cases, the Padé approximants provide a better agreement (i.e. $\overline{F}_{10}^1$, $\overline{F}_3^8$, $\overline{F}_4^7$, and $\overline{F}_5^6$) for the three values of v. This suggests that the Padé approximation should only be used to suggest a fitting formula for the numerical data, since there is no internal self-consistency in the agreement. The off-diagonal approximants do not show any regular pattern of convergence to the numerical data nor are they better than the Taylor series.

3.3.2 Flux for the equal mass case

For binaries of comparable mass on a quasicircular orbit, the flux is known only to 3.5PN order [35]. In Ref. [53] for a quasicircular nonspinning binary, the numerical flux was computed by integrating the spin-weighted spherical harmonic components of the Weyl scalar Ψ_4. The numerical flux data we use

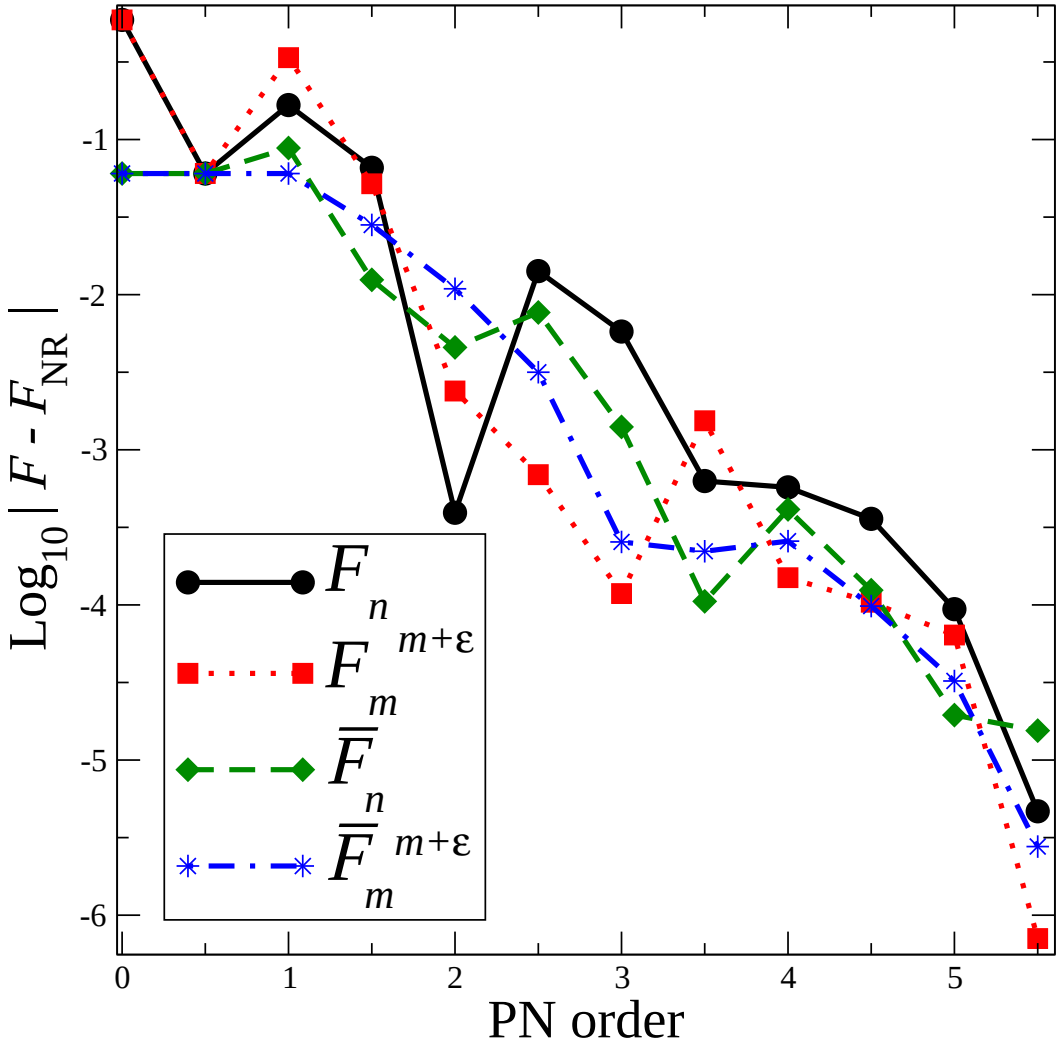

Figure 3.3: Convergence of the flux approximations in the test mass limit for $v = 0.2$. The four flux functions $\overline{F}_n$, $\overline{F}_m^{m+\epsilon}$, F_n and $F_m^{m+\epsilon}$ are given in Eqs. 3.14, 3.15, 3.18 and 3.20 respectively. The Padé approximants do not converge faster than their Taylor series counterparts. The Padé and Taylor series alternate at providing the best agreement with the exact data as the PN order increases. Contrast the behavior here with Fig. 3.1.

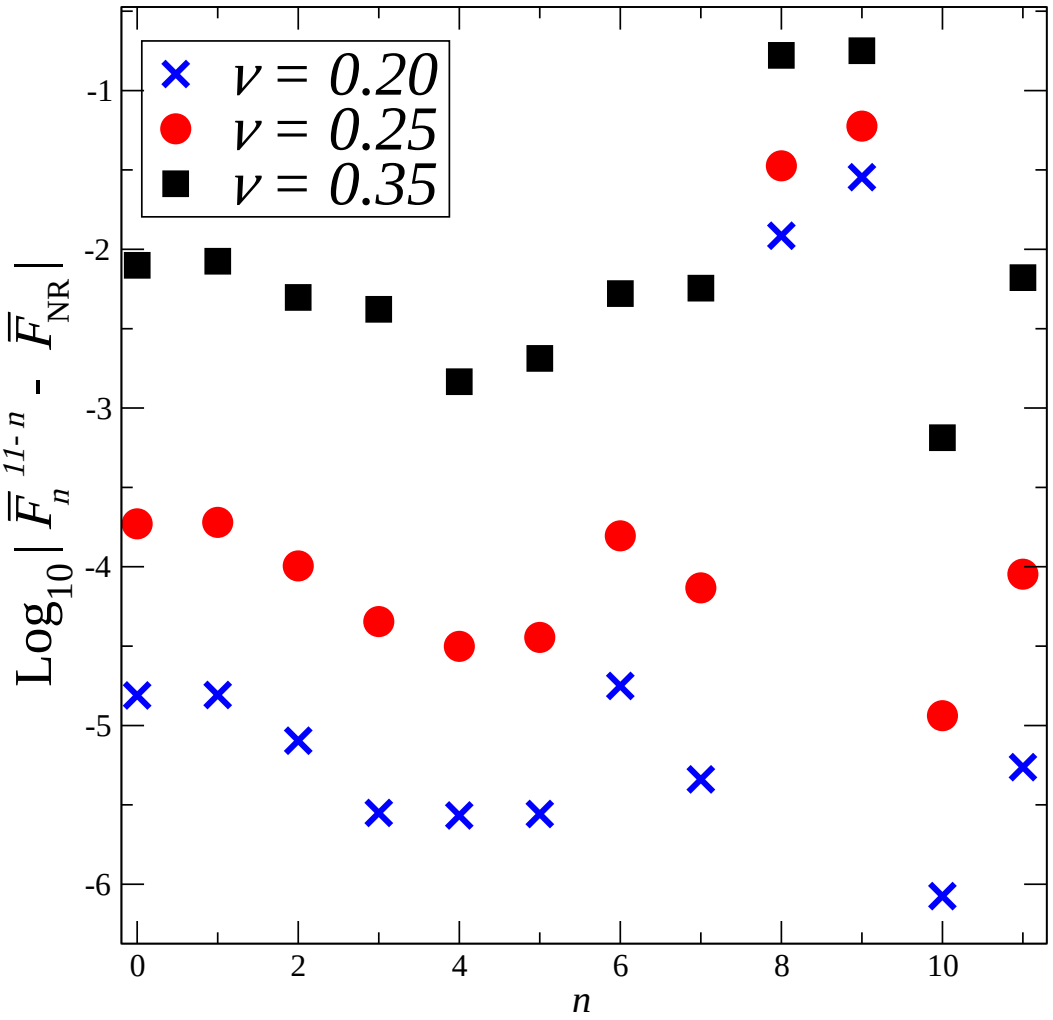

Figure 3.4: Error between maximal Padé approximants of the flux $\overline{F}$ [Eq. 3.15] and the numerical flux in the test mass limit at $\nu = 0.2, 0.25, 0.35$. The 5.5PN Taylor series, denoted by $\overline{F}_0^{11}$, fits the exact numerical data better than the Padé approximants $\overline{F}_1^{10}, \overline{F}_6^5, \overline{F}_8^3, \overline{F}_9^2$. In the other cases, the Padé approximants provide a better agreement (i.e. $\overline{F}_{10}^1$, $\overline{F}_2^9$, $\overline{F}_3^8$, $\overline{F}_4^7$ and $\overline{F}_5^6$, $\overline{F}_7^4$ and $\overline{F}_{11}^0$).

in this paper was provided by Harald P. Pfeiffer and Michael Boyle. The estimated error in measuring the flux data was about 0.2%. The velocity range for the simulation was from $v \sim 0.26$ ($x \sim 0.06$) to $v \sim 0.4$ ($x \sim 0.16$).

In the equal mass case, we cannot do an accurate convergence test early in the evolution as in Fig. 3.3 for two reasons. The first reason is the "junk radiation" (noise early in the evolution from imprecise initial data) during the first few orbits. The second reason is the inability to accurately define the numerical flux as a function of the orbital frequency of the binary. The numerical normalized flux is computed as a function of $\omega_{22}/2$, where ω_{22} is the wave frequency of the $\dot{h}_{22}$ mode. Instead, in Table 3.4 we compare the convergence of the four flux functions $\overline{F}_n$, $\overline{F}_m^{m+\epsilon}$, F_n and $F_m^{m+\epsilon}$ [defined in Eqs. 3.14, 3.15, 3.18 and 3.20 respectively as a function of PN order] for $v = 0.2$ ($x = 0.04$), $v_{\rm pole} = 0.69$ ($x_{\rm pole} = 52/109$) and $v_{\rm lso} = 0.50$ ($x_{\rm lso} = 0.254$). We use the last stable orbit frequency corresponding to the 3PN Taylor series of the energy and the pole corresponding to E_1^1. The convergence does not depend on these values although the flux values listed in Table 3.4 do depend somewhat on the values of $v_{\rm pole}$ and $v_{\rm lso}$. We choose a medium velocity ($v = 0.2$) to make the rate of convergence clear. At 3.5PN order, all four flux functions agree to 2 significant figures. However, after 7 terms, $\overline{F}_n$ converged to 3 significant figures, $\overline{F}_m^{m+\epsilon}$ converged to 4 significant figures, while F_n and $F_m^{m+\epsilon}$ converged to 2 significant figures. The flux function $\overline{F}_m^{m+\epsilon}$ converged to 1 additional significant figure over $\overline{F}_n$; however, $\overline{F}_m^{m+\epsilon}$ cannot reliably be considered more accurate than $\overline{F}_n$, because it converges to a slightly different value. The Padé approximants do not seem to converge to a larger number of significant figures than the Taylor flux function $\overline{F}_n$.

In Fig. 3.5, we plot the numerical normalized flux F_{NR}, the 3.5PN flux $\overline{F}_{3.5}$ and

Table 3.4: Flux convergence in the equal mass case for $v = 0.2$ ($x = 0.04$), $v_{\rm pole} = 0.69$ ($x_{\rm pole} = 52/109$), and $v_{\rm lso} = 0.50$ ($x_{\rm lso} = 0.254$). The four flux functions $\overline{F}_n$, $\overline{F}_m^{m+\epsilon}$, F_n, and $F_m^{m+\epsilon}$ are given in Eqs. 3.14, 3.15, 3.18 and 3.20 respectively. At 3.5PN order, all four flux functions agree to 2 significant figures. After 7 terms, $\overline{F}_n$ converges to 3 significant figures, $\overline{F}_m^{m+\epsilon}$ converges to 4 significant figures, while F_m and $F_m^{m+\epsilon}$ converge to 2 significant figures.

PN order	$\overline{F}_n$	$\overline{F}_m^{m+\epsilon}$	F_n	$F_m^{m+\epsilon}$
0.0	1.000000	1.000000	1.407582	1.407582
0.5	1.000000	1.000000	1.000000	1.000000
1.0	0.822381	1.000000	0.749987	0.353292
1.5	**0.9**22912	0.886577	0.963887	0.865262
2.0	**0.9**22745	**0.9**05792	0.922678	**0.91**0047
2.5	**0.9**04387	**0.91**0595	0.896904	**0.91**2033
3.0	**0.913**204	**0.9122**61	**0.91**6323	**0.91**2613
3.5	**0.913**314	**0.9122**23	**0.91**3275	**0.91**1492

the maximal Padé-approximated flux functions F_4^3, F_3^4, F_2^5, F_1^6, and F_0^7 ($\equiv F_7$). Although $\overline{F}_{3.5}$ diverges from the numerical flux early at $v \sim 0.26$, it still fits the numerical data better than F_3^4, F_1^6, and F_0^7. The quantity F_3^4 has a pole and fails to capture the numerical flux behavior completely. The quantity F_0^7 is by definition the Taylor flux with a pole, F_7. This function shows that adding a pole to the Taylor expansion of the flux $\overline{F}_{3.5}$ degrades the fit with the numerical flux. Moreover, the numerical flux does not suggest the existence of a pole at a large velocity ($v \sim 0.69$); it starts to decrease to 0 at $v \sim 0.4$. Adding a pole does not seem a useful idea in this case at least. On the other hand, F_2^5 and F_4^3 are a better fit to the numerical data during most of the velocity range of the 15-orbit data. The flux function F_2^5 is especially a good fit to the numerical normalized flux at high velocities. However, even though F_2^5 and F_4^3 are a good fit to the numerical flux during the last 15-orbit inspiral before merger, there is no guarantee that this is true at low velocities.

3.4 Padé Waveforms

The construction of the post-Newtonian waveforms requires solving the post-Newtonian equations describing the motion of the binary and the generation of gravitational waves. Substituting the orbital evolution predicted by the equations of motion into the expressions for the waveform would not generate waveforms accurate enough for matched filtering in detecting gravitational waves [87]. To compute the waveform at 3PN order, it is necessary to solve the equations of motion at 5.5PN order, because the radiation reaction contributes to the equations of motion starting at 2.5PN order. However, for a nonspinning binary of equal mass and on a circular orbit, accurate waveforms at 3PN order can be constructed under two further assumptions. The first assumption is that the binary follows a slow adiabatic inspiral. The second assumption is that of energy balance between the orbital binding energy and the energy emitted by the gravitational waves, where the energy balance equation is defined as

$$\frac{dE}{dt} = -F. \tag{3.21}$$

The procedure of constructing the standard Padé waveforms [98] is similar to one used to construct the TaylorT1 waveforms in Refs. [98, 51]. The main difference is the use of Padé approximants of the energy and flux to compute the orbital phase, as described in Secs. 3.2 and 3.3, instead of their Taylor expansions. The orbital phase used in the Padé waveforms is obtained by numerically integrating

$$\frac{d\Omega}{dt} = \frac{32}{5}\nu^2 v^{10} \frac{F_n^m}{dE_l^k/d\Omega}\,. \tag{3.22}$$

The fraction on the right side of Eq. (3.22) is retained as a ratio of the Padé approximants of the post-Newtonian expansions, and is not expanded further

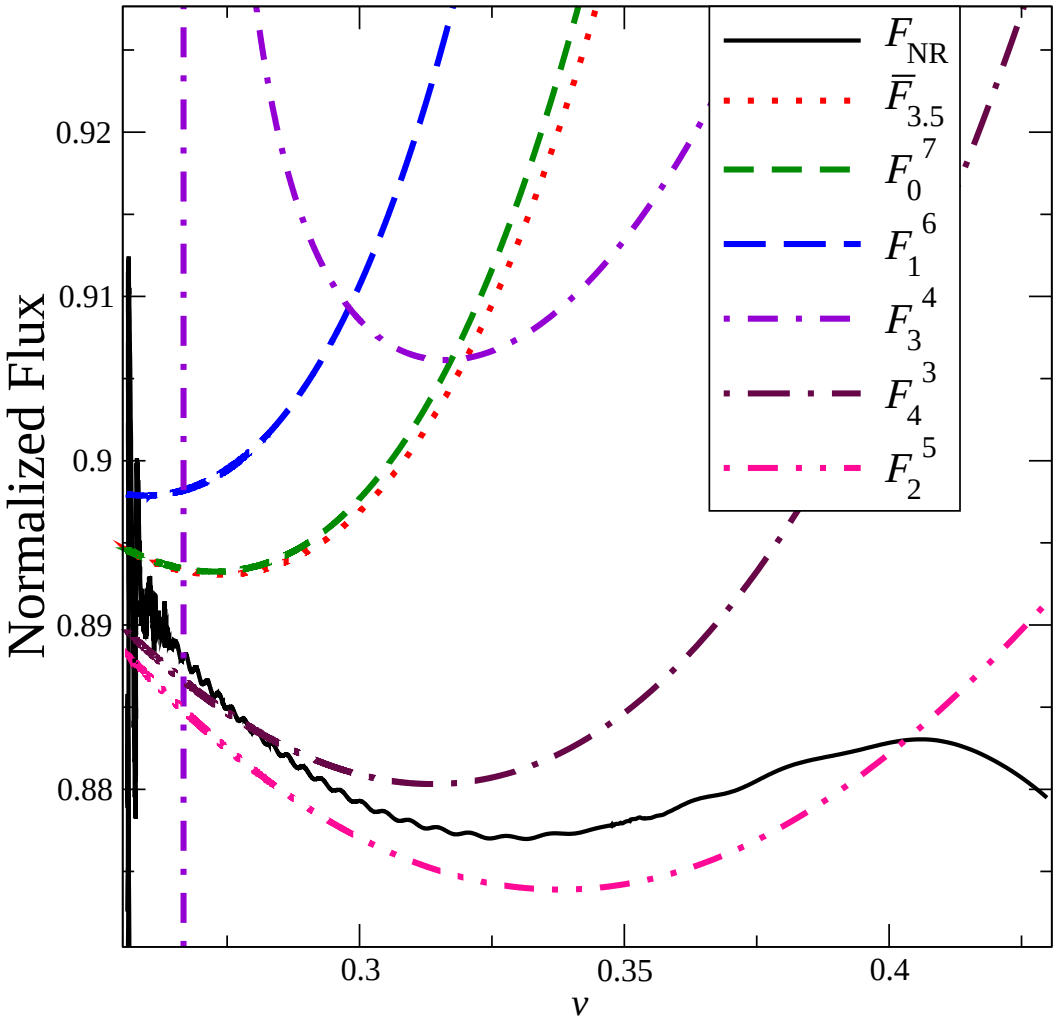

Figure 3.5: Normalized flux for an equal mass nonspinning binary. We plot the numerical flux F_{NR}, the 3.5PN flux $\overline{F}_{3.5}$ and the maximal Padé-approximated flux functions F_4^3, F_3^4, F_2^5, F_1^6, and F_0^7 ($\equiv F_7$). The early noise is caused by the junk radiation.

before numerical integration. The waveform is produced by substituting the orbital phase into the spherical harmonic mode h_{22} of the post-Newtonian waveform, which is known up to 3PN order [164, 162, 163, 28].

Given the expressions for the Padé-approximated energy and flux in Secs. 3.2 and 3.3, and the Taylor series of the waveform amplitude [164, 162, 163, 28], there is still a set of choices that must be made in order to produce a Padé-approximated waveform that can be compared with our numerical waveform. These include

1. the Padé approximant of the orbital energy, E_l^k.
2. the flux function and its Padé approximant F_m^n.
3. the velocity of the pole and the last stable orbit, $v_{\rm pole}$ and $v_{\rm lso}$.
4. the PN order through which terms in the waveform amplitude are kept.

3.4.1 Procedure

We consider numerical gravitational waves extracted with the Newman-Penrose scalar Ψ_4, using the same procedure as in [197]. To minimize gauge effects, we compare its $(2,2)$ component extrapolated to infinite extraction radius according to Ref. [51]. The extracted waveform is split into real phase ϕ and real amplitude A, defined by Ref. [51] as

$$\Psi_4^{22}(r,t) = A(r,t)e^{-i\phi(r,t)}. \tag{3.23}$$

The gravitational-wave frequency is given by

$$\omega = \frac{d\phi}{dt}. \tag{3.24}$$

The spherical harmonic component (2,2) of Ψ_4 is then compared with the numerically twice-differentiated post-Newtonian expression of h_{22}, A_{22}, as in Ref.[51]. Following [17, 141, 51], the matching procedure needed to set the arbitrary time offset t_0 and the arbitrary phase offset ϕ_0 is done by demanding that the PN and NR gravitational wave phase and gravitational wave frequency agree at some fiducial frequency ω_M.

3.4.2 Results

In this section, we compare the numerical waveform to the Padé waveforms corresponding to the 3.5 PN order of energy and flux using the 3PN Taylor series of the post-Newtonian amplitude A_{22}. The energy and flux functions used are those suggested by Ref. [98]. We do not generate all possible waveforms using different Padé approximants of the energy or the flux at low PN orders, since all these resummed series showed no improvement in the convergence rate.

As introduced in Sec. 3.2, we use the Padé-approximated energy E_0^3, E_1^2, E_2^1, and E_3^0 corresponding to the PN Taylor series of the energy, and the Padé-approximated energy E_1^1 corresponding to its 2PN Taylor expansion. For the flux, the diagonal Padé approximant F_3^3 is used in addition to all possible Padé approximants of flux at 3.5PN order F_{7-m}^m, where $0 \leq m \leq 7$, as described in Sec. 3.3.

The Padé-approximated flux has two parameters, $v_{\rm lso}$ and $v_{\rm pole}$ as discussed in Sec. 3.3. The value $v_{\rm pole} = 52/109$ is used. We also tested varying the pole location, but found that we could not improve the agreement significantly.

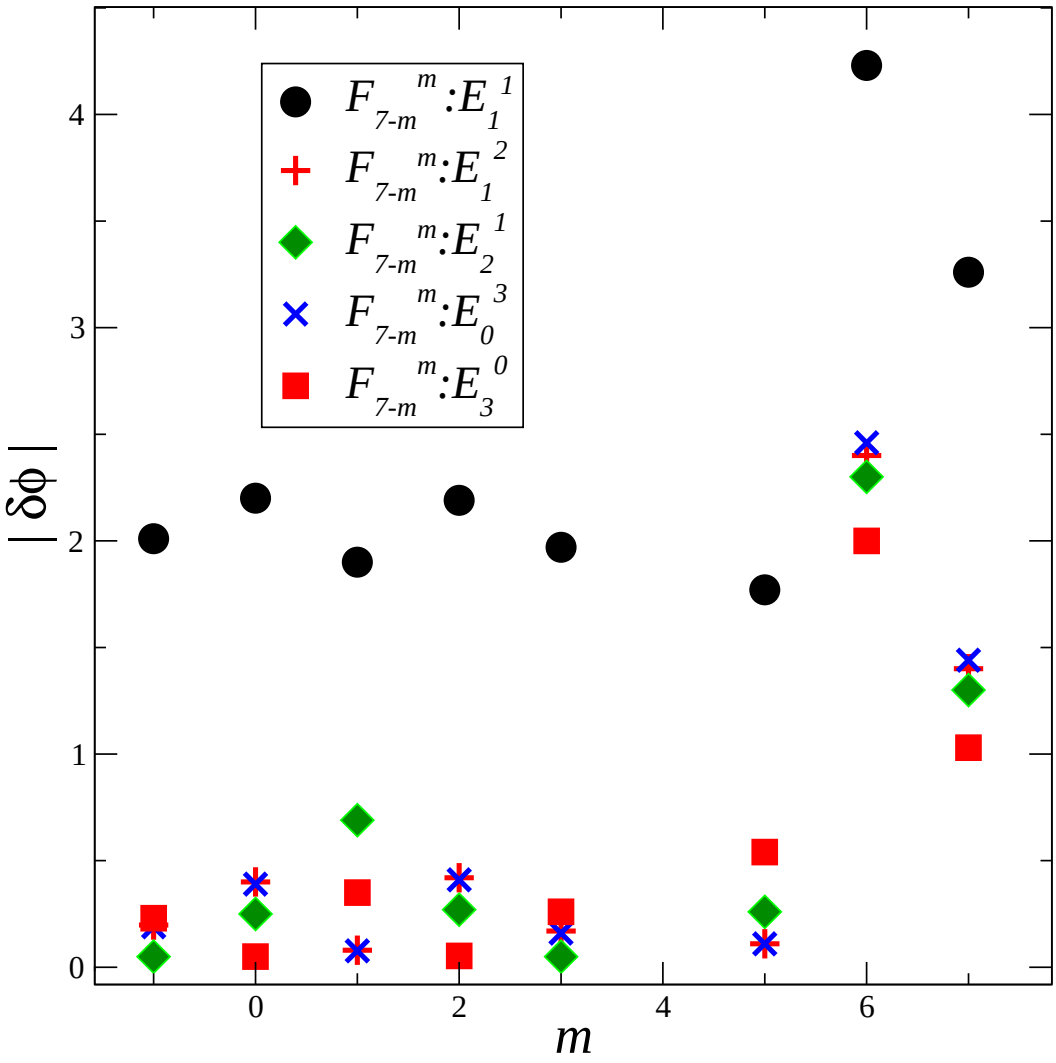

Figure 3.6: Phase difference between the 3 and 3.5 PN Padé approximated and numerical waveforms matched at the wave frequency $M\omega = 0.1$. We use the Padé-approximated flux F^m_{7-m} [Eq. 3.20] and energy E^k_l. We include in the figure the waveforms using the Padé-approximated flux F^3_3 using $m = -1$. There is no entry for $m = 4$, since the Padé-approximated flux F^4_3 has a pole in the frequency range of the simulation.

From Table 3.3, any value of the velocity of the last stable orbit could be used. We use the 3PN value $v_{\rm lso} = 0.254$ and also use $v_{\rm lso} = 0.199$. The latter is used when the Padé approximant E_1^1 is employed in the construction of the waveform. In the remaining cases, we use $v_{\rm lso} = 0.254$ since it is quite close to the estimates from other Padé approximants of the energy. The effect of changing the value of $v_{\rm lso}$ is not significant compared with changing the order of the Padé approximant for the energy or the flux.

To do the comparison, we match the Padé-approximated and numerical waveforms at the wave frequency $M\omega = 0.1$. Then we measure the maximum phase difference between the numerical waveform and each of these Padé waveforms during the inspiral when the numerical wave frequency is between $M\omega = 0.035$ and $M\omega = 0.1$ (as in the upper panel of Fig. 3.7). Our results are summarized in Fig. 3.6, which shows the phase differences for each of the Padé approximants of energy E_l^k and flux F_{7-m}^m. On the same figure, we include phase differences for the waveforms generated using the Padé-approximated flux F_3^3 under the $m = -1$ entry.

When E_1^1 is used, the phase error ranges between 2 and 5 radians as m increases from -1 to 7. Using all the possible Padé approximants of the 3PN energy, the estimated phase difference ranges from 0.05 to 2.5 radians. Using the Taylor series with a pole ($m = 7$) resulted in a large phase difference ranging between 1 and 1.5 radians. The diagonal Padé term F_4^3 of the flux generates similar phase differences, ranging from 0.06 to 0.2 radians as the Padé order of the energy changes.

The Padé-approximated waveforms do not fit the numerical data better than the waveforms using the Taylor expansion of the flux. Although the Padé-

waveforms along the diagonal have a phase difference less than 0.25 radians, none of these waveforms fits the numerical waveforms better than TaylorT4 at 3.5PN order as shown in Ref. [51]. Moreover, the dependence of the phase difference on the Padé order suggests that there is no reason why it should help in estimating the parameters better in data analysis. This is as expected from the poor convergence of the the Padé approximant of the flux discussed in Sec. 3.3.

The Padé resummation techniques were also tested on the Taylor series for the amplitude, and they showed no improvement in the convergence of the series. In addition, none of the tests that were performed on the Padé resummed Taylor series of the T2 and T3 waveforms showed a faster convergence rate. In fact, there is no improvement in convergence for any Taylor series in the PN approximation that we have investigated.

3.5 Simple EOB Model

We have described the failure of the Padé resummation techniques to accelerate the convergence of any PN Taylor series, the absence of any signature of a pole in the flux in the equal mass case, and the erratic pattern of agreement between the Padé waveforms and the numerical waveform. It seems one might as well simply use the Taylor series at all steps of computing waveforms. Also it does not seem that the parameters $v_{\rm pole}$ and $v_{\rm lso}$ are useful. In this section, we show how to get good agreement with the numerical waveform by using a simple EOB model. The only parameter we introduce and fit for is an unknown 4PN contribution to the flux.

3.5.1 EOB waveforms

The EOB formalism [90] is a nonperturbative analytic approach that handles the relative dynamics of two relativistic bodies. This approach of resumming the PN theory is expected to extend the validity of the PN results into the strong-field limit. The procedure for generating an EOB waveform follows closely the steps in Sec. 3.4. Instead of using the energy balance equation, we compute the orbital phase by numerically integrating Hamilton's equations. The EOB waveform is generated by substituting the orbital phase into the waveform amplitude A_{22} at 3PN order. The two fundamental ingredients that allow computing the orbital phase are the real Hamiltonian $\hat{H}$ and the radiation reaction $\mathcal{F}_\phi$.

3.5.2 Hamilton's equations

In terms of the canonical position variables r and ϕ and their conjugate canonical momenta p_r and p_ϕ, where r is the relative separation and ϕ is the orbital phase, the real dynamical Hamiltonian is defined as [112]:

$$\hat{H} = \frac{1}{\nu}\sqrt{1 + 2\nu\,(H_{EOB} - 1)}\,, \tag{3.25}$$

where

$$H_{EOB} = \sqrt{A\Big(1 + \frac{p_\phi^2}{r^2} + \frac{p_r^2}{B} + 2\nu(4 - 3\nu)\frac{p_r^4}{r^2}\Big)}\,, \tag{3.26}$$

and where the radial potential A function is defined as the series

$$A = 1 - \frac{2}{r} + \frac{2\nu}{r^3} + \Big(\frac{94}{3} - \frac{41}{32}\pi^2\Big)\frac{\nu}{r^4}\,. \tag{3.27}$$

The Taylor series of the A function is replaced by its Padé approximant A^1_3. Here the Padé approximant is not used to accelerate the convergence of the Taylor expansion of A. Instead, it leads to the existence of a last stable orbit (see Ref. [113]

and references therein). Otherwise, the EOB Hamiltonian is nonphysical for the last few orbits; the orbital frequency stays nearly constant for several orbits before merger. For the B function, the Taylor expansion suffices:

$$B = \frac{1}{A}\Big[1 - \frac{6\nu}{r^2} + 2(3\nu - 26)\frac{\nu}{r^3}\Big]. \tag{3.28}$$

Then Hamilton's equations of motion are given in the quasicircular case by

$$\partial_t r = \partial_{p_r}\hat{H}, \tag{3.29}$$

$$\partial_t \phi = \partial_{p_\phi}\hat{H}, \tag{3.30}$$

$$\partial_t p_r = -\partial_r \hat{H}, \tag{3.31}$$

$$\partial_t p_\phi = -\mathcal{F}_\phi, \tag{3.32}$$

where $\mathcal{F}_\phi$ is the radiation reaction in the ϕ direction representing the nonconservative part of the dynamics. In Eq. 3.32, $\partial_\phi \hat{H} = 0$ since $\hat{H}$ is independent of ϕ. The radiation reaction is deduced from the post-Newtonian flux as in Refs. [156, 157, 66]

$$\mathcal{F}_\phi = \frac{F + F_8 v^8}{\nu v^3}. \tag{3.33}$$

In this equation, we have introduced an unknown 4PN flux term, F_8, the only parameter that we fit for in this EOB model.

3.5.3 Initial conditions

To integrate Hamilton's equations, we need appropriate initial conditions for a quasicircular orbit. Refs. [66, 97, 60] indicate how to define some "post-adiabatic" initial conditions. However, these initial conditions do not generate an orbit with as low an eccentricity as the numerical simulation, roughly 5×10^{-5}. At a given radius r, starting from the post-adiabatic initial conditions of p_r and

p_ϕ, we therefore reduce the eccentricity iteratively in two steps. The first step includes evolving Hamilton's equations in the conservative regime ($\mathcal{F} = 0$) and iteratively changing the value of p_ϕ until the eccentricity measured from the evolution of the orbital separation is of the order 10^{-9}. The second step is based on evolving the nonconservative Hamilton's equations with the 4PN flux and iteratively changing the p_r momentum until the eccentricity is again of the order 10^{-5}. This circularization procedure is repeated as we iterate F_8 to maximize the agreement between the waveforms.

3.5.4 Best Fit of F_8

To find the best fit for F_8, we iteratively solve for the minimum in the phase difference between the numerical and EOB waveforms. The waveforms are matched as in Sec. 3.4 at the wave frequency $m\omega = 0.1$, and the phase difference is defined as the maximal phase difference during the inspiral phase up to the wave frequency $m\omega = 0.1$. We find a best fit value $F_8 = -333.75$ corresponding to the initial conditions $r = 17$, $\phi = 0$, $p_r = -0.0008$, $p_\phi = 4.53235$. A change of 1% in F_8 changes the maximal phase difference from less than 0.002 radians to about 0.01 radians. Note that without adding the fitting parameter F_8, the phase difference is about 1.7 radians during the 15-orbit inspiral.

3.5.5 Results

In the upper panel of Fig. 3.7, we plot the phase difference between the numerical waveform and the EOB waveform computed using the 3PN Taylor series of

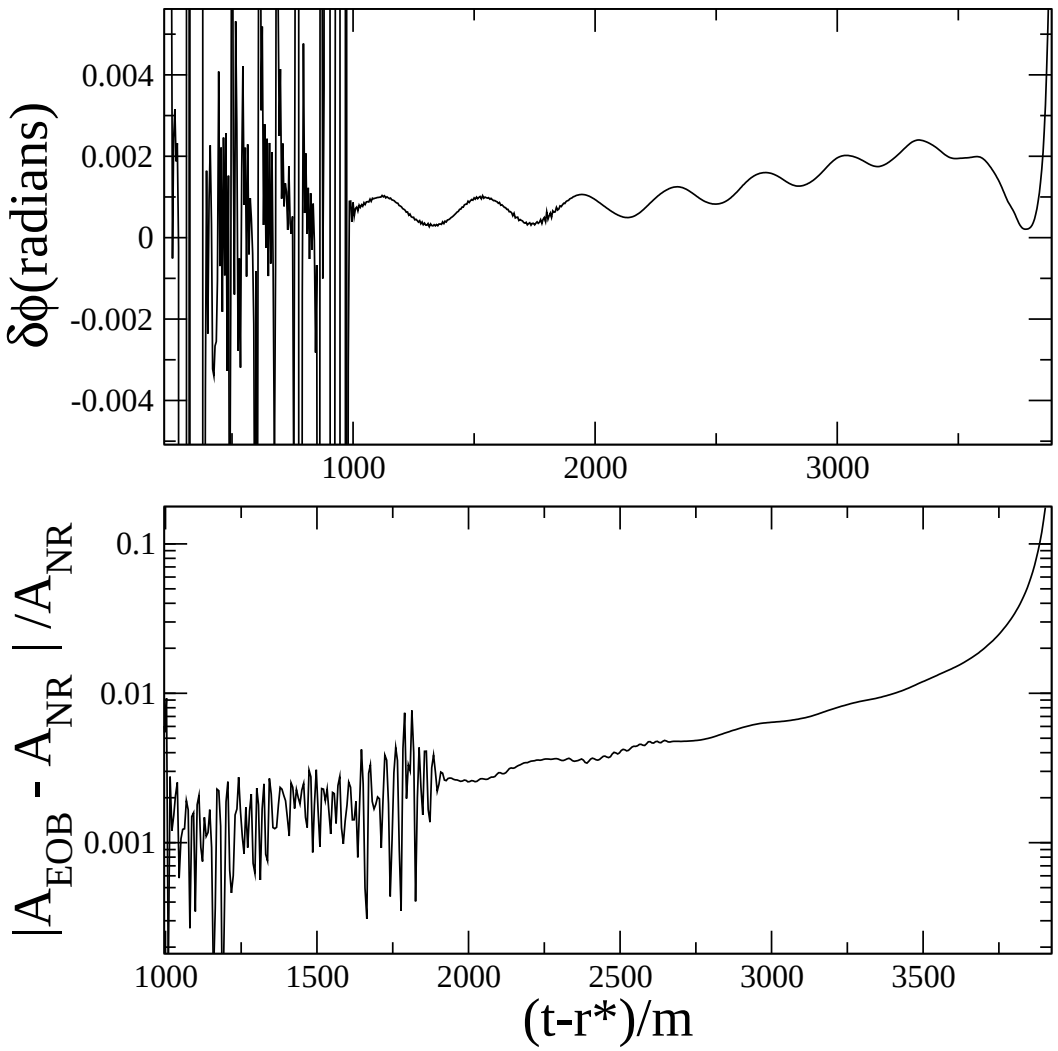

Figure 3.7: Phase and amplitude differences between the EOB waveform and the numerical waveform. After fitting for the best value of F_8, the phase difference is less than 0.002. The early noise is due to junk radiation at the early stage of the numerical simulation. r^* is the tortoise coordinate defined in [51].

the amplitude A_{22}. The phase difference is less than 0.002 radians after maximizing the agreement between the waveforms in the region, where $m\omega \leq 0.1$. The early noise is due to junk radiation at the early stage of the numerical simulation as described in Sec II C of Ref. [51]. The phase uncertainty in the simulation was estimated to be 0.05 radians; See Table III in [51].

In the lower panel of Fig. 3.7, we plot the relative difference between the amplitude of the numerical waveform and the EOB waveform. The EOB waveform amplitude does not fit the numerical waveform amplitude as well as the wave phase does. This is expected because the waveform amplitude is known to 3PN order only, and no free parameter in the amplitude was fitted for. The agreement between the amplitude of this EOB model and the numerical waveform is similar to the agreement between the amplitude of TaylorT4 3.5/3.0 and the numerical waveform in Fig. 21 in [51].

This EOB model is a modification of the ET EOB model of Ref. [61]. It fits the numerical phase very well without using the Padé resummation techniques nor a pole in the flux. Even though we have found very good agreement between the waveforms, these results only suggest that the EOB model is a very good fitting model. Moreover, having fit a particular waveform, there is no guarantee the model will have predictive power for a more general case.

3.6 Conclusions

Convergence tests show that none of the Taylor series in the PN approximation, such as the energy or the flux, could be replaced by a Padé approximant that converges faster. Other attempts where we tried to accelerate the conver-

gence of these series also failed, as, for example, using the Levin method to accelerate convergence [232]. As a result, more reliable waveforms could not be constructed using a Padé resummation scheme. Moreover, the Padé waveforms also do not fit numerical simulation data better than the Taylor waveforms. Thus, they do not seem to be better than the Taylor waveforms in building templates for waveforms. This conclusion is independent of the Padé approximants used to test the convergence. Taking, for example, the subdiagonal Padé approximant does not show any improvement in the convergence rate. In addition, this conclusion is independent of the numerical data we used. We can simply take the highest PN order of the Taylor series or the Padé approximant and use it as the exact value of the function to test the convergence at low frequency.

Based on the dependence of the flux on the velocity in the equal mass case, we do not find it helpful to add a pole to the flux. Therefore, we recommend using Taylor series instead of the Padé approximant to generate waveforms both in the time and frequency domains. The simple EOB model used in this paper agrees with the numerical data very well; the phase difference during the inspiral is much less then the estimated phase uncertainty in the numerical data. This model does not use Padé approximants or poles except in one place to enforce a last stable orbit. Since Padé approximation does not accelerate the convergence of any PN Taylor series, there is no reason why it should estimate parameters better in data analysis of waveforms.

CHAPTER 4

HIGH-ACCURACY NUMERICAL SIMULATION OF BLACK-HOLE BINARIES:COMPUTATION OF THE GRAVITATIONAL-WAVE ENERGY FLUX AND COMPARISONS WITH POST-NEWTONIAN APPROXIMANTS

4.1 Introduction

[1] The first-generation interferometric gravitational wave (GW) detectors, such as LIGO [19, 228], GEO600 [147] and Virgo [117, 3], are now operating at or near their design sensitivities. One of the most promising sources for these detectors is the inspiral and merger of binary black holes (BBHs) with masses $m_1 \sim m_2 \sim 10$–$20\,M_\odot$ [127, 99]. A detailed and accurate understanding of the gravitational waves radiated as the black holes spiral towards each other will be crucial not only for the initial detection of such sources, but also for maximizing the information that can be obtained from signals once they are observed. Both the detection and subsequent analysis of gravitational waves from compact binaries depends crucially on our ability to build an accurate bank of templates, where each template is a theoretical model that accurately represents the gravitational waveform from a binary that has a certain set of parameters (e.g., masses and spins). For detection, the technique of matched filtering is applied to noisy data to extract any signals that match members of the template bank. For analysis, the best-fit parameters are determined, most likely by an iterative process that involves constructing further templates to zero in on the best fit.

[1] This chapter is extracted from Ref. [53] which was written in collaboration with Micheal Boyle, Alessandra Buonanno, Lawrence E. Kidder, Abdul H. Mroué, Yi Pan, Harald P. Pfeiffer, and Mark A. Scheel, and published in 2008.

When the black holes are far apart and moving slowly, the gravitational waveform (i.e., the template) can be accurately computed using a post-Newtonian (PN) expansion. As the holes approach each other and their velocities increase, the post-Newtonian expansion is expected to become less and less reliable. However, until recently there has been no independent way to determine how close comparable-mass holes must be before PN methods become inaccurate. This has changed with recent advances in numerical relativity (NR), which make it possible for the first time to quantify the disagreement between PN predictions [35] and the true waveform [64, 11, 142, 51, 137, 140]. In a previous paper [51], some of us described numerical simulations of 15 orbits of an equal-mass non-spinning binary black hole system. Gravitational waveforms from these simulations covering more than 30 GW cycles and ending about 1.5 GW cycles before merger, were compared with those from quasi-circular PN formulas for several time-domain Taylor approximants computed in the so-called *adiabatic* approximation. We found that there was excellent agreement (within 0.05 radians) in the GW phase between the numerical results and the PN waveforms over the first ~ 15 cycles, thus validating the numerical simulation and establishing a regime where PN theory is accurate. In the last 15 cycles to merger, however, *generic* time-domain Taylor approximants build up phase differences of several radians. But, apparently by coincidence, one specific PN approximant, TaylorT4 at 3.5PN order, agreed much better with the numerical simulations, with accumulated phase differences of less than 0.05 radians over the 30-cycle waveform. Simulations by Hannam et al. [140] for equal-mass, non-precessing spinning binaries confirm that this agreement in the non-spinning case is a coincidence: they find the phase disagreement between TaylorT4 and the numerical waveform can be a radian or more as the spins of the black holes

are increased.

To build a template bank to be used by ground-based GW detectors, one possibility would be to run a separate numerical simulation for each template. This is not currently possible, however, due to the large computational cost per numerical waveform (on the order of a week for a single waveform) and the large number of templates needed to cover the parameter space, especially when spins are present. A more realistic possibility is to perform a small number of simulations and develop an analytic template family (i.e., a fitting formula) which interpolates the parameter space between the simulations [192, 67, 4, 111, 113, 114].

Before the NR breakthrough several analytic prescriptions were proposed to address the loss of accuracy of the adiabatic Taylor approximants. Damour, Iyer and Sathyaprakash [98] introduced the Padé summation of the PN center-of-mass energy and gravitational energy flux in order to produce a series of Padé approximants for the waveforms in the adiabatic. Buonanno and Damour [59, 66, 104, 100] introduced the effective-one-body (EOB) approach which gives an analytic description of the motion and radiation beyond the adiabatic approximation of the binary system through inspiral, merger, and ringdown. The EOB approach also employs the Padé summation of the energy flux and of some crucial ingredients, such as the radial potential entering the conservative dynamics. So far, the EOB waveforms have been compared with several numerical waveforms of non-spinning binary black holes [64, 192, 67, 111, 113, 114]. Buonanno et al. [67] showed that by using three quasi-normal modes [64] and by tuning the pseudo 4PN order coefficient [97] in the EOB radial potential to a specific value, the phase difference accumulated by the end of the ringdown phase can

be reduced to ~ 0.19–0.50 radians, depending on the mass ratio and the number of multipole moments included in the waveform. Those results were obtained using waveforms with 5–16 GW cycles and mass ratios $1:4$, $1:2$, $2:3$ and $1:1$. In Refs. [111, 113, 114] the authors introduced other improvements in the EOB approach, in part obtained by tuning the test-mass limit results [111]—for example Padé summation of the PN amplitude corrections in the inspiral waveform; ringdown matching over an interval instead of a point; inclusion of non-circular terms in the tangential damping force; use of five quasi-normal modes. They found that the phase differences accumulated by the end of the inspiral (ringdown) can be reduced to ± 0.001 (± 0.03) radians for equal-mass binaries [113, 114] and to ± 0.05 radians for binaries with mass ratio $1:2$ [114]. Note that these phase differences are smaller than the numerical errors in the simulations.

The energy flux and the center-of-mass energy are two fundamental quantities of the binary dynamics and crucial ingredients in building GW templates. In this paper we extract these quantities, and compare the results from our numerical inspiral simulation [51] with PN results in both their Taylor-expanded and summed (Padé and EOB) forms. The agreement between the numerical and analytical results for the energy flux and the center-of-mass energy is a further validation of the numerical simulation. It also allows us to study whether or not the agreement of the phase evolution of PN and numerical waveforms is accidental. In addition, we compute waveforms based on adiabatic Padé and non-adiabatic EOB approximants in their *untuned* form (i.e., without introducing fitting coefficients) and study their agreement with our numerical simulations.

We try to understand whether these approximants can reproduce features of the numerical simulations that can be exploited to develop a faithful analytic template family. By introducing unknown higher-order PN coefficients into the dynamics and tuning them to the numerical data, we investigate how to improve the agreement with the numerical results. Although our study only examines non-spinning, equal-mass binary black holes, by combining it with other studies [192, 67, 4, 111, 113, 114] one can already pinpoint which parameters are degenerate and which have the largest effect on the waveforms. This is particularly relevant during the last stages of inspiral and plunge. The overall methodology can be extended to a larger region of the parameter space. We will defer to a future paper a complete study of the flexibility of the EOB approach with the extension of our numerical waveform through merger and ringdown.

This paper is organized as follows: Section 4.2 gives a quick review of the numerical simulations presented in [51], and then presents the computation of the GW energy flux from the simulation. In Sec. 4.3 we summarize the PN approximants that will be compared to the numerical simulation. In Sec. 4.4, we compare the GW energy flux for the various PN approximants with numerical results and explore the possibility of improving the agreement with the numerical flux by adding phenomenological parameters [192, 67, 111, 113, 114]. In Sec. 4.5, we examine the evolution of the center-of-mass energy for the various PN approximants and compare to the numerical results assuming balance between the change in the center-of-mass energy and the energy carried from the system by the gravitational waves. In Sec. 4.6 we compare waveforms constructed from the Padé and EOB approximants with our numerical results, and study how to improve the agreement by exploiting the flexibility of the EOB model (i.e., by fitting free parameters of the EOB model). Finally, we present

some concluding remarks in Sec. 5.6. In the Appendix we review the performance of the Padé summation of the Taylor series of the energy flux in the test particle limit.

4.2 Computation of the numerical gravitational-wave energy flux

4.2.1 Overview and Definitions

The data used in this paper is the same as that described in Sec. II of Boyle et al. [51]. The simulation is a 16-orbit inspiral, with very low spin and eccentricity. Figure 4.1 presents a view of some relevant quantities of that simulation.

The Newman-Penrose scalar Ψ_4, defined using a coordinate-based tetrad, is extracted from the simulation at several extraction radii and expanded in spin-weighted spherical harmonics,

$$\Psi_4(t, r, \theta, \phi) = \sum_{l,m} \Psi_4^{lm}(t, r)\, {}_{-2}Y_{lm}(\theta, \phi)\,. \tag{4.1}$$

Then $\Psi_4^{lm}(t, r)$ is extrapolated to infinite extraction radius using an n-th order polynomial in $1/r$, where typically $n = 3$. This results in the asymptotic field $r\Psi_4^{lm}(t - r^*)$ as function of retarded time[2] $t - r^*$.

Gravitational radiation may also be expressed via the standard metric-perturbation quantities h_+ and $h_\times$, which we similarly write in terms of spin-

[2]See Sec. II F of Ref. [51] for a precise definition of r^* and a description of the extrapolation.

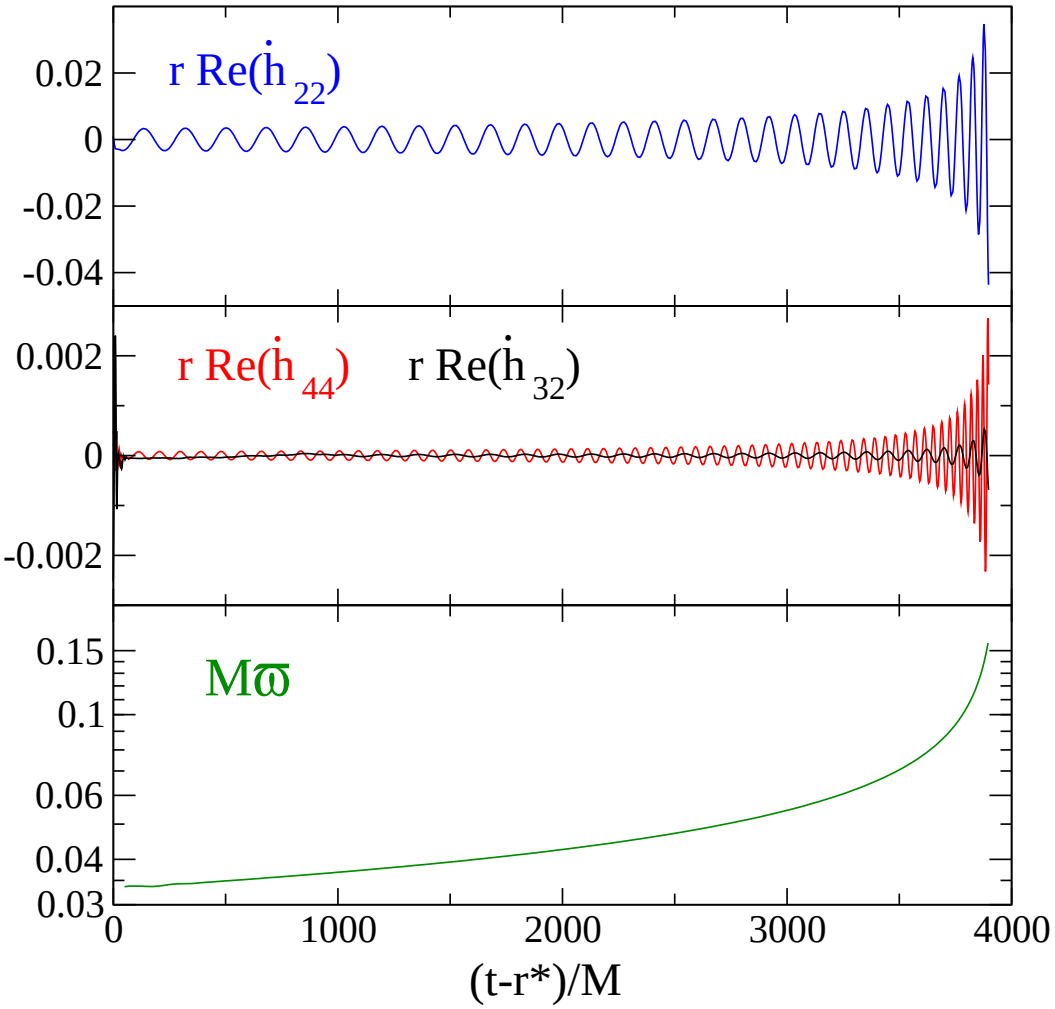

Figure 4.1: Some aspects of the numerical simulation. From top panel to bottom: the leading mode $\dot{h}_{22}$; the two next largest modes, $\dot{h}_{44}$ and $\dot{h}_{32}$ (smallest); the frequency of $\dot{h}_{22}$ [see Eq. (4.5)].

weighted spherical harmonic components,

$$h \equiv h_+ - i h_\times = \sum_{l,m} h_{lm}\, {}_{-2}Y_{lm}\,. \tag{4.2}$$

For linear perturbations around Minkowski space, $\Psi_4^{lm}(t - r^*) = \ddot{h}_{lm}(t - r^*)$. In particular, this relation should be true for the waveforms we have extrapolated to infinity.

However, to compute the energy flux we do not need to determine h; we need only its time derivative $\dot{h}$. The energy flux depends on the spin-weighted spherical harmonic coefficients of the time derivative $\dot{h}$ via

$$F = \frac{1}{16\pi} \sum_{l=2}^{\infty} \sum_{m=-l}^{l} |r\, \dot{h}_{lm}|^2\,. \tag{4.3}$$

We obtain $\dot{h}_{lm}$ by time-integration of Ψ_4^{lm}, as discussed in detail below.

Finally, we define gravitational wave phase and frequency in two ways—one based on Ψ_4^{22}, and one based on $\dot{h}_{22}$:

$$\phi = -\arg(\Psi_4^{22})\,, \qquad \omega = \frac{d}{dt}\phi\,, \tag{4.4}$$

$$\varphi = -\arg\left(\dot{h}_{22}\right)\,, \qquad \varpi = \frac{d}{dt}\varphi\,. \tag{4.5}$$

In both cases, we define the arg function to be the usual function, with discontinuities of 2π removed. Many PN formulae (see Sec. 4.3) involve yet another frequency and phase: the *orbital* phase Φ and *orbital* frequency Ω. Although the three frequencies satisfy $\omega \approx \varpi \approx 2\Omega$, the slight differences between different frequencies are significant at the level of precision of our comparison (see Fig. 4.6 below), so it is important to distinguish carefully between them.

When discussing our numerical solution, we write all dimensionful quantities in terms of the mass scale M, which we choose to be the sum of the irre-

ducible masses of the two black holes.[3]

4.2.2 Calculation of $\dot{h}$

The energy flux depends on the spin-weighted spherical harmonic coefficients of $\dot{h}$ via Eq. (4.3). We therefore need to perform one time integration on Ψ_4^{lm}:

$$\dot{h}_{lm}(t) = \int_{t_0}^{t} \Psi_4^{lm}(t')\, dt' + H_{lm}. \tag{4.6}$$

This integration is performed for each mode (l, m) separately and requires the choice of two integration constants, which are contained in the complex number H_{lm}. Ideally, H_{lm} should be chosen such that $\dot{h}_{lm} \to 0$ for $t \to -\infty$. Because our numerical simulations do not extend into the distant past, this prescription cannot be implemented. Rather, we make use of the approximation that the real and imaginary parts of $\dot{h}_{lm}$ should oscillate symmetrically around zero.

Let us consider a pure sine/cosine wave, with constant amplitude and phase:

$$\Psi_4^{\mathrm{ex}} = A[\cos(\omega t) + i \sin(\omega t)], \tag{4.7}$$

$$\dot{h}^{\mathrm{ex}} = \frac{A}{\omega}[\sin(\omega t) - i \cos(\omega t)] + H^{\mathrm{ex}}, \tag{4.8}$$

where the superscript 'ex' stands for example. The amplitude is given by

$$|\dot{h}^{\mathrm{ex}}|^2 = \frac{A^2}{\omega^2} + 2\frac{A}{\omega}[\mathrm{Re}H^{\mathrm{ex}} \sin(\omega t) - \mathrm{Im}H^{\mathrm{ex}} \cos(\omega t)] + |H^{\mathrm{ex}}|^2. \tag{4.9}$$

Only for the correct choice of integration constants, $H^{\mathrm{ex}} = 0$, is the amplitude $|\dot{h}^{\mathrm{ex}}|$ *constant*.

[3] This quantity was denoted by m in Ref. [51].

Therefore, we propose to determine the integration constants H_{lm} in Eq. (4.6) by minimizing the time derivative of the amplitude over the entire waveform. In particular we minimize

$$\mathcal{I}_{lm} \equiv \int_{t_1}^{t_2} \left(\frac{d}{dt} |\dot{h}_{lm}|^2 \right)^2 dt. \tag{4.10}$$

From this minimization principle it follows that H_{lm} is determined by the linear system

$$\begin{aligned} &\mathrm{Re}H \int (\mathrm{Re}\Psi_4)^2 dt + \mathrm{Im}H \int \mathrm{Re}\Psi_4 \mathrm{Im}\Psi_4 dt \\ &\quad = -\int \left[(\mathrm{Re}\Psi_4)^2 \mathrm{Re}\dot{h}_0 + \mathrm{Re}\Psi_4 \mathrm{Im}\Psi_4 \mathrm{Im}\dot{h}_0 \right] dt, \end{aligned} \tag{4.11a}$$

$$\begin{aligned} &\mathrm{Re}H \int \mathrm{Re}\Psi_4 \mathrm{Im}\Psi_4 dt + \mathrm{Im}H \int (\mathrm{Im}\Psi_4)^2 dt \\ &\quad = -\int \left[(\mathrm{Im}\Psi_4)^2 \mathrm{Im}\dot{h}_0 + \mathrm{Re}\Psi_4 \mathrm{Im}\Psi_4 \mathrm{Re}\dot{h}_0 \right] dt. \end{aligned} \tag{4.11b}$$

Here, we have suppressed the indices lm for clarity, all integrals are definite integrals from t_1 to t_2, and $\dot{h}_0(t) \equiv \int_{t_0}^{t} \Psi_4(t')\, dt'$. For a given integration interval $[t_1, t_2]$, Eqs. (4.11) provide a deterministic procedure to determine the integration constants H_{lm}. We note that there have been several earlier proposals to fix integration constants [197, 24, 203, 92, 213]. While we have not tested those proposals, we point out that Eqs. (4.11) allow for very accurate determination of the integration constants and one can easily obtain an error estimate, as we discuss in the next subsection.

4.2.3 Uncertainties in numerical quantities

Because the amplitude and frequency of the waveform are not constant, this procedure is imperfect, and the result depends somewhat on the chosen values

of t_1 and t_2. To estimate the residual uncertainty in H due to this choice, we select nine different values for t_1 and eleven values for t_2: $t_1 = 200M, 220M, \ldots, 360M$; $t_2 = 2000M, 2100M, \ldots, 3000M$. The values of t_1 vary over roughly one GW cycle and test the sensitivity to the GW phase at the start of the integration interval; the values of t_2 are designed to test the dependence on the amplitude at the end of the integration interval. For $t_2 > 3000M$ we find that the errors in our procedure rapidly increase for several reasons: (a) the minimization principle is based on the approximation that the amplitude is constant; this approximation becomes worse toward merger; (b) $\mathcal{I}_{lm}$ in Eq. (4.10) weights absolute changes in $|\dot{h}|$, not relative ones; close to merger, the amplitude becomes so large that it dominates $\mathcal{I}_{lm}$; and (c) the integration constants shift the waveform $\dot{h}_{lm}$ vertically, and we are trying to determine the particular vertical shift such that $\dot{h}_{lm}$ is centered around zero. Determination of such an offset is most accurate in a regime where the oscillations are *small*, i.e., at early times.

For each of these 99 integration intervals, we compute integration constants using Eqs. (4.11) for the three dominant modes, $\dot{h}_{22}$, $\dot{h}_{44}$ and $\dot{h}_{32}$, and we compute $F(t)$ from Eq. (4.3) using only these modes and we compute $\varpi(t)$. (We will show below that the contributions of other modes are far below our numerical errors on the flux.) We average the 99 functions $F(t)$ and $\varpi(t)$ and then use a parametric plot of $F(t)$ versus $\varpi(t)$ in our comparisons presented below. The variation in these 99 values yields an uncertainty in F due to the choice of integration constants.

The lower panel of Fig. 4.2 shows the variation in flux from the 99 different integration intervals. We find that the *maximum* deviation can be well approximated by $\max|\delta F|/F = 1.5 \times 10^{-5}(M\varpi)^{-3/2}$ (see the solid line in lower panel of

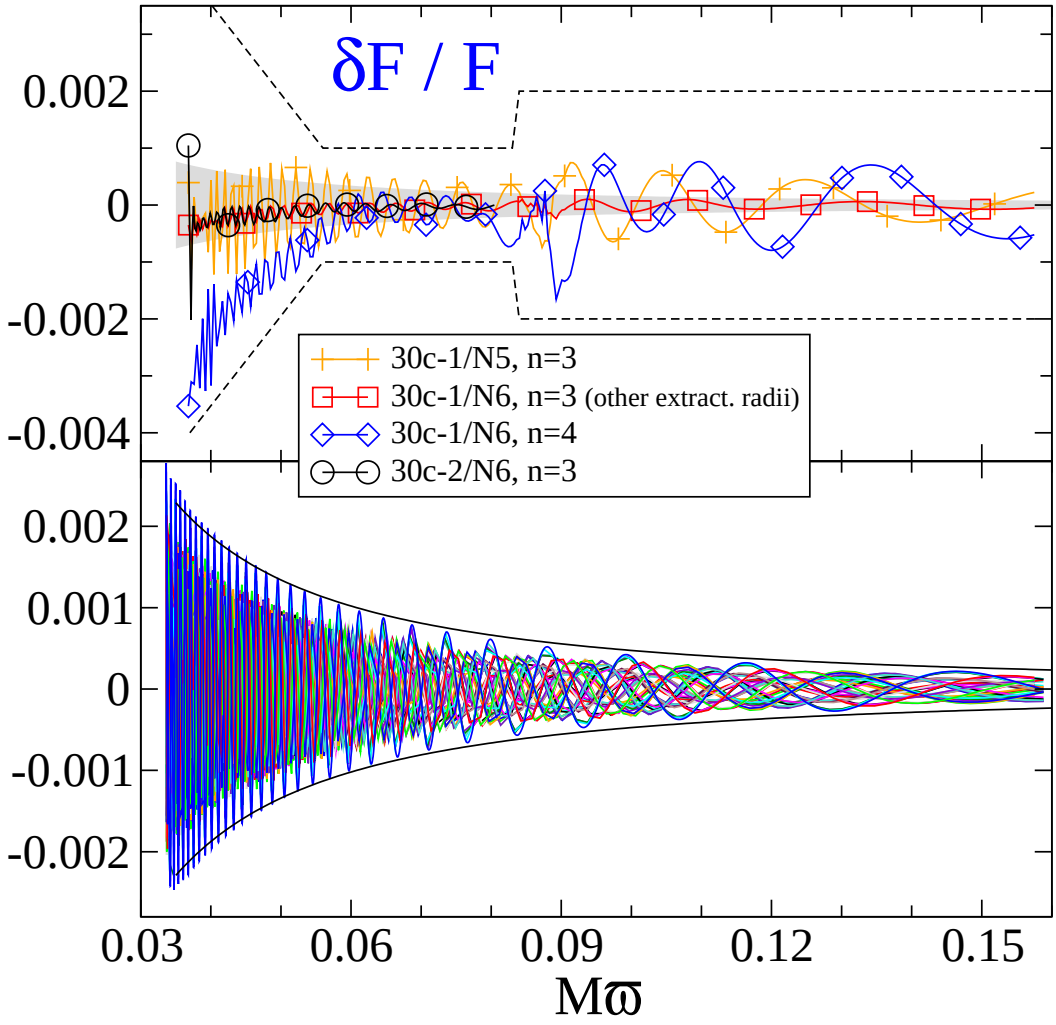

Figure 4.2: **Lower panel:** Relative difference between flux $F(\varpi)$ computed with 99 different intervals $[t_1, t_2]$ and the average of these. **Upper panel:** Relative change in the flux $F(\varpi)$ under various changes to the numerical simulation. The grey area in the upper panel indicates the uncertainty due to the choice of integration constants, which is always dominated by numerical error. The dashed line in the upper panel is our final error estimate, which we plot in later figures.

Fig. 4.2). The *average* F computed from all 99 intervals $[t_1, t_2]$ will have a smaller error. Inspection of the lower panel of Fig. 4.2 reveals that the $\delta F/F$ curves fall into 11 groups, corresponding to the 11 values of t_2. Assuming that δF between these groups is randomly distributed, the error of the average will be reduced by a factor $\sqrt{11}$, i.e., $\delta F/F = 5 \times 10^{-6} (M\varpi)^{-3/2}$. This error is indicated as the grey shaded area in the upper panel of Fig. 4.2.

The upper panel of Fig. 4.2 plots the relative change in $F(\varpi)$ for several changes in our numerical simulation: (a) Computing the flux from a run with lower resolution (0030c/N5 in the language of Boyle et al. [51]); (b) using a different set of extraction radii for the extraction of the gravitational wave; (c) increasing the polynomial order of extrapolation of Ψ_4 to infinite extraction radius from $n = 3$ to $n = 4$; and (d) computing the flux from a separate evolution with a different outer boundary radius (0030c-2/N6). At low frequencies, the error is dominated by extrapolation to infinite radius and is a few tenths of a percent; at intermediate frequencies, $0.055 \lesssim M\varpi < 0.083$, all errors are smaller than 0.1 percent. At frequency $M\varpi \approx 0.084$ we change the gauge conditions in the evolutions to allow wave-escorting; this introduces high-frequency features, which are small when extrapolation order $n = 3$ is used, but which dominate for $n = 4$ extrapolation. The numerical data we use in the PN comparisons below is extrapolated with $n = 3$, for which the features due to change of gauge are small, but nevertheless we will use conservative error bars encompassing the $n = 4$ extrapolation as indicated in Fig. 4.2, i.e. a relative error of 0.2 per cent for $M\varpi > 0.083$. We find that the uncertainty in the flux due to numerical error in determining Ψ_4 is always larger than the uncertainty due to the choice of integration constants.

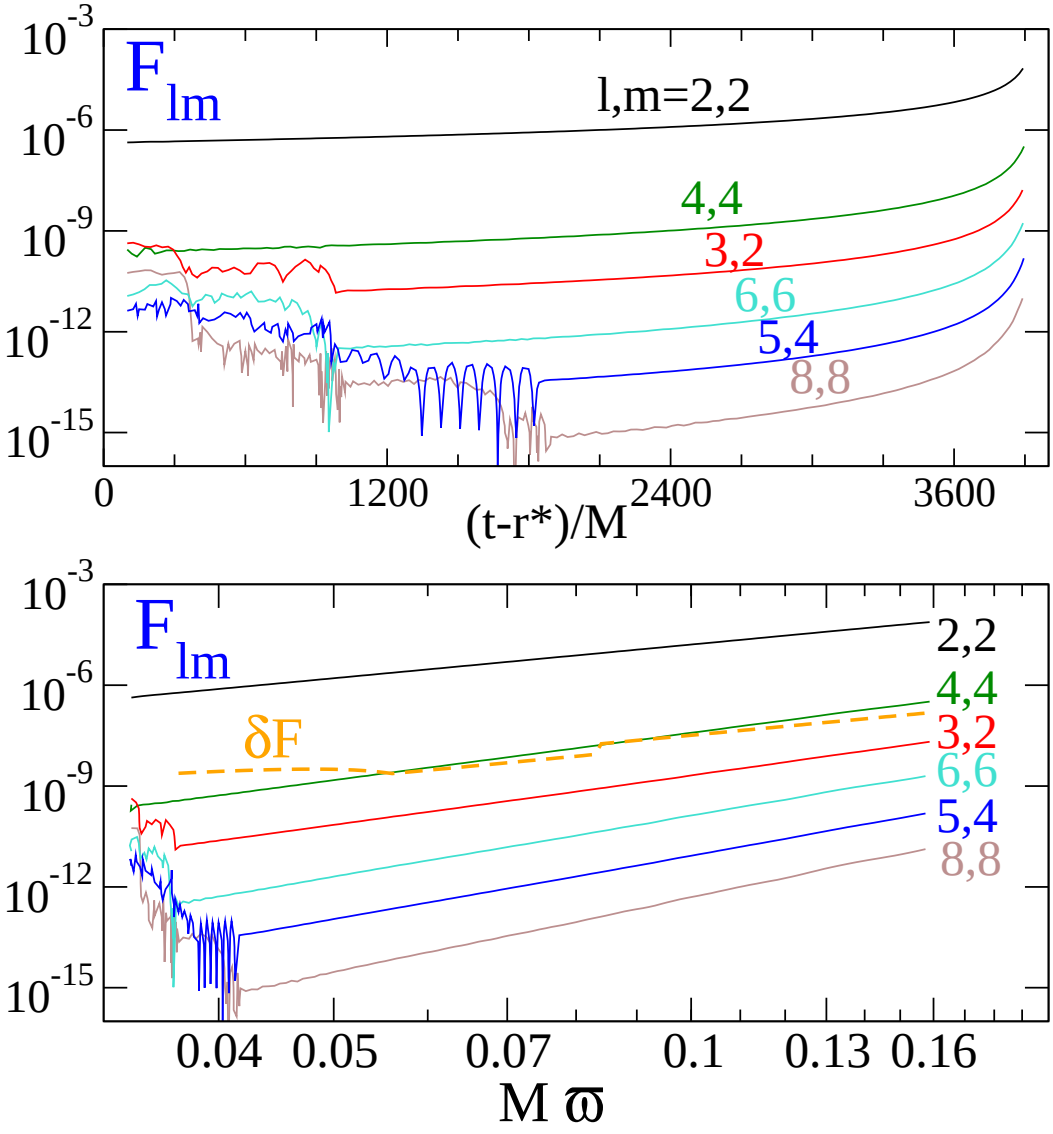

Figure 4.3: Contributions of various (l, m)-modes to the total numerical gravitational wave flux. **Upper panel:** plotted as a function of time. **Lower panel:** Plotted as a function of frequency $M\varpi$. The lower panel also contains the error estimate derived in Fig. 4.2.

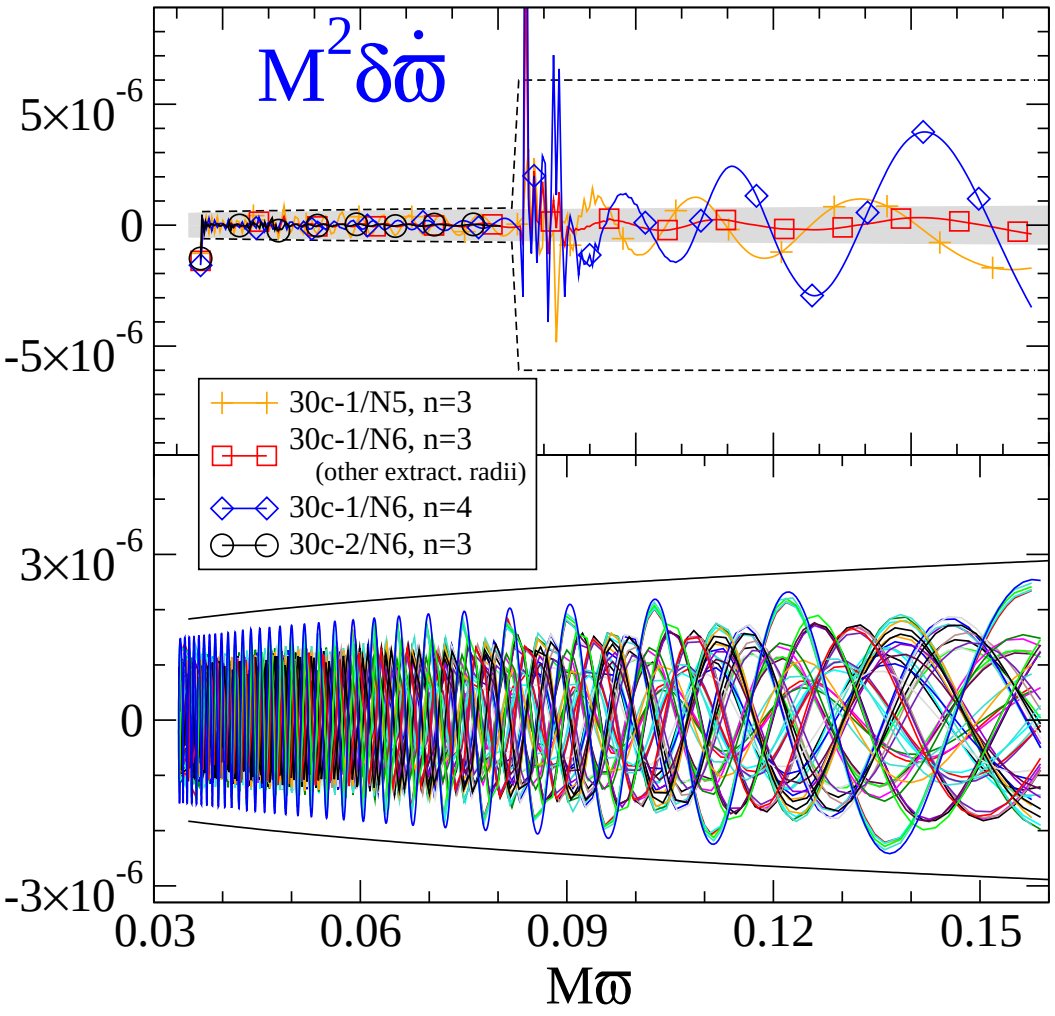

Figure 4.4: **Lower panel:** Difference between frequency derivative $\dot{\varpi}$ computed with 99 different intervals $[t_1, t_2]$ and the average of these. **Upper panel:** Change in the frequency derivative $\dot{\varpi}$ under various changes to the numerical simulation. The grey area in the upper panel indicates the uncertainty due to choice of integration constants, which dominates the overall uncertainty for low frequencies. The dashed line in the upper panel is our final error estimate, which we plot in later figures.

The contributions of the various (l, m)-modes to the total flux [see Eq. (4.3)] are plotted in Fig. 4.3. The top panel plots the flux as a function of time; the lower panel as a function of frequency $M\varpi$. The dashed line in the lower panel corresponds to the error estimate of Fig. 4.2. Because the modes $(5, 4)$, $(6, 6)$, and $(8, 8)$ are significantly smaller than our error estimate, we do not include them in the present analysis.

To estimate the uncertainty in $\dot{\varpi}$, we proceed in a similar fashion. Each one of the 99 different integration intervals yields an $\dot{h}_{22}$ from which we determine $\dot{\varpi}$. We average these to obtain the final $\dot{\varpi}$ to be used in the post-Newtonian comparisons. The lower panel of Fig. 4.4 shows the variation in $\dot{\varpi}$ between the 99 different integration intervals. We find that the *maximum* deviation can be well approximated by $\max|M^2\delta\dot{\varpi}| = 5\times10^{-6}(M\varpi)^{-0.3}$ (see the solid line in lower panel of Fig. 4.4). The *average* $\dot{\varpi}$ computed from all 99 intervals $[t_1, t_2]$ will have a smaller error. Inspection of the lower panel of Fig. 4.4 reveals that the $\delta\dot{\varpi}$ curves fall into 11 groups, corresponding to the 11 values of t_2. As for the case of δF, if we assume that $\delta\dot{\varpi}$ between these groups is randomly distributed, then the error of the average will be reduced by a factor $\sqrt{11}$, i.e., $M^2\delta\dot{\varpi} = 1.5\times10^{-6}(M\varpi)^{-0.3}$. This error is indicated as the grey shaded area in the upper panel of Fig. 4.4.

The upper panel of Fig. 4.4 plots also the change in $\dot{\varpi}(\varpi)$ for the same changes in our numerical simulation already discussed above. We find that at $M\varpi < 0.083$, the uncertainty in $\dot{\varpi}$ is dominated by the choice of integration constants, whereas at higher frequencies the uncertainty is dominated by the numerical errors in the calculation of Ψ_4. As discussed above, at frequency $M\varpi \approx 0.084$ we change the gauge conditions in the evolutions to allow wave-escorting; this introduces high-frequency features leading to more conservative

error estimates.

Note that $\dot{\varpi}$ is a very steep function of ϖ. While the absolute errors in $\dot{\varpi}$ are roughly constant for our simulation, the *relative* errors change significantly: $\delta\dot{\varpi}/\dot{\varpi}$ drops from about 10 per cent early in the run to about 0.2 percent at late times.

We also point out that the first $1000M$ of our simulation are contaminated by noise due to a pulse of "junk-radiation" at the start of the simulation. While this contamination is not apparent on a plot of the waveform as in Fig. 4.1, it nevertheless limits accurate PN-NR comparisons to the region, $t - r^* \gtrsim 1000M$, i.e., $M\varpi \gtrsim 0.037$.

4.3 Post-Newtonian approximants

In this paper we will compare the numerical simulation to various approximants based on the PN expansion. The PN expansion is a slow-motion, weak-field approximation to general relativity with an expansion parameter $\epsilon \sim (v/c)^2 \sim (GM/rc^2)$. For a binary system of two point masses m_1 and m_2, v is the magnitude of the relative velocity, M is the total mass, and r is the separation. For a review of the PN expansion applied to gravitational radiation from inspiralling compact binaries, see Ref. [35].

In Table 4.1 we summarize the PN-approximants that we use, and our notation. We shall use the PN approximants in the so-called adiabatic approximation, both in the standard Taylor-expanded form (reviewed in Sec. 4.3.1) and in a form based on Padé summation (reviewed in Sec. 4.3.2). In addition we

Table 4.1: Summary of PN-approximants. The T-approximants are always Taylor T4 [51] except in Fig. 4.16. The P-approximant in the second row was introduced in Refs. [98, 104, 62] and the *original* E-approximant in third row was introduced in Refs. [65, 66, 104]. The last three rows refer to three possible variations of E-approximants introduced in Refs. [62, 60]. In a few tests aimed at improving the closeness between numerical data and E-approximants, we vary $v_{\rm pole}$ and treat the logarithms as constants when Padé summation to the flux is applied [92]. We shall denote this flux by $\overline{F}_n^m$. Finally, when using tuned PN-approximants with pseudo 4PN order terms in the flux, energy, or Hamiltonian, we denote the latter as pF, pE and pH. Note that if known test-mass limit coefficients in the flux are used, the latter is still denoted as F even at PN orders larger than 3.5PN. Finally, the values of $v_{\rm pole}$ and $v_{\rm lso}$ used in the P-approximants F_n^m and ${}^{\rm nK}F_n^m$ are $v_{\rm pole}^{\rm 2PN} = 0.6907$ and$v_{\rm lso}^{\rm 2PN} = 0.4456$.

approximant	notation	see Eqs.	adiabatic	Keplerian
Taylor (T-)	F_n/E_p	(4.19)/(4.14)	yes	yes
Padé (P-)	F_n^m/E_p^q	(4.39)/(4.33)	yes	yes
EOB (E-)	F_n^m/H_p	(4.63)/(4.43)	no	yes
EOB (E-)	${}^{\rm nK}F_n^m/H_p$	(4.64)/(4.43)	no	no
EOB (E-)	F_n/H_p	(4.68)/(4.43)	no	yes
EOB (E-)	${}^{\rm nK}F_n/H_p$	(4.69)/(4.43)	no	no

shall use the non-adiabatic EOB model (reviewed in Sec. 4.3.3) in its original form [65, 66, 104], as well as several variations that differ in the form of the radiation-reaction force [62, 60, 95]. After summarizing the various PN approximants in Secs. 4.3.1, 4.3.2, and 4.3.3, we describe how we construct the waveform for these approximants in Sec. 4.3.4.

In the adiabatic approximation the inspiral is modeled as a quasi-stationary sequence of circular orbits. The evolution of the inspiral (and in particular of the orbital phase Φ) is completely determined by the *energy-balance equation* [35]

$$\frac{dE(v_\Omega)}{dt} = -F(v_\Omega)\,. \tag{4.12}$$

This equation relates the time derivative of the center-of-mass energy $E(v_\Omega)$ (which is conserved in absence of radiation reaction) to the gravitational wave energy flux $F(v_\Omega)$. Both functions are known for quasicircular orbits as a PN expansion in the invariantly defined velocity

$$v_\Omega = (M\Omega)^{1/3}\,, \tag{4.13}$$

where $\Omega = \dot{\Phi}$ is the orbital frequency (we use units such that $G = c = 1$).[4] We will denote the Taylor-expanded flux (energy) by F_k (E_k) where k denotes the maximum power of v_Ω retained in the series. (Recall that $k = 2N$ for an Nth order PN expansion.) We will denote the Padé-expanded flux (energy) by F^m_n (E^m_n) where $m + n = k$, with m and n denoting the order of the polynomial in the numerator and denominator, respectively.

[4] In Ref. [51] we used $x = v_\Omega^2$ as the expansion parameter.

4.3.1 Adiabatic Taylor approximants

For generic values of the symmetric mass ratio $\nu = m_1 m_2/M^2$, the center-of-mass energy is known through 3PN order [158, 115, 91, 42, 109]. For circular orbits the Taylor PN-approximants (henceforth, T-approximants) to the energy are given by

$$E_{2k}(v_\Omega) = -\frac{M\nu}{2}\, v_\Omega^2 \sum_{i=0}^{k} \mathcal{E}_{2i}(\nu)\, v_\Omega^{2i}\,, \tag{4.14}$$

where the known coefficients are

$$\mathcal{E}_0(\nu) = 1\,, \tag{4.15}$$

$$\mathcal{E}_2(\nu) = -\frac{3}{4} - \frac{\nu}{12}\,, \tag{4.16}$$

$$\mathcal{E}_4(\nu) = -\frac{27}{8} + \frac{19}{8}\,\nu - \frac{1}{24}\,\nu^2\,, \tag{4.17}$$

$$\mathcal{E}_6(\nu) = -\frac{675}{64} + \left(\frac{34445}{576} - \frac{205}{96}\pi^2\right)\nu - \frac{155}{96}\,\nu^2 - \frac{35}{5184}\,\nu^3\,. \tag{4.18}$$

The GW energy flux for arbitrary masses has been computed through 3.5PN order [43, 38]:

$$F_k(v_\Omega) = \frac{32}{5}\,\nu^2\, v_\Omega^{10} \sum_{i=0}^{k} \mathcal{F}_i(\nu)\, v_\Omega^{i}\,, \tag{4.19}$$

where

$$\mathcal{F}_0(\nu) = 1\,, \tag{4.20}$$

$$\mathcal{F}_1(\nu) = 0\,, \tag{4.21}$$

$$\mathcal{F}_2(\nu) = -\frac{1247}{336} - \frac{35}{12}\nu\,, \tag{4.22}$$

$$\mathcal{F}_3(\nu) = 4\pi\,, \tag{4.23}$$

$$\mathcal{F}_4(\nu) = -\frac{44711}{9072} + \frac{9271}{504}\nu + \frac{65}{18}\nu^2\,, \tag{4.24}$$

$$\mathcal{F}_5(\nu) = -\left(\frac{8191}{672} + \frac{583}{24}\nu\right)\pi\,, \tag{4.25}$$

$$\begin{aligned}\mathcal{F}_6(\nu) = {} & \frac{6643739519}{69854400} + \frac{16}{3}\pi^2 - \frac{1712}{105}\gamma_E \\ & -\frac{856}{105}\log(16v_\Omega^2) + \left(-\frac{134543}{7776} + \frac{41}{48}\pi^2\right)\nu \\ & -\frac{94403}{3024}\nu^2 - \frac{775}{324}\nu^3\,,\end{aligned} \tag{4.26}$$

$$\mathcal{F}_7(\nu) = \left(-\frac{16285}{504} + \frac{214745}{1728}\nu + \frac{193385}{3024}\nu^2\right)\pi\,, \tag{4.27}$$

where γ_E is Euler's constant. Notice that starting at 3PN order ($k = 6$) logarithms enter the flux.

4.3.2 Adiabatic Padé approximants

Center-of-mass energy

Damour, Iyer and Sathyaprakash [98] (henceforth DIS) proposed a new class of approximate waveforms constructed by introducing new energy and flux functions and by applying Padé summation [23] to build successive approximants to these two functions (henceforth P-approximants). Their motivation for introducing these new functions and using their P-approximants came from

an examination of the behavior of the standard PN-expansion and the new P-approximants in the test-mass limit in which the exact gravitational energy flux is known numerically [201], the PN expansion of the flux is known through 5.5PN order [224], and the center-of-mass energy is known analytically as

$$\frac{E(v_\Omega;\nu=0)}{\mu} = \frac{1-2v_\Omega^2}{\sqrt{1-3v_\Omega^2}} - 1\,, \tag{4.28}$$

where $\mu = M\nu$ is the reduced mass.

DIS first observed that in the quantum two-body problem the symmetric quantity

$$\epsilon \equiv \frac{E_{\rm tot}^2 - m_1^2 - m_2^2}{2m_1\,m_2}\,, \tag{4.29}$$

(where the total relativistic energy $E_{\rm tot} = E+M$), is the best energy function when treating the two-body problem as an effective one-body problem in an external field. Because in the test-mass limit

$$\epsilon(v_\Omega;\nu=0) = \frac{1-2v_\Omega^2}{\sqrt{1-3v_\Omega^2}}\,, \tag{4.30}$$

DIS defined the new energy function as

$$e(v_\Omega) \equiv \epsilon^2 - 1\,, \tag{4.31}$$

as this function has a simple pole singularity on the real axis in the test-mass limit, and DIS conjectured that such a pole would continue to exist in the comparable mass case.[5] The energy function $E(v_\Omega)$ entering the balance equation (4.12) can be expressed in terms of $e(v_\Omega)$ as

$$E(v_\Omega) = \left\{M^2 + 2\nu M^2\left[\sqrt{1+e(v_\Omega)}-1\right]\right\}^{1/2} - M\,. \tag{4.32}$$

[5] A motivation for having using Eq. (4.31) instead of Eq. (4.29) as a basic quantity is that the former (unlike the latter) is amenable to Padé summation in the test mass limit.

by combining Eqs. (4.29) and (4.31). [Note that the map between the adiabatic functions e and E given by Eq. (4.32) is the same map found in the EOB model between the effective Hamiltonian $H^{\rm eff}$ and the real Hamiltonian $H^{\rm real}$, as given by Eq. (4.43).]

Finally, DIS proposed as approximants to the energy function $e(v_\Omega)$ the diagonal or subdiagonal P-approximants, depending on whether the PN order is even or odd.[6] Investigating the behavior of the P-approximants under variations of an (at the time) unknown coefficient in the 3PN center-of-mass energy, Damour, Jaranowski and Schäfer [104] found it more robust to use the superdiagonal P-approximant instead of the subdiagonal P-approximant at 3PN order.[7] This suggestion was also adopted in Ref. [62] and will be used here; that is, we use subdiagonal P-approximants for 1PN, diagonal for 2PN, and superdiagonal for 3PN.

The P-approximants for the center-of-mass energy are defined as

$$E_p^q(v_\Omega) = \left\{ M^2 + 2\nu M^2 \left[\sqrt{1 + e_p^q(v_\Omega)} - 1 \right] \right\}^{1/2} - M \,, \tag{4.33}$$

where at 2PN order [98]

$$e_2^2(v_\Omega) = -v_\Omega^2 \, \frac{1 + \frac{1}{3}\nu - \left(4 - \frac{9}{4}\nu + \frac{1}{9}\nu^2\right) v_\Omega^2}{1 + \frac{1}{3}\nu - \left(3 - \frac{35}{12}\nu\right) v_\Omega^2} \,, \tag{4.34}$$

and at 3PN order [104]

$$\begin{aligned} e_2^4(v_\Omega) \;=\; & -v_\Omega^2 \, \frac{1}{1 - w_3(\nu)\, v_\Omega^2} \left[1 - \left(1 + \frac{1}{3}\nu + w_3(\nu) \right) v_\Omega^2 \right. \\ & \left. - \left(3 - \frac{35}{12}\nu - \left(1 + \frac{1}{3}\nu \right) w_3(\nu) \right) v_\Omega^4 \right] , \end{aligned} \tag{4.35}$$

[6] As the energy is only a function of even powers of v_Ω, the choice of using diagonal or subdiagonal (superdiagonal) is based on the order of v_Ω^2 that is retained. For notational consistency, the indices on all approximants will refer to the power of v_Ω. Other references define the indices on the energy approximants with respect to v_Ω^2.

[7] Subdiagonal P-approximants were extended to 3PN order in Ref. [101], and LAL [83] software uses those P-approximants for the energy function.

where

$$w_3(\nu) = \frac{40}{36-35\nu}\left[\frac{27}{10}+\frac{1}{16}\left(\frac{41}{4}\pi^2-\frac{4309}{15}\right)\nu + \frac{103}{120}\nu^2-\frac{1}{270}\nu^3\right]. \tag{4.36}$$

Gravitational wave energy flux

As originally pointed out in Refs. [200, 88], the flux function in the test-mass limit has a simple pole at the light-ring position (i.e., the last unstable circular orbit of a photon). Motivated by this, DIS introduced a new flux-type function

$$f_k(v_\Omega) = \left(1-\frac{v_\Omega}{v_{\rm pole}(\nu)}\right) F_k(v_\Omega;\nu)\,, \tag{4.37}$$

with the suggestion that $v_{\rm pole}$ be chosen to be at the light ring (pole singularity) of the new energy function.

In order to construct well behaved approximants, DIS proposed to normalize the velocity v_Ω entering the logarithms in Eq. (4.26) to some relevant scale which they chose to be $v_{\rm lso}(\nu)$, where the last stable orbit (LSO) is defined as the minimum of the energy. Also, they factored out the logarithms yielding

$$f_k(v_\Omega) = \frac{32}{5}\,\nu^2\,v_\Omega^{10}\left[1+\log\frac{v_\Omega}{v_{\rm lso}(\nu)}\left(\sum_{i\geq 6}^{k}\ell_i\,v_\Omega^i\right)\right] \times\left(1-\frac{v_\Omega}{v_{\rm pole}(\nu)}\right)\sum_{i=0}^{k}\mathcal{F}_i^{\text{log-fac}}\,v_\Omega^i\,, \tag{4.38}$$

where ℓ_i and $\mathcal{F}_i^{\text{log-fac}}$ are functions of $\mathcal{F}_i$. Through 3.5PN order, $\ell_6 = -1712/105$, $\ell_7 = 0$, and $\mathcal{F}_i^{\text{log-fac}} = \mathcal{F}_i$ with the replacement of $v_\Omega \to v_{\rm lso}$ in $\mathcal{F}_6$ [see Eq. (4.26)].

Finally, DIS proposed to define the P-approximant of the GW energy flux as

$$F_n^m(v_\Omega) = \frac{1}{1-v_\Omega/v_{\rm pole}(\nu)}\,f_n^m(v_\Omega)\,. \tag{4.39}$$

where

$$f_n^m(v_\Omega) = \frac{32}{5}\,\nu^2\,v_\Omega^{10}\left[1+\log\frac{v_\Omega}{v_{\rm lso}(\nu)}\left(\sum_{i\geq 6}^{k}\ell_i\;v_\Omega^i\right)\right] \times \mathrm{P}_n^m\left[\left(1-\frac{v_\Omega}{v_{\rm pole}(\nu)}\right)\sum_{i=0}^{k}\mathcal{F}_i^{\text{log-fac}}\,v_\Omega^i\right], \tag{4.40}$$

where $\mathrm{P}_n^m[x]$ denotes Padé summation of the series x. DIS proposed to use the diagonal or subdiagonal P-approximants, depending on whether $k = n + m$ is even or odd. Furthermore, DIS proposed to use $v_{\rm lso}(\nu)$ and $v_{\rm pole}(\nu)$ as the minimum and pole of the center-of-mass energy P-approximant of the same PN order. At 2PN (the order to which the PN expansion was known by DIS) $v_{\rm pole}$ is determined from the pole of the Padé energy function e_2^2, yielding

$$v_{\rm pole}^{\rm 2PN}(\nu) = \frac{1}{\sqrt{3}}\,\sqrt{\frac{1+\frac{1}{3}\nu}{1-\frac{35}{36}\nu}}\,. \tag{4.41}$$

When the PN expansion was extended to 3PN order, it was found that none of the 3PN P-approximants have a physical pole. Therefore, somewhat arbitrarily, we will follow previous analyses and use the value (4.41) also at 3PN order. We denote the P-approximants defined by Eqs. (4.39) and (4.33) as F_n^m/E_p^q.

The denominator in the Padé summation of the GW energy flux can have zeros. They are called *extraneous poles* of the P-approximant [23]. It is desirable that these poles be located at high frequency (i.e., beyond the transition from inspiral to plunge). We shall see that depending on the PN order and also the mass ratio, extraneous poles can be present at low frequencies. This could indicate poor convergence of the Padé summation.

In Secs. 4.4.2, 4.6.2 and 4.6.3 we shall investigate how to improve the closeness of the PN-approximants to the numerical data by varying a_5 [97, 67, 113], $v_{\rm pole}$ [97, 113] and also by introducing higher-order PN coefficients in the flux

function. When varying $v_{\rm pole}$ in the P-approximant at 3.5PN order, extraneous poles appear at low values of v_Ω. Therefore, in order to push these poles to very high frequency, we follow the suggestion of Ref. [113], and use P-approximants at 4PN order, where the 4PN coefficient is set to its known value in the test-mass limit. This cure may fail for different mass ratios if new extraneous poles appear at low frequency. Furthermore the logarithm in the flux is not factored out as in Eq. (4.38), but treated as a constant when Padé summation is done. In this case the flux function is denoted $\overline{F}_n^m$.

We notice that DIS motivated the introduction of the P-approximants first in the test-mass limit case by observing much faster and monotonic convergence of the Padé energy, flux and waveforms with respect to Taylor energy, flux and waveforms. Quantitative tests of the convergence were done only for the Padé waveforms (see e.g., Tables III and IV in Ref. [98]), while for the flux and the energy conclusions were drawn qualitatively from Figs. 3 and 4 of Ref. [98]. DIS then conjectured that the comparable mass case is a smooth deformation of the test-mass limit case, and proposed to use close-to-diagonal P-approximants for the flux and the energy when $\nu \neq 0$. In the Appendix we perform a few convergence tests of the P-approximants of the flux function in the test-mass limit case, and conclude that whereas the P-approximants provide a better fit to the numerical flux at 5.5PN order, they do not accelerate the convergence of the Taylor series expansion of the energy flux.

4.3.3 Non-adiabatic effective-one-body approximants

The EOB model goes beyond the adiabatic approximation and can incorporate deviations from the Keplerian law when the radial separation become smaller than the last stable circular orbit.

Here we briefly review the main equations defining the EOB dynamics and refer the reader to previous papers for more details [66, 65, 104, 60, 192, 67, 113, 114, 104]. The non-spinning EOB effective Hamiltonian is [65, 104]:

$$\begin{aligned} H^{\rm eff}(\mathbf{r},\boldsymbol{p}) &= \mu\,\widehat{H}^{\rm eff}(\mathbf{r},\mathbf{p}) \\ &= \mu\left\{A(r)\left[1+\mathbf{p}^2+\left(\frac{A(r)}{D(r)}-1\right)(\mathbf{n}\cdot\mathbf{p})^2 \right.\right. \\ &\quad \left.\left. +\frac{1}{r^2}2(4-3\nu)\,\nu\,(\mathbf{n}\cdot\mathbf{p})^4\right]\right\}^{1/2}, \end{aligned} \tag{4.42}$$

with $\mathbf{r}$ and $\mathbf{p}$ being the reduced dimensionless variables; $\mathbf{n}=\mathbf{r}/r$ where we set $r=|\mathbf{r}|$. In absence of spins the motion is constrained to a plane. Introducing polar coordinates (r,Φ,p_r,p_Φ), the EOB effective metric reads

$$ds^2_{\rm eff}\equiv g^{\rm eff}_{\mu\nu}\,dx^\mu\,dx^\nu = -A(r)\,c^2dt^2+\frac{D(r)}{A(r)}\,dr^2+r^2\,(d\theta^2+\sin^2\theta\,d\phi^2)\,.$$

The EOB real Hamiltonian is

$$H^{\rm real}=M\,\sqrt{1+2\nu\left(\frac{H^{\rm eff}-\mu}{\mu}\right)}-M\,, \tag{4.43}$$

and we define $\hat{H}^{\rm real}=H^{\rm real}/\mu$. The T-approximants to the coefficients $A(r)$ and $D(r)$ in Eqs. (4.42) and (4.43) read [65, 104]

$$A_k(r) = \sum_{i=0}^{k+1}\frac{a_i}{r^i}\,, \tag{4.44}$$

$$D_k(r) = \sum_{i=0}^{k}\frac{d_i}{r^i}\,, \tag{4.45}$$

where

$$a_0 = 1\,, \quad a_1 = 2\,, \quad a_2 = 0\,, \quad a_3(\nu) = 2\nu\,,$$
$$a_4(\nu) = \left(\frac{94}{3} - \frac{41}{32}\pi^2\right)\nu\,, \tag{4.46}$$
$$d_0 = 1\,, \quad d_1 = 0\,, \quad d_2(\nu) = 6\,\nu\,,$$
$$d_3(\nu) = 2\,(3\nu - 26)\,\nu\,. \tag{4.47}$$

In Sec. 4.6.3, we will explore the flexibility of the EOB model by tuning the pseudo 4PN order coefficients $a_5(\nu)$ which we will take to have the following functional form[8]

$$a_5(\nu) = a_5\,\nu\,. \tag{4.48}$$

In order to assure the presence of an horizon in the effective metric, we need to factor out a zero of $A(r)$. This is obtained by applying the Padé summation [104]. Thus, the coefficients $A_k(r)$ and $D_k(r)$ are replaced by the Padé approximants [104]

$$A_2^1(r) = \frac{r\,(-4 + 2r + \nu)}{2r^2 + 2\nu + r\,\nu}\,, \tag{4.49}$$

at 2PN order, and

$$A_3^1(r) = \frac{\mathrm{Num}(A_3^1)}{\mathrm{Den}(A_3^1)}\,, \tag{4.50}$$

with

$$\mathrm{Num}(A_3^1) = r^2\,[(a_4(\nu) + 8\nu - 16) + r\,(8 - 2\nu)]\,, \tag{4.51}$$

and

$$\begin{aligned}\mathrm{Den}(A_3^1) \;=\; & r^3\,(8 - 2\nu) + r^2\,[a_4(\nu) + 4\nu] \\ & + r\,[2a_4(\nu) + 8\nu] + 4[\nu^2 + a_4(\nu)]\,,\end{aligned} \tag{4.52}$$

[8]Note that what we denote a_5 in this paper was denoted λ in Ref. [67].

at 3PN order. When exploring the flexibility of the EOB model, we use the following Padé approximant at 4 PN order [97, 67]:

$$A_4^1(r) = \frac{\mathrm{Num}(A_4^1)}{\mathrm{Den}(A_4^1)}\,, \tag{4.53}$$

with

$$\begin{aligned}\mathrm{Num}(A_4^1) &= r^3\left[32 - 24\nu - 4a_4(\nu) - a_5(\nu)\right] \\ &\quad + r^4[a_4(\nu) - 16 + 8\nu]\,,\end{aligned} \tag{4.54}$$

and

$$\begin{aligned}\mathrm{Den}(A_4^1) &= -a_4^2(\nu) - 8a_5(\nu) - 8a_4(\nu)\nu + 2a_5(\nu)\nu - 16\nu^2 \\ &\quad + r\left[-8a_4(\nu) - 4a_5(\nu) - 2a_4(\nu)\nu - 16\nu^2\right] \\ &\quad + r^2\left[-4a_4(\nu) - 2a_5(\nu) - 16\nu\right] \\ &\quad + r^3\left[-2a_4(\nu) - a_5(\nu) - 8\nu\right] \\ &\quad + r^4\left[-16 + a_4(\nu) + 8\nu\right].\end{aligned} \tag{4.55}$$

For the coefficient $D(r)$, the P-approximant used at 2PN, 3PN, and 4PN order respectively are [104, 97, 67]:

$$D_2^0(r) = 1 - \frac{6\nu}{r^2}\,, \tag{4.56}$$

$$D_3^0(r) = \frac{r^3}{r^3 + 6\nu r + 2\nu(26 - 3\nu)}\,, \tag{4.57}$$

$$D_4^0(r) = \frac{r^4}{r^4 + 6\nu r^2 + 2\nu(26 - 3\nu)r - d_4(\nu) + 36\nu^2}\,, \tag{4.58}$$

and we choose somewhat arbitrarily $d_4(\nu) = 36\nu^2$, so that $D_4^0 = D_3^0$. (We note that the value of d_4 does not affect much the EOB evolution [67].) The EOB Hamilton equations written in terms of the reduced quantities $\widehat{H}^{\mathrm{real}}$ and $\widehat{t} = t/M$,

$\widehat{\Omega} = \Omega M$ [66], are

$$\frac{dr}{d\widehat{t}} = \frac{\partial \widehat{H}^{\rm real}}{\partial p_r}(r, p_r, p_\Phi)\,, \tag{4.59}$$

$$\frac{d\Phi}{d\widehat{t}} \equiv \widehat{\Omega} = \frac{\partial \widehat{H}^{\rm real}}{\partial p_\Phi}(r, p_r, p_\Phi)\,, \tag{4.60}$$

$$\frac{dp_r}{d\widehat{t}} = -\frac{\partial \widehat{H}^{\rm real}}{\partial r}(r, p_r, p_\Phi)\,, \tag{4.61}$$

$$\frac{dp_\Phi}{d\widehat{t}} = \widehat{\mathcal{F}}[\widehat{\Omega}(r, p_r, p_\Phi)]\,, \tag{4.62}$$

where for the Φ component of the radiation-reaction force a few approximants are available. Originally, Ref. [66] suggested the following Keplerian P-approximants to the flux

$${}^{\rm K}\widehat{\mathcal{F}}_n^m \equiv -\frac{1}{\nu v_\Omega^3} F_n^m(v_\Omega; \nu, v_{\rm pole})\,, \tag{4.63}$$

where F_n^m is given by the Padé flux in Eqs. (4.39) and (4.40). Here by Keplerian we mean that in the flux the tangential velocity $V_\Phi = \dot{\Phi} r$ is set to $V_\Phi \equiv v_\Omega = \dot{\Phi}^{1/3}$, having assumed the Keplerian relation $\dot{\Phi}^2 r^3 = 1$. It was then pointed out in Ref. [95] that the Keplerian relation becomes less and less accurate once the binary passes through the last stable orbit. A more appropriate approximant to the flux would be

$${}^{\rm nK}\widehat{\mathcal{F}}_n^m \equiv -\frac{v_\Omega^3}{\nu V_\Phi^6} F_n^m(V_\Phi; \nu, v_{\rm pole})\,, \tag{4.64}$$

where $V_\Phi \equiv \dot{\Phi} r_\Omega$. Notice that because the EOB Hamiltonian is a deformation of the Schwarzschild Hamiltonian, the exact Keplerian relation is $\dot{\Phi}^2 r_\Omega^3 = 1$ with $r_\Omega \equiv r\,[\psi(r, p_\Phi)]^{1/3}$ and ψ is defined following the argument presented around Eq. (19) to (22) in Ref. [95]:

$$\begin{aligned}\frac{1}{\psi r^3} &\equiv \omega_{\rm circ}^2 = \left(\frac{\partial \mathcal{H}(r, p_r = 0, p_\phi)}{\partial p_\phi}\right)^2 \\ &= \frac{1}{r^3}\frac{p_\phi^2 A(r)}{\left(1 + \frac{p_\phi^2}{r^2}\right) r \left(1 + 2\eta\left(\sqrt{w(r, p_\phi)} - 1\right)\right)}\end{aligned} \tag{4.65}$$

where $w(r, p_\phi) = A(r)\left(1 + \frac{p_\phi^2}{r^2}\right)$. The value of p_ϕ of circular orbits are obtained by minimizing with respect to r the circular orbit Hamiltonian $\mathcal{H}(r, p_r = 0, p_\phi)$ and it yields the following relation between r and p_ϕ

$$\frac{2p_\phi^2 A(r)}{r^3} = \left(1 + \frac{p_\phi^2}{r^2}\right) \frac{dA(r)}{dr} \,. \tag{4.66}$$

By inserting Eq. (4.66) in the definition of ψ, and replacing all p_ϕ except the one which implicitly appears in $w(r, p_\phi)$ we obtain

$$\psi = \frac{1 + 2\eta(\sqrt{w(r, p_\phi)} - 1)}{r^2\, dA(r)/dr/2} \,. \tag{4.67}$$

Finally, Refs. [62, 60] introduced another possible variation of the EOB flux approximants which use T-approximants for the flux given by Eq. (4.19), in either the Keplerian or non-Keplerian form, i.e.

$$^{\mathrm{K}}\widehat{\mathcal{F}}_n = -\frac{1}{\nu v_\Omega^3} F_n(v_\Omega) \,, \tag{4.68}$$

and

$$^{\mathrm{nK}}\widehat{\mathcal{F}}_n = -\frac{v_\Omega^3}{\nu V_\Phi^6} F_n(V_\Phi) \,. \tag{4.69}$$

Note that the flux for the non-Keplerian EOB models are not simply functions of the orbital frequency Ω. We denote the original E-approximants [65, 66, 104] which use the Padé flux (4.40) as F_n^m/H_p where H_p is H^{real} computed from A_p^1 and D_p^0. Other E-approximants used in this paper are summarized in Table 4.1. The initial conditions for Eqs. (4.59)–(4.62) are obtained following Ref. [66] and starting the evolution far apart to reduce the eccentricity to negligible values.

4.3.4 Waveforms

The PN waveforms are obtained by substituting the orbital phase and frequency into the spherical harmonic mode (2,2) with amplitude corrections through 3PN

order [167, 162, 28]

$$
\begin{aligned}
h_{22} &= -8\sqrt{\frac{\pi}{5}}\frac{\nu M}{R}e^{-2i\Phi}v_\Omega^2\left\{1 - v_\Omega^2\left(\frac{107}{42} - \frac{55}{42}\nu\right)\right. \\
&+ 2\pi v_\Omega^3 - v_\Omega^4\left(\frac{2173}{1512} + \frac{1069}{216}\nu - \frac{2047}{1512}\nu^2\right) \\
&- v_\Omega^5\left[\left(\frac{107}{21} - \frac{34}{21}\nu\right)\pi + 24i\nu\right] \\
&+ v_\Omega^6\left[\frac{27027409}{646800} - \frac{856}{105}\gamma_E + \frac{2}{3}\pi^2 - \frac{1712}{105}\ln 2\right. \\
&- \frac{856}{105}\ln v_\Omega - \left(\frac{278185}{33264} - \frac{41}{96}\pi^2\right)\nu - \frac{20261}{2772}\nu^2 \\
&\left.\left. + \frac{114635}{99792}\nu^3 + \frac{428i}{105}\pi\right] + O(\epsilon^{7/2})\right\}. \qquad (4.70)
\end{aligned}
$$

For the adiabatic models, the orbital phase is obtained by rewriting the energy balance equation (4.12) as

$$\frac{d\Omega}{dt} = -\frac{F}{dE/d\Omega}\,. \qquad (4.71)$$

and integrating this equation along with $d\Phi/dt = \Omega$. The Taylor approximants are formed first by substituting $F = F_n$ and $E = E_n$ into Eq. (4.71). The P-approximant waveform is formed similarly by substituting $F = F_n^m$ and $E = E_n^m$ into Eq. (4.71). The TaylorT1 and Padé approximants then numerically integrate Eq. (4.71). The TaylorT4 approximant is formed by first re-expanding the right side of Eq. (4.71) as a single Taylor expansion truncated at the appropriate order, and then numerically integrating the resulting equation. The TaylorT2 and TaylorT3 approximants perform the integration analytically. The various Taylor approximants are reviewed in Sec. IIIE of Ref. [51].

For the non-adiabatic EOB models, the orbital phase is determined by solving Hamilton's equations (4.59)-(4.62).

After computing h_{22}, the appropriate time derivatives are taken to form $\dot{h}_{22}$

and Ψ_4^{22}.

4.4 Comparison with post-Newtonian approximants: energy flux

We now compare the numerical GW energy flux with predictions from PN theory. In Sec. 4.4.1 we present comparisons with T-, P- and E-approximants, and in Sec. 4.4.2 we explore ways of fitting the numerical flux by introducing higher-order PN coefficients and varying the value of $v_{\rm pole}$ away from $v_{\rm pole}^{\rm 2PN}$ [Eq. (4.41)].

The PN flux is derived as a function of frequency, so it is natural to perform this comparison as a function of frequency. One alternative, comparison as a function of time, would require computation of the PN phase as a function of time. This depends on the PN energy, so that a comparison with respect to time would mix effects due to flux and energy. Furthermore, comparisons with respect to time are sensitive to (and likely dominated by) secularly accumulating phase differences [16].

The PN flux is given in terms of the *orbital* frequency Ω—see Eqs. (4.19) and (4.13)—so at first glance, it might seem natural to compare PN and NR energy fluxes at particular values of Ω. However, the orbital frequency is gauge-dependent, and there is no simple relation between the NR orbital frequency and the PN orbital frequency. Nor is there a simple relation between the NR orbital frequency and any quantity measured at infinity (where the energy flux is defined). In particular, it is very difficult to determine the NR orbital frequency as a function of retarded time. In contrast, the frequency ϖ (see Eq. (4.5)) of

the GWs at infinity is an observable quantity, and is easily obtained from both PN formulae and from the NR simulation. Therefore, to achieve a meaningful comparison, we compare the PN and NR energy flux at particular values of ϖ.

In order to compute the PN flux as a function of ϖ, we need to find the mapping $\varpi_{\rm PN} : \Omega \to \varpi$. In order to find this mapping, we must build a PN waveform as a function of Ω and compute ϖ as defined by Eq. (4.5). We construct the waveforms as described in Sec. 4.3.4. For the T-approximant of the flux, we will use the TaylorT4 waveform. In Fig. 4.5 we plot both GW frequencies (defined in Eqs. (4.4) and (4.5)). We then invert the mapping to obtain $\Omega_{\rm PN} = \varpi_{\rm PN}^{-1} : \varpi \to \Omega$. So, given the PN flux $F(\Omega)$ from Sec. 4.3, the flux as a function of the GW frequency is given by $F(\varpi) = F(\Omega_{\rm PN}(\varpi))$. The relation $\Omega_{\rm PN}(\varpi)$ depends on the instantaneous evolution of the PN model around frequency Ω, and is therefore (unfortunately) dependent on the PN model, in particular the choice of PN energy. This dependence, however, is local and will not lead to secularly accumulating differences.

Notice from Fig. 4.5 that the orbital frequency and the GW frequency differ by $\sim$ 1%–3% at large frequencies, depending on the PN model and the PN order, and the difference in ϖ between different PN models is about 5%. Because the energy flux is roughly proportional to $\varpi^{10/3}$ (more precisely, $d\log F/d\log(M\varpi)$ increases to ~ 3.6 at $M\varpi = 0.15$), the difference in the flux caused by using GW frequency from different PN models is about three to four times the difference in GW frequencies. Fig. 4.6 illustrates this effect by intentionally plotting the PN flux versus the incorrect frequency Ω. Because changing the PN model has a significant effect on the flux, we consider flux comparisons for several different PN models below.

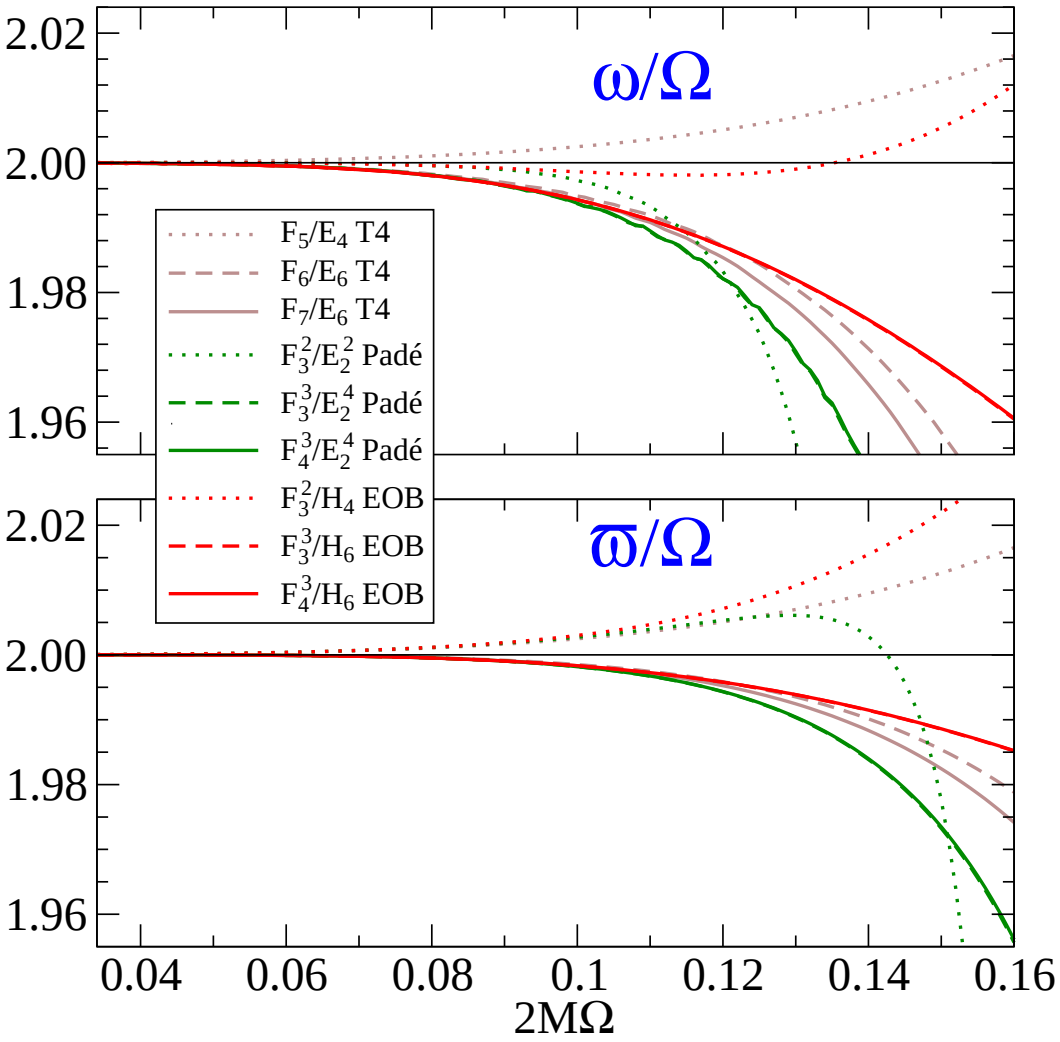

Figure 4.5: Ratio of GW frequencies ω and ϖ to orbital frequency, as a function of (twice) the orbital frequency, for different PN models. The GW frequencies ω and ϖ are defined in Eqs. (4.4) and (4.5). Solid lines correspond to 3.5PN, dashed and dotted lines to 3PN and 2.5PN, respectively.

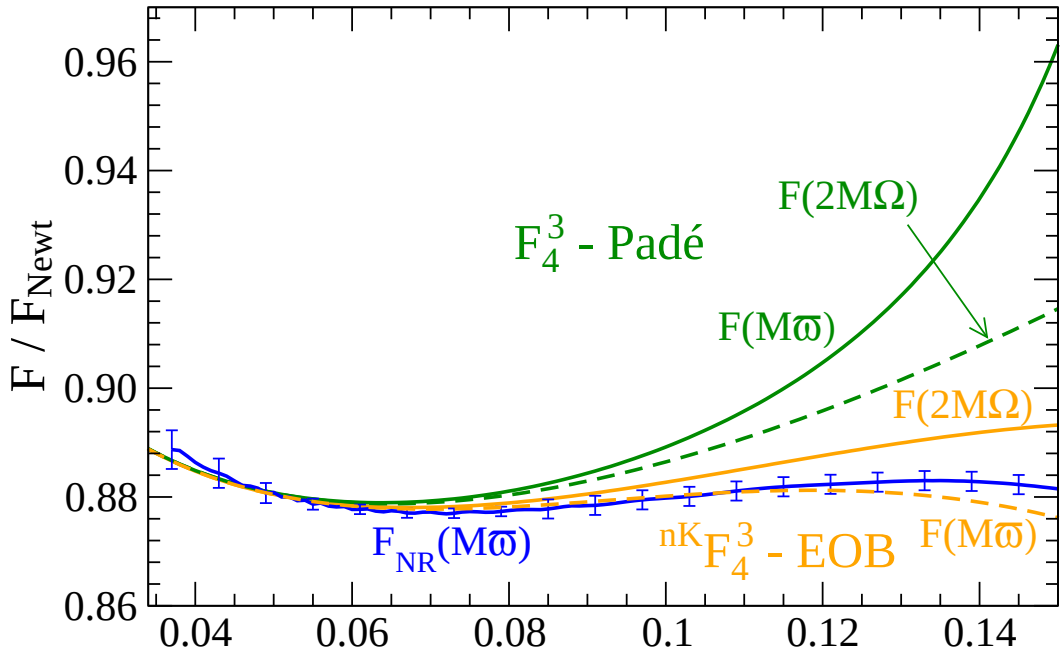

Figure 4.6: Effect of choice of frequency. Shown are the PN fluxes for two representative PN-approximants, plotted (correctly) as function of ϖ and (incorrectly) as function of 2Ω. Plotting as a function of 2Ω changes the PN fluxes significantly relative to the numerical flux $F_{\rm NR}$.

Note that for the flux comparison (and the comparisons of the derivative of the energy in Sec. 4.5), the PN waveforms are used only to define the mapping between Ω and ϖ. The PN flux is taken directly from the PN flux expressions, e.g., Eq. (4.19), and *not* computed by applying Eq. (4.3) to PN waveforms $h(t)$. Equation (4.3) is used only to compute the numerical flux.

4.4.1 Flux comparison

Figure 4.7 plots the NR flux and the fluxes for the T-, P-, and E-approximants at 3.5PN order as a function of the GW frequency ϖ computed from $\dot{h}_{22}$. The T-approximant is TaylorT4 [51]. Along the top of this figure (as in several figures below) we indicate the number of gravitational wave cycles up to merger, where we define "merger" as the maximum of $|\Psi_4^{22}|$. Figure 4.8 zooms over the first 15 GW cycles. We notice that during the first 15 GW cycles the numerical data are fit best by the P- and E-approximants at 3PN and 3.5PN order. At these low frequencies the NR flux is best matched by the Keplerian and non-Keplerian EOB models and the Padé model.

To more clearly show the behavior of the PN approximants, we plot in Fig. 4.9 the energy flux normalized by the Newtonian flux. The normalized flux is computed as

$$\frac{F(\varpi)}{F_{\rm Newt}(\varpi)} \equiv \frac{F(\varpi)}{\frac{32}{5}\nu^2\left(\frac{M\varpi}{2}\right)^{10/3}}\,, \tag{4.72}$$

where for the same reason mentioned above, the Newtonian flux is expressed in terms of the GW frequency. Notice that the P-approximants and some of the E-approximants use the same Padé flux, but they start differing at $M\varpi \sim 0.12$ due to their different GW frequencies (obtained from an adiabatic and non-

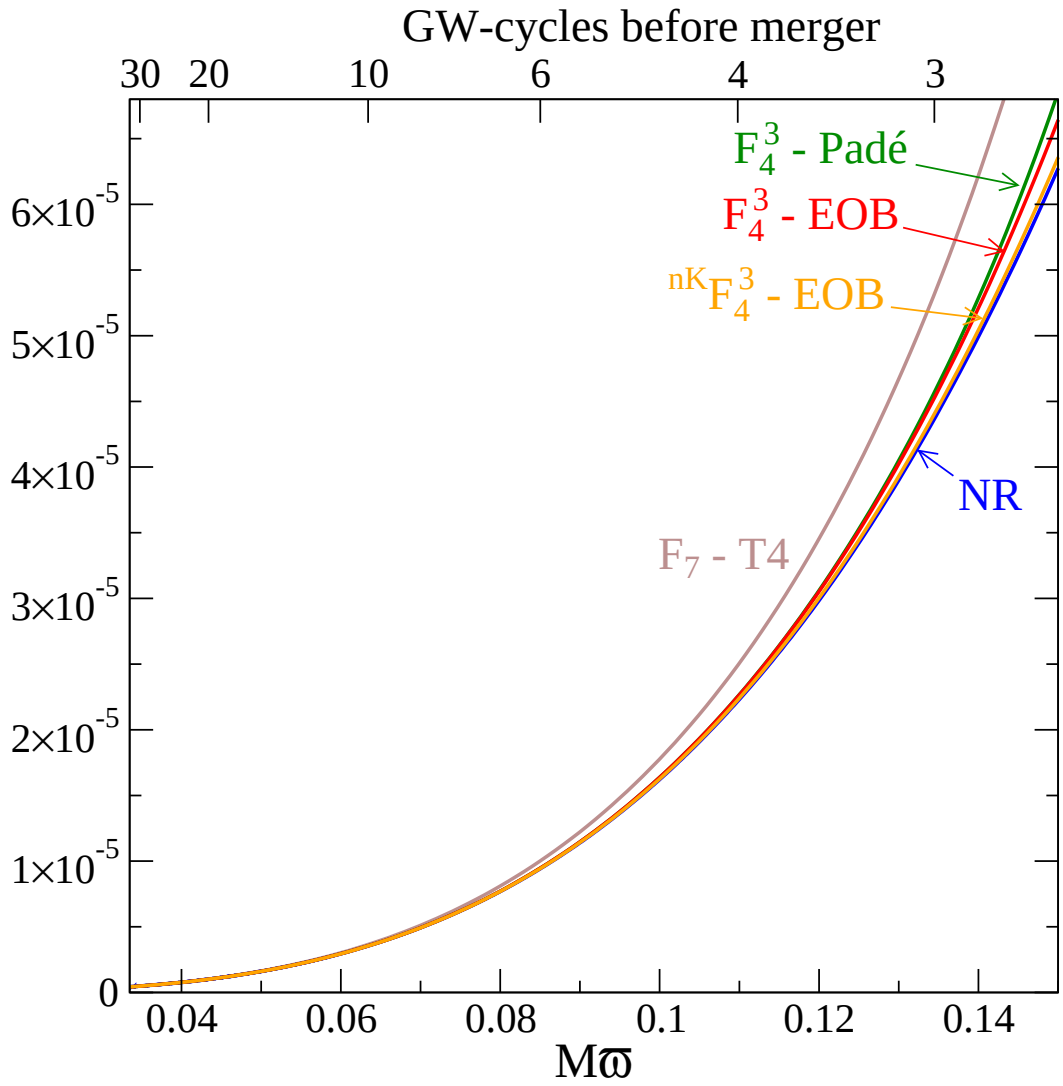

Figure 4.7: Comparison between the numerical energy flux and several PN approximants at 3.5PN order versus GW frequency ϖ extracted from $\dot{h}_{22}$ in the equal-mass case.

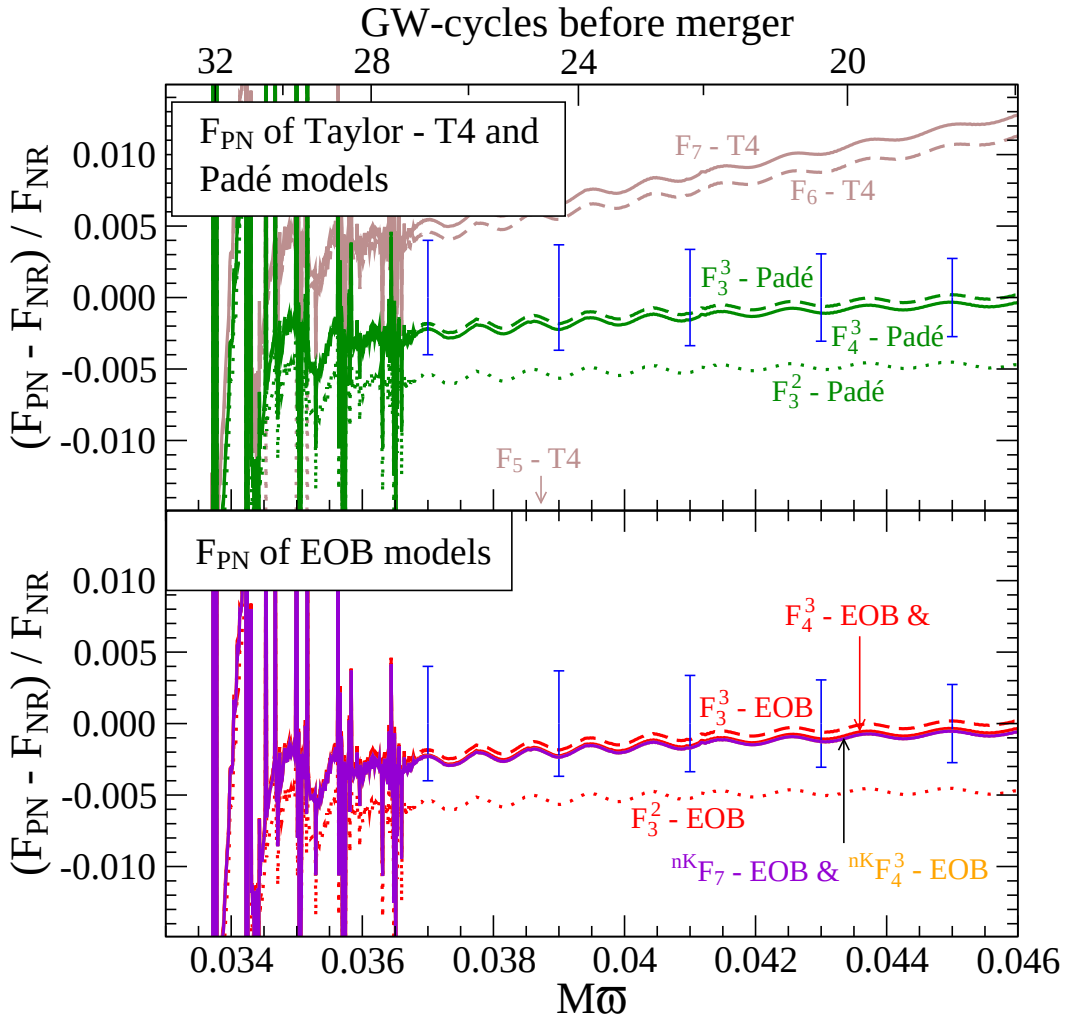

Figure 4.8: Comparison between the numerical energy flux and several PN approximants versus GW frequency ϖ extracted from h_{22} in the equal-mass case. We show the relative difference between numerical flux and PN flux, as well as the estimated error of the numerical flux (blue bars, see Fig. 4.2). Solid lines represent 3.5PN models and NR; dashed and dotted lines correspond to 3PN and 2.5PN models, respectively. For notation see Table 4.1 and caption therein.

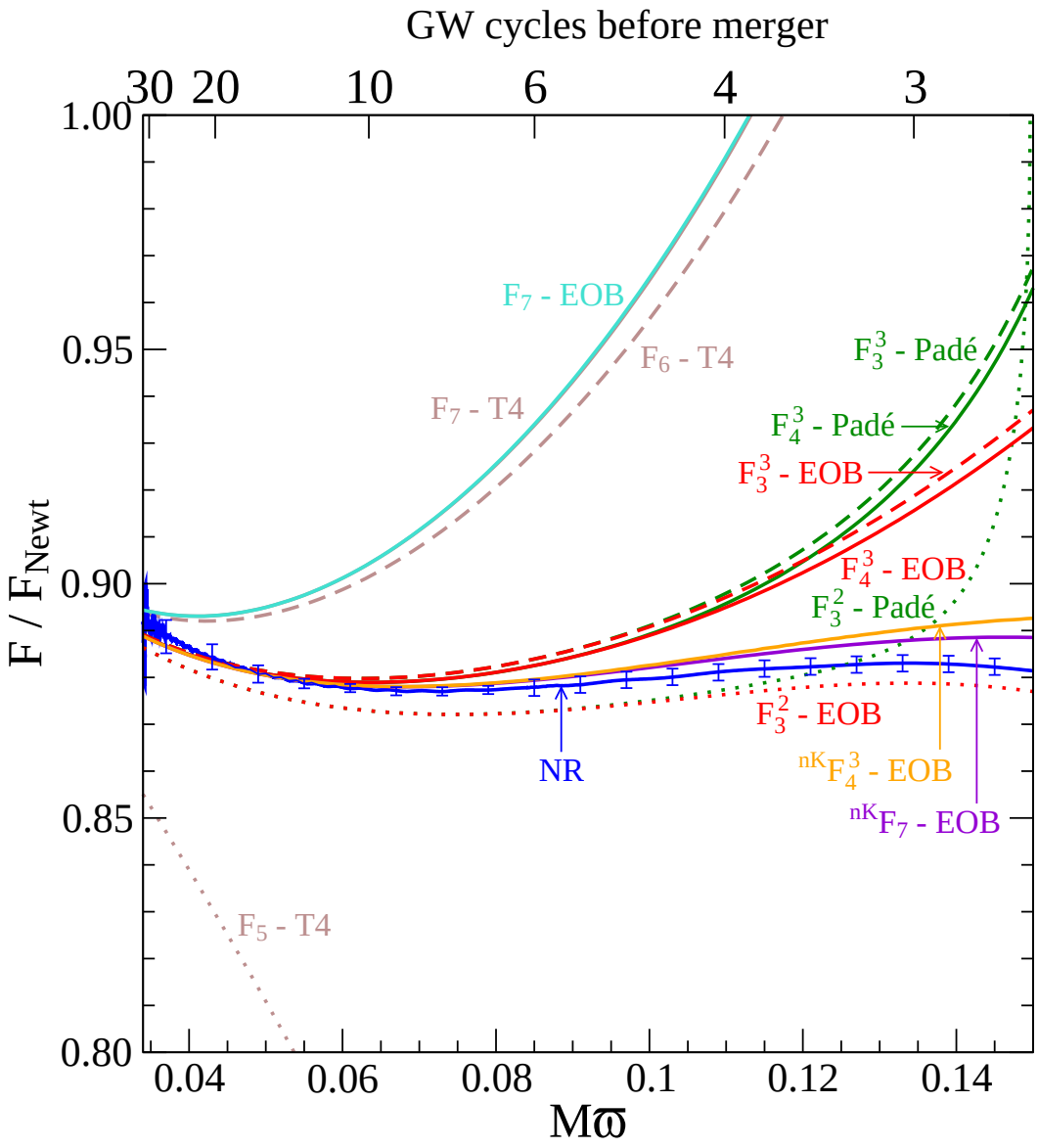

Figure 4.9: Comparison of normalized energy flux $F/F_{\rm Newt}$ [see Eq. (4.72)] for the equal-mass case. Solid lines represent 3.5PN models and NR; dashed and dotted lines correspond to 3PN and 2.5PN models, respectively. For notation see Table 4.1 and caption therein.

Table 4.2: Normalized energy flux $F/F_{\rm Newt}$ for the T- and P-approximants at subsequent PN orders for select velocities v_Ω. $v_\Omega = 0.25$ corresponds to the start of the numerical simulation. The P-approximant flux is given by Eq. (4.39). Note that the P-approximant has an extraneous pole at 1PN order at $v_\Omega = 0.326$. We use $v_{\rm lso} = v_{\rm lso}^{\rm 2PN} = 0.4456$ and $v_{\rm pole} = v_{\rm pole}^{\rm 2PN} = 0.6907$. We use boldface to indicate the range of significant figures that do not change with increasing PN order.

PN order	$v_\Omega = 0.1$, $2M\Omega = 0.002$		$v_\Omega = 0.25$, $2M\Omega = 0.031$		$v_\Omega = 0.3$, $2M\Omega = 0.054$		$v_\Omega = 0.35$, $2M\Omega = 0.086$		$v_\Omega = 0.4$, $2M\Omega = 0.128$	
(n+m)/2	$\frac{F_{n+m}}{F_{\rm Newt}}$	$\frac{F_n^m}{F_{\rm Newt}}$	$\frac{F_{n+m}}{F_{\rm Newt}}$	$\frac{F_n^m}{F_{\rm Newt}}$	$\frac{F_{n+m}}{F_{\rm Newt}}$	$\frac{F_n^m}{F_{\rm Newt}}$	$\frac{F_{n+m}}{F_{\rm Newt}}$	$\frac{F_n^m}{F_{\rm Newt}}$	$\frac{F_{n+m}}{F_{\rm Newt}}$	$\frac{F_n^m}{F_{\rm Newt}}$
0.0	1.0000000	1.1692906	1.0000	1.5673	1.000	1.7678	1.000	2.027	1.000	2.376
0.5	1.0000000	1.0214102	1.0000	1.1507	1.000	1.2325	1.000	1.345	1.000	1.505
1.0	**0.9**555952	**0.9**251084	**0.**7225	-0.8648	0.939	-7.8434	0.456	16.01	1.091	8.443
1.5	**0.96**81616	**0.96**86094	**0.**9188	**0.**9074	0.940	0.9069	0.995	0.924	1.094	0.967
2.0	**0.96**81512	**0.967**6191	**0.**9184	**0.8**850	0.939	**0.8**671	0.993	**0.8**60	1.091	0.867
2.5	**0.967**5775	**0.967**6981	**0.8**624	**0.8**890	0.799	**0.8**754	0.692	**0.87**5	0.504	0.893
3.0	**0.9677**265	**0.9677**247	**0.895**1	**0.891**4	**0.89**5	**0.8**804	**0.9**28	**0.883**	**1.0**22	**0.90**3
3.5	**0.9677**274	**0.9677**233	**0.895**7	**0.891**2	**0.89**7	**0.8**798	**0.9**34	**0.882**	**1.0**36	**0.90**0

adiabatic evolution, respectively). The E-approximants with Keplerian and non-Keplerian flux increase less abruptly at high frequency than the P- and T-approximants. This is a consequence of non-adiabatic effects captured by the EOB model. Quite remarkably, the E-approximants with non-Keplerian fluxes are rather close to the NR result for the entire range of frequency spanned by the simulation.[9] We observe that somewhat accidentally the PN-approximants at 2.5PN order are also close to the numerical flux.

The normalized NR flux starts to decrease at $M\varpi \sim 0.13$. We notice that this behavior is rather different from the behavior of the normalized flux in the test-mass limit (see Fig. A.1 in the Appendix). The E-approximants with non-Keplerian Padé or Taylor flux show a similar decreasing behavior at high frequency.

Both Figs. 4.8 and 4.9 show that in the equal-mass case P-approximants fit the numerical results better than T-approximants. In numerical analysis, however, Padé summation is often used as a technique to accelerate the convergence of a slowly-converging Taylor series (e.g., see Tables 8.9 and 8.12 in Ref. [23]); hence it is natural to ask in the PN case whether Padé summation indeed accelerates the convergence of the series. In Table 4.2 we list the T- and P-approximants of $F/F_{\rm Newt}$ computed at subsequent PN orders and for several values of v_Ω [from left to right $v_\Omega = 0.1, 0.25$ (i.e., beginning of the numerical simulation), $0.3, 0.35$, and 0.4.] In Fig. 4.10 we perform a Cauchy convergence test and compute the difference between T- and P-approximants at subsequent PN orders. The figures do not suggest an acceleration of the convergence. We notice that in the

[9] We notice that whereas the Keplerian Padé-based (or Taylor-based) approximants to the flux differ from each other only when expressed in terms of the GW frequency, the non-Keplerian Padé-based (or Taylor-based) approximants to the flux differs from the others because their functional dependence on the frequency is different (e.g., compare Eq. (4.64) with Eq. (4.63)).

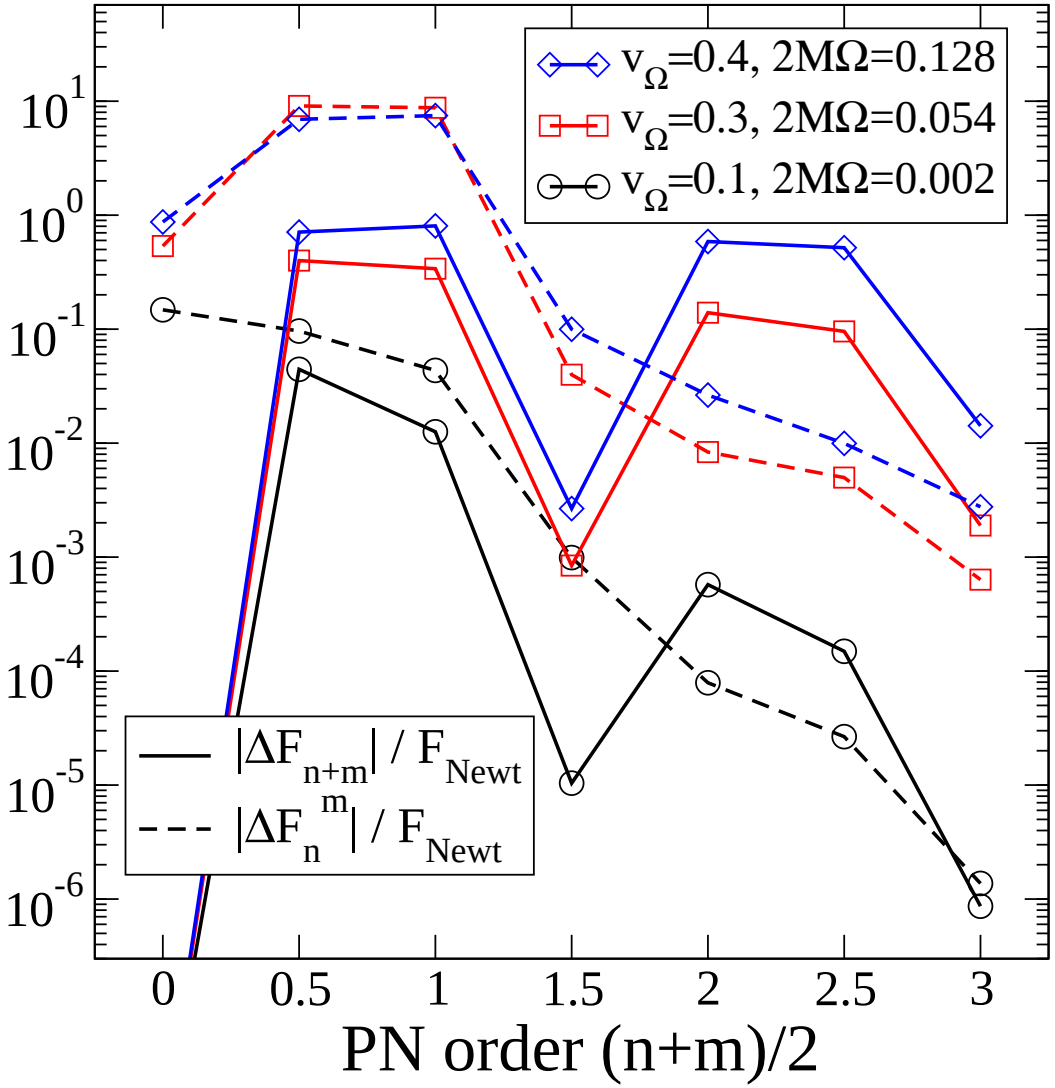

Figure 4.10: Cauchy convergence test of $F/F_{\rm Newt}$ for T- and P-approximants. We plot $\Delta F_{n+m} \equiv F_{n+m+1} - F_{n+m}$, and $\Delta F_n^m \equiv F_{n+1}^m - F_n^m$ for different values of v_Ω. The T- and P-approximants are given by Eqs. (4.19) and (4.39), respectively. Note that the P-approximant has an extraneous pole at 1PN order at $v_\Omega = 0.326$. We use $v_{\rm lso} = v_{\rm lso}^{\rm 2PN}$, and $v_{\rm pole} = v_{\rm pole}^{\rm 2PN}$.

equal-mass case P-approximants are converging more systematically than T-approximants. However, this fact seems to depend on the mass ratio, as can be seen by comparing Fig. 4.10 with Table A.1 and Fig. A.3 in the Appendix which are obtained in the test-mass limit.

4.4.2 On the fitting of the numerical relativity energy flux

In view of building accurate analytical templates that can interpolate the NR waveforms during inspiral, merger and ringdown, we explore here the possibility of improving the PN-approximants to the energy flux by introducing *phenomenological* higher-order PN coefficients and/or by varying the value of $v_{\rm pole}$. This study should be considered a first exploration of the problem, demonstrating only the *flexibility* of the PN models. None of the *quantities* derived here should be used as the basis for further work.

We will minimize the difference between the PN flux and the numerical flux by varying particular coefficients in the PN model. Ideally, the PN and numerical fluxes should be expressed as functions of ϖ before taking this difference, so that the fluxes are compared in a physically meaningful way. Unfortunately, the calculation of ϖ for the PN models is time-consuming, because for each trial value of the phenomenological coefficient it is necessary to compute a full waveform to determine the mapping between ϖ and Ω. So instead, in this section we simply compare PN and numerical fluxes as functions of Ω, where we define the numerical orbital frequency as $\Omega \equiv \varpi/2$. In Fig. 4.6, we can see that the error introduced by the discrepancy between Ω and $\varpi/2$ will be significant. As we will show in Sec. 4.6.2, the waveforms produced using these "tuned" flux

functions will improve agreement with the numerical waveform at a significant level. Nevertheless, the values derived in this section may not be optimal. Thus, we emphasize that the results of this section constitute merely an exercise demonstrating the feasibility of adjusting the PN parameters to optimize the agreement of the PN flux function with numerical data.

The least-squares fits are done on $F(\varpi)/F_{\rm Newt}(\varpi)$ [see Eq. (4.72)]. In the case of T-approximants, we fit for the unknown 4PN-order coefficient in Eq. (4.19) for the equal-mass case. We perform a least-squares fit of the 4PN-order function $\mathcal{F}_8(\nu = 1/4) = A_8 + B_8 \log v_\Omega$ over the orbital-frequency range $M\Omega = 0.02$–0.08 which starts after the first 9 GW cycles. We obtain $A_8 = -141\,, B_8 = 102$. We notice that when we perform the fit over the first 15 (or 20) GW cycles, spanning the frequency region $M\Omega = 0.0168$–0.0235 ($M\Omega = 0.0168$–0.0283), the agreement becomes worse. The resulting flux is shown in Fig. 4.11. The relative difference with the numerical flux is at most $\sim 0.8\%$.

We repeat this analysis in the case of P-approximants. Because the latter also depend upon $v_{\rm pole}$, we perform two least-squares fits. In the first fit, we fix $v_{\rm pole}$ to the value given by Eq. (4.41) and apply the least-squares fit to $\mathcal{F}_8(\nu = 1/4)$ obtaining $A_8 = -1382\,, B_8 = 197$.

In the second fit, we vary $v_{\rm pole}$. When varying $v_{\rm pole}$ in the P-approximant at 3.5PN order, extraneous poles appear at low values of v_Ω. Therefore, in order to push these poles to very high frequency, we follow the suggestion of Ref. [113], and use P-approximants at 4PN order, where the 4PN coefficient is set to its known value in the test-mass limit. Furthermore the logarithm in the flux is not factored out, but treated as a constant when Padé summation is done. This cure may fail for different mass ratios if new extraneous poles ap-

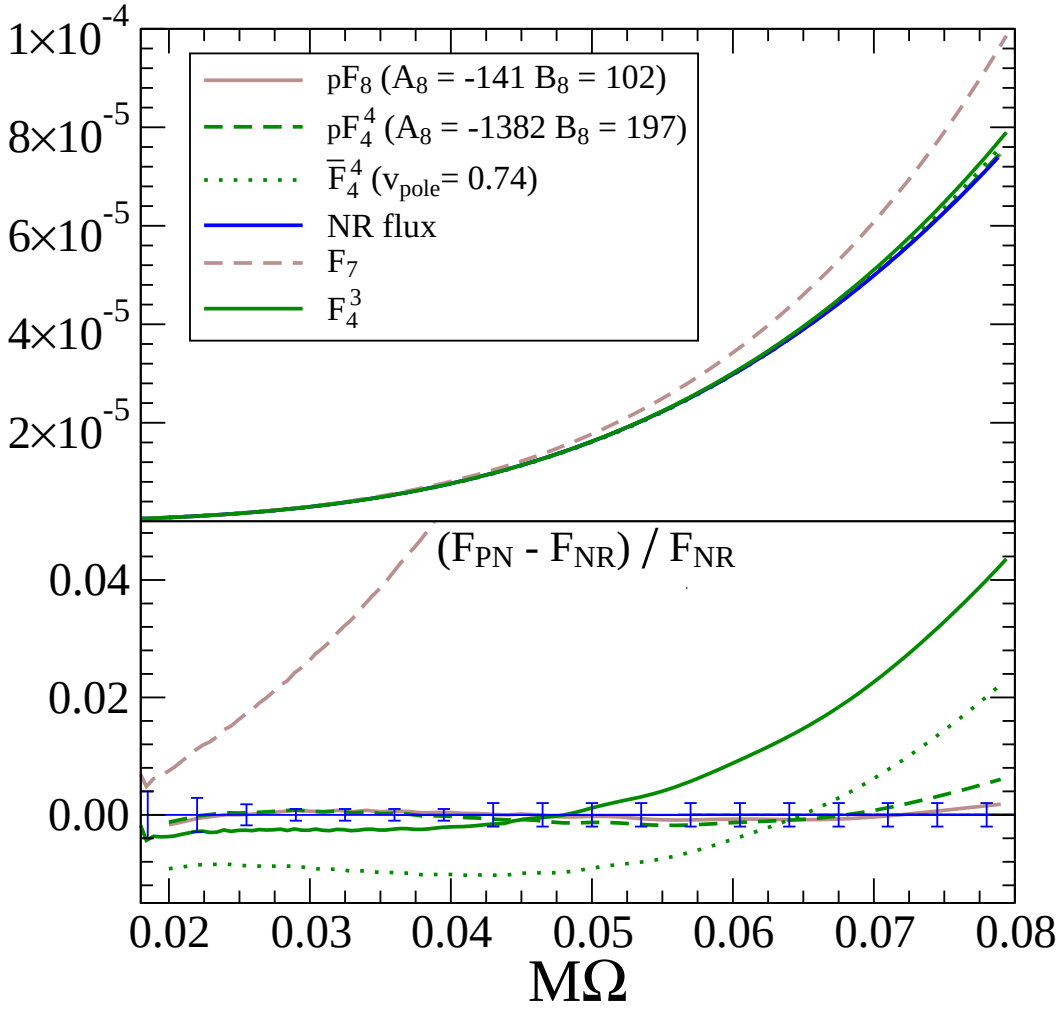

Figure 4.11: Fitting several PN-approximants to the numerical flux. The *x*-axis denote the orbital frequency Ω. Because the numerical flux is computed as function of the GW frequency, we use for the numerical flux $\Omega \equiv \varpi/2$. The blue bars indicate estimated errors on the numerical flux, see Fig. 4.2. For notation see Table 4.1 and caption therein.

pear at low frequency. The least-squares fit gives $v_{\rm pole} = 0.74$. All the results for the P-approximants are displayed in Fig. 4.11, where we also show the T- and P-approximants at 3.5PN order without any fit.

Figure 4.11 might suggest that by introducing higher-order PN coefficients in the flux, the numerical flux can be fit better by T-approximants than by P-approximants. However, this result can depend on the use of orbital frequency instead of GW frequency. In Sec. 4.6.3 (see Fig. 4.18) we employ the fit values obtained in this study and show phase differences between NR and tuned EOB models.

Finally, we attempted to extract PN coefficients higher than 3.5PN order from the numerical flux, as was done at 2PN, 2.5PN and 3PN order in Ref. [88] in the test-mass limit. Unfortunately, the differences between numerical flux and T-approximants are so large —even at the beginning of the numerical waveform—that we were not able to extract even known PN coefficients, like the ones at 3PN and 3.5PN order. Thus, to fit unknown PN coefficients would require a numerical simulation with more cycles starting at lower frequency.

4.5 Estimation of the (derivative of the) center-of-mass energy

In the previous section, we analyzed and compared PN and numerical energy fluxes. The energy of the binary is the second fundamental ingredient in the construction of adiabatic PN-approximants. Unfortunately, there is no way to extract the energy for the numerical simulation as a function of a gauge-invariant quantity such as the GW frequency, so that it is impossible to compare PN and NR energies directly. The frequency derivative, $\dot{\varpi}$, however, is easily accessible

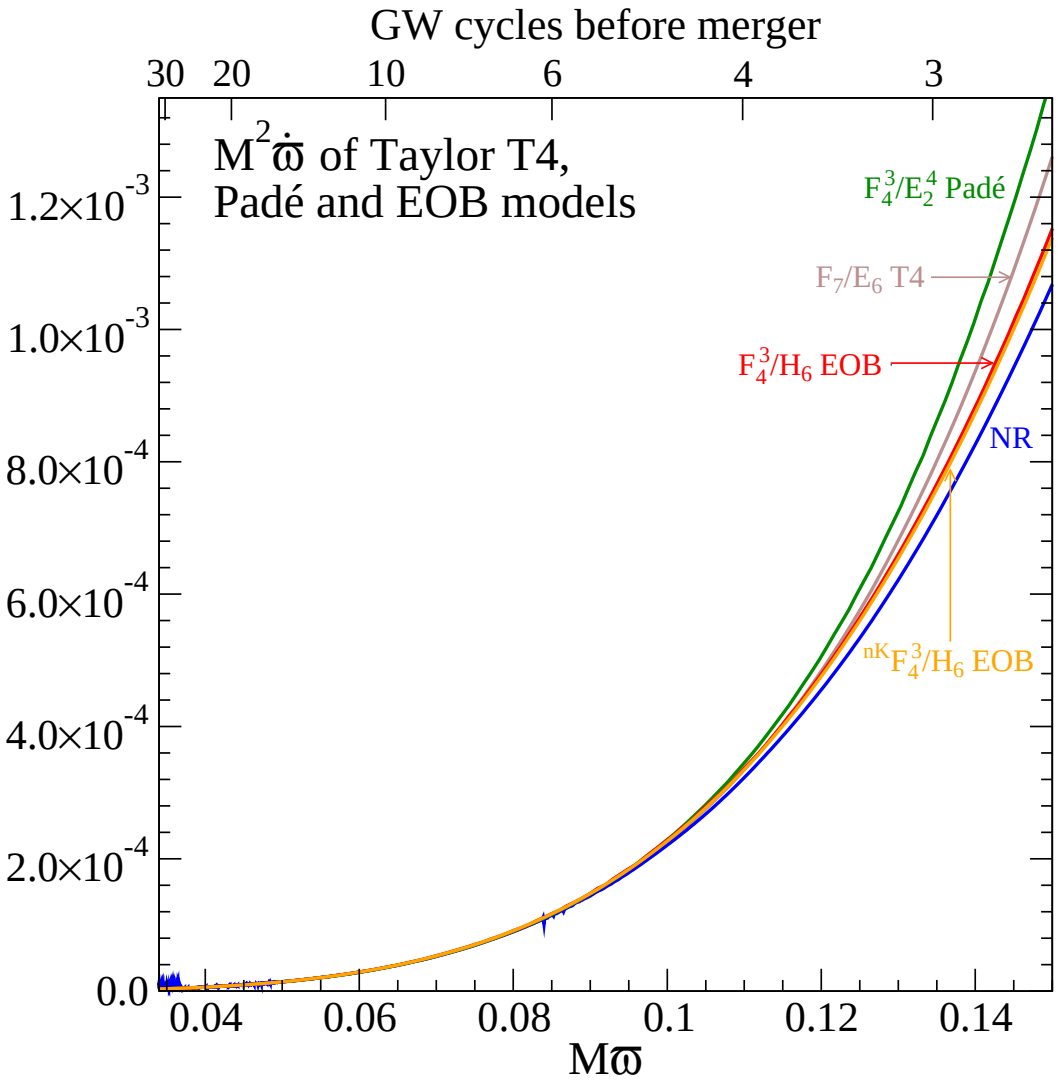

Figure 4.12: GW frequency derivative $\dot{\varpi}$ for the numerical relativity simulation and various PN approximants at 3.5PN order. For notation see Table 4.1 and caption therein.

in the numerical data, and, in the adiabatic approximation is intimately related to the energy, as can be seen by rewriting the energy balance, Eq. (4.12), in the form

$$\frac{d\varpi}{dt} = -\frac{F}{dE/d\varpi}. \tag{4.73}$$

Therefore, we begin this section with a comparison between numerical $\dot{\varpi}$ and the predictions of various PN-approximants. For the PN-approximants, we compute h_{22} as usual (i.e., using energy balance to compute the orbital frequency derivative $\dot{\Omega}$), and take a time derivative to obtain $\dot{h}_{22}$ and extract $\dot{\varpi}$ from it. The waveform h_{22} for the E-approximants is computed using Eqs. (4.42), (4.43), (4.44) and (4.45) in Sec. 4.3.3. Figure 4.12 plots the numerical $\dot{\varpi}$ and its value for T-, P- and also E-approximants at 3.5PN order.

In order to emphasize differences between the different $\dot{\varpi}$, we normalize the data in Fig. 4.12 by the Newtonian value of $\dot{\varpi}$,

$$\frac{\dot{\varpi}}{\dot{\varpi}_{\rm Newt}} \equiv \frac{\dot{\varpi}}{\frac{192}{5}\frac{\nu}{M^2}\left(\frac{M\varpi}{2}\right)^{11/3}}\,. \tag{4.74}$$

The normalization is used only to eliminate the leading-order behavior of the various curves in Fig. 4.12; therefore, to compute the denominator of Eq. (4.74) we have simply substituted $\varpi/2$ rather than Ω into the Newtonian formula for the frequency derivative.

The normalized frequency derivatives are shown in Fig. 4.13. At low frequencies, $\dot{\varpi}$ is very challenging to compute in numerical simulations, resulting in comparatively large numerical uncertainties. Therefore, for frequencies $M\varpi \lesssim 0.045$ we can merely conclude that PN and NR are consistent with each other (i.e., are within the numerical error bars of about 10 per cent).

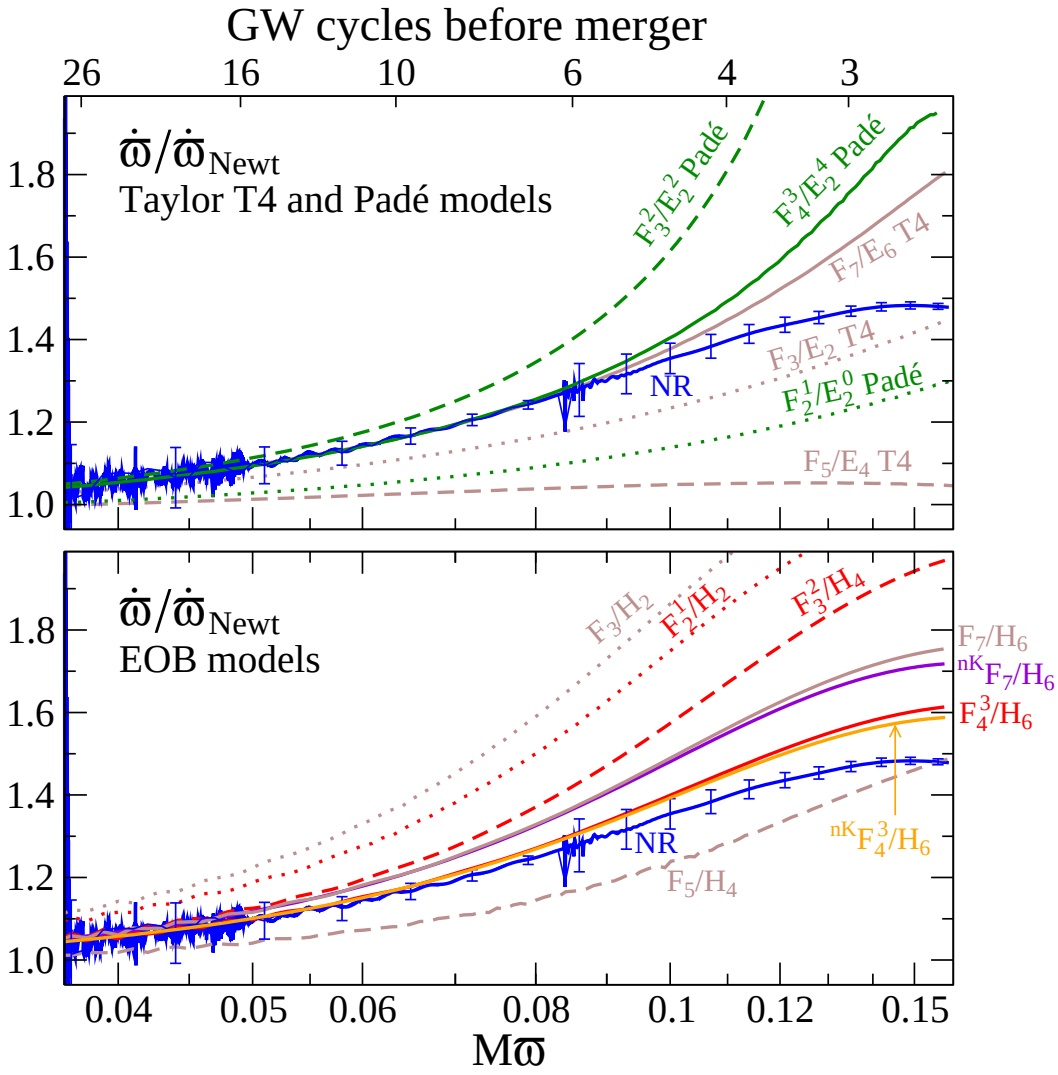

Figure 4.13: Comparison of $\dot{\varpi}$ for the numerical results and various PN approximants. Dotted, dashed and solid lines correspond to 1.5PN, 2.5PN and 3.5PN models, respectively. For notation see Table 4.1 and caption therein.

The 3.5PN Taylor T4 model (labeled F_7/E_6T4) agrees very well with the numerical simulation up to $M\varpi \approx 0.1$; this observation is consistent with the excellent agreement between TaylorT4 (3.5PN) and the numerical simulation observed in Boyle et al. [51], who compared up to this frequency. Beyond $m\varpi = 0.1$, however, $\dot{\varpi}/\dot{\varpi}_{\rm Newt}$ for Taylor T4 continues to increase (as for all other Taylor and Padé models considered here), whereas for the numerical simulation, $\dot{\varpi}/\dot{\varpi}_{\rm Newt}$ flattens (this behavior was also observed in Ref. [113].) Only the E-approximants at 3.5PN order reproduce the flattening of $\dot{\varpi}/\dot{\varpi}_{\rm Newt}$ at high frequencies, with the closest being the one which uses the non-Keplerian Padé flux (${}^{\rm nK}F_4^3$). Because the frequency derivative is the relevant quantity that determines the phase evolution, the turning over of $\dot{\varpi}/\dot{\varpi}_{\rm Newt}$ for the non-adiabatic models in Fig. 4.13 suggests that, at high frequency, non-adiabatic analytical models might be superior to adiabatic models.

If sufficient smoothing is applied to the numerical $\dot{\varpi}$ it becomes a smooth curve even at low frequencies. Figure 4.14 presents a comparison between such a heavily smoothed numerical curve and the PN-approximants. As already pointed out, all PN approximants are consistent to within our estimated numerical errors at low frequencies. However, the NR result in Fig. 4.14 is notably closer to the 3.5PN approximants than to lower order PN approximants. This good agreement provides a further validation of the numerical code used in Boyle et al. [51]. It also indicates that our error analysis in Sec. 4.2 may be overly conservative.

Our comparisons of $\dot{\varpi}$ reveal a lot of information about the PN approximants. However, $\dot{\varpi}$ depends on both flux and energy (see Eq. (4.73)), and so these comparisons do not yield information about flux or energy separately. To

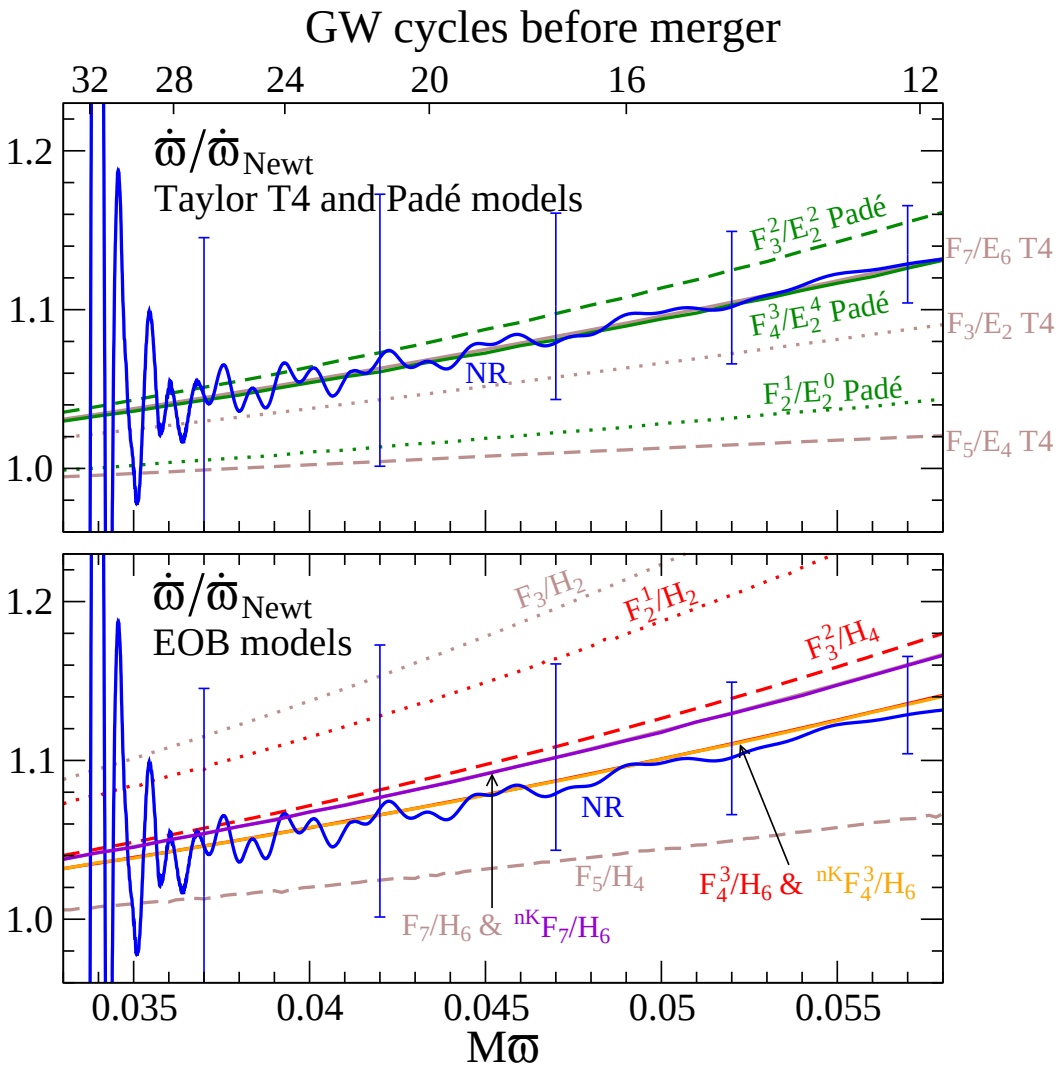

Figure 4.14: Comparison of PN $\dot{\omega}$ with a heavily smoothed version of the numerical $\dot{\omega}$. Solid lines represent 3.5PN models and NR; dashed and dotted lines correspond to 3PN and 2.5PN models, respectively. For notation see Table 4.1 and caption therein.

isolate effects due to the PN energy, we rearrange Eq. (4.73) further, such that it yields in the adiabatic approximation the derivative of the center-of-mass energy for the numerical simulation:

$$\left[\frac{dE}{d\varpi}\right]_{\rm NR} = -\frac{F_{\rm NR}}{[d\varpi/dt]_{\rm NR}}\,. \tag{4.75}$$

The relative error in $[dE/d\varpi]_{\rm NR}$ is obtained as the root-square-sum of the relative errors of flux and frequency derivative (see Figs. 4.2 and 4.4). In Fig. 4.15 we compare the latter with T-, P- and E-approximants. For adiabatic T4 and Padé models, we compute $dE/d\varpi$ by taking derivatives of $E(\Omega)$ in Eq. (4.14) with respect to Ω and then expressing the derivative in terms of $\varpi(\Omega)$. For non-adiabatic EOB models, we compute $dE/d\varpi$ from the ratio of $F_{\rm PN}$ and $[d\varpi/dt]_{\rm PN}$ as obtained from Figs. 4.7 and 4.12. The closeness between the numerical result and adiabatic PN-approximants is expected only in the range of frequencies over which the balance equation and the adiabatic approximation are valid. The upper panel of Fig. 4.15 shows the Taylor and Padé adiabatic models. The plot suggests that around $M\varpi \sim 0.08$ non-adiabatic effects are no longer negligible. At lower frequencies, both 3.5PN order adiabatic approximants (Padé and Taylor T4) match the numerical result very well. Taylor T4 at 2.5PN matches well, too, although its frequency derivative $\dot{\varpi}$ and flux differ significantly from NR (see Figs. 4.13 and 4.9). The T-approximant at 3.5PN order is closest to the numerical result. The lower panel of Fig. 4.15 shows the non-adiabatic E-approximants. We notice that the non-adiabatic models, especially at 3.5PN order, follow quite nicely the behavior of the numerical derivative of the center of mass energy. The E-approximant with non-Keplerian flux is closest to the numerical result. This analysis emphasizes again the relevance of including non-adiabatic effects in the analytical model [66].

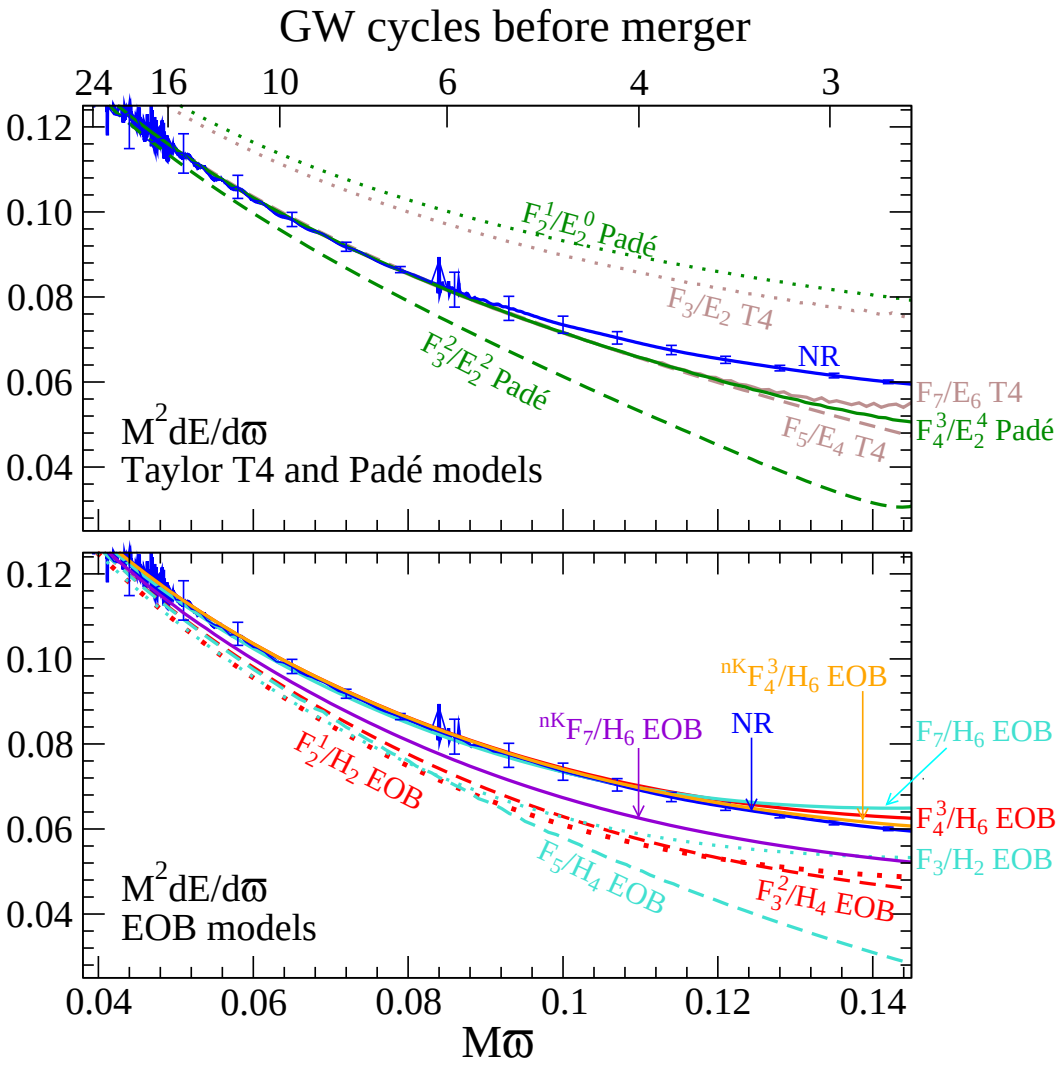

Figure 4.15: We compare $dE/d\varpi$ versus GW frequency ϖ for numerical relativity [see Eq. (4.75)] and PN approximants. Solid lines represent 3.5PN models and NR; dashed and dotted lines correspond to 3PN and 2.5PN models, respectively. For notation see Table 4.1 and caption therein.

4.6 Comparing waveforms

Here we compare the numerical waveform to various PN waveforms, basically extending the analysis of Boyle et al. [51] to include Padé and EOB waveforms. Because the $(2,2)$ mode dominates the waveform for an equal-mass nonspinning binary, we restrict the comparison to only this mode. As in [51], we use Ψ_4^{22} and the GW phase and frequency ω defined by Eq. (4.4) when comparing waveforms.

For the comparisons presented in this section, the uncertainty in the phase of the numerical waveform is roughly 0.02 radians. This number includes numerical errors (e.g. due to convergence and extrapolation of the waveform to infinite extraction radius), as well as modelling errors due to slightly nonzero eccentricity and spin of the numerical simulation; see Ref. [51] Sec. V. for details. We note that the modelling errors have decreased since the analysis in Ref. [51] because the new matching procedure reduces the impact of eccentricity, and because the more sophisticated spin-diagnostics presented in Ref. [181]) resulted in a smaller bound on the residual spin.

4.6.1 Matching procedure

Each PN waveform has an arbitrary time offset, t_0, and phase offset, ϕ_0 with respect to the NR waveform. The procedure used by Boyle et al. [51]—as well as in various other papers before it, such as [17, 141]—sets these constants by ensuring that the GW phase and frequency match at a fiducial time. Unfortunately, when matching at low frequency this method is sensitive to noise and to

residual eccentricity in the numerical waveform, and does not easily translate into a robust and automatic algorithm. Since we want to match as early as possible (where we expect the PN approximants to be valid), we propose to use, instead, a matching procedure which achieves the same goal, but extends over a range of data. This procedure is similar to the one proposed by Ajith et al. [4], but whereas we match only the GW phase, Ajith et al. match the entire gravitational waveform—including the amplitude—and include an overall amplitude scaling. This method can be easily implemented as a fairly automatic algorithm, robust against noise and residual eccentricity.

Using the phase of the numerical and PN waveforms, we define the quantity

$$\Xi(\Delta t, \Delta\phi) = \int_{t_1}^{t_2} \left[\phi_{\rm NR}(t) - \phi_{\rm PN}(t - \Delta t) - \Delta\phi\right]^2 \, dt \,. \tag{4.76}$$

Here, t_1 and t_2 represent the chosen range over which to compare. Minimizing this quantity by varying the time and phase offsets Δt and $\Delta\phi$ produces the optimal values for these quantities in a least-squares sense. Then to compare PN and NR waveforms, we compare the (unchanged) NR waveform with an offset PN waveform defined by

$$\Psi_{4,\rm PN}(t) = A_{\rm PN}(t + \Delta t)\, e^{-i\left[\phi_{\rm PN}(t+\Delta t)+\Delta\phi\right]} \,. \tag{4.77}$$

With reasonable first guesses for Δt and $\Delta\phi$, the function Ξ is quite nicely paraboloidal. Thus, even simple minimization routines work well. However, in cases where speed is an issue, the problem can be reduced to one dimension. For a given value of Δt, the optimization over $\Delta\phi$ may be done analytically by setting

$$\Delta\phi(\Delta t) = \frac{\int_{t_1}^{t_2} \left[\phi_{\rm NR}(t) - \phi_{\rm PN}(t - \Delta t)\right] \, dt}{t_2 - t_1} \,. \tag{4.78}$$

Using this value of $\Delta\phi$ for a given value of Δt decreases the number of function evaluations needed to find the minimum. This can be very useful for large data sets, or situations where many such matches need to be done.

The choice of t_1 and t_2 involves some degree of judgment. Preferably, t_1 should be as early as possible, while not being contaminated by junk radiation. We choose $t_1 = 1100M$, corresponding to $M\omega = 0.037$. Similarly, t_2 should be as early as possible, but far enough from t_1 so that the integration averages over the noise. In addition, the effects of the small but nonzero orbital eccentricity show up as oscillations in the phase, as can be seen, for example, in the range $t \in [1100, 1900]M$ in Fig. 4.17. We would like t_2 to be large enough so that the integration averages over several cycles of this oscillation, thus resulting in less bias due to eccentricity. Here we use $t_2 = 1900M$, corresponding to $M\omega = 0.042$. We have checked that changing the values of t_1 and t_2 by $\pm 100M$ changes the resulting phases by less than a few thousandths of a radian through the end of the numerical waveform.

This method is quite similar to the one suggested in Ref. [4]. However, here we consider only the phase and not the amplitude of the waveform. Because we restrict the analysis only to the $(2, 2)$ waveform mode of an equal-mass binary and compare only the phase and not the amplitude, we think it is reasonable to have neglected the amplitude in the matching procedure.

4.6.2 Padé waveforms

In Fig. 4.16 we plot the phase difference between the numerical, T- and P-approximants [98, 104, 62] at the times when the numerical waveform reaches

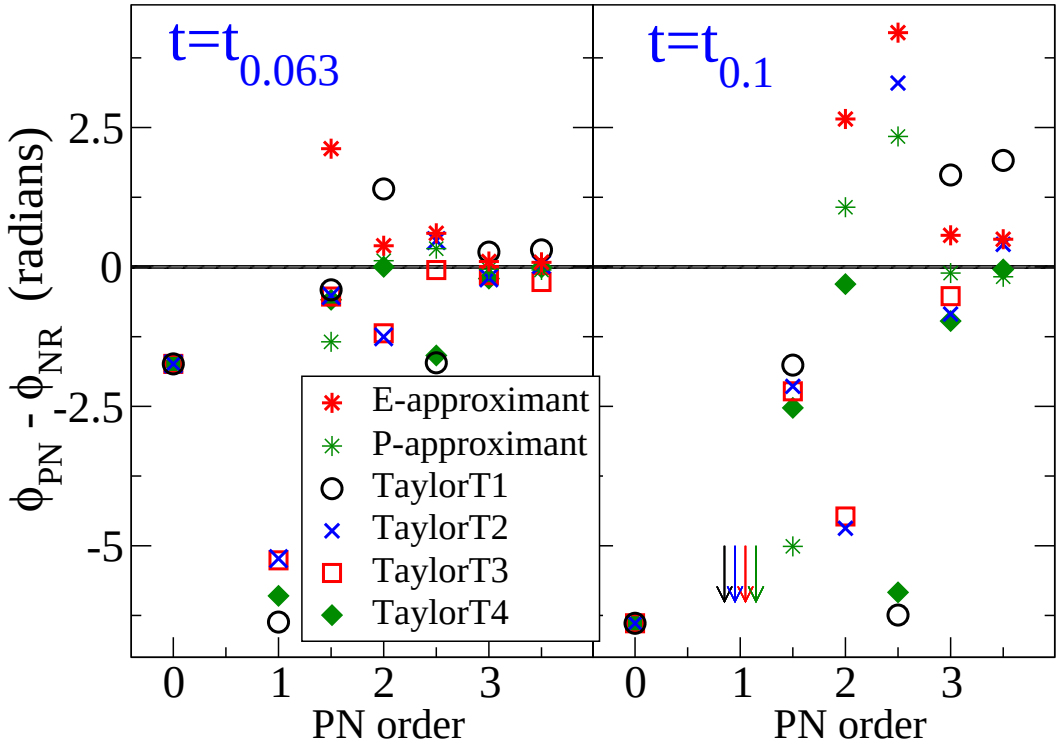

Figure 4.16: Phase differences between the numerical waveform, and untuned, original EOB, untuned Padé, and Taylor waveforms, at two selected times close to merger. The E-approximants are F_n^m/H_p, while the P-approximants are F_n^m/E_p^q (see Table 4.1 and caption therein). Waveforms are matched with the procedure described in Sec. 4.6.1 and phase differences are computed at the time when the numerical simulation reaches $M\omega = 0.063$ (left panel) and $M\omega = 0.1$ (right panel). Differences are plotted versus PN order. Note that at 1PN order the Padé flux has an extraneous pole at $v = 0.326$ causing a very large phase difference. The thick black line indicates the uncertainty of the comparison as discussed in Sec. 4.6, $|\Phi_{\rm PN} - \Phi_{\rm NR}| \leq 0.02$ radians.

GW frequencies $M\omega = 0.063$ and $M\omega = 0.1$. The phase differences are plotted versus the PN order. The phase difference at $M\omega = 0.1$ of the P-approximant at 3.5PN order is -0.12 radians. When comparing with generic Taylor approximants, we notice that the phase differences of the P-approximants are less scattered as the PN order is increased. This might be due to the fact that P-approximants of the energy flux are closer to the NR flux, especially for lower v_Ω where the phase accumulates the most. Figure 4.16 could be contrasted with Tables III and IV of Ref. [98] which show the overlaps between the numerical waveform and P-approximants at subsequent PN orders, in the test-mass limit case. The behavior of the P-approximants in Fig. 4.16 are consistent with the behavior of $\dot{\varpi}$ seen in Fig. 4.13: At 1.5PN, Padé has smaller $\dot{\varpi}$ than the numerical simulation, at 2.5PN, Padé has larger $\dot{\varpi}$. Consequently, $\Phi_{\rm PN} - \Phi_{\rm NR}$ is negative at 1.5PN order and positive at 2.5PN order. For 3.5PN order, the P-approximant in Fig. 4.13 agrees very well with the numerical simulation (at least for $M\varpi \lesssim 0.1$), which translates into excellent agreement in Fig. 4.16.

In Fig. 4.17 we explore the possibility of reducing the phase differences between the numerical waveform and P-approximants: By (i) varying $v_{\rm pole}$ or (ii) introducing the pseudo 4PN order coefficient $\mathcal{F}_8(\nu = 1/4) = A_8 + B_8 \log v_\Omega$ in the energy flux. We tune the coefficients by minimizing the sum of the squares of the phase difference at $t_{0.063}$ and $t_{0.1}$. We find that if $v_{\rm pole} = 0.633$, the P-approximant F_4^4/E_2^4 has a maximum phase difference before $M\omega = 0.1$ smaller than the numerical error in the simulation. A similar result is obtained for the the P-approximant pF_4^4/E_2^4 if we use $v_{\rm pole} = v_{\rm pole}^{\rm 2PN} = 0.6907$, and tune $A_8 = -493$, $B_8 = 330$.

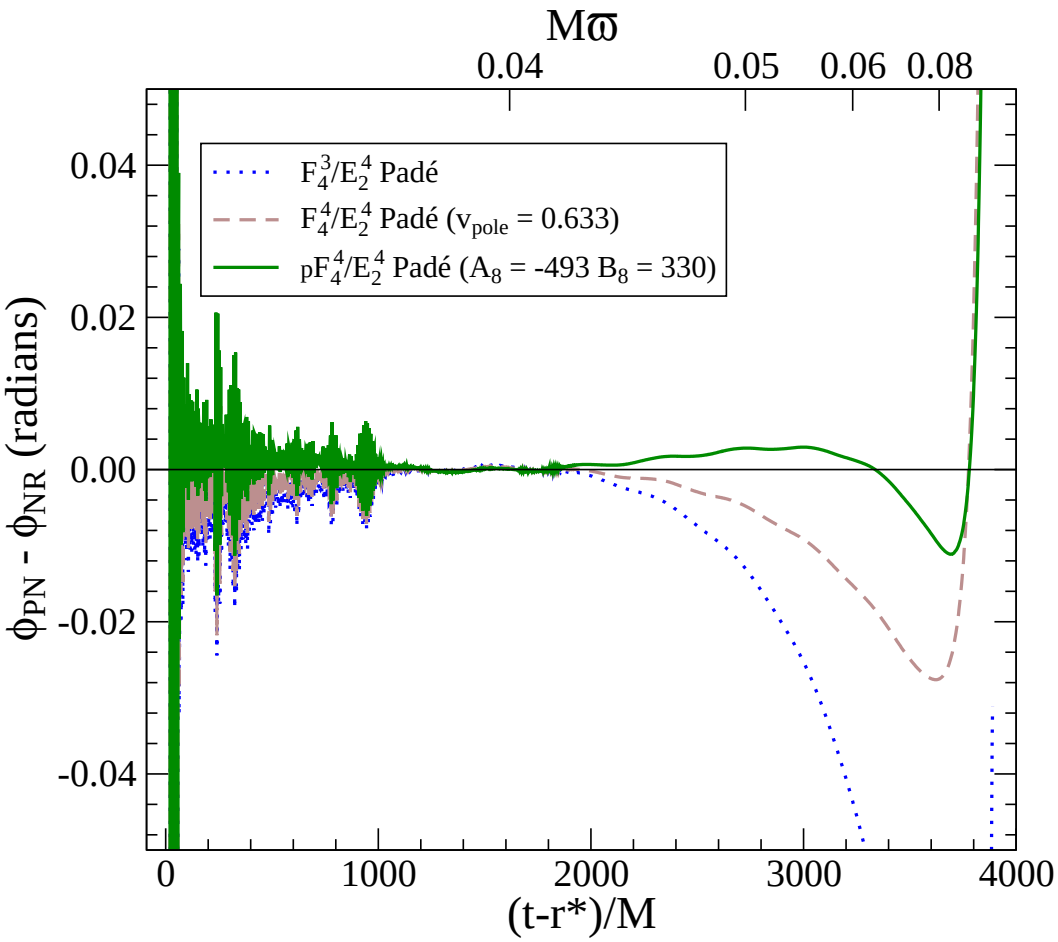

Figure 4.17: Phase differences between untuned and tuned P-approximants and NR. The untuned P-approximant is F_4^3/E_2^4 ($v_{\rm lso} = v_{\rm lso}^{\rm 2PN}$, $v_{\rm pole} = v_{\rm pole}^{\rm 2PN}$). The tuned P-approximants are F_4^4/E_2^4 and tunable $v_{\rm pole}$ ($v_{\rm lso} = v_{\rm lso}^{\rm 2PN}$) and pF_4^4/E_2^4 ($v_{\rm lso} = v_{\rm lso}^{\rm 2PN}$, $v_{\rm pole} = v_{\rm pole}^{\rm 2PN}$) with tunable A_8 and B_8. In all cases, waveforms are matched over $t - r^* \in [1100, 1900]M$.

4.6.3 Effective-one-body waveforms

In Fig. 4.16 we also plot the phase differences between the numerical and the untuned, original E-approximants [65, 66, 104] F_n^m/H_p. At 3.5PN order the phase difference at $M\omega = 0.1$ is 0.50 radians. We also computed the phase differences at $M\omega = 0.1$ of the E-approximants ${}^{\rm nK}F_4^3/H_7$, ${}^{\rm nK}F_7/H_7$ and F_7/H_7 and found 0.45, 2.56 and 2.7 radians, respectively. Thus, for untuned EOB models it is crucial to have introduced the Padé flux. When contrasting the original E-approximants with generic Taylor approximants, we find that the phase differences are less scattered as the PN order is increased. However, despite the fact that the Padé-based EOB flux is closer to the numerical flux (see Figs. 4.8 and 4.9), untuned, original E-approximants accumulate more phase difference than P-approximants. This could be a consequence of the fact that independently of the flux and the energy functions, what seems to matter is the way the equations of motions are solved to get the phasing.

Because of the reduction of the dynamics to *a few* crucial functions determining the inspiral evolution [65, 66, 100], notably A, D and $\mathcal{F}$, and because of the rather simple procedure to match the inspiral(-plunge) waveform to the ringdown waveform, the EOB model turned out to be particularly suitable for matching the full numerical waveforms [64, 67, 113, 92, 111]. In view of a future study which will include merger and ringdown, we start here exploring the possibility of improving the agreement with numerical waveforms by tuning the pseudo 4PN order coefficients a_5, A_8 and B_8 and/or, if present, the pole location $v_{\rm pole}$. In the lower panel of Fig. 4.18, using different $v_{\rm pole}$ values, we show the phase differences computed at $t_{0.063}$ and $t_{0.1}$ as functions of the unknown PN-expansion coefficient a_5 [see Eq. (4.48)]. As first pointed out and discussed

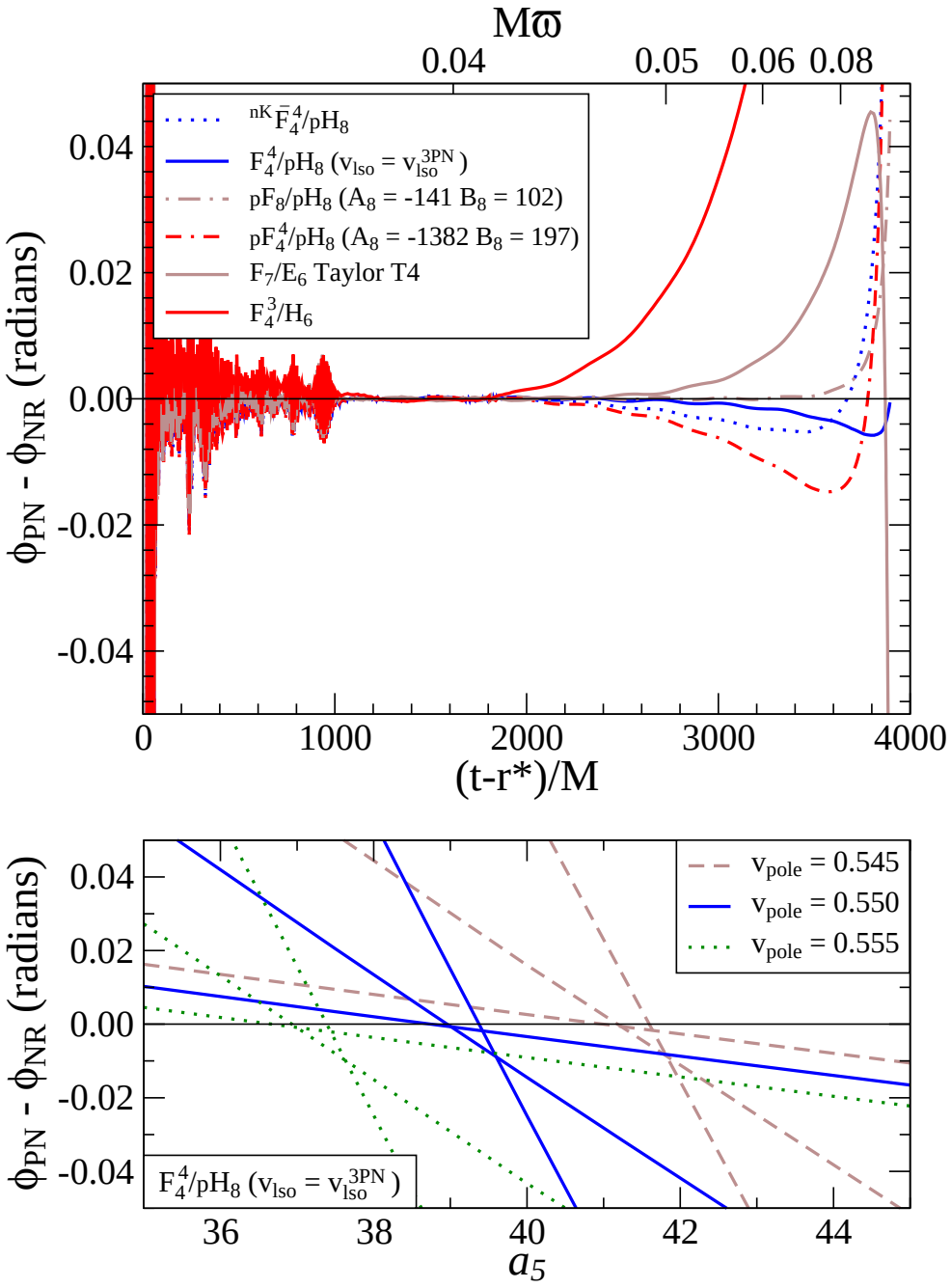

Figure 4.18: The **upper panel** shows phase differences versus time (lower x-axis) and versus GW frequency (upper x-axis) for several tuned and untuned E-approximants. For the tuned models, the optimal a_5 and v_{pole} values displayed in Table 4.3. In the **lower panel** we show phase differences between numerical and E-approximants computed at $t_{0.063}$, $t_{0.1}$, and the end of the numerical simulation $t_{0.16}$, as functions of a_5. For the same color and style, the curve with the steepest slope corresponds to $t_{0.16}$ and the curve with the smallest slope corresponds to $t_{0.063}$ (For notation see Table 4.1 and caption therein).

in Ref. [113] (see e.g., Fig. 3 therein), we find that there is a strong degeneracy between a_5 and $v_{\rm pole}$. In fact, for different $v_{\rm pole}$ values, the curves in Fig. 4.18 are almost identical except for a shift in a_5. Although in this test we use the E-approximant $F_4^4/pH_8(v_{\rm lso} = v_{\rm lso}^{\rm 2PN})$, we find that this degeneracy appears in all E-approximants considered.

To obtain the optimal a_5 and $v_{\rm pole}$ that minimize phase differences during the entire numerical simulation, we first choose an arbitrary $v_{\rm pole}$ in the range of degeneracy. Then, we determine the a_5 value by minimizing the sum of the squares of the phase difference at $t_{0.063}$ and $t_{0.1}$. In the upper panel of Fig. 4.18, we show phase differences in time and GW frequency for several E-approximants using those optimal a_5 and $v_{\rm pole}$ values, which are given in Table 4.3. In Fig. 4.18, we also show phase differences for E-approximants with pseudo 4PN order coefficients determined by the flux fit of Sec. 4.4.2 (see Fig. 4.11) and tunable a_5. The optimal a_5 values are shown in Table 4.3. The smaller phase differences along the entire inspiral are obtained with the E-approximants with Padé flux F_4^4/pH_8 ($v_{\rm lso} = v_{\rm lso}^{\rm 2PN}$) and tunable $v_{\rm pole}, a_5$ and Taylor flux pF_8/pH_8 with tunable A_8, B_8, a_5. We notice that for $t > t_{0.1}$ the phase difference increases more abruptly for the latter model. In the best case, the absolute phase difference during the entire numerical simulation is within the numerical error, i.e., within 0.02 radians. The choice of the best tuned E-approximant [192, 67, 113, 114, 92] will be determined once merger and ringdown are included, and when long and accurate comparisons with numerical simulations are extended to BBH with mass ratio different from one.

Finally, in Ref. [113], Damour and Nagar extracted the data of the numerical simulation used in the present paper from one of the figures of Ref. [51] and

Table 4.3: Optimal a_5 and $v_{\rm pole}$ that minimize phase differences between tuned EOB models and the numerical simulation.

EOB model and fixed parameters		a_5	$v_{\rm pole}$
${}^{\rm nK}\overline{F}_4^4/pH_8$	—	29.78	0.52
F_4^4/pH_8	$v_{\rm lso}=v_{\rm lso}^{\rm 2PN}$	39.35	0.55
pF_8/pH_8	$A_8=-141, B_8=102$	5.32	N/A
pF_4^4/pH_8	$A_8=-1382, B_8=197,$ $v_{\rm lso}=v_{\rm lso}^{\rm 2PN}, v_{\rm pole}=v_{\rm pole}^{\rm 2PN}$	-3.10	N/A

compared those data with the EOB approach. They found for their "non-tuned" EOB model phase differences ±0.05 radians. This phase difference is smaller than the phase differences we discuss in this paper for untuned EOB models (see Fig. 4.16 and discussion around it). However, we notice that ±0.05 radians in Ref. [113] refers to *half* the maximum phase difference accumulated over the entire evolution when matching the numerical and EOB phases at $M\omega = 0.1$. By contrast, in this paper, and in particular in Fig. 4.16, we match numerical and EOB phases in a time interval and compute the phase differences at $M\omega = 0.1$.

Moreover, we observe that their "non-tuned" EOB model is not really untuned, because it uses the Padé summation of the radial potential at 4PN order and *then* sets $a_5 = 0$. This is not equivalent to using the radial potential at 3.5PN order with $a_5 = 0$. In fact, to recover the 3.5PN order Padé radial potential from the 4PN order Padé potential one should use $a_5 = -17.16$. They also use the non-Keplerian flux at 4PN order ${}^{\rm nK}\overline{F}_4^4$ which is different from the 3.5PN order one ${}^{\rm nK}F_4^3$. For our untuned EOB model at 3.5PN order which uses ${}^{\rm nK}F_4^3$ and the EOB dynamics at 3PN order, if we apply Ref. [113] procedure and compute *half* the maximum phase difference when matching the numerical and EOB phases at $M\omega = 0.1$, we find a phase difference of ±0.18 radians

4.7 Conclusions

In this paper, using a highly accurate and long numerical simulation [51] of a non-spinning equal-mass black hole binary, we compute the gravitational waveform, GW energy flux, and GW frequency derivative. Imposing the balance equation, we also estimate the (derivative of) center-of-mass energy. We compare these quantities to those computed using adiabatic TaylorT4 and Padé [98, 104, 62], and non-adiabatic EOB PN approximants [65, 66, 104].

We find that for the first 15 GW cycles, the 3.5PN order T-approximant and the 3.5PN order untuned P- and E-approximants (see Table 4.1) reproduce the numerical results for energy flux, GW frequency derivative and (derivative of) center-of-mass energy quite well (see Figs. 4.8, 4.9, 4.13, 4.14, and 4.15), but with interesting differences.

We attempted to study the convergence of the PN expansion for the energy flux.[10] We find that Padé approximants to the flux introduced in Ref. [98] do not accelerate the convergence of the Taylor series, but are closer to the numerical flux than are the T-approximants. In particular, the Taylor flux at all orders through 3.5 PN is outside the numerical flux error bars even ~ 25 GW cycles before merger (see Fig. 4.8). We find that the non-adiabatic non-Keplerian E-approximants to the flux at 3.5PN order are within $\sim 2\%$ of the numerical flux over the entire frequency range we consider (see Fig. 4.9).

Quite interestingly, in the equal-mass case the numerical normalized energy flux $F/F_{\rm Newt}$ starts decreasing at high frequency during the late part of

[10] We also tried to apply the criterion suggested in Ref. [235] to assess the region of validity of the PN series for the flux in the equal-mass case. Unfortunately, the numerical simulation starts at too high a frequency, when the Taylor series at 3.5PN order seems to already be outside the region of validity.

the inspiral and blurred plunge (see Fig. 4.9). This differs from the behavior of $F/F_{\rm Newt}$ in the test-mass limit (see Fig. A.1). Both the Taylor and Padé-based E-approximants with non-Keplerian flux [95] show a similar decreasing behavior at high frequency. This fact suggests that if a pole is present in the energy flux of equal-mass binaries, it is located at a larger frequency than that at which the common apparent horizon forms. As seen in Sec. 4.4.2, when fitting for $v_{\rm pole}$ we obtain $v_{\rm pole}(\nu = 1/4) = 0.74$, which is to be contrasted with the test-mass case $v_{\rm pole}(\nu = 0) = 1/\sqrt{3} \approx 0.58$. These values of $v_{\rm pole}$ correspond to orbital frequencies $M\Omega = 0.405$ and $M\Omega = 0.192$, respectively.

For the GW frequency derivative $\dot{\varpi}$, we find that at low frequency the Taylor, Padé and EOB models at 3.5PN order are within the numerical error (see Fig. 4.13). At high frequency, as already observed in Ref. [113], only the non-adiabatic E-approximant has a GW frequency derivative that flattens out, as does the numerical result. The non-Keplerian E-approximant at 3.5PN order is closest to the numerical data (see Fig. 4.14).

When estimating the derivative of center-of-mass energy $dE/d\varpi$, we expect the numerical result and adiabatic PN-approximants to be close only in the range of frequencies over which the balance equation and the adiabatic approximation are valid. We find that this range of frequencies is $M\varpi \lesssim 0.08$ (see Fig. 4.15) for the 2.5PN T-approximant and all the 3.5PN approximants.[11] At higher frequency, the 3.5PN order non-adiabatic E-approximants are closer to the numerical $dE/d\varpi$ than are the adiabatic approximants, and the non-Keplerian E-approximant is the closest.

[11] It is not clear whether the failure of the adiabatic models is a result of the assumption of adiabaticity, or if the accuracy of those models would continue to improve if terms at order higher than 3.5PN were known.

Applying a new matching procedure, we compared the numerical waveforms with TaylorT4, Padé, and EOB waveforms. We find that the accumulated phase difference from the numerical solution at $M\omega = 0.1$ is -0.12 radians for the untuned 3.5PN P-approximant [98, 104, 62], 0.50 radians for the untuned, original 3.5PN E-approximant [65, 66, 104], and 0.45 radians for the untuned non-Keplerian [95] 3.5PN E-approximant (see Fig. 4.16). Although those phase differences are larger than for 3.5PN TaylorT4 (-0.04 radians), the phase differences for the P-approximants are less scattered as a function of PN order than are the phase differences for generic Taylor approximants.

The analyses of the flux, GW frequency derivative and (derivative of the) center-of-mass energy emphasize again the importance of including non-adiabatic effects during the last stages of inspiral [66]. Roughly, we can say that non-adiabatic effects are no longer negligible starting from a frequency $M\varpi \sim 0.08$–0.12, as can be seen in Figs. 4.9, 4.13, and 4.15. As seen in these figures, non-adiabatic E-approximants can capture some of the relevant features of the late time evolution. We expect that by further improving these models by fitting higher-order PN coefficients to the numerical data, they will become excellent candidates for developing an analytic template bank of coalescing BBHs [64, 67, 111, 113, 92].

In this paper we started to explore the possibility of reducing the phase differences between numerical and E-approximant waveforms by fitting the unknown parameters a_5, $\mathcal{F}_8$, and $\nu_{\rm pole}$ (see Fig. 4.18). As a first step, for several E-approximants we searched for a local minimal phase difference by varying a_5, $\mathcal{F}_8$, and $\nu_{\rm pole}$. We found that we were able to reduce phase differences to below the numerical uncertainty. In a future work which will include merger

and ringdown, we plan to determine the *region* of the parameter space (a_5, $\mathcal{F}_8$, $v_{\rm pole}$) in which the phase difference is within the numerical uncertainty of the simulation.

CHAPTER 5

EXTRAPOLATING GRAVITATIONAL-WAVE DATA FROM NUMERICAL SIMULATIONS

5.1 Introduction

[1] As numerical simulations of black-hole binaries improve, the criterion for success moves past the ability of a code to merely persist through many orbits of inspiral, merger, and ringdown. Accuracy becomes the goal, as related work in astrophysics and analysis of data from gravitational-wave detectors begins to rely more heavily on results from numerical relativity. The greatest challenge in the field today is to find and eliminate systematic errors that could pollute results built on numerics. Though there are many possible sources of such error, one stands out as being particularly easy to manage and—as we show—a particularly large effect: the error made by extracting gravitational waveforms from a simulation at finite radius, and treating these waveforms as though they were the asymptotic form of the radiation.

The desired waveform is the one to which post-Newtonian approximations aspire, and the one sought by gravitational-wave observatories: the asymptotic waveform. This is the waveform as it is at distances of over $10^{14}\,M$ from the system generating the waves. In typical numerical simulations, data extraction takes place at a distance of order $100\,M$ from the black holes. At this radius, the waves are still rapidly changing because of real physical effects. Near-field effects [50] are plainly evident, scaling with powers of the ratio of the reduced

[1] This is extracted with minor revisions from Ref. [54] which was written in collaboration with Micheal Boyle. It has been submitted to *Physical Review D*, and is under review.

wavelength to the radius, $(\lambda\!\!\!^{-}/r)^k$.[2] Extraction methods aiming to eliminate the influence of gauge effects alone (*e.g.*, improved Regge–Wheeler–Zerilli or quasi-Kinnersley techniques) will not be able to account for these physical changes.

Even using a rather naive, gauge-dependent extraction method, the near-field effects dominate the error in extracted waves throughout the inspiral [50]. For extraction at $r = 50\,M$, in the early stages of a 16-orbit equal-mass binary inspiral, these effects can account for an error of more than 50% in amplitude, or a phase difference of more than one radian. Crucially, the amplitude and phase differences change most rapidly during the merger, meaning that coherence is lost between the inspiral and merger/ringdown segments of the waveform.

We can see the importance of this decoherence by looking at its effect on the matched-filtering technique frequently used to analyze data from gravitational-wave detectors. Matched filtering [123, 124, 52] compares two signals, $s_1(t)$ and $s_2(t)$. It does this by Fourier transforming each into the frequency domain, taking the product of the signals, weighting each inversely by the noise—which is a function of frequency—and integrating over all frequencies. This match is optimized over the time and phase offsets of the input waveforms. For appropriately normalized waveforms, the result is a number between 0 and 1, denoted $< s_1|s_2 >$, with 0 representing no match, and 1 representing a perfect match. If we take the extrapolated waveform as s_1 and the waveform extracted at finite radius as s_2, we can evaluate the match between them. If the extrapolated waveform accurately represents the "true" physical waveform, the mismatch (defined as $1- < s_1|s_2 >$) shows us the loss of signal in data analysis if we were to use the finite-radius waveforms to search for physical waveforms in detector data.

[2] We use the standard notation $\lambda\!\!\!^{-} \equiv \lambda/2\pi$.

The waveforms have a simple scaling with the total mass of the system, which sets the frequency scale relative to the noise present in the detector. In Figs. 5.1 and 5.2, we show mismatches for a range of masses of interest to LIGO data analysis, using the Initial- and Advanced-LIGO noise curves, respectively, to weight the matches. The value of R denotes the coordinate radius of extraction for the finite-radius waveform.

These figures demonstrate that the mismatch can be several percent when extracting at a radius of $R = 50\,M$. For extraction at $R = 225\,M$, the mismatch is never more than about 0.1%. Lindblom *et al.* [178] cite a target mismatch of less than 0.5% between the physical waveform and a class of model templates to be used for *detection* of events in current LIGO detector data.[3] Thus, for example, if these numerical waveforms were to be used in construction of template banks, the waveform extracted at $R = 50\,M$ would be entirely insufficient, though the $R = 225\,M$ waveform may be acceptable. For the loudest signals expected to be seen by Advanced LIGO, the required mismatch may be roughly 10^{-4} [178]. In this case, even extraction at $R = 225\,M$ would be insufficient; some method must be used to obtain the asymptotic waveform. For both Initial and Advanced LIGO, estimating the parameters of the waveform—masses and spins of the black holes, for instance—requires still greater accuracy.

We can identify three main obstacles to obtaining the asymptotic form of gravitational-wave data from numerical simulations:

1. Getting the "right" data at any given point, independent of gauge effects (*e.g.*, using quasi-Kinnersley techniques and improved Regge–Wheeler–

[3]This number of 0.5% results from assumptions about typical event magnitude, template bank parameters, and requirements on the maximum frequency of missed events. The parameters used to arrive at this number are typical for Initial LIGO.

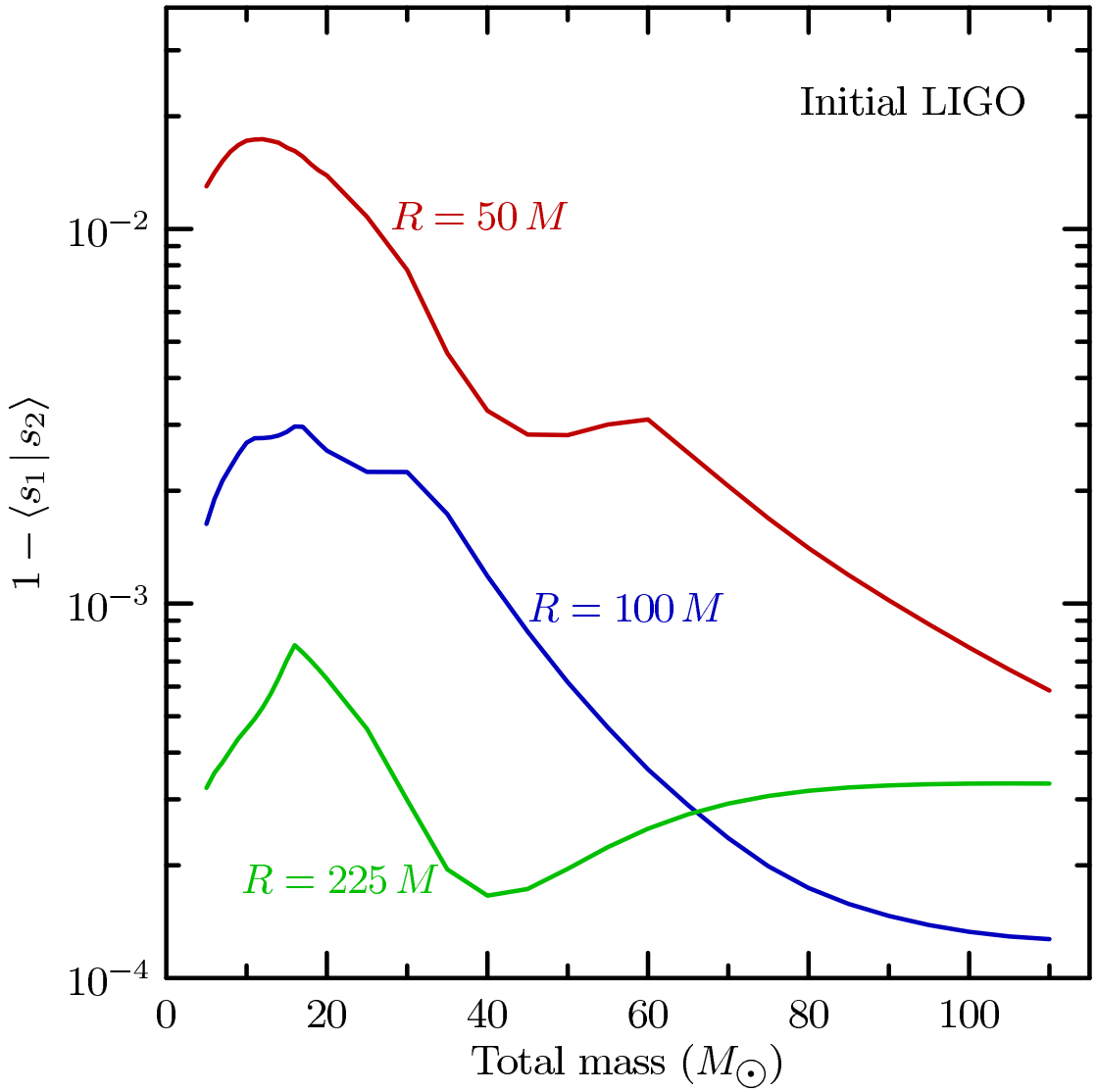

Figure 5.1: Data-analysis mismatch between finite-radius waveforms and the extrapolated waveform for Initial LIGO. This plot shows the mismatch between extrapolated waveforms and waveforms extracted at several finite radii, scaled to various values of the total mass of the binary system, using the Initial-LIGO noise curve. The waveforms are shifted in time and phase to find the optimal match.

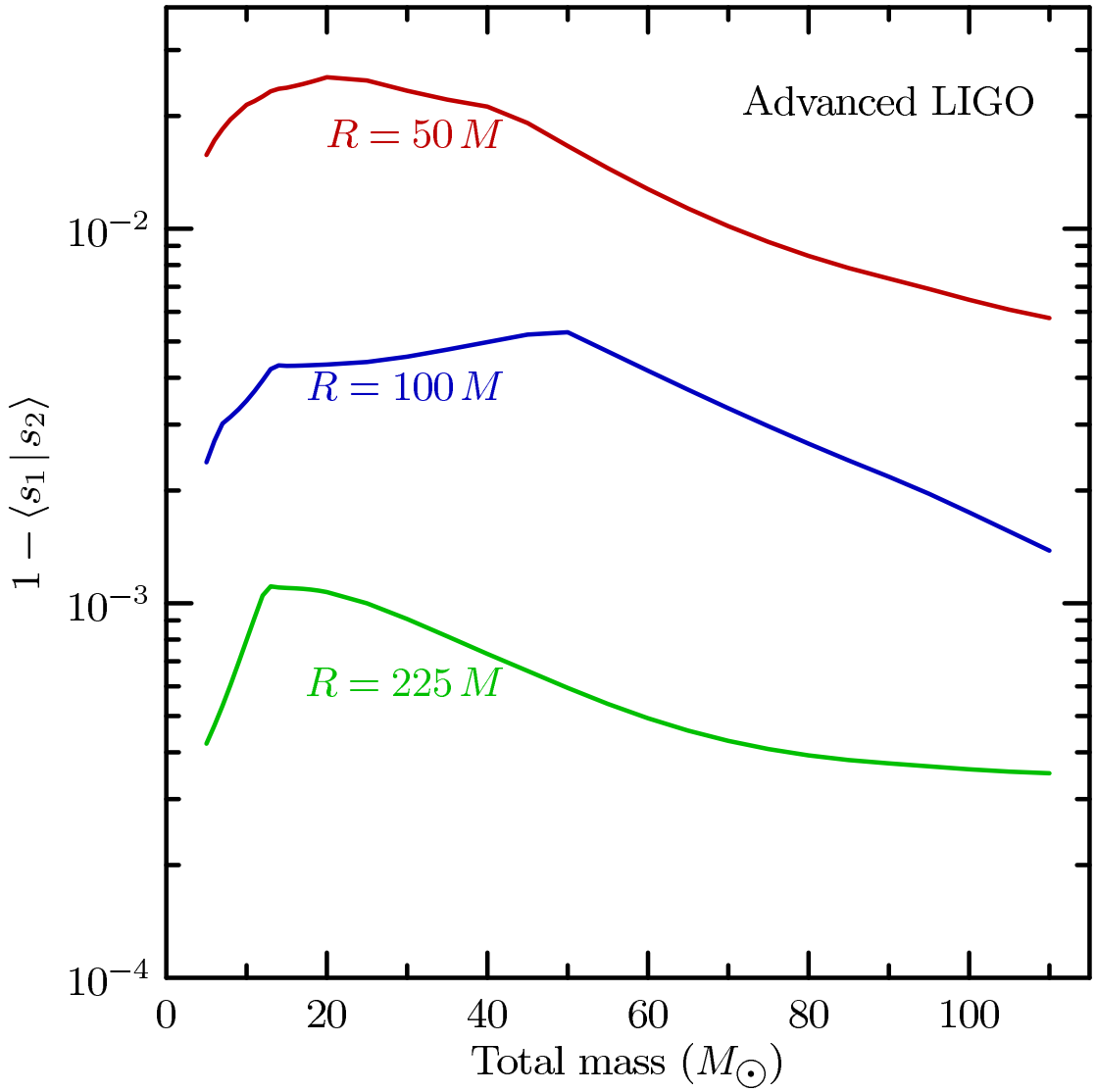

Figure 5.2: Data-analysis mismatch between finite-radius waveforms and the extrapolated waveform for Advanced LIGO. This plot shows the mismatch between extrapolated waveforms and waveforms extracted at several finite radii, scaled to various values of the total mass of the binary system, using the Advanced-LIGO noise curve. The waveforms are shifted in time and phase to find the optimal match.

Zerilli techniques);

2. Removing near-field effects;

3. Extracting data along a physically relevant path.

Many groups have attempted to deal with the first of these problems.[4] While this is, no doubt, an important objective, even the best extraction technique to date is imperfect at finite radii. Moreover, at finite distances from the source, gravitational waves continue to undergo real physical changes as they move away from the system [225], which are frequently ignored in the literature. Some extraction techniques have been introduced that attempt to incorporate corrections for these near-field effects [1, 2, 116]. However, these require assumptions about the form of those corrections, which we prefer not to impose. Finally, even if we have the optimal data at each point in our spacetime, it is easy to see that extraction along an arbitrary (timelike) path through that spacetime would produce a nearly arbitrary waveform, bearing no resemblance to a waveform that could be observed in a nearly inertial detector.

We propose a simple method using existing data-extraction techniques which should be able to overcome each of these three obstacles, given certain very basic assumptions. The data are to be extracted at a series of radii—either on a series of concentric spheres, or at various radii along an outgoing null ray. These data can then be expressed as functions of extraction radius and retarded time using either of two simple methods we describe. For each value of retarded time, the waveforms can then be fit to a polynomial in inverse powers of the extraction radius. The asymptotic waveform is simply the first nonzero term in the polynomial. Though this method also incorporates certain assumptions,

[4] See [189] and [210], and references therein for descriptions of quasi-Kinnersley and RWZ methods, respectively.

they amount to assuming that the data behave as radially propagating waves, and that the metric itself is asymptotically Minkowski in the coordinates chosen for the simulation.

Extrapolation is, by its very nature, a dangerous procedure. The final result may be numerically unstable, in the sense that it will fail to converge as the order of the extrapolating polynomial is increased. This is to be expected, as the size of the effects to be removed eventually falls below the size of noise in the waveform data. There are likely better methods of determining the asymptotic form of gravitational waves produced by numerical simulations. For example, characteristic evolution is a promising technique that may become common in the near future [26, 150, 9, 10]. Nonetheless, extrapolation does provide a rough and ready technique which can easily be implemented by numerical-relativity groups using existing frameworks.

This paper presents a simple method for implementing the extrapolation of gravitational-wave data from numerical simulations, and the motivation for doing so. In Sec. 5.2, we begin by introducing an extrapolation method that uses approximate tortoise coordinates, which is the basic method used to extrapolate data in various papers [51, 53, 211, 52, 68] by the Caltech–Cornell collaboration. The method is tested on the inspiral, merger, and ringdown waveform data of the equal mass, nonspinning, quasicircular 15-orbit binary simulation of the Caltech–Cornell collaboration. We present the convergence of the wave phase and amplitude as the extrapolation order increases, and we also compare data extrapolated using various extraction radii. In Sec. 5.3, we propose a different extrapolation method that uses the wave phase to independently check our results, again demonstrating the convergence properties of the method. In

Sec. 5.4, we compare the extrapolated waveforms of both methods at various extrapolation orders, showing that they agree to well within the error estimates of the two methods. We include a brief section on techniques for filtering noisy data, which is particularly relevant here because extrapolation amplifies noise. Finally, a brief discussion of the pitfalls and future of extrapolation is found in Sec. 5.6.

5.2 Extrapolation using approximate tortoise coordinates

There are many types of data that can be extracted from a numerical simulation of an isolated source of gravitational waves. The two most common methods of extracting gravitational waveforms involve using the Newman–Penrose Ψ_4 quantity, or the metric perturbation $h$extracted using Regge–Wheeler–Zerilli techniques. Even if we focus on a particular type of waveform, the data can be extracted at a series of points along the z axis, for example, or decomposed into multipole components and extracted on a series of spheres around the source. To simplify this introductory discussion of extrapolation, we ignore the variety of particular types of waveform data. Rather, we generalize to some abstract quantity f, which encapsulates the quantity to be extrapolated and behaves roughly as a radially outgoing wave. We assume that f travels along outgoing null cones, which we parametrize by a retarded time t_{ret}. Along each of these null cones, we further assume that f can be expressed as a convergent (or at least asymptotic) series in $1/r$—where r is some radial coordinate—for all radii of interest. That is, we assume

$$f(t_{\text{ret}}, r) = \sum_{k=0}^{\infty} \frac{f_{(k)}(t_{\text{ret}})}{r^k} , \tag{5.1}$$

for some functions $f_{(k)}$. The asymptotic behavior of f is given by the lowest nonzero $f_{(k)}$.[5]

Given data for such an f at a set of retarded times, and a set of radii $\{r_i\}$, it is a simple matter to fit the data for each value of $t_{\rm ret}$ to a polynomial in $1/r$. That is, for each value of $t_{\rm ret}$, we take the set of data $\{f(t_{\rm ret}, r_i)\}$ and fit it to a finite polynomial so that

$$f(t_{\rm ret}, r_i) \simeq \sum_{k=0}^{N} \frac{f_{(k)}(t_{\rm ret})}{r_i^k} \,. \tag{5.2}$$

Standard algorithms [232] can be used to accomplish this fitting; here we use the least-squares method. Of course, because we are truncating the series of Eq. (5.1) at $k = N$, some of the effects from $k > N$ terms will appear at lower orders. We will need to choose N appropriately, checking that the extrapolated quantity has converged sufficiently with respect to this order.

5.2.1 Radial parameter

One subtlety to be considered is the choice of r parameter to be used in the extraction and fitting. For numerical simulation of an isolated system, one simple and obvious choice is the coordinate radius R used in the simulation. Alternatively, if the data is measured on some spheroidal surface, it is possible to define an areal radius $R_{\rm areal}$ by measuring the area of the sphere along with f, and setting $R_{\rm areal} \equiv \sqrt{\text{area}/4\pi}$. Still other choices are certainly possible.

One objective in choosing a particular r parameter is to ensure the physical relevance of the final extrapolated quantity. If we try to detect the wave, for ex-

[5] For example, if $f = r\Psi_4$, then $f_{(0)}$ gives the asymptotic behavior; if $f = \Psi_4$, then $f_{(1)}$ gives the asymptotic behavior.

ample, we may want to think of the detector as being located at some constant value of r. Or, we may want r to asymptotically represent the luminosity distance. These conditions may be checked by inspecting the asymptotic behavior of the metric components in the given coordinates. For example, if the metric components in a coordinate system including r asymptotically approach those of the standard Minkowski metric, it is not hard to see that an inertial detector could follow a path of constant r parameter.

Suppose we have two different parameters r and $\tilde{r}$ which can be related by a series expansion

$$r = \tilde{r}\,[1 + a/\tilde{r} + \ldots]\ . \tag{5.3}$$

For the data presented in this paper, we can show that the coordinate radius R and areal radius $R_{\rm areal}$ are related in this way. Introducing the expansion coefficients $\tilde{f}_{(k)}$, we can write

$$f(t_{\rm ret}, r) = \sum_{k=0}^{\infty} \frac{f_{(k)}(t_{\rm ret})}{r^k} = \sum_{k=0}^{\infty} \frac{\tilde{f}_{(k)}(t_{\rm ret})}{\tilde{r}^k}\ . \tag{5.4}$$

Inserting Eq. (5.3) into this formula, Taylor expanding, and equating terms of equal order k, shows that $f_{(0)} = \tilde{f}_{(0)}$ and $f_{(1)} = \tilde{f}_{(1)}$. Thus, if the asymptotic behavior of f is given by $f_{(0)}$ or $f_{(1)}$, the final extrapolated data should not depend on whether r or $\tilde{r}$ is used. On the other hand, in practice we truncate these series at finite order. This means that higher-order terms could "pollute" $f_{(0)}$ or $f_{(1)}$. The second objective in choosing an r parameter, then, is to ensure fast convergence of the series in Eq. (5.2). If the extrapolated quantity does not converge quickly as the order of the extrapolating polynomial N is increased, it may be due to a poor choice of r parameter.

The coordinate radius used in a simulation may be subject to large gauge variations that are physically irrelevant, and hence are not reflected in the

wave's behavior. That is, the wave may not fall off nicely in inverse powers of that coordinate radius. For the data discussed later in this paper, we find that using the coordinate radius of extraction spheres is indeed a poor choice, while using the areal radius of those extraction spheres improves the convergence of the extrapolation.

5.2.2 Retarded-time parameter

Similar considerations must be made for the choice of retarded-time parameter $t_{\rm ret}$ to be used in extrapolation. It may be possible to evolve null geodesics in numerical simulations, and use these to define the null curves on which data is to be extracted. While this is an interesting possibility that deserves investigation, we propose two simpler methods here based on an approximate retarded time constructed using the coordinates of the numerical simulation and the phase of the waves measured in that coordinate system.

Again, we have two criteria for choosing a retarded-time parameter. First is the physical suitability in the asymptotic limit. For example, we might want the asymptotic $t_{\rm ret}$ to be (up to an additive term constant in time) the proper time along the path of a detector located at constant r. Again, checking the asymptotic behavior of the metric components with respect to $t_{\rm ret}$ and r should be a sufficient test of the physical relevance of the parameters. Second, we wish to have rapid convergence of the extrapolation series using the chosen parameter, which also needs to be checked.

As before, we can also show the equivalence of different choices for the $t_{\rm ret}$ parameter. Suppose we have two different approximations $t_{\rm ret}$ and $\check{t}_{\rm ret}$ that can

be related by a series expansion

$$t_{\rm ret} = \check{t}_{\rm ret}\ [1 + b/r + \ldots]\ . \tag{5.5}$$

Using the new expansion coefficients $\check{f}_{(k)}$, we can write

$$f(t_{\rm ret}, r) = \sum_{k=0}^{\infty} \frac{f_{(k)}(t_{\rm ret})}{r^k} = \sum_{k=0}^{\infty} \frac{\check{f}_{(k)}(\check{t}_{\rm ret})}{r^k}\ . \tag{5.6}$$

Now, however, we need to assume that the functions $f_{(k)}$ can be well-approximated by Taylor series. If this is true, we can again show that $f_{(0)} = \check{f}_{(0)}$ or, *if* we have $f_{(0)} = \check{f}_{(0)} = 0$, that $f_{(1)} = \check{f}_{(1)}$. The condition that f be well-approximated by a Taylor series is nontrivial, and can help to inform the choice of f. Similarly, the speed of convergence of the extrapolation can help to inform the choice of a particular $t_{\rm ret}$ parameter.

Since we will be considering radiation from an isolated compact source, our basic model for $t_{\rm ret}$ comes from the Schwarzschild spacetime; we assume that the system in question approaches this spacetime at increasing distance. In analogy with the time-retardation effect on outgoing null rays in a Schwarzschild spacetime [80], we define a "tortoise coordinate" r_* by:

$$r_* \equiv r + 2M_{\rm ADM} \ln\left(\frac{r}{2M_{\rm ADM}} - 1\right)\ , \tag{5.7}$$

where $M_{\rm ADM}$ is the ADM mass of the initial data.[6] In standard Schwarzschild coordinates, the appropriate retarded time would be given by $t_{\rm ret} = t - r_*$. It is not hard to see that the exterior derivative $\partial t_{\rm ret}$ is null with respect to the Schwarzschild metric.

[6] Kocsis and Loeb [169] pointed out that the propagation of a roughly spherical gravitational wave should be affected primarily by the amount of mass *interior to* the wave. Because the waves from a merging binary can carry off a significant fraction (typically a few percent) of the binary's mass, this suggests that we should allow the mass in this formula to vary in time, falling by perhaps a few percent over the duration of the waveform. However, this is a small correction of a small correction; we have not found it necessary. Perhaps with more refined methods, this additional correction would be relevant.

Taking inspiration from this, we can attempt to account for certain differences from a Schwarzschild background. Let T and R denote the simulation's coordinates, and suppose that we extract the metric components g^{TT}, g^{TR}, and g^{RR} from the simulation. We seek a $t_{\rm ret}(T,R)$ such that

$$\partial t_{\rm ret} = \frac{\partial t_{\rm ret}}{\partial T}\,\partial T + \frac{\partial t_{\rm ret}}{\partial R}\,\partial R \tag{5.8}$$

is null with respect to these metric components. That is, we seek a $t_{\rm ret}$ such that

$$g^{TT}\left(\frac{\partial t_{\rm ret}}{\partial T}\right)^2 + 2g^{TR}\left(\frac{\partial t_{\rm ret}}{\partial T}\right)\left(\frac{\partial t_{\rm ret}}{\partial R}\right) + g^{RR}\left(\frac{\partial t_{\rm ret}}{\partial R}\right)^2 = 0\,. \tag{5.9}$$

We introduce the ansatz $t_{\rm ret} = t - r_*$, where t is assumed to be a slowly varying function of R,[7] and r_* is given by Eq. (5.7) with R in place of r on the right side. If we ignore $\partial t/\partial R$ and insert our ansatz into Eq. (5.9), we have

$$g^{TT}\left(\frac{\partial t}{\partial T}\right)^2 - 2g^{TR}\left(\frac{\partial t}{\partial T}\right)\left(\frac{1}{1-2M_{\rm ADM}/R}\right) + g^{RR}\left(\frac{1}{1-2M_{\rm ADM}/R}\right)^2 = 0\,. \tag{5.10}$$

We can solve this for $\partial t/\partial T$:

$$\frac{\partial t}{\partial T} = \frac{1}{1-2M_{\rm ADM}/R}\,\frac{g^{TR} \pm \sqrt{(g^{TR})^2 - g^{TT}\,g^{RR}}}{g^{TT}}\,. \tag{5.11}$$

Substituting the Schwarzschild metric components shows that we should choose the negative sign in the numerator of the second factor. Finally, we can integrate (numerically) to find

$$t = \int_0^T \frac{1}{g^{TT}}\,\frac{g^{TR} - \sqrt{(g^{TR})^2 - g^{TT}\,g^{RR}}}{1-2M_{\rm ADM}/R}\,\partial T'\,. \tag{5.12}$$

Now, in the case where g^{TR} is small compared to 1, we may wish to ignore it, in which case we have

$$t = \int_0^T \frac{\sqrt{-g^{RR}/g^{TT}}}{1-2M_{\rm ADM}/R}\,\partial T'\,. \tag{5.13}$$

[7] More specifically, we need $|\partial t/\partial R| \ll |\partial r_*/\partial R|$. This condition needs to be checked for all radii used, at all times in the simulation. For the data presented below, we have checked this, and shown it to be a valid assumption, at the radii used for extrapolation.

It is not hard to see that this correctly reduces to $t = T$ in the Schwarzschild case.

For the data discussed later in this paper, we make further assumptions that $g^{RR} = 1 - 2M_{\rm ADM}/R$, and that $R = R_{\rm areal}$. That is, we define the corrected time

$$t_{\rm corr} \equiv \int_0^T \sqrt{\frac{-1/g^{TT}}{1 - 2M_{\rm ADM}/R_{\rm areal}}}\, \partial T' \tag{5.14a}$$

and the retarded time

$$t_{\rm ret} \equiv t_{\rm corr} - r_* \,. \tag{5.14b}$$

We find that this corrected time leads to a significant improvement over the naive choice of $t(T) = T$, while no improvement results from using Eq. (5.12).

5.2.3 Application to a binary inspiral

To begin the extrapolation procedure, we extract the (spin-weight $s = -2$) $(l, m) = (2, 2)$ component of Ψ_4 data on a set of spheres at constant coordinate radius in the simulation. In the black-hole binary simulations used here (the same as those discussed in Refs. [51, 50, 53, 211]), these spheres are located every $\Delta R = 10M_{\rm irr}$ (where $M_{\rm irr}$ is the sum of the irreducible masses of the black holes in the initial data) from an inner radius of $R = 50M_{\rm irr}$ to an outer radius of $R = 225M_{\rm irr}$, where $M_{\rm irr}$ denotes the total apparent-horizon mass of the two holes at the beginning of the simulation. This extraction occurs at time steps of $\Delta T \approx 0.5M_{\rm irr}$ throughout the simulation. We also measure the areal radius, $R_{\rm areal}$, of these spheres by integrating the induced area element over the sphere to find the area, and defining $R_{\rm areal} \equiv \sqrt{\rm area/4\pi}$. This typically differs from

[7] See Ref. [211] for details of the extraction procedure.

the coordinate radius R by roughly $M_{\rm irr}/R$. Because of gauge effects, the areal radius of a coordinate sphere changes as a function of time, so we measure this as a function of time. Finally, we measure the average value of g^{TT} as a function of coordinate time on the extraction spheres to correct for the dynamic lapse function. The areal radius and g^{TT} are then used to compute the retarded time $t_{\rm ret}$ defined in Eq. (5.14).

The gravitational-wave data Ψ_4, the areal radius $R_{\rm areal}$, and the lapse N are all measured as functions of the code coordinates T and R. We can use these to construct the retarded time defined in Eq. (5.14), using $R_{\rm areal}$ in place of r. This, then, will also be a function of the code coordinates. The mapping between $(t_{\rm ret}, R_{\rm areal})$ and (T, R) is invertible, so we can rewrite Ψ_4 as a function of $t_{\rm ret}$ and $R_{\rm areal}$.

As noted in Sec. 5.2.2, we need to assume that the extrapolated functions are well approximated by Taylor series. Because the real and imaginary parts of Ψ_4 are rapidly oscillating in the data presented here, we prefer to use the same data in smoother form. We define the complex amplitude A and phase ϕ of the wave:

$$R_{\rm areal}\, M_{\rm irr}\, \Psi_4 \equiv A\, \mathrm{e}^{\mathrm{i}\phi}\ , \tag{5.15}$$

where A and ϕ are functions of $t_{\rm ret}$ and $R_{\rm areal}$. Note that this definition factors out the dominant $1/r$ behavior of the amplitude. This equation defines the phase with an ambiguity of multiples of 2π. In practice, we ensure that the phase is continuous as a function of time by adding suitable multiples of 2π. The continuous phase is easier to work with for practical reasons, and is certainly much better approximated by a Taylor series, as required by the argument surrounding Eq. (5.6).

A slight complication arises in the relative phase offset between successive

radii. Noise in the early parts of the waveform makes the overall phase offset go through multiples of 2π essentially randomly. We choose some fairly noise-free (retarded) time and ensure that phases corresponding to successive extraction spheres are matched at that time, by simply adding multiples of 2π to the phase of the entire waveform—that is, we add a multiple of 2π to the phase at all times.

Extrapolation of the waveform, then, basically consists of finding the asymptotic forms of these functions, A and ϕ as functions of time. We apply the general technique discussed above to A and ϕ. Explicitly, we fit the data to polynomials in $1/R_{\text{areal}}$ for each value of retarded time:

$$A(t_{\text{ret}}, R_{\text{areal}}) \simeq \sum_{k=0}^{N} \frac{A_{(k)}(t_{\text{ret}})}{R_{\text{areal}}^{k}} , \tag{5.16a}$$

$$\phi(t_{\text{ret}}, R_{\text{areal}}) \simeq \sum_{k=0}^{N} \frac{\phi_{(k)}(t_{\text{ret}})}{R_{\text{areal}}^{k}} . \tag{5.16b}$$

The asymptotic waveform is fully described by $A_{(0)}$ and $\phi_{(0)}$. When the order of the approximating polynomials is important, we will denote by A_N and ϕ_N the asymptotic waveforms resulting from approximations using polynomials of order N.

We show the results of these extrapolations in the figures below. Figs. 5.3 through 5.5 show convergence plots for extrapolations using orders $N = 1$–5. The first two figures show the relative amplitude and phase difference between successive orders of extrapolation, using the corrected time of Eq. (5.14). Here, we define

$$\frac{\delta A}{A} \equiv \frac{A_{N_a} - A_{N_b}}{A_{N_b}} \tag{5.17a}$$

and

$$\delta\phi \equiv \phi_{N_a} - \phi_{N_b} . \tag{5.17b}$$

Note that the broad trend is toward convergence, though high-frequency noise is more evident as the order increases, as we discuss further in the next subsection. The peak amplitude of the waves occurs at time $t_{\rm ret}/M_{\rm irr} \approx 3954$. Note that the scale of the horizontal axis changes just before this time to better show the merger/ringdown portion. We see that the extrapolation is no longer convergent, with differences increasing slightly as the order of the extrapolating polynomial is increased. The oscillations we see in these convergence plots have a frequency equal to the frequency of the waves themselves. Their origin is not clear, but may be due to numerics, gauge, or other effects that violate our assumptions about the outgoing-wave nature of the data. It is also possible that there are simply no higher-order effects to be extrapolated, so low-order extrapolation suffices.

Figure 5.5 shows the same data as in Fig. 5.4, except that no correction is used for dynamic lapse. That is, for this figure (and only this figure), we use $t_{\rm ret} \equiv T - r_*$, where T is simply the coordinate time. This demonstrates the need for improved time-retardation methods after merger. Note that the extrapolated data during the long inspiral is virtually unchanged (note the different vertical axes). After the merger—occurring at roughly $t_{\rm ret}/M_{\rm irr} = 3954$—there is no convergence when no correction is made for dynamic lapse. It is precisely the merger and ringdown segment during which extreme gauge changes are present in the data used here [211]. On the other hand, the fair convergence of the corrected waveforms indicates that it is possible to successfully remove these gauge effects.

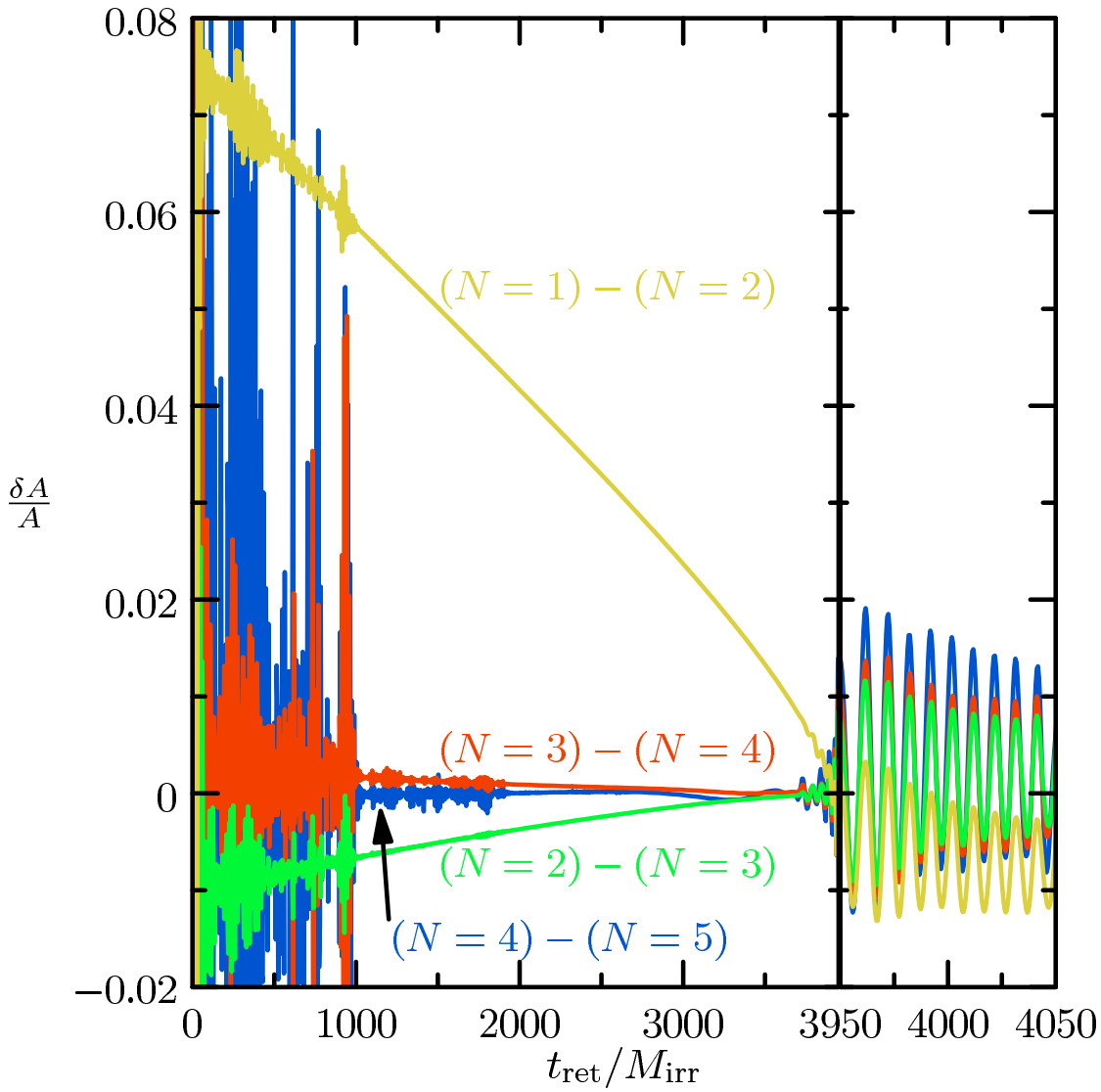

Figure 5.3: Convergence of the amplitude of the extrapolated Ψ_4, with increasing order of the extrapolating polynomial, N. This figure shows the convergence of the relative amplitude of the extrapolated Newman–Penrose waveform, as the order N of the extrapolating polynomial is increased. (See Eq. (5.16).) That is, we subtract the amplitudes of the two waveforms, and normalize at each time by the amplitude of the second waveform. We see that increasing the order tends to amplify the apparent noise during the early and late parts of the waveform. Nonetheless, the broad (low-frequency) trend is towards convergence. Note that the differences decrease as the system nears merger; this is a first indication that the extrapolated effects are due to near-field influences. Also note that the horizontal axis changes in the right part of the figure, which shows the point of merger, and the ringdown portion of the waveform. After the merger, the extrapolation is slightly non-convergent.

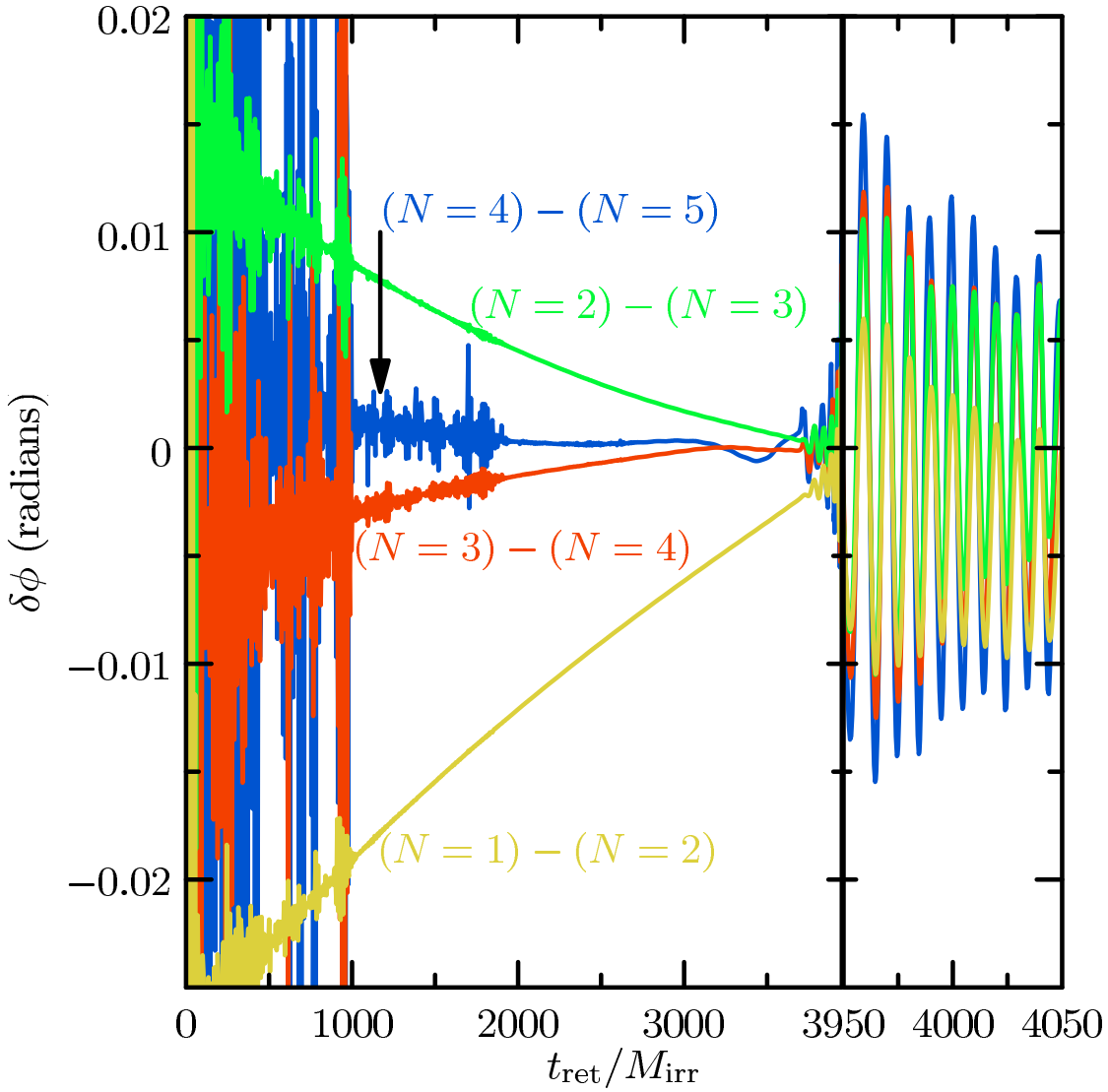

Figure 5.4: Convergence of the phase of the extrapolated Ψ_4, with increasing order of the extrapolating polynomial, N. This figure is the same as Fig. 5.3, except that it shows the convergence of phase. Again, increasing the extrapolation order tends to amplify the noise during the early and late parts of the waveform, though the broad (low-frequency) trend is towards convergence. The horizontal-axis scale changes just before merger.

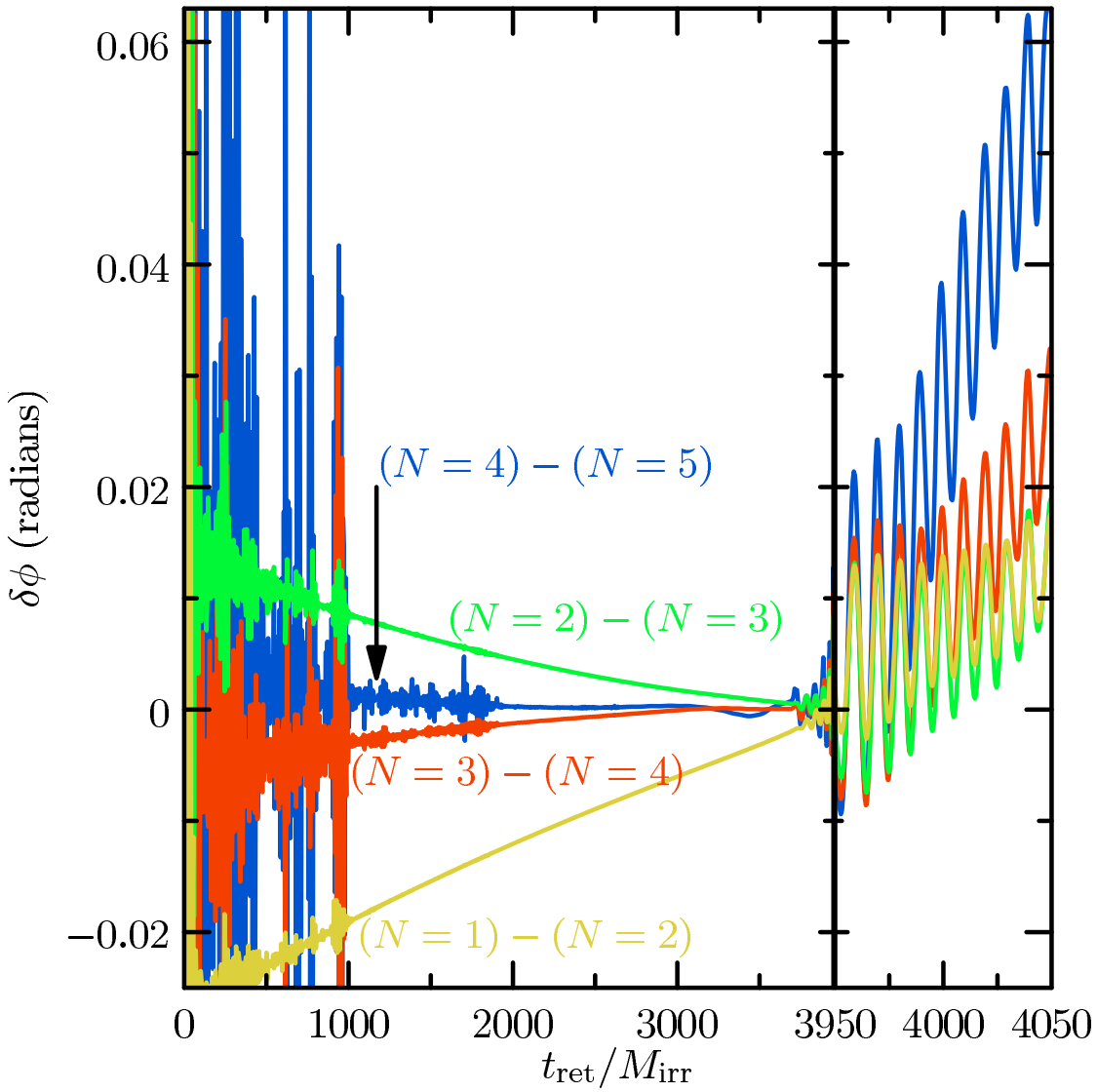

Figure 5.5: Convergence of the phase of Ψ_4, extrapolated with no correction for the dynamic lapse. This figure is the same as Fig. 5.4, except that no correction is made to account for the dynamic lapse. (See Eq. (5.14) and surrounding discussion.) Observe that the convergence is very poor after merger (at roughly $t_{\rm ret}/M_{\rm irr} = 3954$). This corresponds to the time after which sharp features in the lapse are observed. We conclude from this graph and comparison with the previous graph that the correction is crucial to convergence of Ψ_4 extrapolation through merger and ringdown.

5.2.4 Choosing the order of extrapolation

Deciding on an appropriate order of extrapolation to be used for a given purpose requires balancing competing effects. As we see in Fig. 5.3, for example, there is evidently some benefit to be gained from using higher-order extrapolation during the inspiral; there is clearly some convergence during inspiral for each of the orders shown. On the other hand, higher-order methods amplify the apparent noise in the waveform.[8] Moreover, late in the inspiral, and on into the merger and ringdown, the effects being extrapolated may be present only at low orders; increasing the extrapolation order would be useless as higher-order terms would simply be fitting to noise.

The optimal order depends on the accuracy needed, and on the size of effects that need to be eliminated from the data. For some applications, little accuracy is needed, so a low-order extrapolation (or even no extrapolation) is preferable. If high-frequency noise is not considered an issue, then simple high-order extrapolation should suffice. Of course, if both high accuracy and low noise are required, data may easily be filtered, mitigating the problem of noise amplification. (See Sec. 5.5 for more discussion.) There is some concern that this may introduce subtle inaccuracy: filtering is more art than science, and it is difficult to establish precise error bars for filtered data.

[8] So-called "junk radiation" is a ubiquitous feature of initial data for current numerical simulations of binary black-hole systems. It is clearly evident in simulations as large-amplitude, high-frequency waves that die out as the simulation progresses. While it is astrophysically extraneous, it is nevertheless a correct result of evolution from the initial data. Better initial data would, presumably, decrease its magnitude. This is the source of what looks like noise in the waveforms at early times. It is less apparent in h data than in Ψ_4 data because Ψ_4 effectively amplifies high-frequency components, because of the relation $\Psi_4 \approx -\ddot{h}$.

5.2.5 Choosing extraction radii

Another decision needs to be made regarding the number and location of extraction surfaces. Choosing the number of surfaces is fairly easy, because there is typically little cost in increasing the number of extraction radii (especially relative to the cost of—say—running a simulation). The only restriction is that the number of data points needs to be significantly larger than the order of the extrapolating polynomial; more can hardly hurt. More careful consideration needs to be given to the *location* of the extraction surfaces.

For the extrapolations shown in Figs. 5.3 and 5.4, data was extracted on spheres spaced by roughly $10M_{\rm irr}$, from $R = 75M_{\rm irr}$ to $R = 225M_{\rm irr}$. The outer radius of $225M_{\rm irr}$ was chosen simply because this is the largest radius at which data exists throughout the simulation; presumably, we always want the outermost radii at which the data are resolved. In choosing the inner radius, there are two competing considerations.

On one hand, we want the largest spread possible between the inner and outer extraction radii to stabilize the extrapolation. A very rough rule of thumb seems to be that the distance to be extrapolated should be no greater than the distance covered by the data. Because the extrapolating polynomial is a function of $1/R$, the distance to be extrapolated is $1/R_{\rm outer} - 1/\infty = 1/R_{\rm outer}$. The distance covered by the data is $1/R_{\rm inner} - 1/R_{\rm outer}$, so if the rule of thumb is to be satisfied, the inner extraction radius should be no more than half of the outer extraction radius, $R_{\rm inner} \lesssim R_{\rm outer}/2$ (noting, of course, that this is a *very* rough rule of thumb).

On the other hand, we would like the inner extraction radius to be as far out

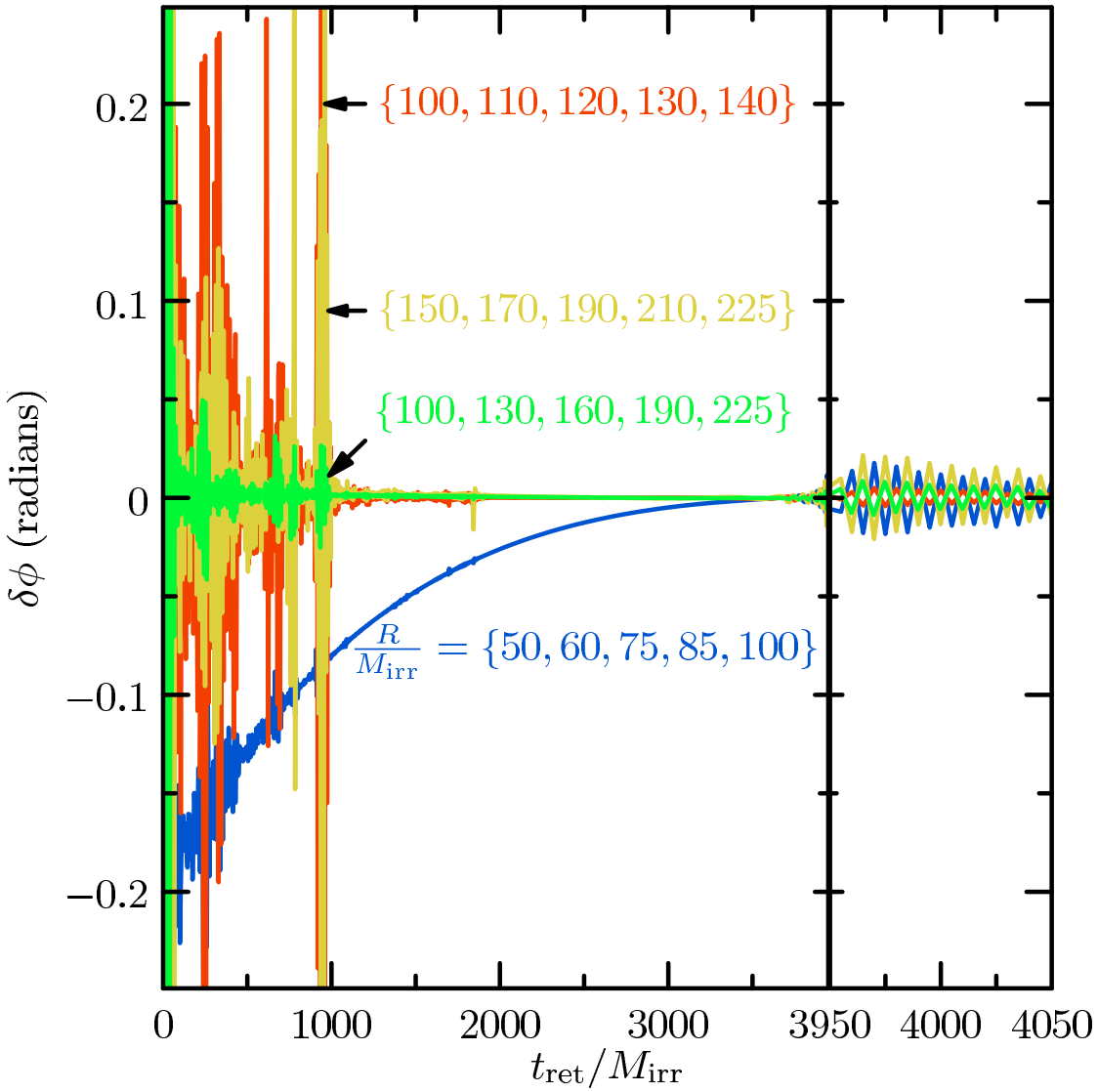

Figure 5.6: Comparison of extrapolation of Ψ_4 using different sets of extraction radii. This figure compares the phase of waveforms extrapolated with various sets of radii. All comparisons are with respect to the data set used elsewhere in this paper, which uses extraction radii $R/M_{\rm irr} = \{75, 85, 100, 110, 120, \ldots, 200, 210, 225\}$. The order of the extrapolating polynomial is $N = 3$ in all cases.

as possible. Extracting data near the violent center of the simulation is a bad idea for many reasons. Coordinate ambiguity, tetrad errors, near-field effects—all are more severe near the center of the simulation. The larger these errors are, the more work the extrapolation needs to do. This effectively means that higher-order extrapolation is needed if data are extracted at small radii. The exact inner radius needed for extrapolation depends on the desired accuracy and, again, the portion of the simulation from which the waveform is needed.

We can compare data extrapolated using different sets of radii. Figure 5.6 shows a variety, compared to the data used elsewhere in this paper. The extrapolation order is $N = 3$ in all cases. Note that the waveforms labeled $R/M_{\rm irr} = \{50, \ldots, 100\}$ and $R/M_{\rm irr} = \{100, \ldots, 225\}$ both satisfy the rule of thumb that the inner radius should be at most half of the outer radius, while the other two waveforms do not; it appears that violation of the rule of thumb leads to greater sensitivity to noise. One waveform is extrapolated using only data from small radii, $R/M_{\rm irr} = \{50, \ldots, 100\}$. It is clearly not converged, and would require higher-order extrapolation if greater accuracy is needed. The source of the difference is presumably the near-field effect [50], which is proportionally larger at small radii.

Clearly, there is a nontrivial interplay between the radii used for extraction and the order of extrapolation. Indeed, because of the time-dependence of the various elements of these choices, it may be advisable to use different radii and orders of extrapolation for different time portions of the waveform. The different portions could then be joined together using any of various methods [4, 52].

5.3 Extrapolation using the phase of the waveform

While the tortoise-coordinate method just described attempts to compensate for nontrivial gauge perturbations, it is possible that it does not take account of all effects adequately. As an independent check, we propose what is essentially a second—very different—formulation of the retarded-time parameter. If waves extrapolated with the two different methods agree, then we can be reasonably confident that unmodeled gauge effects are not diminishing the accuracy of the final result. As we will explain below, the method in this section cannot be used naively with general data (*e.g.*, data on the equatorial plane). In particular, we must assume that the data to be extrapolated consists of a strictly monotonic phase. It is, however, frequently possible to employ a simple technique to make purely real, oscillating data into complex data with strictly monotonic phase, as we describe below. The results of this technique agree with those of the tortoise-coordinate extrapolation as we show in Sec. 5.4.

Instead of extrapolating the wave phase ϕ and amplitude A as functions of time and radius, we extrapolate the time $t_{\rm ret}$ and the amplitude A as functions of wave phase ϕ and radius $R_{\rm areal}$. In other words, we measure the amplitude and the arrival time to some radius $R_{\rm areal}$ of a fixed phase point in the waveform. This is the origin of the requirement that the data to be extrapolated consist of a strictly monotonic phase $\phi(t_{\rm ret}, R_{\rm areal})$ (*i.e.*, it must be invertible). For the data presented here, the presence of radiation in the initial data—junk radiation—and numerical noise cause the extracted waveforms to fail to satisfy this requirement at early times. In this case, the extrapolation should be done in two steps. First, the data is separated into invertible segments, and then each segment is extrapolated separately.

5.3.1 Description of the method

This extrapolation technique consists of extrapolating the retarded time and the amplitude as functions of the wave phase ϕ and the radius $R_{\rm areal}$. In other words, when extrapolating the waveform, we are estimating the amplitude and the arrival time of a fixed phase point at infinity. Here, we extract the same Ψ_4, g^{TT}, and areal-radius data used in the previous section. As in the previous method, we first shift each waveform in time using $t_{\rm ret} = t_{\rm corr} - r_*$, where $t_{\rm corr}$ is defined in Eq. (5.14) and the basic tortoise coordinate r_* is defined in Eq. (5.7) with areal radius as the radial parameter. The amplitude and wave phase are again defined using Eq. (5.15), and the phase is made continuous as in Sec. 5.2.3. Thus, we begin with the same data, shifted as with the tortoise-coordinate method.

Now, however, we change the method, in an attempt to allow for unmodeled effects. Instead of extrapolating $\phi(t_{\rm ret}, R_{\rm areal})$ and $A(t_{\rm ret}, R_{\rm areal})$, as with the previous method, we invert these functions to get $t_{\rm ret}(\phi, R_{\rm areal})$ and $A(\phi, R_{\rm areal})$ as functions of the wave phase ϕ. In other words, we extrapolate the arrival time and the amplitude of a signal to a coordinate radius R for each wave phase value. This is done by fitting the retarded time $t_{\rm ret}$ and the amplitude A data to polynomials in $1/R_{\rm areal}$ for each value of the wave phase:

$$A(R_{\rm areal}, \phi) \simeq \sum_{k=0}^{N} \frac{A_{(k)}(\phi)}{R_{\rm areal}^k} \,, \tag{5.18a}$$

$$t(R_{\rm areal}, \phi) \simeq r_* + \sum_{k=0}^{N} \frac{t_{(k)}(\phi)}{R_{\rm areal}^k} \,, \tag{5.18b}$$

where the asymptotic waveform is fully described by $A_{(0)}(\phi)$ and $t_{(0)}(\phi)$. By inverting the extrapolated $t_{(0)}(\phi)$, we obtain the phase as a function of time, which can be used in turn to obtain the amplitude as a function time.

Choosing the extraction radii and extrapolation order for this method fol-

lows the same rough recommendations described in Secs. 5.2.4 and 5.2.5. Note also that the restriction that the data have an invertible phase as a function of time is not insurmountable. For example, data for Ψ_4 in the equatorial plane is purely real, hence has a phase that simply jumps from 0 to π discontinuously. However, we can define a new quantity

$$w(t) \equiv \Psi_4(t) + i\dot{\Psi}_4(t) \,. \tag{5.19}$$

This is simply an auxiliary quantity used for the extrapolation, with a smoothly varying, invertible phase. The imaginary part is discarded after extrapolation.

5.3.2 Results

In Figs. 5.7 and 5.8 we plot the convergence of the relative amplitude and phase of the extrapolated $(l, m) = (2, 2)$ mode of the Ψ_4 waveform for extrapolation orders $N = 1, \ldots, 5$. A common feature of both plots is that during the inspiral, the higher the extrapolation order, the better the convergence. However, the noise is amplified significantly for large orders of extrapolation. This method of extrapolation amplifies high-frequency noise significantly, compared to the tortoise-coordinate method.

In the inspiral portion, we have a decreasing error in the extrapolation of the phase and the amplitude as the wavelength of the gravitational waves decreases. In the merger/ringdown portion, a more careful choice of the radii and order of extrapolation needs to be made. Since near-field effects are less significant in the data extracted at larger radii, extrapolation at low order ($N = 2, 3$) seems sufficient. Data extrapolated at large order ($N = 4, 5$) has a larger error in the phase and amplitude after merger than data extrapolated at order

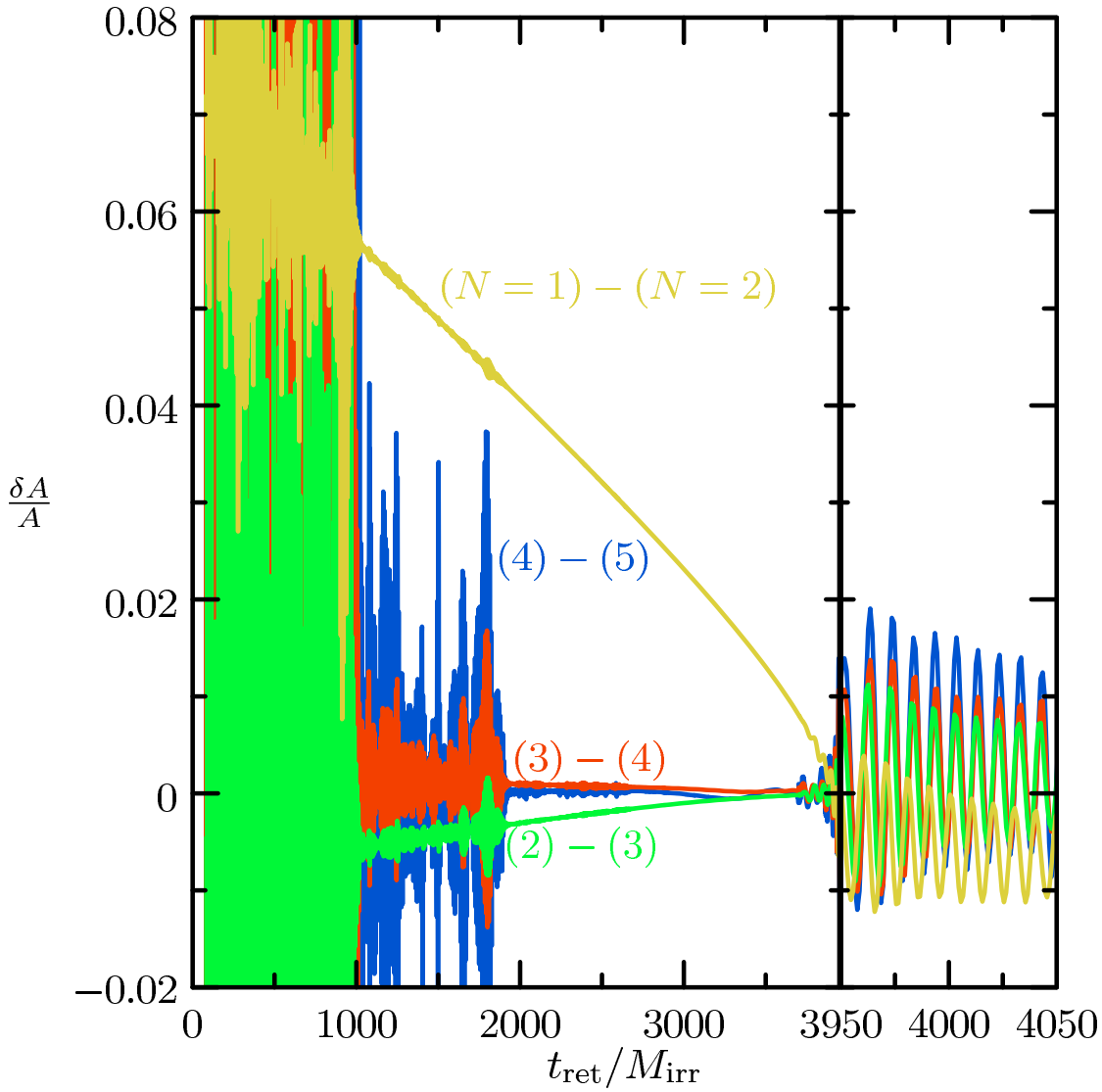

Figure 5.7: Convergence of the amplitude of Ψ_4 extrapolated using the wave phase, with increasing order N of the extrapolating polynomial. This figure shows the convergence of the relative amplitude of the extrapolated Newman–Penrose waveform extrapolated using the wave phase, as the order N of the extrapolating polynomial is increased. (See Eq. (5.18).) Increasing the extrapolation order tends to amplify the apparent noise during the early and late parts of the waveform, but it improves convergence. The dotted vertical line denotes merger.

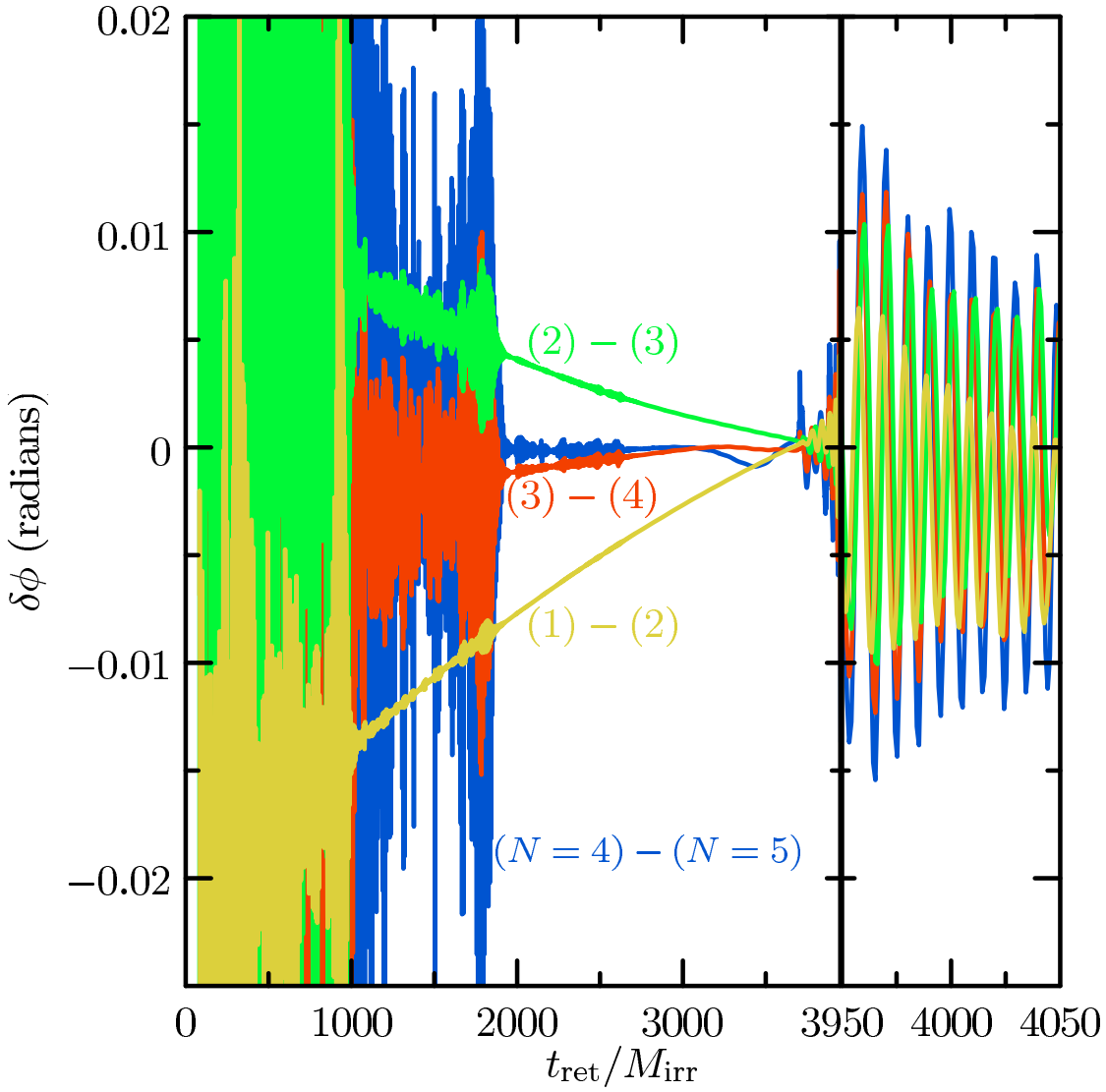

Figure 5.8: Convergence of the phase of Ψ_4 as a function of time extrapolated using the wave phase, with increasing order N of the extrapolating polynomial. Again, increasing the extrapolation order tends to amplify the apparent noise during the early and late parts of the waveform, though convergence is improved significantly.

$N = 2$ or 3. Moreover, the outermost extraction radius could be reduced, say to $R_{\rm outer}/M_{\rm irr} = 165$ instead of $R_{\rm outer}/M_{\rm irr} = 225$, without having large extrapolation error at late times. Using the radius range $R/M_{\rm irr} = 75, \ldots, 160$ instead of the range $R/M_{\rm irr} = 75, \ldots, 225$ would leave the extrapolation error during the merger/ringdown almost unchanged, while the extrapolation error during the inspiral would increase by about 70%.

We note that this method allows easy extrapolation of various portions of the waveform using different extraction radii and orders since—by construction—the wave phase is an independent variable. For example, solve for the phase value of the merger $\phi_{\rm merger}$ (defined as the phase at which the amplitude is a maximum), then use the radius range $R/M_{\rm irr} = 75, \ldots, 225$ for all phase values less than $\phi_{\rm merger}$ and the range $R/M_{\rm irr} = 75, \ldots, 160$ for all larger phase values.

This method has been tested also using the coordinate radius R and the naive time coordinate T, in place of areal radius and corrected time. We found results similar to those discussed in Sec. 5.2. Using the new time coordinate $t_{\rm corr}$ instead of the naive time coordinate T improved the extrapolation during the merger/ringdown, as found in Sec. 5.2.

As with the previous extrapolation method, increasing the extrapolation order gives a faster convergence rate of waveform phase and amplitude, but it amplifies noise in the extrapolated waveform. To improve convergence without increasing the noise, we need a good filtering technique for the inspiral data. The junk-radiation noise decreases significantly as a function of time, disappearing several orbits before merger. However, this noise could be reduced by using more extraction radii in the extrapolation process, or by running the data through a low-pass filter. See Sec. 5.5 for further discussion of filtering.

5.4 Comparison of the two methods

Both methods showed good convergence of the amplitude and the phase of the waveform as N increased in the inspiral portion. (See Figs. 5.3 and 5.7 for the amplitude, and Figs. 5.4 and 5.8 for the phase.) The wave-phase extrapolation method was more sensitive to noise. In the merger/ringdown portion, both methods have similar convergence as N increases, especially when the correction is taken to account for the dynamic lapse. The use of the time parameter $t_{\rm corr}$ improved the agreement between the methods significantly in the merger/ringdown portion for all extrapolation orders. Extrapolating at order $N = 2$ or 3 seems the best choice as the difference is a minimum then.

In Fig. 5.9, we show the relative amplitude difference between data extrapolated at various orders ($N = 1, \ldots, 5$). There is no additional time or phase offset used in the comparison. Ignoring high-frequency components, the difference in the relative amplitude is always less than 0.3% for different extrapolation orders. Even including high-frequency components, the differences between the two methods are always smaller than the error in each method, as judged by convergence plots. In Fig. 5.10, we show the *phase* difference between the data extrapolated using both methods. As in the relative amplitude-difference plots, the best agreement is achieved during the inspiral portion. Ignoring high-frequency components, the difference is less than 0.02 radians for all orders. In the merger/ringdown portion, the best agreement between extrapolated waveforms is at order $N = 2$ or 3 where the phase difference is less than 0.01 radians.

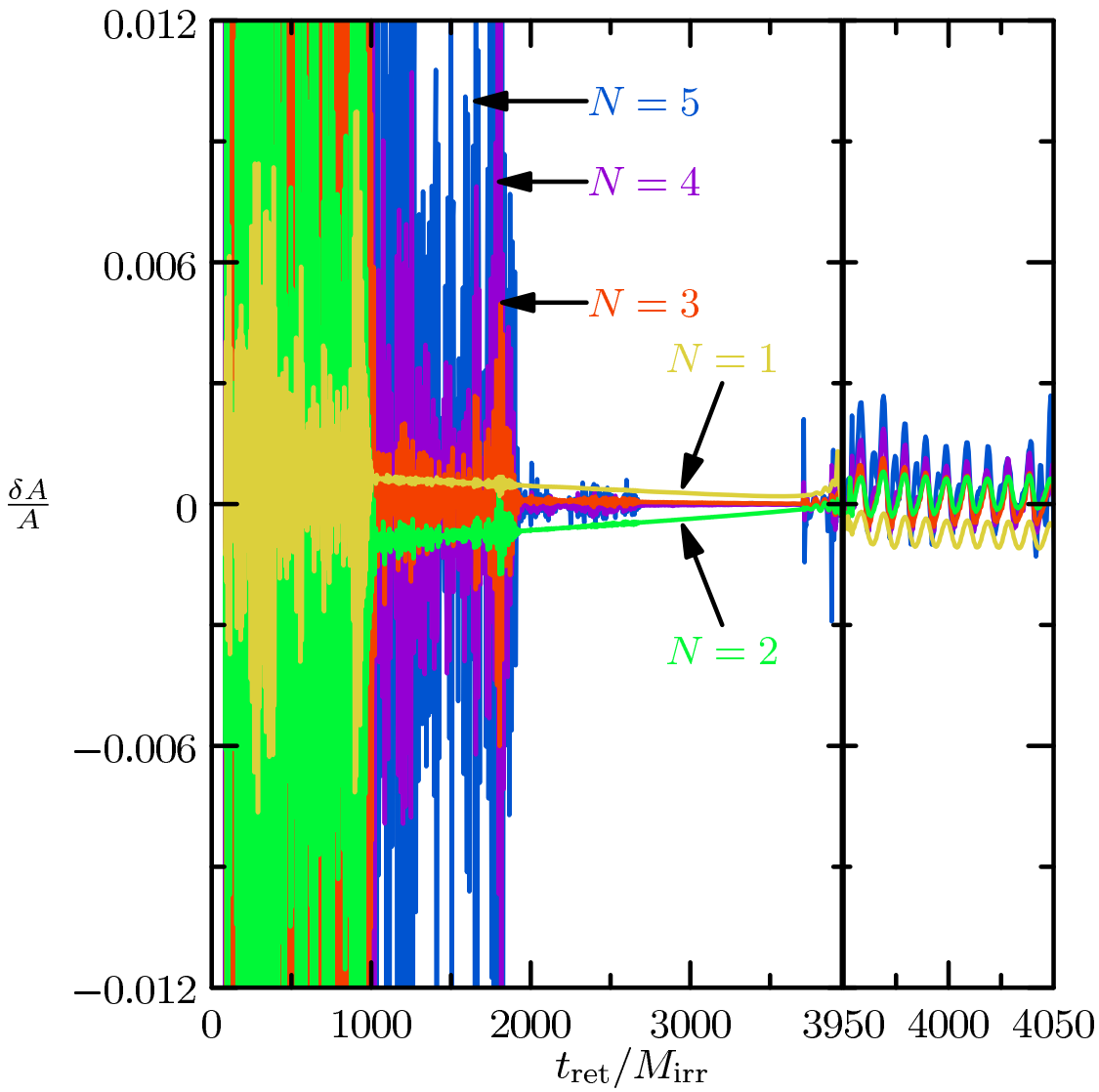

Figure 5.9: Relative difference in the amplitude of the two extrapolation methods as we increase the order of extrapolation. The best agreement between both methods is at orders $N = 2$ and 3 extrapolation, for which the relative difference in the amplitude is less than 0.3% during most of the evolution.

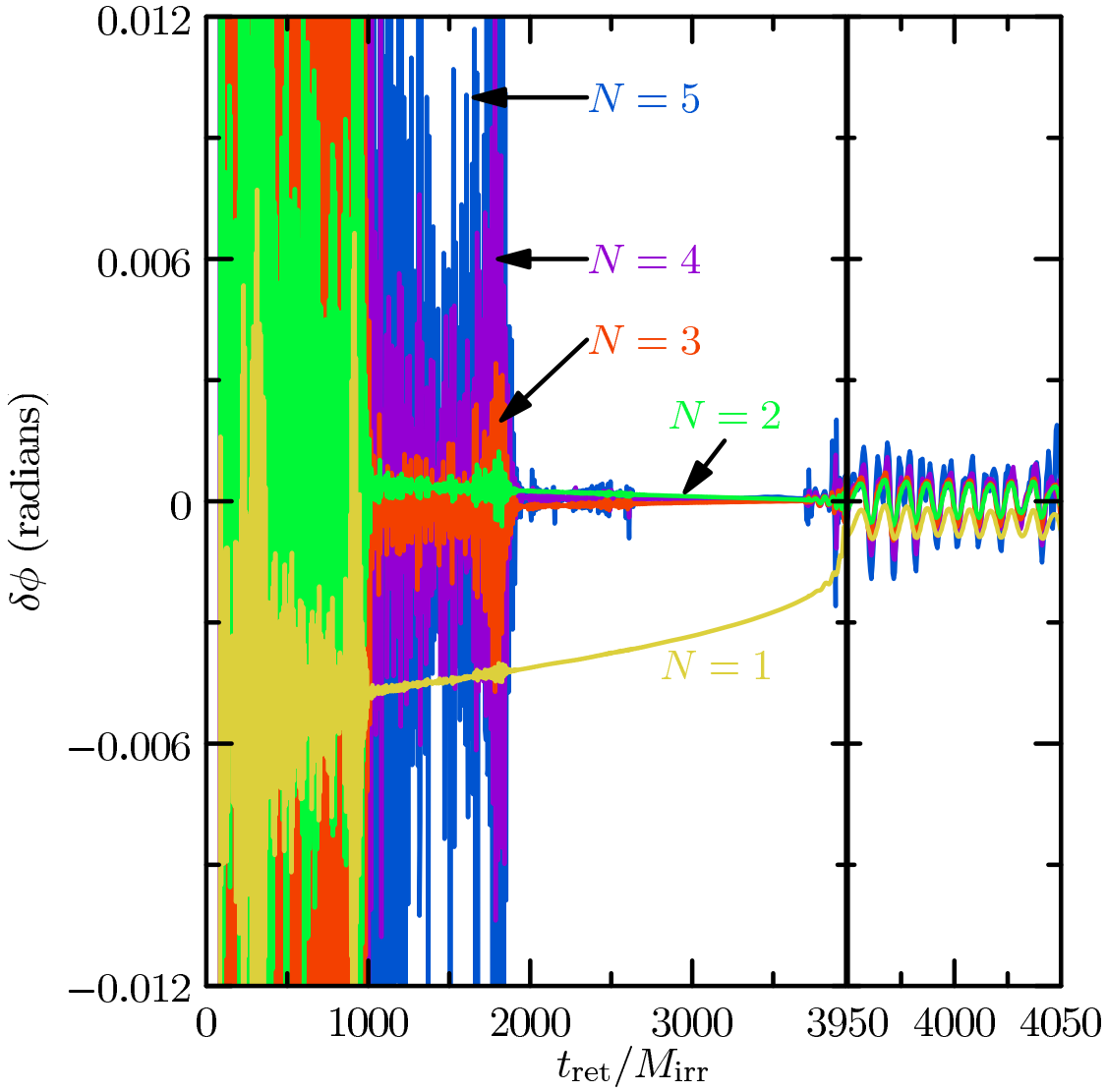

Figure 5.10: Phase difference of the two extrapolation methods as we increase the order of extrapolation. This figure shows the phase difference between waveforms extrapolated using each of the two methods. The best agreement between the methods after merger is at orders $N = 2$ and 3. The relative difference in the amplitude is less than 0.02 radians during most of the evolution.

5.5 Filtering

Extrapolating waveforms containing poorly resolved high-frequency components amplifies the magnitude of the noise in the signal at infinity. One possible solution to the problem is to filter out the junk radiation from the gravitational waveform. This is possible when the noise has higher frequency than the physical data of interest. The MATLAB function `filtfilt`, using a low-pass Butterworth filter with cutoff frequency between the noise frequency and the highest gravitational-wave frequency, is satisfactory for many uses when applied to the early parts of the data. This filtering may be applied to either the complex data, or to its amplitude and phase—the latter allowing for a lower cutoff frequency. There is also a marginal benefit to be gained when the input data are filtered before extrapolation, though filtering of the final result is also necessary. It is also possible to fit a low-order polynomial to the data, filter the residual, and add the filtered data back to the fit; this removes very low-frequency components, reducing the impact of Gibbs phenomena.

For the data presented here, we use a sixth-order Butterworth filter with a physical cutoff frequency of $\omega_{\rm cutoff} = 0.075/M_{\rm irr}$,[9] which is roughly eight times the maximum frequency of the physical waveforms expected in the filtered region. The filter is applied individually (using the `filtfilt` function) to the amplitude and phase data, in turn. Because of remaining Gibbs phenomena at late times, we use unfiltered data after $t_{\rm ret}/M_{\rm irr} = 3000$.

One basic diagnostic of the filtering process is to simply look at the difference between filtered and unfiltered data. If there are low-frequency components in these curves, we know the cutoff frequency needs to be raised. In

[9]Note that MATLAB expects the input frequency as a fraction of the data's Nyquist frequency.

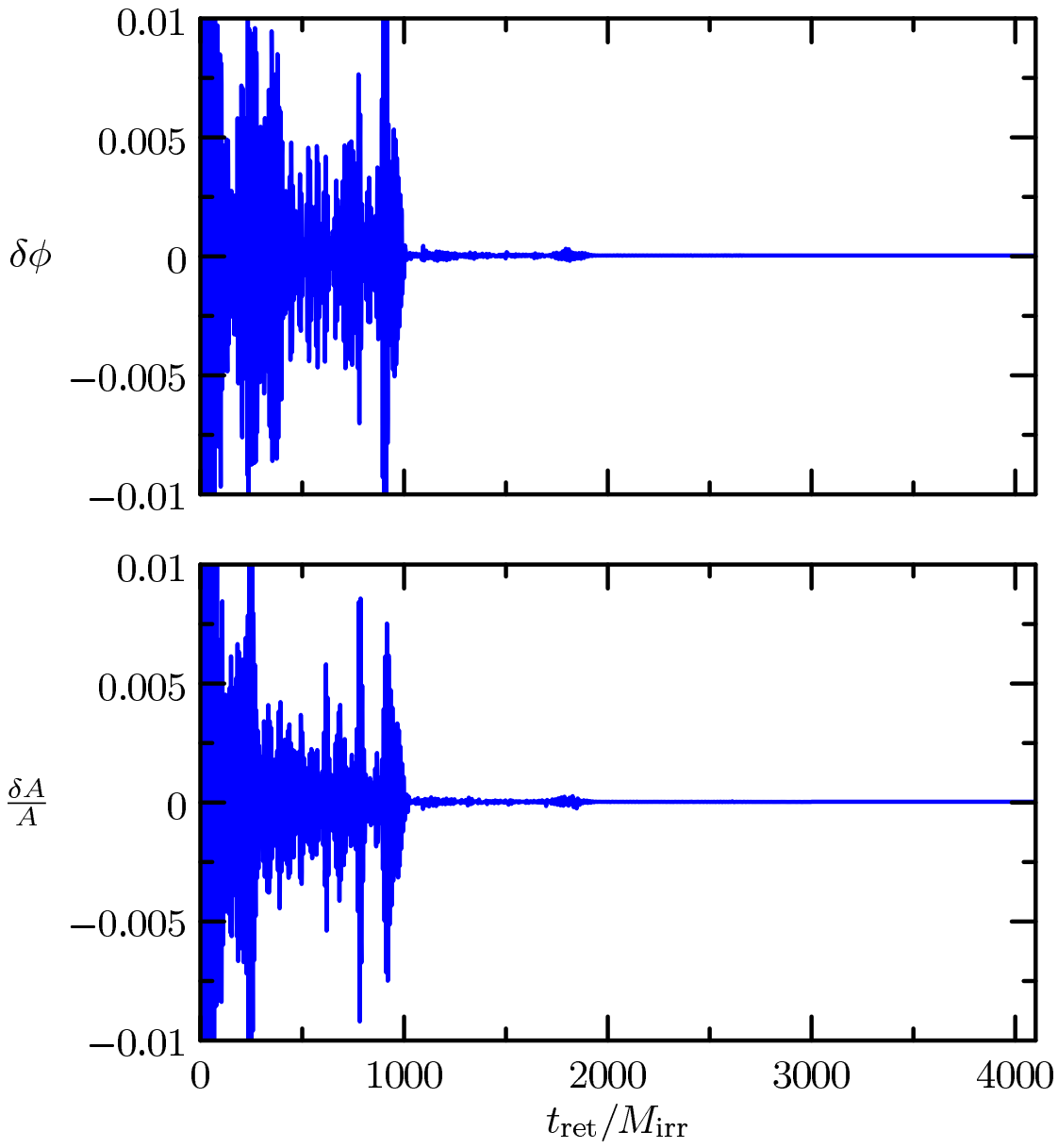

Figure 5.11: Difference between the filtered and unfiltered amplitude and phase of the waveform with third-order extrapolation. The upper panel shows the relative amplitude difference between the filtered and unfiltered waveforms; the lower panel shows the phase difference.

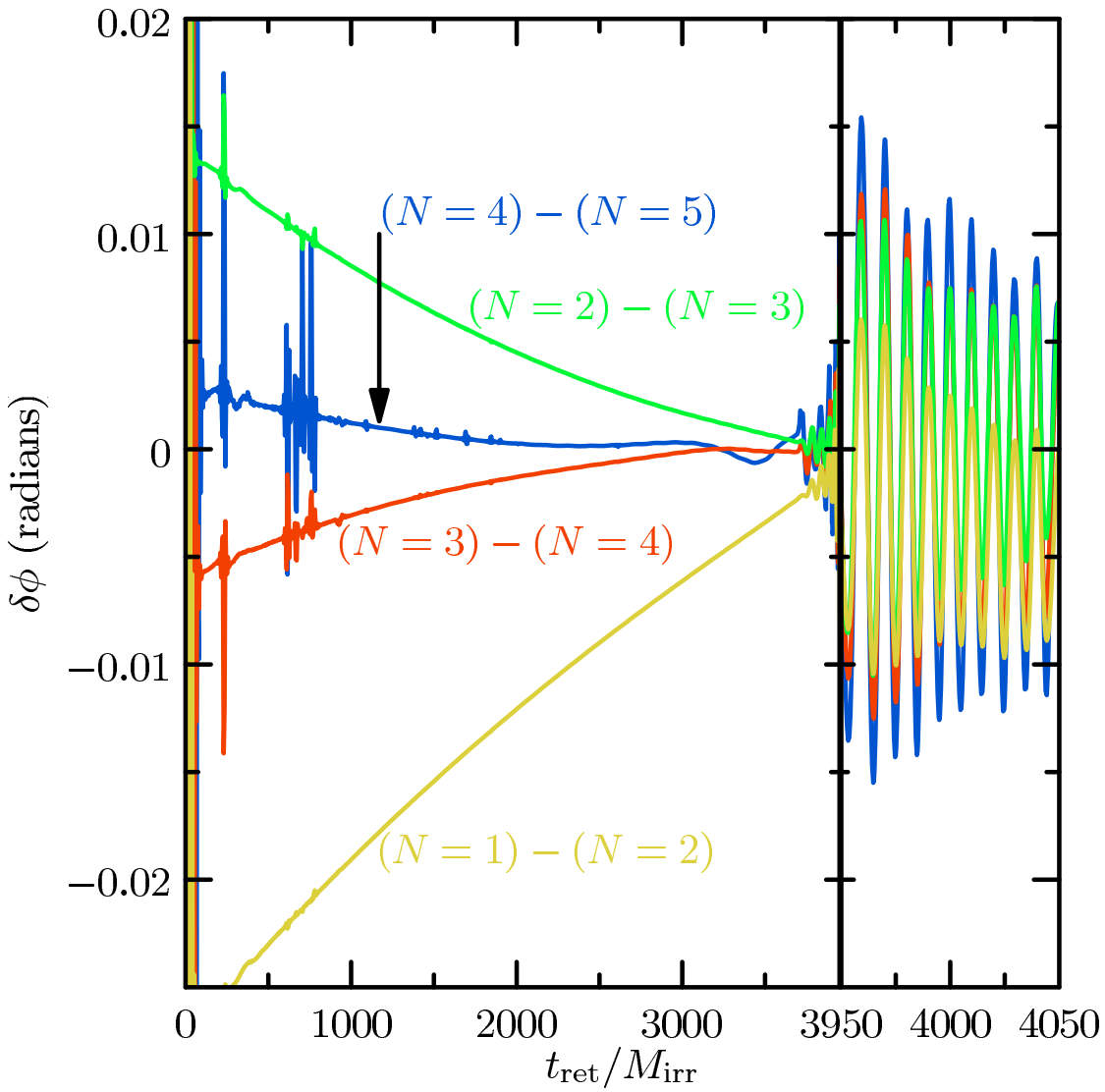

Figure 5.12: The filtered version of Fig. 5.4. We filtered the extrapolated waveforms and redid Fig. 5.4, which shows the phase difference between waveforms extrapolated at various orders. This plot shows much smaller high-frequency components at early times.

Fig. 5.11, we show the difference in relative amplitude (upper panel), and phase (lower panel). Because there is no difference between the filtered and unfiltered waveforms on the timescale of the physical gravitational waves ($\gtrsim 100\, M_{\rm irr}$), we conclude that the filter's cutoff frequency is high enough to retain the physical information.

On the other hand, to check that the filter's cutoff frequency is low enough to achieve its purpose, we look at data which previously showed the undesirable high-frequency characteristics. In Fig. 5.12, we show the same data as in Fig. 5.4, when the data are filtered before subtraction. The size of the noise at early times is greatly reduced. There are still significant high-frequency features in the plot, though they are much smaller than in the unfiltered data. Presumably these features are simply so large in the input data that even with the large suppression from the filter, they are still noticeable. It may be possible to remove them by further decreasing the filter's cutoff frequency, though this would require better handling of Gibb's phenomena from the beginning and end of the wave. We find the present filter sufficient for the demonstration purposes of this section.

5.6 Conclusions

We have demonstrated two simple techniques for extrapolating gravitational-wave data from numerical-relativity simulations. We took certain basic gauge information into account to improve convergence of the extrapolation during times of particularly dynamic gauge, and showed that the two methods agree to within rough error estimates. We have determined that the first method presented here is less sensitive to noise, and more immediately applies to arbitrary

wavelike data; this method has become the basic standard in use by the Caltech–Cornell collaboration. In both cases, there were problems with convergence after merger. The source of these problems is still unclear, but will be a topic for further investigation.

As with any type of extrapolation, a note of caution is in order. It is entirely possible that the "true" function being extrapolated bears little resemblance to the approximating function we choose, outside of the domain on which we have data. We may, however, have reason to believe that the true function takes a certain form. If the data in question are generated by a homogeneous wave equation, for instance, we know that well-behaved solutions fall off in powers of $1/r$. In any case, there is a certain element of faith that extrapolation is a reasonable thing to do. While that faith may be misplaced, there are methods of checking whether or not it is: goodness-of-fit statistics, error estimates, and convergence tests. To be of greatest use, goodness-of-fit statistics and error estimates for the output waveform require error estimates for the input waveforms. We leave this for future work.

We still do not know the correct answers to the questions numerical relativity considers. Thus, large systematic errors could be hidden in plain view. To eliminate them, we need to use multiple, independent methods for our calculations. For example, we might extract Ψ_4 directly by calculating the Riemann tensor and contracting appropriately with our naive coordinate tetrad, and extract the metric perturbation using the formalism of Regge–Wheeler–Zerilli and Moncrief. By differentiating the latter result twice and comparing to Ψ_4, we could verify that details of the extraction methods are not producing systematic errors. (Just such a comparison was done in Ref. [68] for waveforms extrapolated

using the technique in this paper.) Nonetheless, it is possible that infrastructure used to find both could be leading to errors.

In the same way, simulations need to be performed using different gauge conditions, numerical techniques, code infrastructures, boundary conditions, and even different extrapolation methods. Only when multiple schemes arrive at the same result can we be truly confident in any of them. But to arrive at the same result, the waveforms from each scheme need to be processed as carefully as possible. We have shown that extrapolation is crucial for highly accurate gravitational waveforms, and for optimized detection of mergers in detector data.

CHAPTER 6

MEASURING ORBITAL ECCENTRICITY AND PERIASTRON ADVANCE IN QUASI-CIRCULAR BLACK HOLE SIMULATIONS

6.1 Introduction

[1] The inspiral and merger of binary black holes or neutron stars is one of the most promising sources for current and future generations of laser interferometric gravitational wave detectors such as LIGO and VIRGO. The late stage of the inspiral, corresponding to the final few orbits and merger of the binary, is highly dynamical and involves strong gravitational fields, and it must be handled by numerical relativity. Breakthroughs in numerical relativity have allowed a system of two inspiraling black holes to be evolved through merger and the ringdown of the remnant black hole [204, 206, 72, 14, 74, 143, 118, 212, 215, 57, 182, 121, 217, 51, 211].

During the inspiral of an isolated binary, the orbit circularizes via the emission of gravitational waves [194, 195]. As a result, even binaries starting with some eccentricity at the beginning of their stellar evolution end up having negligible eccentricities by the time the frequency of the emitted gravitational radiation enters the bandwidth of ground based detectors. This motivated modeling these binaries as point particles in quasi-circular orbits by constructing binary black hole initial data and evolving them.

However, different physical scenarios [172, 161, 184, 81, 128, 129, 230] sug-

[1] This chapter will be incorporated into a paper to be published with Lawrence E. Kidder, Harald P. Pfeiffer, and Saul A. Teukolsky. The data comes courtesy of Mark A. Scheel, Luisa Buchman and Geoffrey Lovelace.

gest that binaries could approach merger with a significant eccentricity without being circularized by radiation reaction. This implies that eccentric binaries are a potential gravitational wave source for ground based interferometers. For example, in globular clusters, the Kozai mechanism [172] could increase the eccentricity of an inner binary's orbit through a secular resonance caused by a third perturbing black hole on an outer orbit [184]. Many-body encounters of black holes in globular clusters could also result in the merger of highly eccentric binaries [161]. Ref. [230] predicted that 30% of the hierarchical triple black hole systems formed in a globular cluster will possess eccentricities greater than 0.1 when their emitted gravitational waves pass through a frequency of 10Hz.

For these reasons, analytical templates have been constructed for the gravitational wave signal emitted by compact binaries moving in inspiraling eccentric orbits [96, 170, 209]. In this case, orbits involve three different time scales: orbital period, periastron precession and radiation reaction time scales. By combining these three time scales, one computes "postadiabatic" short-period contributions to the orbital phasing and gravitational wave polarizations. These gravitational wave polarizations are needed for astrophysical measurements with gravitational wave interferometers.

Beyond the Newtonian limit, the orbital eccentricity is not uniquely defined. Ref. [177] used a definition of the eccentricity for which a Newtonian orbit is momentarily tangent to the true orbit (the "osculating" eccentricity), while other authors [93, 96, 170, 209] defined multiple "eccentricities" to encapsulate different aspects of noncircular orbits at post-Newtonian (PN) order. Another useful definition for large eccentricity in numerical simulations is given in Refs. [25, 185].

Similarly, numerical relativists [197, 152, 64] introduced several methods for defining and measuring the eccentricity using the residual oscillations in the orbital frequency, proper horizon separation and coordinate separation. These eccentricity definitions are necessary to compare the numerical waveforms with the waveforms produced by analytic techniques (i.e. PN methods). They behave differently depending on the magnitude of the eccentricity and the noise in the run. This makes it important to specify the validity regimes of these definitions.

In Ref. [226], the authors studied the transition from inspiral to plunge in general relativity by computing gravitational waveforms of eccentric nonspinning, equal mass black-hole binaries. They analyzed the radiation of energy and angular momentum in gravitational waves, the contribution of different multipolar components and the final spin of the remnant black hole.

Ref. [149] presented results from numerical simulations of equal-mass, nonspinning binary black hole inspiral and merger for various eccentricities, and they measured the final mass and spin of the remnant black hole. Ref. [148] compared a numerical relativity simulation of an eccentric binary system with eccentricity 0.1 with corresponding PN results. They found a better agreement when the eccentric PN expressions are expanded in terms of the frequency-related parameter ($x \equiv (\Omega M)^{2/3}$, where Ω is orbital frequency and M is total mass of the binary) rather than the mean motion $n = 2\pi/P$, where P is the orbital period.

In this paper, we look at several eccentricity definitions that are useful for low eccentricity quasi-circular runs. In Section 6.2, we compare all of these approaches, as well as some new ones, on the 15-orbit inspiral presented by Boyle

et al. [51]. Next, by measuring the extrema in the eccentricity residual, we estimate the radial frequency. This allows us in Section 6.3 to estimate the periastron advance for this quasi-circular run from the ratio of the orbital frequency to the radial frequency for the 15-orbit equal mass inspiral as well as the precession of a quasi-circular nonspinning binary of mass ratio 2. The numerically estimated periastron advance is then compared to the 3PN formula of the periastron advance [209, 93, 91]. As a check to our results in the quasi-circular case, we evolved an eccentric nonspinning equal mass binary simulation ($e = 0.05$) that allows measuring the precession more easily before the plunge phase.

6.2 Eccentricity estimates

For a quasi-circular orbit with zero eccentricity, orbital variables and their time derivatives change monotonically as the holes inspiral to merger. In practice, however, a small eccentricity is introduced by the imperfect initial data. As a result, a small residual oscillation that is proportional to the eccentricity is added to the monotonically changing orbital variables and their derivatives. To estimate the eccentricity, one needs to determine these residual oscillations.

Different methods to estimate the eccentricity [197, 152, 64] used the orbital frequency, (coordinate or proper horizon) separation between the holes, or some Newtonian formula containing both of these variables. Similarly, time derivatives of these variables could be used in these definitions of the eccentricity. Basically all approaches construct a quantity $e_X(t)$ such that for Newtonian orbits

$$e_X(t) = e\cos(\Omega_r t), \tag{6.1}$$

where $e_X(t)$ is the residual eccentricity, e is the eccentricity and Ω_r is the frequency of radial oscillations in the quasi-circular orbit. One then assumes that this expression holds for general relativistic inspirals, plots $e_X(t)$ for the binary black holes and reads off the eccentricity e as the amplitude. These eccentricity estimates are not local nor continuous variables but rather orbit-averaged quantities.

The estimated value of the eccentricity will differ slightly depending on the method used and the noise in the numerical data. In this paper, we compare typical eccentricity estimates using a Newtonian formula as in Ref. [64] or the orbital frequency and separation as in Ref. [152]. These eccentricities are also compared to new ones computed from the wave phase and frequency extracted at a given radius. Other definitions of the eccentricity could be used, but we restrict the study to these typical definitions.

The run used to compute the eccentricity data is 0030c1 described in Ref. [51]. The data is for a 15-orbit quasi-circular, equal mass and nonspinning binary. The eccentricity estimated for this run was about 6×10^{-5}.

6.2.1 Measuring eccentricity from a Newtonian definition

In Ref. [64], a relationship that holds in the Newtonian limit is used to define the eccentricity $e_{\rm Newt}$:

$$\left[\Omega(t)^2 r(t)^3/M - 1\right] = e_{\rm Newt} \cos\phi(t)\,, \tag{6.2}$$

where Ω is the orbital frequency, r is the coordinate separation D or the proper horizon separation S, and $\phi(t)$ is the radial phase. The amplitude of the residual

oscillation of $\Omega(t)^2 r(t)^3/M$ is defined as the eccentricity $e_{\rm BCP}$ (BCP stands for the authors of Ref. [64]):

$$e_{\rm BCP} = \Omega(t)^2 r(t)^3/M - \left[\Omega(t)^2 r(t)^3/M\right]_{\rm fit} . \tag{6.3}$$

To estimate this eccentricity $e_{\rm BCP}$, we fit the function $\Omega(t)^2 r(t)^3/M$ to a polynomial in time defined as

$$f(t) = \sum_{i=0}^{n} a_i t^i . \tag{6.4}$$

We found that a polynomial of fifth order is enough to get a good fit. The eccentricity is then measured as the extremum in the residual function at a given time.

In Fig. 6.1, we plot the estimated eccentricity residual computed using the coordinate separation and proper horizon separation as described above. Using the proper horizon separation S, the estimated eccentricity, 1.5×10^{-4}, is larger by a factor of 4 than in the case where the coordinate separation D is used (4×10^{-5}). This is partially because these distances scale as $(S/D)^3 \sim 1.8$. Both eccentricity residuals are in phase during the whole time interval as expected. In both cases, the eccentricity magnitude decreases between $t = 500M$ and $t = 1500M$. However, beyond this time interval, the magnitude of the residual oscillations starts to increase for the horizon-based eccentricity as relativistic and tidal effects become more important. On the other hand, the eccentricity measurement using the coordinate separation does not show such behavior before merger.

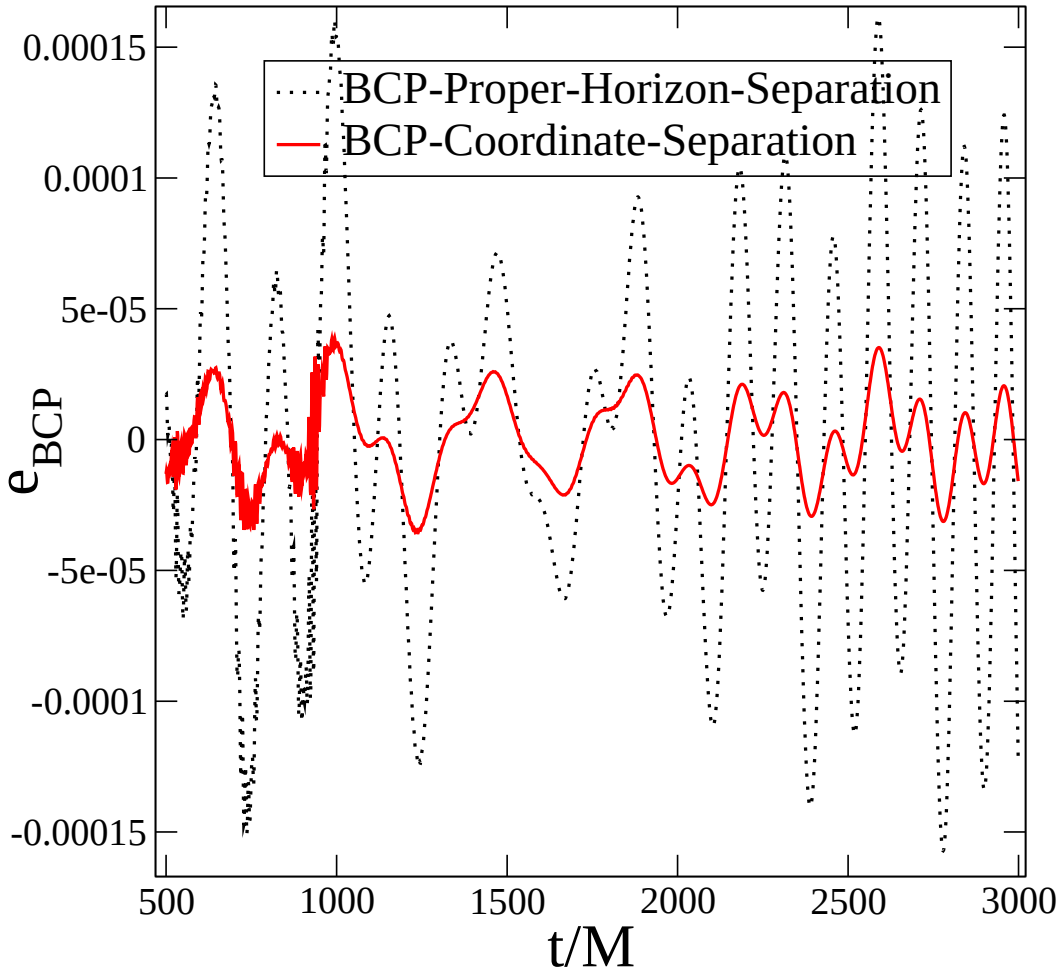

Figure 6.1: The eccentricity residual $e_{\rm BCP}$ defined in Ref. [64] measured from the coordinate separation and the proper horizon separation as a function of time. The estimated eccentricity from the horizon separation is larger than the estimated eccentricity from the coordinate separation.

6.2.2 Measuring eccentricity from residual oscillations of orbital variables

A simpler method to define and measure the eccentricity was given in Ref. [152]. Instead of using a Newtonian relation to extract the residual eccentricity, one can simply read out the residual oscillation due to the eccentricity by fitting the orbital frequency, Ω, coordinate separation, D, or proper horizon separation, S, to a polynomial of order $n/2$ of the form

$$X(t) = \sum_{i=1}^{n} a_i (t_m - t)^{i/2} , \tag{6.5}$$

where t_m, the coalescence time, and the parameters a_i are estimated from a least-squares fit. Then, the eccentricity is defined as

$$e_{\rm X}(t) = \frac{X_{\rm NR}(t) - X_{\rm fit}(t)}{k X_{\rm fit}(t)} , \tag{6.6}$$

where $X_{\rm NR}(t)$ is the numerical orbital variable as a function in time, and $X_{\rm fit}(t)$ is the polynomial fit of $X_{\rm NR}(t)$. The factor k is 2 in the denominator when the orbital frequency is used to measure the eccentricity and 1 otherwise. In the Newtonian limit, these eccentricities are identical to first order in eccentricity.

These definitions of the eccentricity could be derived from the following relations [187]:

$$\frac{d}{a} = 1 - e\cos\mathcal{M} + \frac{e^2}{2}(1 - \cos 2\mathcal{M}) + O(e^3) , \tag{6.7}$$

and

$$\Phi = \mathcal{M} + 2e\sin\mathcal{M} + \frac{5}{4}e^2 \sin 2\mathcal{M} + O(e^3) , \tag{6.8}$$

where d is the distance between the two bodies, a is the semi-major axis, $\mathcal{M}$ is the mean anomaly and Φ is the orbital phase. The factor k can easily be seen to be 1 from Eq. (6.7) and 2 from Eq. (6.8). These equations (6.7 and 6.8) measure the

deviation of the eccentric orbital variables d and Φ from those of a circular orbit. The derivatives of these variables could also be used to measure the eccentricity. Notice that for the current eccentricity magnitude ($e = 6 \times 10^{-5}$), the next-to-leading eccentricity terms [$O(e^2)$] are negligible for our numerical simulations.

In Fig. 6.2, the eccentricity residuals are computed using the method described above by using the orbital frequency, the proper horizon separation and the coordinate separation. The value of the eccentricity, 6×10^{-5}, estimated from the amplitude of the residual oscillations is nearly identical for the three orbital variables at early times ($t < 2500M$). The phasing is also consistent between the different eccentricity estimates; the orbital frequency is a maximum when the separation is a minimum and vice-versa. The decrease in the eccentricity magnitude is consistent for the coordinate separation and orbital frequency; both decrease until $t = 2500M$ and then they start to increase as additional harmonics become significant. However contrary to Fig. 6.1, the proper horizon separation method shows no increase in the eccentricity during the late stages of the inspiral, and no additional significant harmonics appears even up to $t = 3500M$. The order of the polynomial fit depends on the time range of the fit. In this case, a polynomial of fifth order was enough to capture the oscillatory behavior in the eccentricity residual in the time range $500M < t < 3500M$. Note that the orbital phase could also be used to measure the residual eccentricity using Eq.(6.6).

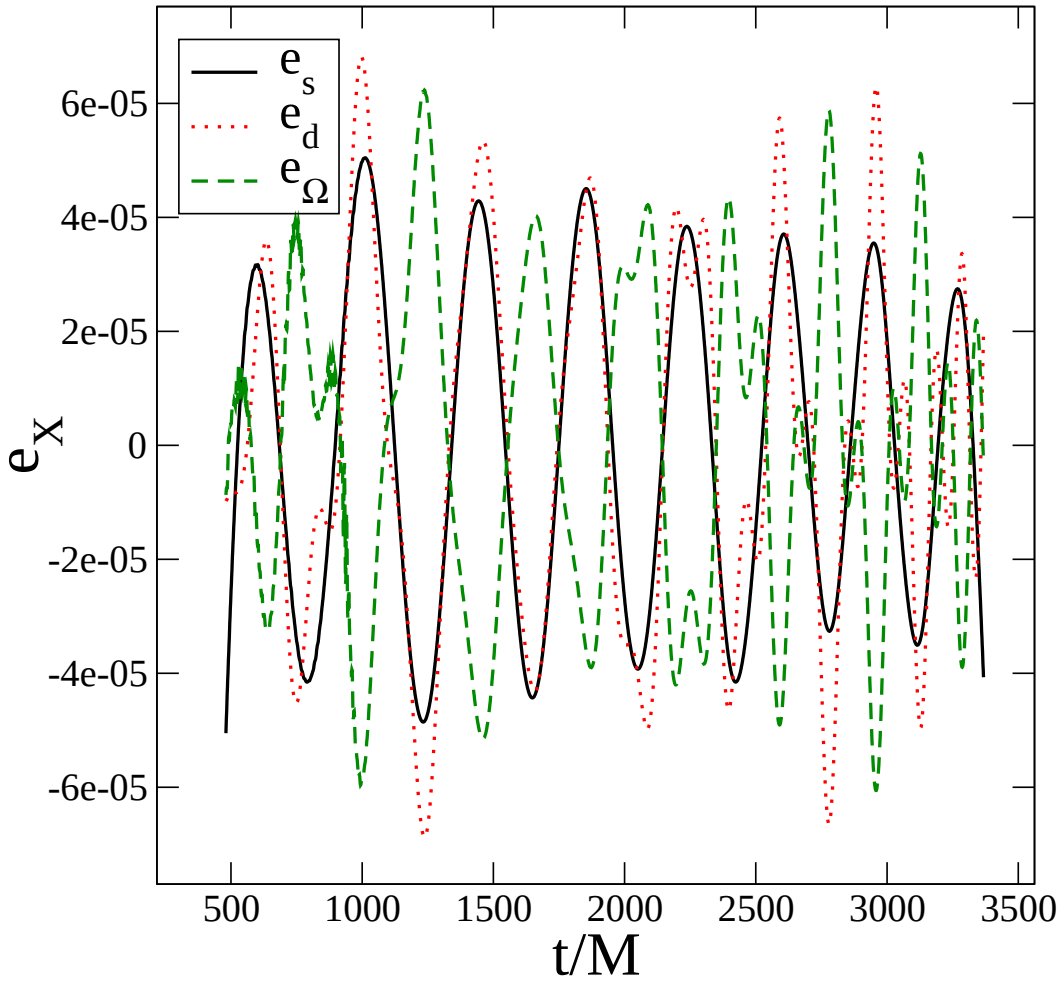

Figure 6.2: The eccentricity residuals e_Ω, e_s and e_d computed from orbital frequency, proper horizon separation and coordinate separation using Eq.(6.6). For the three cases, the residual eccentricities are consistently decreasing below the amplitude 6×10^{-5} up to $t = 2500M$. Beyond this time, the magnitudes of e_Ω and e_D are affected by additional harmonics. Still, the curves have one dominant oscillating mode during the whole interval. Contrast the behavior of the residual eccentricities in this figure with the eccentricity residuals of Fig. 6.1.

6.2.3 Measuring eccentricity from the residual wave oscillations

The well-behaved residual eccentricity computed using Eq. (6.6) motivates using it to measure the eccentricity from the wave phase and frequency. More importantly, we would like to define the eccentricity based on a gauge invariant quantity such as the phase or frequency of the waveform extrapolated at infinity. The eccentricity residual could be computed from the wave phase or frequency extracted at various radii or extrapolated to infinity using Eq.(6.6) with k equal to 2. The eccentricity estimate is independent of the radius value at which the wave is extracted. Similarly, the wave phase could be used to measure the eccentricity using the following equation:

$$e_\phi = \frac{\phi_{\rm NR}(t) - \phi_{\rm fit}(t)}{4}\,, \tag{6.9}$$

where an additional factor of $1/2$ is used because the wave phase is nearly twice the orbital phase.

The waveforms used to measure the eccentricity are contaminated by high frequency noise because of "junk radiation" (due to imperfect initial data). To measure the amplitudes and locations of the extrema in the residual eccentricity more accurately, the residual functions are filtered using a low-pass Butterworth filter with the Matlab function "filtfilt". The filtered data can be used to measure the eccentricity starting at early retarded time around $t - r^* = 1000M$ where r^* is the tortoise-coordinate radius defined as:

$$r^* \equiv r + 2M_{\rm ADM} \ln\left(\frac{r}{2M_{\rm ADM}} - 1\right)\,, \tag{6.10}$$

where $M_{\rm ADM}$ is the ADM mass of the initial data.

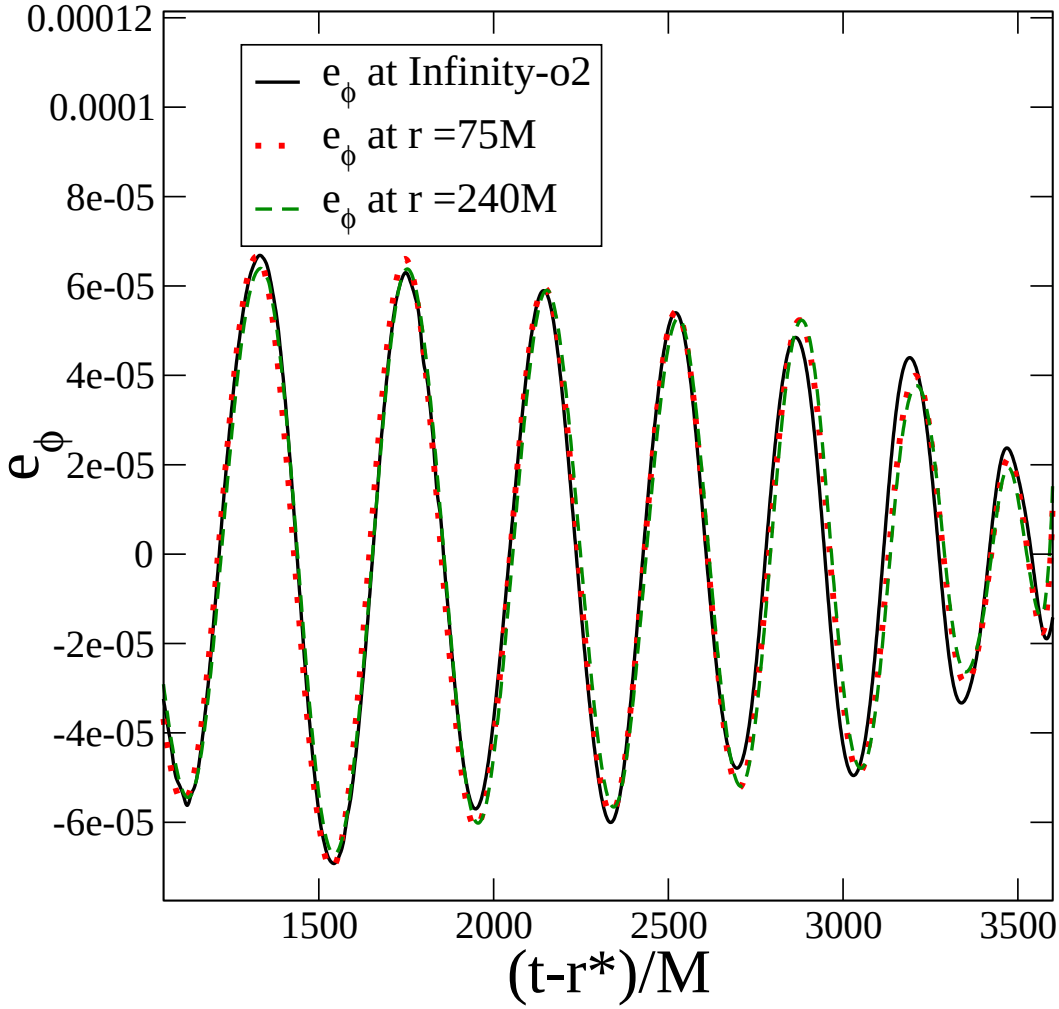

Figure 6.3: The eccentricity residual e_ϕ computed from the gravitational wave phase as a function of retarded time $t - r^*$. In this plot, the residual eccentricity is computed from the gravitational wave extracted at the radius $r = 75M$ and $r = 240M$ and from the extrapolated gravitational wave phase to infinity at second order. The three curves agree in amplitude and phase to within 5% in the time interval $1000M < t - r^* < 3000M$.

In Fig. 6.3, we plot the eccentricity residual computed from the gravitational wave phase of the (2,2) mode extracted at the radii $r = 75M$, $r = 240M$ and extrapolated to infinity using terms up to $1/r^2$versus $t - r^*$ of Ref. [51]. The residual eccentricity curves agree to within 5% in both amplitude and phase for different radii of extraction.

In Fig. 6.4, the same procedure is used to compute the residual eccentricity from the wave frequency extracted at $r = 75M$ and $r = 240M$. The extrapolated data to infinity is not shown because of its sensitivity to noise. The two curves have a nearly sinusoidal behavior with the phase agreeing to within 10%. However, the amplitude differs by 25% between the wave data measured at $r = 75M$ and $r = 240M$. Because of the noise from junk radiation early in the evolution, only a portion of the inspiral was accurate enough to be used in the estimate of the eccentricity, mainly beyond the retarded time $t - r^* \sim 2000M$. This gives the method using the wave phase a significant advantage over wave frequency.

The last two methods using wave data at finite radius (or extrapolated at infinity) seem more reliable in measuring eccentricity than the methods using orbital variables. Only one harmonic mode appears in the data, and the eccentricity is decreasing as the binaries inspiral toward merger. This improvement is mostly because the coordinate and gauge effects disappear as the data are extracted further away from the holes.

Had the noise been smaller, one could as well look at a definition of the eccentricity based on taking the time derivative of the wave frequency. Using Eq. (6.8), the second time derivative of the orbital phase is given by:

$$\ddot{\Phi} = \dddot{\mathcal{M}} + 2e(\ddot{\Phi}\cos\Phi + \dot{\mathcal{M}}^2\sin\Phi) + O(e^2)\,. \tag{6.11}$$

The eccentricity computed from the time derivative of the wave frequency $e_{d\omega}$

is then defined as

$$e_{d\omega} = \frac{\ddot{\phi}_{\rm NR} - \ddot{\phi}_{\rm fit}}{\sqrt{\ddot{\phi}^2_{\rm fit} + \dot{\phi}^4_{\rm fit}}} \,. \tag{6.12}$$

The main advantage of a such a definition is that it requires a lower order fitting polynomial, but it is more noise sensitive.

6.2.4 Eccentricity Evolution

Ref. [194] derived the evolution of the orbital eccentricity during the inspiral due to the emission of gravitational waves using the quadrupole approximation. To first order in eccentricity and in the limit of small eccentricity, the eccentricity e is related to the proper horizon separation as

$$e \propto S^{19/12} \,. \tag{6.13}$$

Using the eccentricity definitions e_ϕ (wave phase) and e_S (proper horizon separation) that give the best eccentricity residual curves,we estimate the eccentricity amplitude as a function of time. This is done by defining the "average" eccentricity over an orbit as the difference between two consecutive minima and maxima in the eccentricity residual function, so the amplitude of the eccentricity is given by:

$$e = \frac{|A_{\rm min} - A_{\rm max}|}{2} \,, \tag{6.14}$$

and the time corresponding to this "average" eccentricity is given by:

$$t(e) = \frac{t(A_{\rm min}) + t(A_{\rm max})}{2} \,, \tag{6.15}$$

where A denotes the extremum in the residual function. Given the time of this average eccentricity, the separation is easily measured numerically. In the case

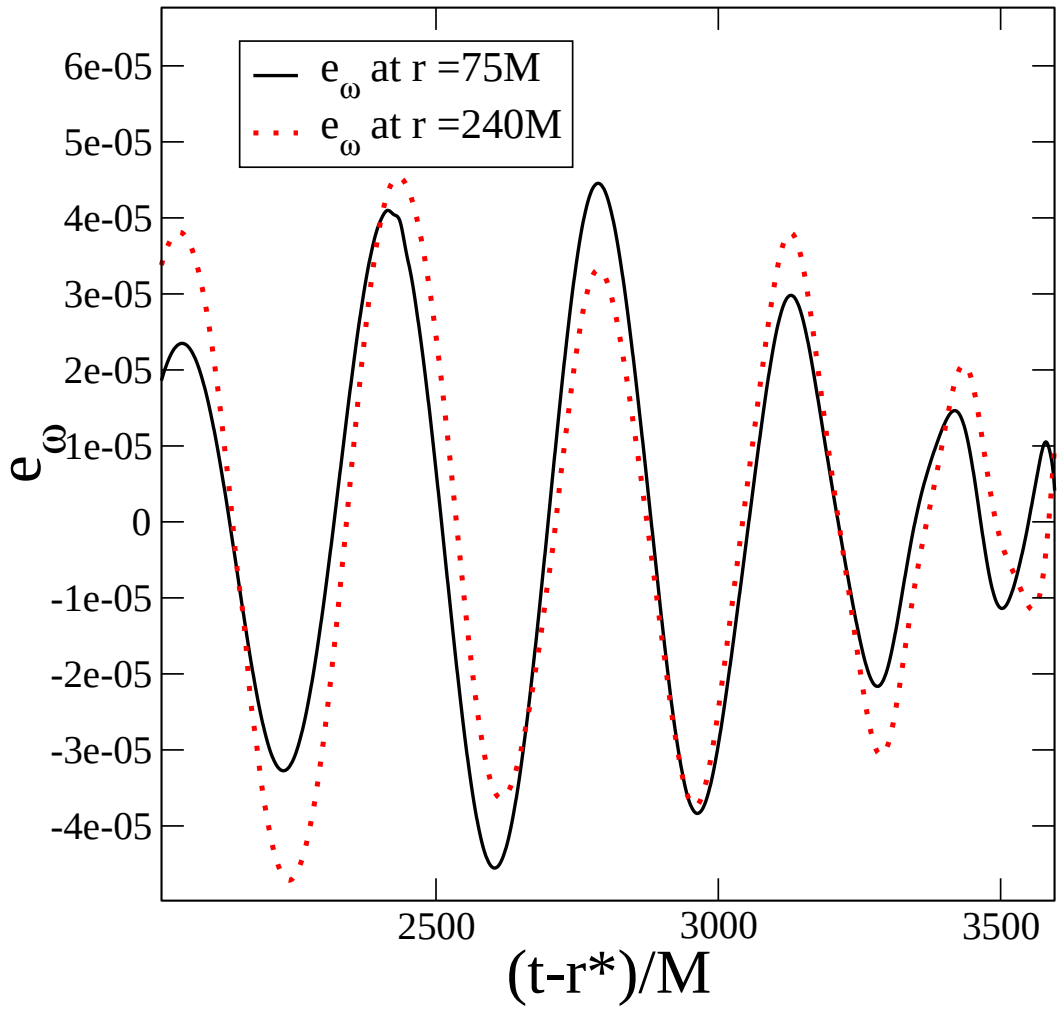

Figure 6.4: The eccentricity residual e_ω computed from the gravitational wave frequency as a function of the retarded time $t - r^*$. In this plot, the residual eccentricity is computed from the gravitational wave extracted at $r = 75M$ and $r = 240M$. The eccentricity residual is contaminated by a significant noise caused by imperfect initial data at a time earlier than $t/M = 2000$.

when gravitational wave data is used, the wave phase is approximated as a function of the separation by using the retarded time $t - r^*$. Once the variation of the eccentricity as a function of separation is measured, the power law dependence of the eccentricity on the separation is read out by fitting to the form

$$\log e = \alpha + \beta \log S \ . \tag{6.16}$$

After fitting for various eccentricities, the value β was found to be equal to 1.4 and 1.35 during the evolution of e_ϕ and e_S respectively. However, the amplitude of the residual oscillation of proper horizon separation is nearly half the residual oscillation in the wave phase. These decay estimates are in reasonable agreement with the Peters-Mathews' prediction ($\beta = 19/12 \sim 1.583$). These functions are plotted in Fig. 6.5.We note that at the beginning of the plunge phase the estimated β is about 4.2. The estimate of eccentricity amplitude is increasingly affected by the plunge when fitting the data rather than the residual oscillations during the inspiral.

All of these results were obtained using binary data with a with very low eccentricity. However for larger eccentricity, bigger differences between the various definitions of eccentricity show up as higher order corrections to these definitions become significant. We evolved an eccentric binary of black holes during the inspiral and until the plunge phase. The numerical data corresponded to an eccentric ($e = 0.05$) equal mass and nonspinning binary with total mass $M = 2.076$. With such eccentricity, we can easily measure the decay of the eccentricity during binary inspiral. In Fig. 6.7, we plot the proper separation as well as the orbital frequency as a function of time for this eccentric binary. We find the value of $\beta = 1.43$ to best fit the numerical data of the eccentricity as a power law of the proper horizon separation. This agrees very well with the numerical

value of β for the quasi-circular binary.

6.3 Periastron precession

6.3.1 Numerical method for measuring the periastron advance

Eccentricity measures e_X [see Eq. (6.6) above] yield not only the eccentricity (via the amplitude of e_X), but also their oscillation periods reveal the frequency of the radial motion, Ω_r. While in Newtonian gravity this radial frequency is equal to the orbital frequency Ω_Φ, in general relativity Ω_r is less than Ω_Φ, causing a periastron advance. The period of the radial oscillations is estimated as twice the time interval separating two consecutive extrema in the residual eccentricity curve. The procedure for computing the periastron advance from the residual eccentricity goes as follows:

- Compute a well-defined residual eccentricity e_X, which is given as some noisy oscillatory curve as a function of time.
- Find the times of the extrema of the residual eccentricity curve. This gives a time list $(t_0, t_1, ..., t_i, ...)$ corresponding to all perihelia or apohelia (i.e. extrema in the residual radial velocity).
- Between t_i and t_{i+1}, the "radial phase" changes by π. Map the time list $(t_0, t_1, ..., t_i, ...)$ to the radial phase list $(0, \pi, ..., i\pi, ...)$. This defines an averaged radial phase of the quasi-circular orbit.
- After adding a set of interpolated points for stability of the fit spaced by

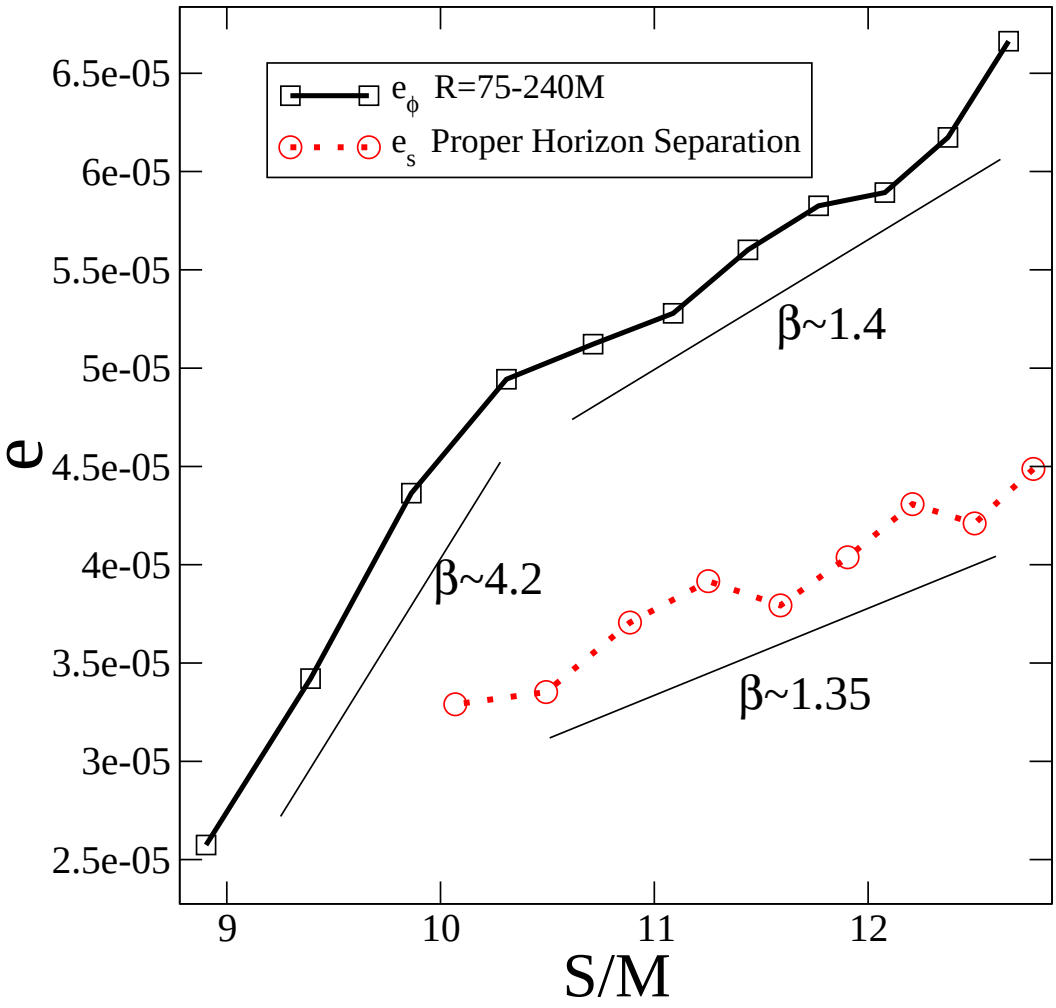

Figure 6.5: The estimated amplitude of the eccentricity as a function of proper horizon separation. We plot the estimated amplitude of the eccentricity residual using the wave phase data and the eccentricity residual of the proper horizon separation. Both curves show the eccentricity decaying with a reasonable agreement with Peter-Mathew's law before the plunge phase. Early in the inspiral, the decay of the eccentricity follows a power law nearly like 1.4 (See Eq. 6.16) compared to the Peter-Mathew's prediction of 1.58 (See. Eq. 6.13). However, the amplitude of the residual oscillation of proper horizon separation is nearly half the residual oscillation in the wave phase. Note the significance deviation from Peter-Mathew's near the plunge phase.

$5M$, plot this radial phase function and fit for it as 3^{rd} or 4^{th} order polynomial in time.

- Interpolate the orbital phase to the times of the "radial phase". This will give the orbital and radial phases evaluated at the same time list.
- Compute the orbital and radial frequencies via centered differences on both the radial and orbital phase.
- Divide the orbital frequency by the radial frequency to estimate the periastron advance.

This method allows us to measure the periastron advance from the wave phase in Fig. 6.6 for the 15-orbit quasi-circular binary black hole simulation.

6.3.2 PN Periastron advance

In Post-Newtonian approximations, the periastron advance was calculated to 3PN order in [91] for circular orbits in terms of the frequency-related parameter x ($\equiv (GM\Omega_\Phi/c^3)^{2/3}$), where Ω_Φ is the angular frequency of circular orbits, $G = 1$ is the gravitational constant and $c = 1$ is the speed of light. The fractional periastron advance per orbit, k, is defined as:

$$k \equiv \frac{\Delta\Phi}{2\pi}\,, \tag{6.17}$$

where $\Delta\Phi = \Phi - 2\pi$ is the periastron advance per orbit. The dimensionless parameter k is related to the radial frequency Ω_r and the orbital frequency Ω_Φ through:

$$k = \frac{\Omega_\Phi}{\Omega_r} - 1\,. \tag{6.18}$$

In the nonspinning circular case, the explicit expression of k is given by Eq.(5.11) of Ref [91] in the terms of the angular momentum density j for circular orbits and the symmetric mass ratio ($\nu \equiv m_1 m_2/(m_1+m_2)^2$, where m_1 and m_2 are the masses of the two bodies) as:

$$\begin{aligned} k_{\rm circ} &= \frac{3}{j^2} + \frac{1}{2}(45-12\nu)\frac{1}{j^4} + 6\Big[\frac{135}{4} + (\frac{41}{64}\pi^2 - \frac{101}{3})\nu \\ &\quad + \frac{53}{24}\nu^2 - \nu\omega_{\rm static} - \nu^2\omega_{\rm kinetic}\Big]\frac{1}{j^6}\,, \end{aligned} \tag{6.19}$$

where the value of the ambiguity parameter $\omega_{\rm static}$ was computed by Ref. [108] to be zero, and the ambiguity parameter $\omega_{\rm kinetic}$ was shown to be 41/24 by Ref. [41]. The ratio $1/j^2$ is replaced for circular orbits by $1/j^2_{circ}$ where

$$\begin{aligned} \frac{1}{j^2_{circ}} &= x\Big\{1 - \frac{1}{3}(9+\nu)x + \frac{25}{4}\nu x^2 \\ &\quad - \frac{16}{3}\Big[\frac{1}{64}\left(41\pi^2 - \frac{5269}{6}\right)\nu + \frac{511}{192}\nu^2 \\ &\quad - \frac{1}{432}\nu^3 - (\nu\omega_{\rm static} + \nu^2\omega_{\rm kinetic})\Big]x^3\Big\}\,, \end{aligned} \tag{6.20}$$

when $\nu \neq 0$ and by

$$\frac{1}{j^2_{circ}} = x(1-3x)\,, \tag{6.21}$$

in the test mass case. Using these formulas, we plot in Fig. 6.6 the precession curve $(k+1)$ as a function of the orbital frequency at 3PN order for the equal mass case $\nu = 1/4$ and the test mass case $\nu = 0$.

6.3.3 Test mass periastron advance for a Schwarzschild Black Hole

We can measure numerically the precession of a test particle freely falling into a Schwarzschild black hole using From Ref. [229], these geodesic equations are

given in term the radius r of the position vector as a function of time t by

$$r^2 \frac{d\Phi}{dt} = JB(r), \tag{6.22}$$

and

$$\frac{A(r)}{B(r)}\left(\frac{dr}{dt}\right)^2 + \frac{J^2}{r^2} - \frac{1}{B(r)} = -E \tag{6.23}$$

where E and J are constants of motion, with

$$B(r) = \left(1 - \frac{2MG}{r}\right), \tag{6.24}$$

and

$$A(r) = \left(1 - \frac{2MG}{r}\right)^{-1}. \tag{6.25}$$

Since we are interested in measuring the precession, we obtain the shape of the orbit using Eqs.(6.22) and (6.23):

$$\frac{A(r)}{r^4}\left(\frac{dr}{d\Phi}\right)^2 + \frac{1}{r^2} - \frac{1}{J^2 B(r)} = -\frac{E}{J^2}. \tag{6.26}$$

At the perihelia and aphelia of a test particle bound in an orbit around a black hole of mass M, r reaches its minimum r_- and maximum r_+ when $dr/d\Phi$ vanishes, so we can write

$$\frac{1}{r_\pm^2} - \frac{1}{J^2 B(r_\pm)} = -\frac{E}{J^2}. \tag{6.27}$$

From the above relation, the constants of motion E and J could be written as:

$$E = \frac{r_+^2/B(r_+) - r_-^2/B(r_-)}{r_+^2 - r_-^2}, \tag{6.28}$$

and

$$J^2 = \frac{1/B(r_+) - 1/B(r_-)}{1/r_+^2 - 1/r_-^2}. \tag{6.29}$$

By integrating Eq. (6.26), the angle swept out by the position vector as r increases from r_- to r_+ is given by:

$$\begin{aligned}\Phi(r_+) &= \Phi(r_-) \\ &\quad + \int_{r_-}^{r_+} A^{1/2}(r)\left[\frac{1}{J^2 B(r)} - \frac{E}{J^2} - \frac{1}{r^2}\right]^{-1/2} \frac{dr}{r^2}\,.\end{aligned} \tag{6.30}$$

Then, the orbit precesses in each revolution by an angle $\Delta\Phi$ defined as:

$$\Delta\Phi = 2|\Phi(r_+) - \Phi(r_-)| - 2\pi\,. \tag{6.31}$$

To compute the precession curve ($\Omega_\Phi/\Omega_r = k + 1$) as a function of the orbital frequency (Ω_Φ) for a quasi-circular orbit, we pick a set of values for (r_-, r_+) such that $r_+ = r_- + \epsilon$ where ϵ is a small positive number. The fractional periastron advance is estimated using Eq. (6.30), and the orbital frequency is estimated using Eq. (6.22) for each pair (r_-, r_+). Then, the precession curve is plotted in Fig. 6.6 for a test particle orbiting around a Schwarzschild black hole of mass $M = 1$ on quasi-circular orbits. (While this procedure can be carried out using elliptic integrals for Eq.(6.30), in practice it is simpler just to evaluate it by numerical quadrature.)

6.3.4 Results

In Fig. 6.6, we plot the ratio of the orbital frequency to the radial frequency versus the orbital frequency (Ω_Φ/Ω_r) estimated from the eccentricity residual of the wave phase defined in Eq. (6.9) using the waveform data at $R/M = 75, 240$ and extrapolated to infinity as in Fig. 6.3. To do so, we approximated the wave frequency to be twice the orbital frequency. This is justified in this paper because the deviation from this value of the orbital and wave frequencies ratio is

much smaller than the error in estimating the eccentricity and the precession. The estimated error in the precession curve of the numerical data is within 7% between $\Omega_\Phi = 0.02$ and $\Omega_\Phi = 0.03$ for different methods even for such a low eccentricity orbit. However, at the edges of this orbital frequency interval, the error in the estimated precession is becomes larger especially near the plunge. The eccentricity residual are dependent on the details of polynomial fitting the data, and it is more difficult to read these small eccentricity residuals near the plunge. The difference between the numerical precession curve and the 3PN precession formula in the equal mass is about 3% initially at $\Omega_\Phi = 0.02$, 7% at $\Omega_\Phi = 0.03$ and about 20% at $\Omega_\Phi = 0.035$. Similarly, we plot the estimated precession for a shorter quasi-circular nonspinning binary black evolution of mass ratio 2. The estimated precession is more or less near the equal mass precession data, but the error is however more than twice larger because the data available corresponds to a few number of orbits starting at a relatively high frequency $\Omega_\Phi = 0.027$ when compared to initial orbital frequency $\Omega_\Phi = 0.02$ of the 15-orbit data.

On the same plot, the precession in the test mass limit of a Schwarzschild black hole is shown, as well as the periastron advance test mass limit at 3PN order. The difference between the numerical data and the 3PN formula is more than twice as large than in the equal mass case.

As a separate check, we computed the precession curve of an eccentric run of a small eccentricity ($e \sim 0.05$) to reduce the sensitive of the fits at the beginning and the end of the numerical data. In this case, the precession curve does not show a decrease at $\Omega_\Phi = 0.03$ and instead it is a monotonically increasing function of the orbital frequency Ω_Φ (see Fig. 6.6). The difference between the

numerical precession curve and the 3PN formula is again about 3% initially at $\Omega_\Phi = 0.02$ and it diverges by 30% at $\Omega_\Phi = 0.045$ from the 3PN precession formula. Moreover, the precession does not decrease as orbital frequency increases beyond $\Omega_\Phi = 0.03$ for this eccentric binary. This indicates that the procedure to estimate the precession of the quasi-circular binaries beyond this orbital frequency was dominated by the plunge rather than the residual oscillations.

6.3.5 Laplace-Runge-Lenz vector

Had the eccentricity been significantly larger, the periastron advance could have been measured continuously using the Laplace-Runge-Lenz vector $\vec{A}$. This vector is defined in ADM coordinates using the canonically conjugate position $\vec{R}$ and momentum $\vec{P}$ as [93]:

$$\vec{A} = \vec{P} \times \vec{L} - GM\mu^2 \frac{\vec{R}}{R}, \tag{6.32}$$

where $\vec{L} = \vec{R} \times \vec{P}$ and μ is the reduced mass. Since the magnitude A of this vector goes like e, any relativistic effects such as gauge effects are not negligible. Moreover, the numerical data does not give the canonical position and momentum. This makes it impossible to measure the precession from the Laplace-Runge-Lenz vector for such low eccentricity runs.

6.4 Discussion

Even though Figs. 6.1, 6.2, 6.3 and 6.4 each showed a different behavior for the eccentricity residual, these definitions reduce precisely to the usual eccentricity

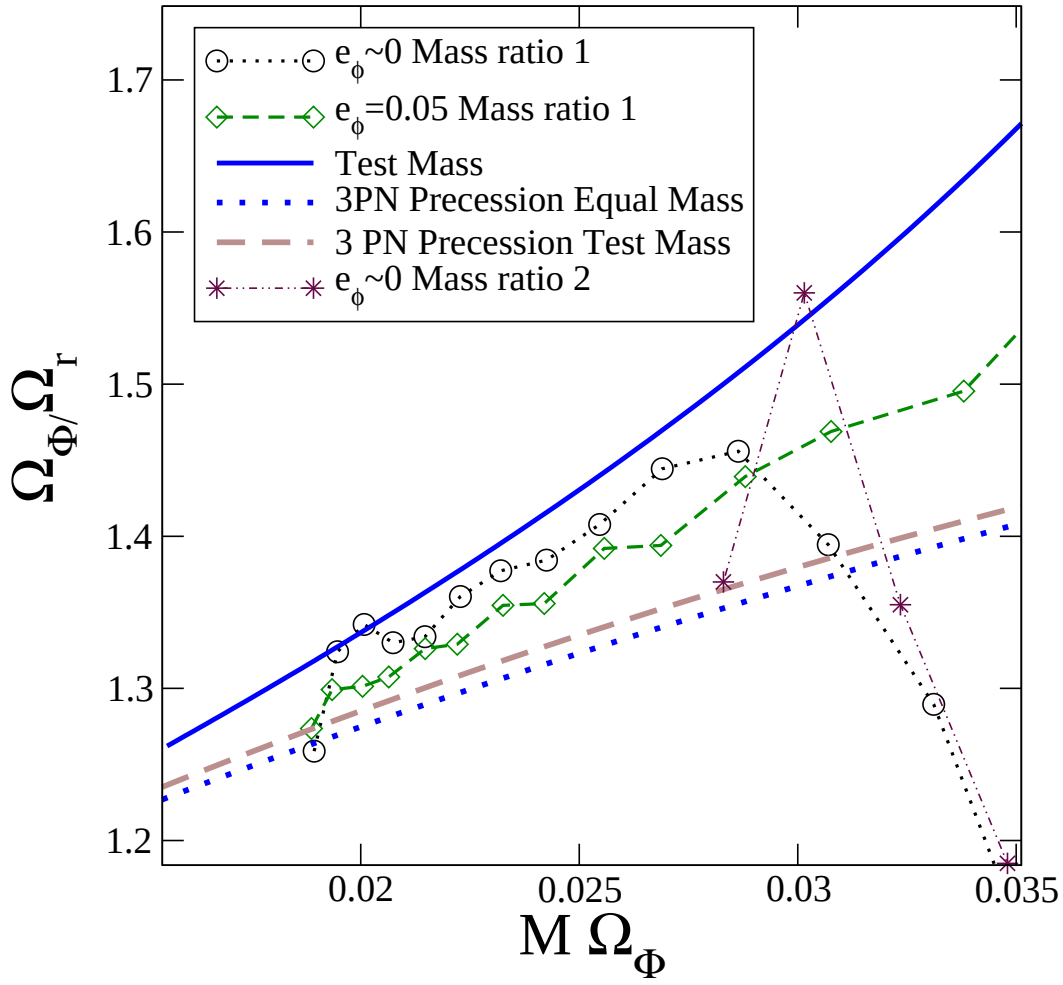

Figure 6.6: The ratio of the orbital frequency to the radial frequency, Ω_Φ/Ω_r, versus the orbital frequency $M\Omega_\Phi$, where is the total mass of the binary. The data corresponds to equal mass nonspinning quasi-circular binaries of the mass ratios 1 and 2 and to an equal mass nonspinning eccentric ($e \sim 0.05$) binary. We also plot Ω_Φ/Ω_r versus $M\Omega_\Phi$ for quasi-circular orbits of a test-mass around a Schwarzschild black hole. The numerical data agree to within few % initially with the 3PN periastron advance formula, and it diverges significantly as the binaries approach the merger. The precession increases as function of the orbital frequency. Nevertheless, the drop in the precession rate for the quasi-circular binaries is an artifact of method to measure the precession before merger. For the more eccentric binary ($e = 0.05$), we can estimate the precession even further closer to the merger.

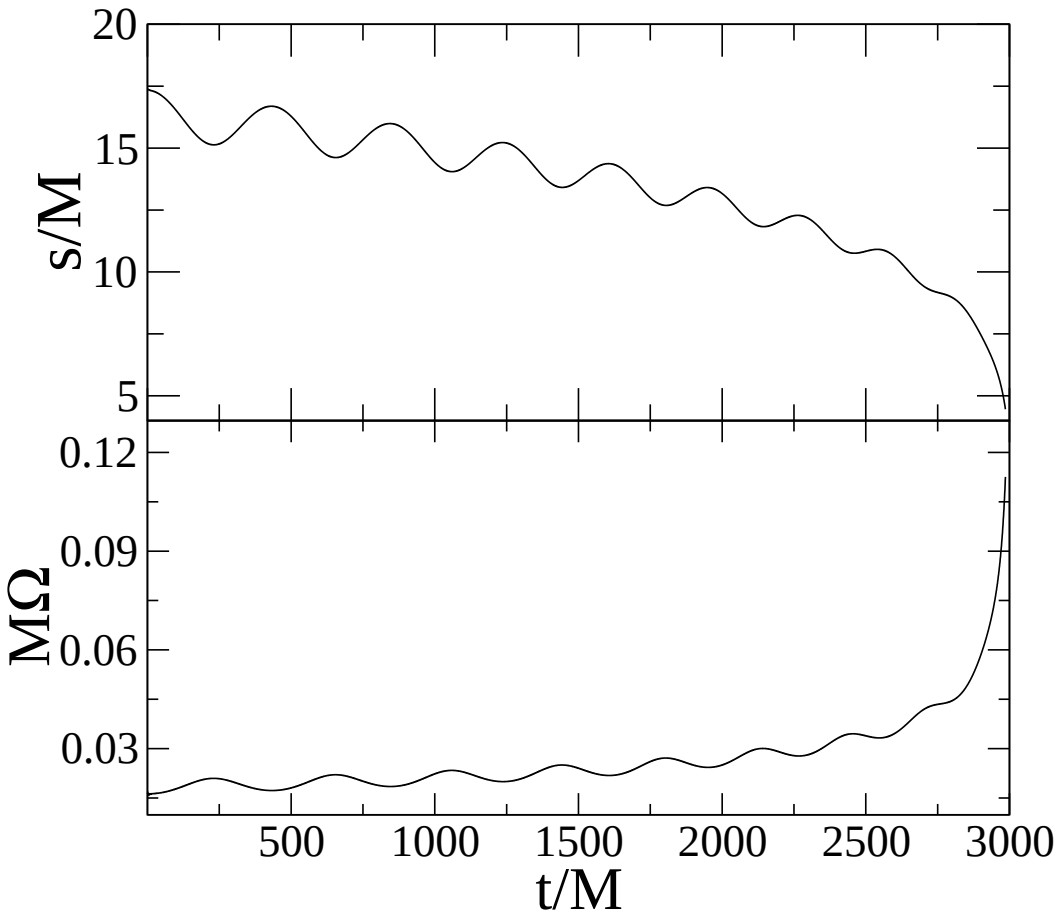

Figure 6.7: The proper horizon separation and the orbital frequency of the equal mass nonspinning eccentric binary ($e = 0.05$) as functions of time. For such a value of the eccentricity, we can easily measure the decay rate of the eccentricity and better estimate the periastron advance of the binary near the merger.

e in the Newtonian limit. Differences appear mainly because the data corresponds to a binary in the last phase of the inspiral before merger when relativistic effects are significant; the Newtonian relations between the orbital variables are no longer valid. These eccentricities have an orbit-averaged value rather than being continuously well defined as a function of time, and their magnitudes decrease because of radiation reaction [194] as the distance D between the holes decreases.

The eccentricity residual $e_{\rm BCP}$ is surprisingly bad (see Fig. 6.1). This might be because it uses a definition where eccentricity comes in the next-to-leading term, and the leading order Newtonian expression is not satisfied. Also, the high power of the contribution of the orbital variable makes the eccentricity easily affected by high-order harmonic modes in the orbital variables. This has been seen also in similar definitions of the eccentricity based on Newtonian formulas combining orbital variables.

Eccentricity measures based on orbital quantities (see Fig.6.2) give the right amplitude (for $t < 2500M$ in the case of e_Ω and e_D), and the phasing is quite consistent between the different eccentricity residuals. For instance, the orbital frequency is maximal when the separation is minimal. On the other hand, higher-order harmonics are clearly visible as the binary approach the merger. This is especially the case for the coordinate separation and the orbital frequency. The eccentricity measured from the proper horizon separation is the least tainted by these coordinate effects.

Eccentricity measures based on extracted gravitational waves (see Figs. 6.3 and 6.4) give a very nice oscillatory behavior, even for eccentricities as small as considered here. No high-order harmonics are noticeable in the wave extrap-

Table 6.1: Summary of the eccentricity measurement methods. t_i (t_f) is the initial (final) time of fitting. n is the order of the best fitting polynomial in the time interval $[t_i/M, t_f/M]$. e is the eccentricity estimate at the time t with the relative error $\delta e/e$.

Method	Ecc. Res.	Definition	t_i/M	t_f/M	n	$e(t/M = 1000)$	$e(t/M = 2000)$	$e(t/M = 3000)$	$\delta e/e$
Wave Phase	e_ϕ	$\Delta\phi/4$	952	3861	7	$6.4\times1‘0^{-5}$	5.7×10^{-5}	4.8×10^{-5}	4-6%
Wave Frequency	e_ω	$\Delta\omega/(2\omega_{\rm fit})$	1922	3861	7	-	4.3×10^{-5}	3.7×10^{-5}	15-25%
Coordinate distance	e_D	$\Delta D/D_{\rm fit}$	480	3367	7	6.7×10^{-5}	4.9×10^{-5}	6.3×10^{-5}	15-40%
Proper Horizon separation	e_S	$\Delta S/S_{\rm fit}$	480	3367	5	5.0×10^{-5}	3.9×10^{-5}	3.4×10^{-5}	10-20%
Orbital frequency	e_Ω	$\Delta\Omega/(2\Omega_{\rm fit})$	480	3367	7	6.2×10^{-5}	4.1×10^{-5}	3.4×10^{-5}	20-30%
BCP	e_{BCP}	$\Delta(\Omega(t)^2 r^3)$	480	3367	5	3.5×10^{-5}	2.4×10^{-5}	2×10^{-5}	50-80%

olated at infinity during the time interval we considered. These are the best eccentricity definitions since they are mainly measured from the oscillations in quantities extrapolated to infinity or at large separation from the holes. The eccentricity is calculated from the maximum and minimum values in the oscillating function without concern for the coordinate location in the orbit. It is especially straightforward to calculate numerically the eccentricity from the wave phase extrapolated at infinity without resorting to any notions of "distance" between the holes.

Notice that the eccentricity measurement could be affected by noise sources such as the "junk radiation" early in the simulation or ill-posed boundary conditions causing radiation reflection at the outer boundary. These additional oscillations could easily be interpreted as eccentricity. However in principle, one should be able to distinguish them from the eccentricity by the frequency of the oscillation. Oscillations due to eccentricity have a frequency very close to the orbital frequency or twice its value. In Table 6.1, we summarize the eccentricity definitions used in this paper, the data range between t_i/M and t_f/M used during the fits and the order of the fitting polynomial n for the 15-orbits quasi-circular nonspinning binary. We also give give an estimate of the eccentricity value at $t/M = 1000, 2000$ and 3000 and its estimated error $\delta e/e$ for each method.

6.5 Conclusions

With the use of the wave phase, preferably extrapolated to infinity, for measuring the eccentricity, we easily estimate the eccentricity and its evolution without much of the secondary effects as the noise. The amplitude and phase of the ec-

centricity could be estimated to about 5% allowing measurement of the precession to within 7%. The difference in periastron advance from the 3PN estimate was about 4% at the orbital frequency $\Omega_\Phi = 0.02$, and it diverges significantly to about 30% at $\Omega_\Phi = 0.045$ as the binary approaches the merger.

Other methods that are based on more complex forms of the eccentricity have larger error caused mainly by additional modes and noise especially close to the merger. We find that the most practical definition of eccentricity is from the phase of the wave especially for quasi-circular orbits, Eq. (6.9), since wave information is what will be accessible in detections.

APPENDIX A

PADÉ APPROXIMANTS TO THE ENERGY FLUX IN THE TEST PARTICLE LIMIT

In the test-mass-limit case the GW energy flux is known through 5.5PN order [224]. The explicit coefficients entering Eq. (4.19) for $i \geq 8$ and $\nu = 0$ can be read from Eqs. (4.1) and (4.2) of Ref. [98].

In Fig. A.1 we compare the normalized energy flux function [201] $F/F_{\rm Newt}$ to the T- and P-approximants. To easily compare Fig. A.1 with the other figures in the paper, we plot quantities as functions of the approximate GW frequency defined by $2M\Omega$. As noticed in Ref. [98], the P-approximants approach the numerical data more systematically. The differences between different PN orders are difficult to see in Fig. A.1. To obtain a clearer view, Fig. A.2 plots the differences between PN flux and numerical flux at four fixed frequencies. Fig. A.2 shows this somewhat better behavior of Padé; however, the Padé-approximants show little improvement between PN orders 3.5 and 4.5, and at order 5 there occurs an extraneous pole. At frequency $2M\Omega = 0.04$, P-approximants with order ≥ 2.5 are within 0.5 percent of the numerical data, as are T-approximants with order ≥ 3.5. Good agreement at low frequency is rather important because that is where the majority of the waveform phasing accumulates.

Table A.1 and Fig. A.3 test the internal convergence of T- and P-approximants *without* referring to a numerical result. Table A.1 displays the flux at all known PN-orders at select frequencies, with boldface highlighting the digits that have already converged. Although the Padé summation does not accelerate the convergence, the P-approximant at 5.5PN order is closest to the numerical data (see Fig. A.2).

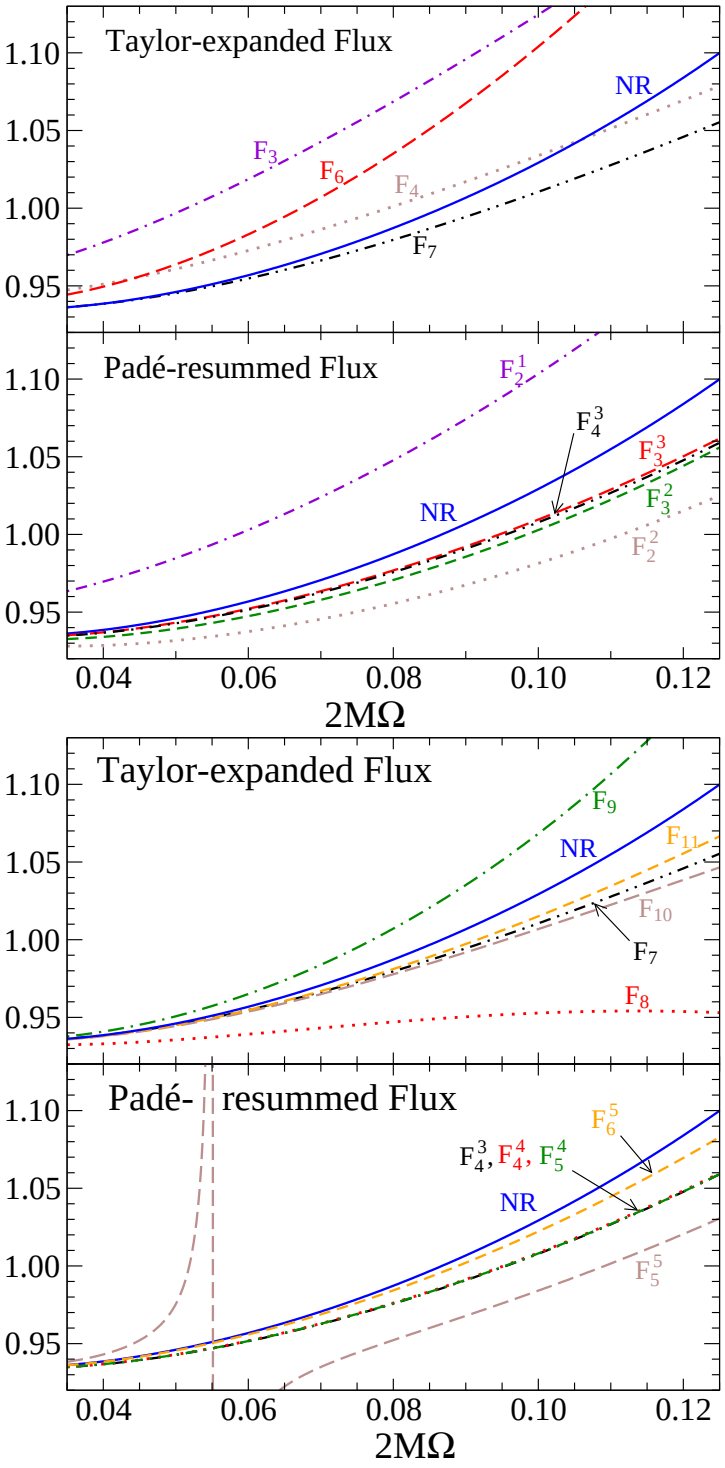

Figure A.1: Normalized energy flux $F/F_{\rm Newt}$ versus GW frequency 2Ω in the test-mass limit. For notation see Table 4.1 and caption therein. For comparison, both panels also include the result of the numerical calculation of Poisson [201], labeled with 'NR'.

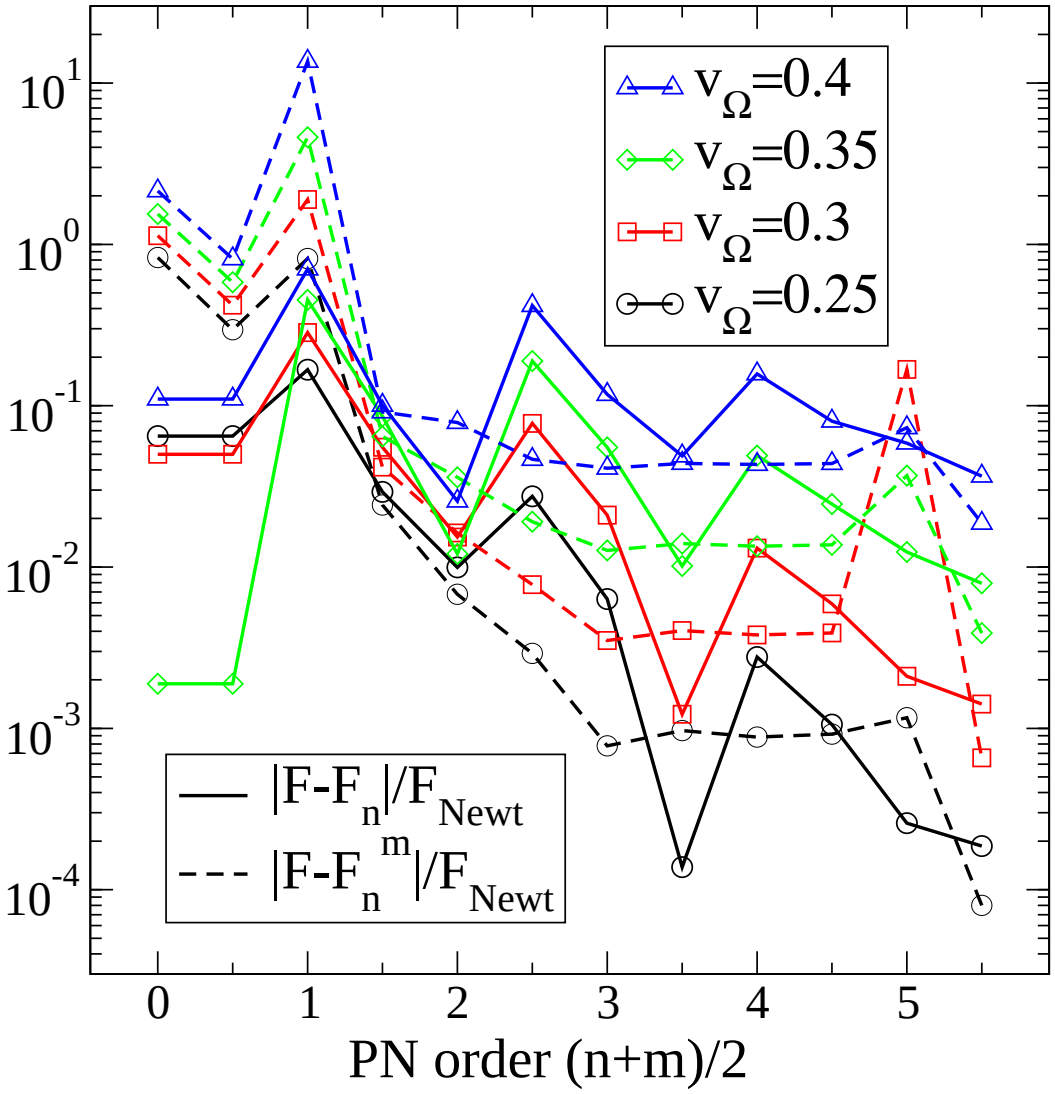

Figure A.2: Convergence of the PN-approximants in the test-mass limit. Plotted are differences of $F/F_{\rm Newt}$ from the numerical result. The P-approximants do not converge faster than the Taylor series.

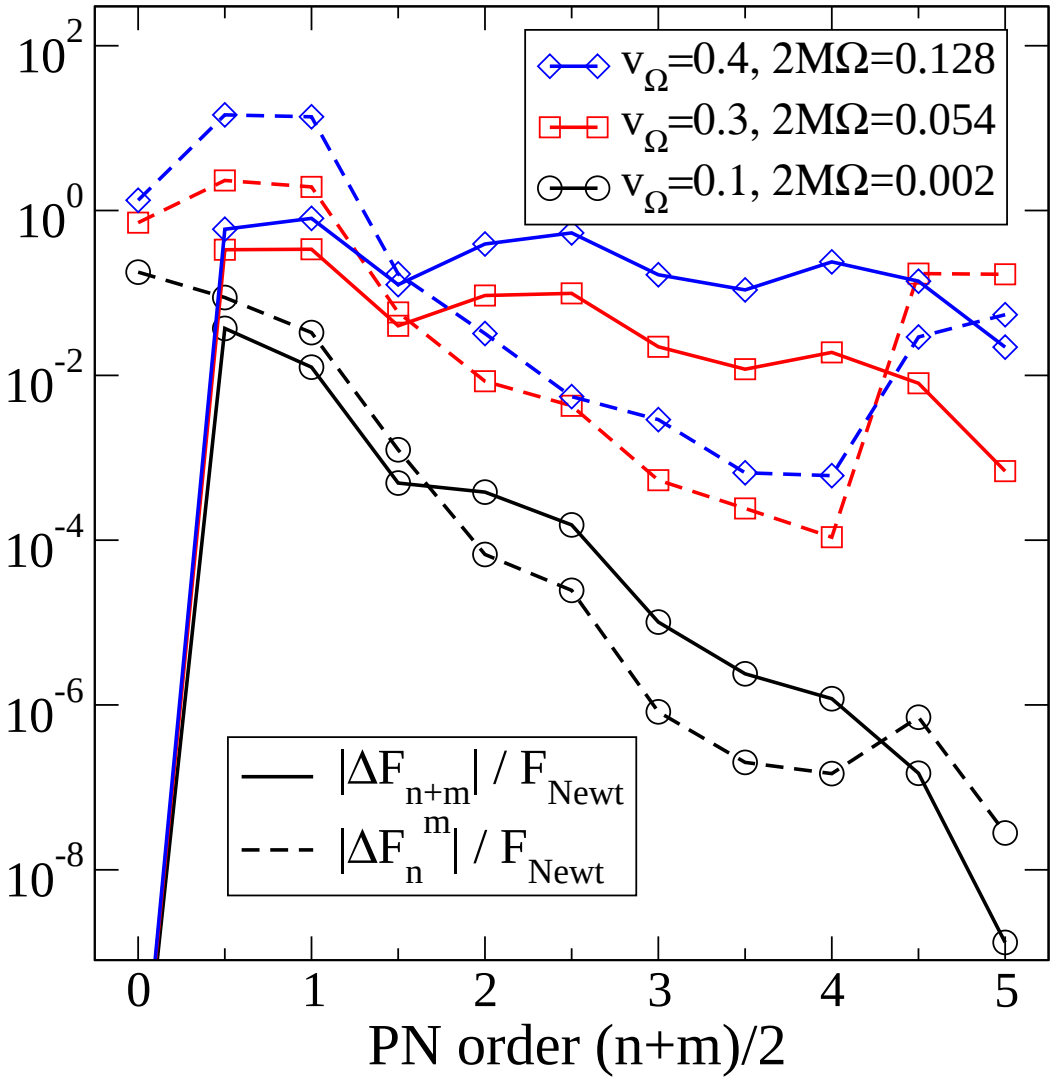

Figure A.3: Cauchy convergence test of $F/F_{\rm Newt}$ in the test-mass limit for the T- and P-approximants. We plot $\Delta F_{n+m} \equiv F_{n+m+1} - F_{n+m}$, and $\Delta F_n^m \equiv F_{n+1}^m - F_n^m$ at three different frequencies. At high frequencies, the 4.5 and 5 PN Padé approximants are contaminated by the extraneous pole of the 5PN Padé series; for low frequencies ($v_\Omega = 0.1$), the pole is apparently irrelevant.

Table A.1: Normalized energy flux $F/F_{\rm Newt}$ in the test-mass limit for the T- and P-approximants at different PN orders and at three different frequencies. We use boldface to indicate the range of significant figures that do not change with increasing PN order.

PN order	$v_\Omega = 0.1$; $2M\Omega = 0.002$		$v_\Omega = 0.3$; $2M\Omega = 0.054$		$v_\Omega = 0.4$; $2M\Omega = 0.128$	
(n+m)/2	$F_{n+m}/F_{\rm Newt}$	$F^m_n/F_{\rm Newt}$	$F_{n+m}/F_{\rm Newt}$	$F^m_n/F_{\rm Newt}$	$F_{n+m}/F_{\rm Newt}$	$F^m_n/F_{\rm Newt}$
0.0	1.0000000000	1.20948977	1.0000	2.0817	1.000	3.255
0.5	1.0000000000	1.03092783	1.0000	1.3699	1.000	1.923
1.0	**0.9**628869047	**0.9**4287089	0.6660	-0.9467	0.406	-12.52
1.5	**0.97**54532753	**0.97**587569	1.0053	0.9916	1.210	**1**.201
2.0	**0.974**9604292	**0.974**62770	**0.**9653	0.9337	1.084	**1.0**31
2.5	**0.974**5775009	**0.974**69475	**0.**8723	0.9422	0.692	**1.0**63
3.0	**0.9747**307757	**0.97471**937	**0.9**710	0.9465	1.227	**1.0**69
3.5	**0.9747**206248	**0.97471**854	**0.9**488	0.9460	1.061	**1.0**66
4.0	**0.97471**82352	**0.97471**874	**0.9**369	0.9462	0.952	**1.0**67
4.5	**0.97471**94262	**0.97471**859	**0.9**559	0.9461	**1**.190	**1.0**66
5.0	**0.9747192**776	**0.97471**930	**0.94**79	1.1178	**1.0**51	**1.0**37
5.5	**0.9747192**763	**0.97471**928	**0.94**85	**0.94**93	**1.0**73	**1.0**91

Comparing Table A.1 with Table 4.2, and Fig. A.3 with Fig. 4.10 we observe that the P-approximants converge more systematically in the equal-mass case than in the test-mass limit. This is also evident by comparing Fig. A.2 with Fig. 4.8: We see that P-approximants at 3PN and 3.5PN orders are inside the numerical flux error whereas T-approximants at all orders through 3.5 PN are outside the numerical flux error bars even ~ 25 GW cycles before merger. However, as the Padé approximant does not converge faster, it is not immediately clear whether similar superior behavior of Padé can be expected for more generic binary black holes.

BIBLIOGRAPHY

[1] Andrew M. Abrahams and Charles R. Evans. Reading off gravitational radiation waveforms in numerical relativity calculations: Matching to linearized gravity. *Phys. Rev. D*, 37(2):318–332, Jan 1988.

[2] Andrew M. Abrahams and Charles R. Evans. Gauge-invariant treatment of gravitational radiation near the source: Analysis and numerical simulations. *Phys. Rev. D*, 42(8):2585–2594, Oct 1990.

[3] F Acernese, P Amico, M Alshourbagy, F Antonucci, S Aoudia, S Avino, D Babusci, G Ballardin, F Barone, L Barsotti, M Barsuglia, F Beauville, S Bigotta, S Birindelli, M A Bizouard, C Boccara, F Bondu, L Bosi, C Bradaschia, S Braccini, A Brillet, V Brisson, L Brocco, D Buskulic, E Calloni, E Campagna, F Cavalier, R Cavalieri, G Cella, E Cesarini, E Chassande-Mottin, C Corda, F Cottone, A-C Clapson, F Cleva, J-P Coulon, E Cuoco, A Dari, V Dattilo, M Davier, R De Rosa, L Di Fiore, A Di Virgilio, B Dujardin, A Eleuteri, D Enard, I Ferrante, F Fidecaro, I Fiori, R Flaminio, J-D Fournier, O Francois, S Frasca, F Frasconi, A Freise, L Gammaitoni, F Garufi, A Gennai, A Giazotto, G Giordano, L Giordano, R Gouaty, D Grosjean, G Guidi, S Hebri, H Heitmann, P Hello, L Holloway, S Karkar, S Kreckelbergh, P La Penna, M Laval, N Leroy, N Letendre, M Lorenzini, V Loriette, M Loupias, G Losurdo, J-M Mackowski, E Majorana, C N Man, M Mantovani, F Marchesoni, F Marion, J Marque, F Martelli, A Masserot, M Mazzoni, L Milano, C Moins, J Moreau, N Morgado, B Mours, A Pai, C Palomba, F Paoletti, S Pardi, A Pasqualetti, R Passaquieti, D Passuello, B Perniola, F Piergiovanni, L Pinard, R Poggiani, M Punturo, P Puppo, K Qipiani, P Rapagnani, V Reita, A Remillieux, F Ricci, I Ricciardi, P Ruggi, G Russo, S Solimeno, A Spallicci, R Stanga, R Taddei, M Tonelli, A Toncelli, E Tournefier, F Travasso, G Vajente, D Verkindt, F Vetrano, A Viceré, J-Y Vinet, H Vocca, M Yvert, and Z Zhang. The Virgo status. *Class. Quantum Grav.*, 23(19):S635–S642, 2006.

[4] P. Ajith, S. Babak, Y. Chen, M. Hewitson, B. Krishnan, A. M. Sintes, J. T. Whelan, B. Brügmann, P. Diener, N. Dorband, J. Gonzalez, M. Hannam, S. Husa, D. Pollney, L. Rezzolla, L. Santamar´ia, U. Sperhake, and J. Thornburg. Template bank for gravitational waveforms from coalescing binary black holes: Nonspinning binaries. *Phys. Rev. D*, 77(10):104017, 2008.

[5] P. Ajith, S. Babak, Y. Chen, M. Hewitson, B. Krishnan, J. T. Whelan, B. Brügmann, P. Diener, J. Gonzalez, M. Hannam, S. Husa, M. Koppitz, D. Pollney, L. Rezzolla, L. Santamar´ia, A. M. Sintes, U. Sperhake, and

J. Thornburg. A phenomenological template family for black-hole coalescence waveforms. *Class. Quantum Grav.*, 24(19):S689–S699, 2007.

[6] K. G. Arun, Luc Blanchet, Bala R. Iyer, and Moh'd. S. S. Qusailah. The 2.5PN gravitational wave polarizations from inspiralling compact binaries in circular orbits. *Class. Quantum Grav.*, 21(15):3771–3801, 2004.

[7] Abhay Ashtekar, Christopher Beetle, and Jerzy Lewandowski. Mechanics of rotating isolated horizons. *Phys. Rev. D*, 64(4):044016, Jul 2001.

[8] Abhay Ashtekar and Badri Krishnan. Dynamical horizons and their properties. *Phys. Rev. D*, 68(10):104030, Nov 2003.

[9] Maria Babiuc, Bela Szilagyi, Ian Hawke, and Yosef Zlochower. Gravitational wave extraction based on cauchy-characteristic extraction and characteristic evolution. *Class. Quantum Grav.*, 22(23):5089–5107, 2005.

[10] Maria C. Babiuc, Nigel T. Bishop, Béla Szilágyi, and Jeffrey Winicour. Strategies for the characteristic extraction of gravitational waveforms. *Phys. Rev. D*, 79(8):084011, 2009.

[11] John G. Baker, William D. Boggs, Joan Centrella, Bernard J. Kelly, Sean T. McWilliams, M. Coleman Miller, and James R. van Meter. Modeling kicks from the merger of non-precessing black-hole binaries. *Astrophys. J.*, 668:1140, 2007.

[12] John G. Baker, Manuela Campanelli, Frans Pretorius, and Yosef Zlochower. Comparisons of binary black hole merger waveforms. *Class. Quantum Grav.*, 24:S25–S31, 2007.

[13] John G. Baker, Joan Centrella, Dae-Il Choi, Michael Koppitz, and James van Meter. Binary black hole merger dynamics and waveforms. *Phys. Rev. D*, 73(10):104002, 2006.

[14] John G. Baker, Joan Centrella, Dae-Il Choi, Michael Koppitz, and James van Meter. Gravitational-wave extraction from an inspiraling configuration of merging black holes. *Phys. Rev. Lett.*, 96(11):111102, 2006.

[15] John G. Baker, Joan Centrella, Dae-Il Choi, Michael Koppitz, James R. van Meter, and M. Coleman Miller. Getting a kick out of numerical relativity. *Astrophys. J.*, 653:L93–L96, 2006.

[16] John G. Baker, Sean T. McWilliams, James R. van Meter, Joan Centrella, Dae-Il Choi, Bernard J. Kelly, and Michael Koppitz. Binary black hole late inspiral: Simulations for gravitational wave observations. *Phys. Rev. D*, 75:124024, 2007.

[17] John G. Baker, James R. van Meter, Sean T. McWilliams, Joan Centrella, and Bernard J. Kelly. Consistency of post-Newtonian waveforms with numerical relativity. *Phys. Rev. Lett.*, 99(18):181101, 2007.

[18] James M. Bardeen and Luisa T. Buchman. Numerical tests of evolution systems, gauge conditions, and boundary conditions for 1D colliding gravitational plane waves. *Phys. Rev. D*, 65:064037, Mar 2002.

[19] Barry C. Barish and Rainer Weiss. LIGO and the detection of gravitational waves. *Phys. Today*, 52(10):44–50, Oct 1999.

[20] Thomas Baumgarte, Patrick R. Brady, Jolien D. E. Creighton, Luis Lehner, Frans Pretorius, and Ricky DeVoe. Learning about compact binary merger: The interplay between numerical relativity and gravitational-wave astronomy. *Phys. Rev. D*, 77(8):084009, 2008.

[21] Thomas W. Baumgarte, Gregory B. Cook, Mark A. Scheel, Stuart L. Shapiro, and Saul A. Teukolsky. Implementing an apparent-horizon finder in three dimensions. *Phys. Rev. D*, 54(8):4849–4857, Oct 1996.

[22] Christopher Beetle, Marco Bruni, Lior M. Burko, and Andrea Nerozzi. Towards a wave-extraction method for numerical relativity. I. Foundations and initial-value formulation. *Phys. Rev. D*, 72(2):024013, 2005.

[23] Carl M. Bender and Steven A. Orszag. *Advanced Mathematical Methods for Scientists and Engineers*. McGraw-Hill, New York, 1978.

[24] Emanuele Berti, Vitor Cardoso, José A. Gonzalez, Ulrich Sperhake, Mark Hannam, Sascha Husa, and Bernd Brügmann. Inspiral, merger, and ring-down of unequal mass black hole binaries: A multipolar analysis. *Phys. Rev. D*, 76:064034, 2007.

[25] Emanuele Berti, Sai Iyer, and Clifford M. Will. Eccentricity content of binary black hole initial data. *Phys. Rev. D*, 74(6):061503, 2006.

[26] Nigel T. Bishop, Roberto Gómez, Luis Lehner, and Jeffrey Winicour.

Cauchy-characteristic extraction in numerical relativity. *Phys. Rev. D*, 54(10):6153–6165, Nov 1996.

[27] Morten Bjørhus. The ODE formulation of hyperbolic PDEs discretized by the spectral collocation method. *SIAM J. Sci. Comput.*, 16(3):542–557, 1995.

[28] L. Blanchet, G. Faye, B. R. Iyer, and S. Sinha. The third post-Newtonian gravitational wave polarizations and associated spherical harmonic modes for inspiralling compact binaries in quasi-circular orbits. *Classical and Quantum Gravity*, 25(16):165003–+, August 2008.

[29] Luc Blanchet. Energy losses by gravitational radiation in inspiraling compact binaries to 5/2 post-Newtonian order. *Phys. Rev. D*, 54(2):1417–1438, Jul 1996.

[30] Luc Blanchet. Gravitational radiation reaction and balance equations to post-Newtonian order. *Phys. Rev. D*, 55(2):714–732, Jan 1997.

[31] Luc Blanchet. Gravitational-wave tails of tails. *Class. Quantum Grav.*, 15(1):113–141, 1998. Erratum: [34].

[32] Luc Blanchet. On the multipole expansion of the gravitational field. *Class. Quantum Grav.*, 15(7):1971–1999, 1998.

[33] Luc Blanchet. Quadrupole-quadrupole gravitational waves. *Class. Quantum Grav.*, 15(1):89–111, 1998.

[34] Luc Blanchet. Erratum: Gravitational-wave tails of tails. *Class. Quantum Grav.*, 22(16):3381, 2005.

[35] Luc Blanchet. Gravitational radiation from post-Newtonian sources and inspiralling compact binaries. *Living Rev. Rel.*, 9, 2006.

[36] Luc Blanchet, Alessandra Buonanno, and Guillaume Faye. Higher-order spin effects in the dynamics of compact binaries. II. Radiation field. *Phys. Rev. D*, 74(10):104034, 2006.

[37] Luc Blanchet and Thibault Damour. Hereditary effects in gravitational radiation. *Phys. Rev. D*, 46(10):4304–4319, Nov 1992.

[38] Luc Blanchet, Thibault Damour, and Gilles Esposito-Farèse. Dimensional

regularization of the third post-Newtonian dynamics of point particles in harmonic coordinates. *Phys. Rev. D*, 69(12):124007, Jun 2004.

[39] Luc Blanchet, Thibault Damour, Gilles Esposito-Farèse, and Bala R. Iyer. Gravitational radiation from inspiralling compact binaries completed at the third post-Newtonian order. *Phys. Rev. Lett.*, 93(9):091101, Aug 2004.

[40] Luc Blanchet, Thibault Damour, Gilles Esposito-Farèse, and Bala R. Iyer. Dimensional regularization of the third post-Newtonian gravitational wave generation from two point masses. *Phys. Rev. D*, 71(12):124004, 2005.

[41] Luc Blanchet and Guillaume Faye. On the equations of motion of point-particle binaries at the third post-Newtonian order. *Phys. Lett.*, 271:58–64(7), 2000.

[42] Luc Blanchet and Guillaume Faye. General relativistic dynamics of compact binaries at the third post-Newtonian order. *Phys. Rev. D*, 63(6):062005, Feb 2001.

[43] Luc Blanchet, Guillaume Faye, Bala R. Iyer, and Benoit Joguet. Gravitational-wave inspiral of compact binary systems to 7/2 post-Newtonian order. *Phys. Rev. D*, 65(6):061501, Feb 2002. Erratum: [44].

[44] Luc Blanchet, Guillaume Faye, Bala R. Iyer, and Benoit Joguet. Erratum: Gravitational-wave inspiral of compact binary systems to 7/2 post-Newtonian order. *Phys. Rev. D*, 71(12):129902, 2005.

[45] Luc Blanchet and Bala R. Iyer. Third post-Newtonian dynamics of compact binaries: equations of motion in the centre-of-mass frame. *Class. Quantum Grav.*, 20(4):755–776, 2003.

[46] Luc Blanchet and Bala R. Iyer. Hadamard regularization of the third post-Newtonian gravitational wave generation of two point masses. *Phys. Rev. D*, 71(2):024004, 2005.

[47] Luc Blanchet, Bala R. Iyer, and Benoit Joguet. Gravitational waves from inspiraling compact binaries: Energy flux to third post-Newtonian order. *Phys. Rev. D*, 65(6):064005, Feb 2002. Erratum: [48].

[48] Luc Blanchet, Bala R. Iyer, and Benoit Joguet. Erratum: Gravitational waves from inspiraling compact binaries: Energy flux to third post-Newtonian order. *Phys. Rev. D*, 71(12):129903, 2005.

[49] Luc Blanchet and Gerhard Schäfer. Gravitational wave tails and binary star systems. *Class. Quantum Grav.*, 10(12):2699–2721, 1993.

[50] Michael Boyle. *Accurate gravitational waveforms from binary black-hole systems*. PhD thesis, California Institute of Technology, October 2008.

[51] Michael Boyle, Duncan A. Brown, Lawrence E. Kidder, Abdul H. Mroue, Harald P. Pfeiffer, Mark A. Scheel, Gregory B. Cook, and Saul A. Teukolsky. High-accuracy comparison of numerical relativity simulations with post-Newtonian expansions. *Phys. Rev. D*, 76(12):124038, 2007.

[52] Michael Boyle, Duncan A. Brown, and Larne Pekowsky. Comparison of high-accuracy numerical simulations of black-hole binaries with stationary-phase post-Newtonian template waveforms for Initial and Advanced LIGO. *Class. Quantum Grav.*, 26(11):114006, 2009.

[53] Michael Boyle, Alessandra Buonanno, Lawrence E. Kidder, Abdul H. Mroué, Yi Pan, Harald P. Pfeiffer, and Mark A. Scheel. High-accuracy numerical simulation of black-hole binaries: Computation of the gravitational-wave energy flux and comparisons with post-Newtonian approximants. *Phys. Rev. D*, 78(12):104020, 2008.

[54] Michael Boyle and Abdul H. Mroué. Extrapolating gravitational-wave data from numerical simulations.

[55] J. David Brown and James W. York. Quasilocal energy and conserved charges derived from the gravitational action. *Phys. Rev. D*, 47(4):1407–1419, Feb 1993.

[56] Bernd Brügmann, José A. González, Mark Hannam, Sascha Husa, and Ulrich Sperhake. Exploring black hole superkicks. *Phys. Rev. D*, 77(12):124047, 2008.

[57] Bernd Brügmann, José A. González, Mark Hannam, Sascha Husa, Ulrich Sperhake, and Wolfgang Tichy. Calibration of moving puncture simulations. *Phys. Rev. D*, 77(2):024027, 2008.

[58] Luisa T. Buchman and Olivier C. A. Sarbach. Towards absorbing outer boundaries in general relativity. *Class. Quantum Grav.*, 23:6709–6744, 2006.

[59] A. Buonanno and T. Damour. Binary black holes coalescence: transition from adiabatic inspiral to plunge. In V. G. Gurzadyan, R. T. Jantzen, and

R. Ruffini, editors, *The Ninth Marcel Grossmann Meeting*, pages 1637–1638, 2002.

[60] Alessandra Buonanno, Yanbei Chen, and Thibault Damour. Transition from inspiral to plunge in precessing binaries of spinning black holes. *Phys. Rev. D*, 74(10):104005, 2006.

[61] Alessandra Buonanno, Yanbei Chen, Yi Pan, and Michele Vallisneri. A quasiphysical family of gravity-wave templates for precessing binaries of spinning compact objects: Application to double-spin precessing binaries. *Phys. Rev. D*, 70:104003, 2004.

[62] Alessandra Buonanno, Yanbei Chen, and Michele Vallisneri. Detection template families for gravitational waves from the final stages of binary–black-hole inspirals: Nonspinning case. *Phys. Rev. D*, 67(2):024016, Jan 2003. Erratum: [63].

[63] Alessandra Buonanno, Yanbei Chen, and Michele Vallisneri. Erratum: Detection template families for gravitational waves from the final stages of binary–black-hole inspirals: Nonspinning case. *Phys. Rev. D*, 74(2):029903, 2006.

[64] Alessandra Buonanno, Gregory B. Cook, and Frans Pretorius. Inspiral, merger, and ring-down of equal-mass black-hole binaries. *Phys. Rev. D*, 75(12):124018, 2007.

[65] Alessandra Buonanno and Thibault Damour. Effective one-body approach to general relativistic two-body dynamics. *Phys. Rev. D*, 59(8):084006, 1999.

[66] Alessandra Buonanno and Thibault Damour. Transition from inspiral to plunge in binary black hole coalescences. *Phys. Rev. D*, 62(6):064015, 2000.

[67] Alessandra Buonanno, Yi Pan, John G. Baker, Joan Centrella, Bernard J. Kelly, Sean T. McWilliams, and James R. van Meter. Approaching faithful templates for non-spinning binary black holes using the effective-one-body approach. *Phys. Rev. D*, 76:104049, 2007.

[68] Alessandra Buonanno, Yi Pan, Harald P. Pfeiffer, Mark A. Scheel, Luisa T. Buchman, and Lawrence E. Kidder. Effective-one-body waveforms calibrated to numerical relativity simulations: coalescence of non-spinning, equal- mass black holes. 2009.

[69] Lior M. Burko, Thomas W. Baumgarte, and Christopher Beetle. Towards a wave-extraction method for numerical relativity. III. Analytical examples for the Beetle–Burko radiation scalar. *Phys. Rev. D*, 73(2):024002, 2006.

[70] Gioel Calabrese, Jorge Pullin, Oscar Reula, Olivier Sarbach, and Manuel Tiglio. Well posed constraint-preserving boundary conditions for the linearized Einstein equations. *cmp*, 240:377–395, 2003.

[71] Manuela Campanelli, Bernard Kelly, and Carlos O. Lousto. The Lazarus project. II. Spacelike extraction with the quasi-Kinnersley tetrad. *Phys. Rev. D*, 73(6):064005, 2006.

[72] Manuela Campanelli, Carlos O. Lousto, Pedro Marronetti, and Yosef Zlochower. Accurate evolutions of orbiting black-hole binaries without excision. *Phys. Rev. Lett.*, 96(11):111101, 2006.

[73] Manuela Campanelli, Carlos O. Lousto, and Yosef Zlochower. Gravitational radiation from spinning-black-hole binaries: The orbital hang up. *Phys. Rev. D*, 74:041501(R), 2006.

[74] Manuela Campanelli, Carlos O. Lousto, and Yosef Zlochower. Last orbit of binary black holes. *Phys. Rev. D*, 73:061501(R), 2006.

[75] Manuela Campanelli, Carlos O. Lousto, and Yosef Zlochower. Spin-orbit interactions in black-hole binaries. *Phys. Rev. D*, 74:084023, 2006.

[76] Manuela Campanelli, Carlos O. Lousto, Yosef Zlochower, Badri Krishnan, and David Merritt. Spin flips and precession in black-hole binary mergers. *Phys. Rev. D*, 75:064030, 2007.

[77] Manuela Campanelli, Carlos O. Lousto, Yosef Zlochower, and David Merritt. Large merger recoils and spin flips from generic black hole binaries. *Astrophys. J. Lett.*, 659(1):L5–L8, 2007.

[78] Manuela Campanelli, Carlos O. Lousto, Yosef Zlochower, and David Merritt. Maximum gravitational recoil. *Phys. Rev. Lett.*, 98:231102, 2007.

[79] Matthew Caudill, Greg B. Cook, Jason D. Grigsby, and Harald P. Pfeiffer. Circular orbits and spin in black-hole initial data. *Phys. Rev. D*, 74(6):064011, 2006.

[80] Subrahmanyan Chandrasekhar. *The Mathematical Theory of Black Holes*. Oxford University Press, 1992.

[81] H.K. Chaurasia and M. Bailes. On the eccentricities and merger rates of double neutron star binaries and the creation of "double supernovae". *Astrophys. J.*, 632:1054–1059, 2005.

[82] Dae-Il Choi, Bernard J. Kelly, William D. Boggs, John G. Baker, Joan Centrella, and James van Meter. Recoiling from a kick in the head-on case. *Phys. Rev. D*, 76:104026, 2007.

[83] LIGO Scientific Collaboration. LSC Algorithm Library software packages LAL, LALWRAPPER, and LALAPPS.

[84] Gregory B. Cook. Corotating and irrotational binary black holes in quasi-circular orbits. *Phys. Rev. D*, 65(8):084003, Mar 2002.

[85] Gregory B. Cook and Harald P. Pfeiffer. Excision boundary conditions for black-hole initial data. *Phys. Rev. D*, 70(10):104016, Nov 2004.

[86] Gregory B. Cook and Bernard F. Whiting. Approximate Killing vectors on S^2. *Phys. Rev. D*, 76(4):041501(R), 2007.

[87] Curt Cutler, Theocharis A. Apostolatos, Lars Bildsten, Lee Smauel Finn, Eanna E. Flanagan, Daniel Kennefick, Dragoljub M. Markovic, Amos Ori, Eric Poisson, Gerald Jay Sussman, and Kip S. Thorne. The last three minutes: Issues in gravitational-wave measurements of coalescing compact binaries. *Phys. Rev. Lett.*, 70(20):2984–2987, May 1993.

[88] Curt Cutler, Lee Samuel Finn, Eric Poisson, and Gerald Jay Sussman. Gravitational radiation from a particle in circular orbit around a black hole. II. Numerical results for the nonrotating case. *Phys. Rev. D*, 47(4):1511–1518, Feb 1993.

[89] T. Damour. In N. Deruelle and T. Piran, editors, *Gravitational Radiation*, pages 59–144. North-Holland, Amsterdam, 1983.

[90] T. Damour. Introductory lectures on the effective one body formalism. 2008.

[91] T. Damour, P. Jaranowski, and G. Schäfer. Dynamical invariants for gen-

eral relativistic two-body systems at the third post-Newtonian approximation. *Phys. Rev. D*, 62(4):044024, Jul 2000.

[92] T. Damour, A. Nagar, M. Hannam, S. Husa, and B. Brügmann. Accurate Effective-One-Body waveforms of inspiralling and coalescing black-hole binaries. *Phys. Rev. D*, 78:044039, 2008.

[93] T. Damour and G. Schäfer. Higher-order relativistic periastron advances and binary pulsars. *Nuovo Cinmento Soc. Ital. Fis.*, 101 B(2):127, 1988.

[94] Thibault Damour. Coalescence of two spinning black holes: An effective one-body approach. *Phys. Rev. D*, 64(12):124013, Nov 2001.

[95] Thibault Damour and Achamveedu Gopakumar. Gravitational recoil during binary black hole coalescence using the effective one body approach. *Phys. Rev. D*, 73(12):124006, 2006.

[96] Thibault Damour, Achamveedu Gopakumar, and Bala R. Iyer. Phasing of gravitational waves from inspiralling eccentric binaries. *Phys. Rev. D*, 70:064028, September 2004.

[97] Thibault Damour, Bala R. Iyer, Piotr Jaranowski, and B. S. Sathyaprakash. Gravitational waves from black hole binary inspiral and merger: The span of third post-Newtonian effective-one-body templates. *Phys. Rev. D*, 67(6):064028, Mar 2003.

[98] Thibault Damour, Bala R. Iyer, and B. S. Sathyaprakash. Improved filters for gravitational waves from inspiraling compact binaries. *Phys. Rev. D*, 57(2):885–907, Jan 1998.

[99] Thibault Damour, Bala R. Iyer, and B. S. Sathyaprakash. Frequency-domain P-approximant filters for time-truncated inspiral gravitational wave signals from compact binaries. *Phys. Rev. D*, 62(8):084036, Sep 2000.

[100] Thibault Damour, Bala R. Iyer, and B. S. Sathyaprakash. Comparison of search templates for gravitational waves from binary inspiral. *Phys. Rev. D*, 63(4):044023, Jan 2001. Erratum: [102].

[101] Thibault Damour, Bala R. Iyer, and B. S. Sathyaprakash. Comparison of search templates for gravitational waves from binary inspiral: 3.5PN update. *Phys. Rev. D*, 66(2):027502, Jul 2002. Erratum: [103].

[102] Thibault Damour, Bala R. Iyer, and B. S. Sathyaprakash. Erratum: Comparison of search templates for gravitational waves from binary inspiral. *Phys. Rev. D*, 72(2):029902, 2005.

[103] Thibault Damour, Bala R. Iyer, and B. S. Sathyaprakash. Erratum: Comparison of search templates for gravitational waves from binary inspiral: 3.5PN update. *Phys. Rev. D*, 72(2):029901, 2005.

[104] Thibault Damour, Piotr Jaranowski, and Gerhard Schäfer. Determination of the last stable orbit for circular general relativistic binaries at the third post-Newtonian approximation. *Phys. Rev. D*, 62(8):084011, Sep 2000.

[105] Thibault Damour, Piotr Jaranowski, and Gerhard Schäfer. Determination of the last stable orbit for circular general relativistic binaries at the third post-Newtonian approximation. *Phys. Rev. D*, 62(8):084011, Sep 2000.

[106] Thibault Damour, Piotr Jaranowski, and Gerhard Schäfer. Erratum: Poincaré invariance in the ADM Hamiltonian approach to the general relativistic two-body problem. *Phys. Rev. D*, 63(2):029903, Dec 2000.

[107] Thibault Damour, Piotr Jaranowski, and Gerhard Schäfer. Poincaré invariance in the ADM Hamiltonian approach to the general relativistic two-body problem. *Phys. Rev. D*, 62(2):021501, Jun 2000. Erratum: [106].

[108] Thibault Damour, Piotr Jaranowski, and Gerhard Schäfer. Dimensional regularization of the gravitational interaction of point masses. *Phys. Lett. B*, 513:147–155(9), 2001.

[109] Thibault Damour, Piotr Jaranowski, and Gerhard Schäfer. Equivalence between the ADM-Hamiltonian and the harmonic-coordinates approaches to the third post-Newtonian dynamics of compact binaries. *Phys. Rev. D*, 63(4):044021, Jan 2001. Erratum: [110].

[110] Thibault Damour, Piotr Jaranowski, and Gerhard Schäfer. Erratum: Equivalence between the ADM-Hamiltonian and the harmonic-coordinates approaches to the third post-Newtonian dynamics of compact binaries. *Phys. Rev. D*, 66(2):029901, Jul 2002.

[111] Thibault Damour and Alessandro Nagar. Faithful effective-one-body waveforms of small-mass-ratio coalescing black hole binaries. *Phys. Rev. D*, 76(6):064028, 2007.

[112] Thibault Damour and Alessandro Nagar. Final spin of a coalescing black-hole binary: An effective-one-body approach. *Phys. Rev. D*, 76:044003, 2007.

[113] Thibault Damour and Alessandro Nagar. Comparing effective-one-body gravitational waveforms to accurate numerical data. *Phys. Rev. D*, 77(2):024043, 2008.

[114] Thibault Damour, Alessandro Nagar, Ernst Nils Dorband, Denis Pollney, and Luciano Rezzolla. Faithful effective-one-body waveforms of equal-mass coalescing black-hole binaries. *Phys. Rev. D*, 77(8):084017, 2008.

[115] Vanessa C. de Andrade, Luc Blanchet, and Guillaume Faye. Third post-Newtonian dynamics of compact binaries: Noetherian conserved quantities and equivalence between the harmonic-coordinate and ADM-Hamiltonian formalisms. *Class. Quantum Grav.*, 18(5):753–778, 2001.

[116] Edvin Deadman and John M. Stewart. Numerical relativity and asymptotic flatness. *Class. Quantum Grav.*, 26(6):065008, 2009.

[117] Luciano di Fiore. The present status of the VIRGO Central Interferometer. *Class. Quantum Grav.*, 19(7):1421–1428, 2002.

[118] Peter Diener, Frank Herrmann, Denis Pollney, Erik Schnetter, Edward Seidel, Ryoji Takahashi, Jonathan Thornburg, and Jason Ventrella. Accurate evolution of orbiting binary black holes. *Phys. Rev. Lett.*, 96:121101, 2006.

[119] Olaf Dreyer, Badri Krishnan, Deirdre Shoemaker, and Erik Schnetter. Introduction to isolated horizons in numerical relativity. *Phys. Rev. D*, 67(2):024018, Jan 2003.

[120] E.K. Porter and B.S. Sathyaprakash. Improved gravitational waveforms from spinning black hole binaries. *Phys. Rev. D*, 71:024017, 2005.

[121] Zachariah B. Etienne, Joshua A. Faber, Yuk Tung Liu, Stuart L. Shapiro, and Thomas W. Baumgarte. Filling the holes: Evolving excised binary black hole initial data with puncture techniques. *Phys. Rev. D*, 76:101503, 2007.

[122] Guillaume Faye, Luc Blanchet, and Alessandra Buonanno. Higher-order spin effects in the dynamics of compact binaries. I. Equations of motion. *Phys. Rev. D*, 74(10):104033, 2006.

[123] Lee S. Finn. Detection, measurement, and gravitational radiation. *Phys. Rev. D*, 46:5236–5249, 1992.

[124] Lee Samuel Finn and David F. Chernoff. Observing binary inspiral in gravitational radiation: One interferometer. *Phys. Rev. D*, 47:2198–2219, 1993.

[125] David R. Fiske, John G. Baker, James R. van Meter, Dae-Il Choi, and Joan M. Centrella. Wave zone extraction of gravitational radiation in three-dimensional numerical relativity. *Phys. Rev. D*, 71(10):104036, 2005.

[126] E. E. Flanagan and S. A. Hughes. Measuring gravitational waves from binary black hole coalescences. I. Signal to noise for inspiral, merger, and ringdown. *Phys. Rev. D*, 57:4535, 1998.

[127] E. E. Flanagan and S. A. Hughes. Measuring gravitational waves from binary black hole coalescences: II. The waves' information and its extraction, with and without templates. *Phys. Rev. D*, 57:4566–4587, 1998.

[128] E.B. Ford and F.A. Rasio. Secular evolution of hierarchical triple star systems. *Astron. J.*, 535:385–401, 2000.

[129] E.B. Ford and F.A. Rasio. Erratum: "secular evolution of hierarchical triple star systems". *Astron. J.*, 605:966–966, 2004.

[130] Helmut Friedrich. On the hyperbolicity of Einstein's and other gauge field equations. *Commun. Math. Phys.*, 100(4):525–543, 1985.

[131] Helmut Friedrich and Gabriel Nagy. The initial boundary value problem for Einstein's vacuum field equation. *Commun. Math. Phys.*, 201(3):619–655, 1999.

[132] P. Fritschel. Second generation instruments for the Laser Interferometer Gravitational Wave Observatory (LIGO). In M. Cruise and P. Saulson, editors, *Society of Photo-Optical Instrumentation Engineers (SPIE) Conference Series*, volume 4856 of *Society of Photo-Optical Instrumentation Engineers (SPIE) Conference Series*, pages 282–291, March 2003.

[133] G. Schäfer. *Gen. Relativ. Gravit.*, 18:255–270, 1986.

[134] David Garfinkle. Harmonic coordinate method for simulating generic singularities. *Phys. Rev. D*, 65(4):044029, 2002.

[135] J. A. Gonzalez, M. D. Hannam, U. Sperhake, B. Brügmann, and S. Husa. Supermassive recoil velocities for binary black-hole mergers with antialigned spins. *Phys. Rev. Lett.*, 98:231101, 2007.

[136] Jose A. Gonzalez, Ulrich Sperhake, Bernd Brügmann, Mark Hannam, and Sascha Husa. Maximum kick from nonspinning black-hole binary inspiral. *Phys. Rev. Lett.*, 98:091101, 2007.

[137] Achamveedu Gopakumar, Mark Hannam, Sascha Husa, and Bernd Brügmann. Comparison between numerical relativity and a new class of post-Newtonian gravitational-wave phase evolutions: the non-spinning equal-mass case. *Phys. Rev. D*, 78:064026, 2008.

[138] D. Gottlieb and J. S. Hesthaven. Spectral methods for hyperbolic problems. *J. Comput. Appl. Math.*, 128(1–2):83–131, 2001.

[139] Carsten Gundlach. Pseudospectral apparent horizon finders: An efficient new algorithm. *Phys. Rev. D*, 57(2):863–875, Jan 1998.

[140] Mark Hannam, Sascha Husa, Bernd Brügmann, and Achamveedu Gopakumar. Comparison between numerical-relativity and post-Newtonian waveforms from spinning binaries: the orbital hang-up case. *Phys. Rev. D*, 78:104007, 2007.

[141] Mark Hannam, Sascha Husa, José A. González, Ulrich Sperhake, and Bernd Brügmann. Where post-Newtonian and numerical-relativity waveforms meet. *Phys. Rev. D*, 77:044020, 2008.

[142] Mark Hannam, Sascha Husa, Frank Ohme, Bernd Brügmann, and Niall Ó Murchadha. Wormholes and trumpets: Schwarzschild spacetime for the moving-puncture generation. *Phys. Rev. D*, 78:064020, 2008.

[143] F. Herrmann, I. Hinder, D. Shoemaker, and P. Laguna. Unequal mass binary black hole plunges and gravitational recoil. *Class. Quantum Grav.*, 24:S33–S42, 2007.

[144] F. Herrmann, Ian Hinder, D. Shoemaker, P. Laguna, and Richard A. Matzner. Gravitational recoil from spinning binary black hole mergers. *Astrophys. J.*, 661:430–436, 2007.

[145] Frank Herrmann, Ian Hinder, Deirdre M. Shoemaker, Pablo Laguna, and

Richard A. Matzner. Binary black holes: Spin dynamics and gravitational recoil. *Phys. Rev. D*, 76:084032, 2007.

[146] J. S. Hesthaven. Spectral penalty methods. *Appl. Num. Math.*, 33:23–41, 2000.

[147] S. Hild. The status of GEO 600. *Class. Quantum Grav.*, 23(19):S643–S651, 2006.

[148] Ian Hinder, Frank Herrmann, Pablo Laguna, and Deirdre Shoemaker. Comparisons of eccentric binary black hole simulations with post-Newtonian models. 2008.

[149] Ian Hinder, Birjoo Vaishnav, Frank Herrmann, Deirdre M. Shoemaker, and Pablo Laguna. Circularization and final spin in eccentric binary-black-hole inspirals. *Phys. Rev. D*, 77(8):081502, 2008.

[150] Peter Hübner. From now to timelike infinity on a finite grid. *Class. Quantum Grav.*, 18(10):1871–1884, 2001.

[151] Sascha Husa, José A. González, Mark Hannam, Bernd Brügmann, and Ulrich Sperhake. Reducing phase error in long numerical binary black hole evolutions with sixth order finite differencing. *Class. Quantum Grav.*, 25:105006, 2008.

[152] Sascha Husa, Mark Hannam, José A. González, Ulrich Sperhake, and Bernd Brügmann. Reducing eccentricity in black-hole binary evolutions with initial parameters from post-Newtonian inspiral, 2007.

[153] Yousuke Itoh. Equation of motion for relativistic compact binaries with the strong field point particle limit: Third post-Newtonian order. *Phys. Rev. D*, 69(6):064018, Mar 2004.

[154] Yousuke Itoh and Toshifumi Futamase. New derivation of a third post-Newtonian equation of motion for relativistic compact binaries without ambiguity. *Phys. Rev. D*, 68(12):121501, Dec 2003.

[155] Yousuke Itoh, Toshifumi Futamase, and Hideki Asada. Equation of motion for relativistic compact binaries with the strong field point particle limit: The second and half post-Newtonian order. *Phys. Rev. D*, 63(6):064038, Feb 2001.

[156] B. R. Iyer and C. M. Will. Post-newtonian gravitational radiation reaction for two-body systems. *Phys. Rev. Lett.*, 70:113–116, 1993.

[157] B. R. Iyer and C. M. Will. Post-newtonian gravitational radiation reaction for two-body systems: Nonspinning bodies. *Phys. Rev. D*, 52:6882, 1995.

[158] Piotr Jaranowski and Gerhard Schäfer. Third post-Newtonian higher order ADM Hamilton dynamics for two-body point-mass systems. *Phys. Rev. D*, 57(12):7274–7291, Jun 1998. Erratum: [160].

[159] Piotr Jaranowski and Gerhard Schäfer. Binary black-hole problem at the third post-Newtonian approximation in the orbital motion: Static part. *Phys. Rev. D*, 60(12):124003, Nov 1999.

[160] Piotr Jaranowski and Gerhard Schäfer. Erratum: Third post-Newtonian higher order ADM Hamilton dynamics for two-body point-mass systems. *Phys. Rev. D*, 63(2):029902, Dec 2000.

[161] K. Gültekin, M.C. Miller and D.P. Hamilton. Three-body encounters of black holes in globular clusters. In J. M. Centrella, editor, *The astrophysics of gravavitational wave sources, AIP Conference Proceedings*, volume 686, pages 135–140. AIP, 2003.

[162] K.G. Arun, L. Blanchet, B.R. Iyer and M.S.S. Qusailah. The 2.5pn gravitational wave polarizations from inspiralling compact binaries in circular orbits. *Class. Quantum Grav.*, 21:3771–3801, 2004.

[163] K.G. Arun, L. Blanchet, B.R. Iyer and M.S.S. Qusailah. Corrigendum: The 2.5pn gravitational wave polarizations from inspiralling compact binaries in circular orbits. *Class. Quantum Grav.*, 22:3115–3117, 2005.

[164] L. E. Kidder. Multipolar decomposition of post-newtonian waveforms from inspiralling compact binaries in circular orbits. *Phys. Rev. D*, 77:044016, 2008.

[165] L. E. Kidder, L. Blanchet, and B. R. Iyer. Radiation reaction in the 2.5PN waveform from inspiralling binaries in circular orbits. *Class. Quantum Grav.*, 24:5307–5312, 2007.

[166] Lawrence E. Kidder. Coalescing binary systems of compact objects to (post)$^{5/2}$-Newtonian order. V. Spin effects. *Phys. Rev. D*, 52(2):821–847, Jul 1995.

[167] Lawrence E. Kidder. Using full information when computing modes of post-Newtonian waveforms from inspiralling compact binaries in circular orbit. *Phys. Rev. D*, 77:044016, 2008.

[168] Lawrence E. Kidder, Lee Lindblom, Mark A. Scheel, Luisa T. Buchman, and Harald P. Pfeiffer. Boundary conditions for the Einstein evolution system. *Phys. Rev. D*, 71:064020, 2005.

[169] Bence Kocsis and Abraham Loeb. Distortion of gravitational-wave packets due to their self-gravity. *Phys. Rev. D*, 76(8):084022, 2007.

[170] Christian Königsdörffer and Achamveedu Gopakumar. Phasing of gravitational waves from inspiralling eccentric binaries at the third-and-a-half post-Newtonian order. *Phys. Rev. D*, 73(12):124012, 2006.

[171] Michael Koppitz, Denis Pollney, Christian Reisswig, Luciano Rezzolla, Jonathan Thornburg, Peter Diener, and Erik Schnetter. Recoil velocities from equal-mass binary-black-hole mergers. *Phys. Rev. Lett.*, 99:041102, 2007.

[172] Y. Kozai. Secular perturbations of asteroids with high inclination and eccentricity. *Astron. J.*, 67:591, 1962.

[173] Andrzej Królak, Kostas D. Kokkotas, and Gerhard Schäfer. Estimation of the post-Newtonian parameters in the gravitational-wave emission of a coalescing binary. *Phys. Rev. D*, 52(4):2089–2111, Aug 1995.

[174] L. Blanchet. On the accuracy of the post-newtonian approximation. 2002.

[175] L. Blanchet, T. Damour, B.R. Iyer, C.M. Will and A.G. Wiseman. Gravitational-radiation damping of compact binary systems to second post-newtonian order. *Phys. Rev. Lett.*, 74:3515, 1995.

[176] Luis Lehner and Osvaldo M. Moreschi. Dealing with delicate issues in waveform calculations. *Phys. Rev. D*, 76(12):124040, 2007.

[177] C.W. Lincoln and C.M. Will. Coalescing binary systems of compact objects to (post)$^{5/2}$-Newtonian order: Late-time evolution and gravitational-radiation emission. *Phys. Rev. D*, 42:1123–1143, 1990.

[178] Lee Lindblom, Benjamin J. Owen, and Duncan A. Brown. Model wave-

form accuracy standards for gravitational wave data analysis. *Phys. Rev. D*, 18(12):124020, 2008.

[179] Lee Lindblom, Mark A. Scheel, Lawrence E. Kidder, Robert Owen, and Oliver Rinne. A new generalized harmonic evolution system. *Class. Quantum Grav.*, 23:S447–S462, 2006.

[180] Geoffrey Lovelace. *Topics in Gravitational Wave Physics*. PhD thesis, California Institute of Technology, 2007.

[181] Geoffrey Lovelace, Robert Owen, Harald P. Pfeiffer, and Tony Chu. Binary-black-hole initial data with nearly-extremal spins. *Phys. Rev. D*, 78:084017, 2008.

[182] Pedro Marronetti, Wolfgang Tichy, Bernd Brügmann, Jose Gonzalez, Mark Hannam, Sascha Husa, and Ulrich Sperhake. Binary black holes on a budget: Simulations using workstations. *Class. Quantum Grav.*, 24:S43–S58, 2007.

[183] Mark Miller. Circular orbit approximation for binary compact objects in general relativity. *Phys. Rev. D*, 69(12):124013, Jun 2004.

[184] M.C. Miller and D.P. Hamilton. Four-body effects in globular cluster black hole coalescence. *Astrophys. J.*, 576:894–898, 2002.

[185] T. Mora and C.M. Will. Numerically generated quasiequilibrium orbits of black holes: Circular or eccentric? *Phys. Rev. D*, 66:101501(R), 2002.

[186] Abdul H. Mroué, Lawrence E. Kidder, and Saul A. Teukolsky. Ineffectiveness of Padé resummation techniques in post-Newtonian approximations. *Phys. Rev. D*, 78:044004, 2008.

[187] C.D. Murray and S.F. Dermott. *Solar System Dynamics*. Cambridge University Press, Cambridge, UK, first edition, 1999.

[188] N. Yunes and E. Berti. Accuracy of the post-newtonian approximation: Optimal asymptotic expansion for quasi-circular, extreme-mass ratio inspirals. 2008.

[189] Andrea Nerozzi, Christopher Beetle, Marco Bruni, Lior M. Burko, and Denis Pollney. Towards a wave-extraction method for numerical relativity. II. The quasi-Kinnersley frame. *Phys. Rev. D*, 72(2):024014, 2005.

[190] Andrea Nerozzi, Marco Bruni, Lior M. Burko, and Virginia Re. Towards a novel wave-extraction method for numerical relativity. In *Proceedings of the Albert Einstein Century International Conference, Paris, France*, pages 702–707, 2005. [AIP Conf. Proc. 861, 702 (2006)].

[191] Robert Owen. *Topics in Numerical Relativity: The periodic standing-wave approximation, the stability of constraints in free evolution, and the spin of dynamical black holes*. PhD thesis, California Institute of Technology, 2007.

[192] Yi Pan, Alessandra Buonanno, John G. Baker, Joan Centrella, Bernard J. Kelly, Sean T. McWilliams, Frans Pretorius, and James R. van Meter. Data-analysis driven comparison of analytic and numerical coalescing binary waveforms: Nonspinning case. *Phys. Rev. D*, 77(2):024014, 2008.

[193] Enrique Pazos, Ernst Nils Dorband, Alessandro Nagar, Carlos Palenzuela, Erik Schnetter, and Manuel Tiglio. How far away is far enough for extracting numerical waveforms, and how much do they depend on the extraction method? *Class. Quantum Grav.*, 24(12):S341–S368, 2007.

[194] P. C. Peters. Gravitational radiation and the motion of two point masses. *Phys. Rev.*, 136(4B):B1224–B1232, Nov 1964.

[195] P. C. Peters and J. Mathews. Gravitational radiation from point masses in a keplerian orbit. *Phys. Rev.*, 131(1):435–440, Jul 1963.

[196] H. P. Pfeiffer, L. E. Kidder, M. A. Scheel, and S. A. Teukolsky. A multidomain spectral method for solving elliptic equations. *Comput. Phys. Commun.*, 152:253–273, 2003.

[197] Harald P. Pfeiffer, Duncan A. Brown, Lawrence E. Kidder, Lee Lindblom, Geoffrey Lovelace, and Mark A. Scheel. Reducing orbital eccentricity in binary black hole simulations. *Class. Quantum Grav.*, 24(12):S59–S81, 2007.

[198] Harald P. Pfeiffer, Saul A. Teukolsky, and Gregory B. Cook. Quasicircular orbits for spinning binary black holes. *Phys. Rev. D*, 62(10):104018, Oct 2000.

[199] Harald P. Pfeiffer and James W. York. Extrinsic curvature and the Einstein constraints. *Phys. Rev. D*, 67(4):044022, Feb 2003.

[200] Eric Poisson. Gravitational radiation from a particle in circular orbit

around a black hole. I. Analytical results for the nonrotating case. *Phys. Rev. D*, 47(4):1497–1510, Feb 1993.

[201] Eric Poisson. Gravitational radiation from a particle in circular orbit around a black hole. VI. Accuracy of the post-Newtonian expansion. *Phys. Rev. D*, 52(10):5719–5723, Nov 1995.

[202] Eric Poisson. Absorption of mass and angular momentum by a black hole: Time-domain formalisms for gravitational perturbations, and the small-hole or slow-motion approximation. *Phys. Rev. D*, 70(8):084044, Oct 2004.

[203] Denis Pollney et al. Recoil velocities from equal-mass binary black-hole mergers: a systematic investigation of spin-orbit aligned configurations. *Phys. Rev.*, D76:124002, 2007.

[204] Frans Pretorius. Evolution of binary black-hole spacetimes. *Phys. Rev. Lett.*, 95(12):121101, 2005.

[205] Frans Pretorius. Numerical relativity using a generalized harmonic decomposition. *Class. Quantum Grav.*, 22(2):425–451, 2005.

[206] Frans Pretorius. Simulation of binary black hole spacetimes with a harmonic evolution scheme. *Class. Quantum Grav.*, 23(16):S529–S552, 2006.

[207] Oliver Rinne. Stable radiation-controlling boundary conditions for the generalized harmonic Einstein equations. *Class. Quantum Grav.*, 23:6275–6300, 2006.

[208] Oliver Rinne, Lee Lindblom, and Mark A. Scheel. Testing outer boundary treatments for the Einstein equations. *Class. Quantum Grav.*, 24:4053–4078, 2007.

[209] R.M. Memmesheimer, A. Gopakumar and G. Schäfer. Third post-newtonian accurate generalized quasi-keplerian parametrization for compact binaries in eccentric orbits. *Phys. Rev. D*, 70:104011, 2004.

[210] Olivier Sarbach and Manuel Tiglio. Gauge-invariant perturbations of Schwarzschild black holes in horizon-penetrating coordinates. *Phys. Rev. D*, 64:084016, Sep 2001.

[211] Mark A. Scheel, Michael Boyle, Tony Chu, Lawrence E. Kidder, Keith D.

Matthews, and Harald P. Pfeiffer. High-accuracy waveforms for binary black-hole inspiral, merger, and ringdown. *Phys. Rev. D*, 79:024003, 2009.

[212] Mark A. Scheel, Harald P. Pfeiffer, Lee Lindblom, Lawrence E. Kidder, Oliver Rinne, and Saul A. Teukolsky. Solving Einstein's equations with dual coordinate frames. *Phys. Rev. D*, 74:104006, 2006.

[213] J. D. Schnittman, A. Buonanno, J. R. van Meter, J. G. Baker, W. D. Boggs, J. Centrella, B. J. Kelly, and S. T. McWilliams. Anatomy of the binary black hole recoil: A multipolar analysis. *Phys. Rev. D*, 77:044031, 2008.

[214] Carlos F. Sopuerta, Nicolas Yunes, and Pablo Laguna. Gravitational recoil velocities from eccentric binary black hole mergers. *Astrophys. J.*, 656:L9–L12, 2007.

[215] Ulrich Sperhake. Binary black-hole evolutions of excision and puncture data. *Phys. Rev. D*, 76:104015, 2007.

[216] J. M. Stewart. The Cauchy problem and the initial boundary value problem in numerical relativity. *Class. Quantum Grav.*, 15(9):2865–2889, 1998.

[217] Béla Szilágyi, Denis Pollney, Luciano Rezzolla, Jonathan Thornburg, and Jeffrey Winicour. An explicit harmonic code for black-hole evolution using excision. *Class. Quantum Grav.*, 24:S275–S293, 2007.

[218] Béla Szilágyi, Bernd Schmidt, and Jeffrey Winicour. Boundary conditions in linearized harmonic gravity. *Phys. Rev. D*, 65(6):064015, Feb 2002.

[219] Béla Szilágyi and Jeffrey Winicour. Well-posed initial-boundary evolution in general relativity. *Phys. Rev. D*, 68(4):041501 (R), Aug 2003.

[220] T. Damour, A. Nagar, M. Hannam, S. Husa and B. Brugmann. Accurate effective-one-body waveforms of inspiralling and coalescing black-hole binaries. 2008.

[221] T. Damour, N. Deruelle. Radiation reaction and angular momentum loss in small angle gravitational scattering. *Phys. Rev. Lett.*, 87A:81, 1981.

[222] T. Damour, P. Jaranowski and G. Schäfer. Effective one body approach to the dynamics of two spinning black holes with next-to-leading order spin-orbit coupling. 2008.

[223] Takahiro Tanaka, Yasushi Mino, Misao Sasaki, and Masaru Shibata. Gravitational waves from a spinning particle in circular orbits around a rotating black hole. *Phys. Rev. D*, 54(6):3762–3777, Sep 1996.

[224] Takahiro Tanaka, Hideyuki Tagoshi, and Misao Sasaki. Gravitational waves by a particle in circular orbits around a Schwarzschild black hole—5.5 post-Newtonian formulation. *Prog. Theor. Phys.*, 96(6):1087, 1996.

[225] Kip S. Thorne. Multipole expansions of gravitational radiation. *Rev. Mod. Phys.*, 52(2):299–339, Apr 1980.

[226] U. Sperhake, E. Berti, V. Cardoso, J. González, B. Brügmann and M. Ansorg. Eccentric binary black-hole mergers: The transition from inspiral to plunge in general relativity. *prd*, 78:064069, 2008.

[227] Hugo Wahlquist. The Doppler response to gravitational waves from a binary star source. *Gen. Relativ. Gravit.*, 19(11):1101–1113, Nov 1987.

[228] Samuel J. Waldman. Status of LIGO at the start of the fifth science run. *Class. Quantum Grav.*, 23(19):S653–S660, 2006.

[229] S. Weinberg. *Gravitation and Cosmology: Principles and Applications of the theory of relativity*. John Wiley & Sons, Inc., New York, USA, first edition, 1972.

[230] L. Wen. On the eccentricity distribution of coalescing black hole binaries driven by the kozai mechanism in globular clusters. *Astrophys. J.*, 598:419–430, 2003.

[231] Clifford M. Will and Alan G. Wiseman. Gravitational radiation from compact binary systems: Gravitational waveforms and energy loss to second post-Newtonian order. *Phys. Rev. D*, 54(8):4813–4848, Oct 1996.

[232] William H. Press, Saul A. Teukolsky, William T. Vetterling and Brian P. Flannery. *Numerical Recipes: The Art of Scientific Computing, 3rd ed.* Cambridge University Press, New York, 2007.

[233] Alan G. Wiseman. Coalescing binary systems of compact objects to (post)$^{5/2}$-Newtonian order. IV. The gravitational wave tail. *Phys. Rev. D*, 48(10):4757–4770, Nov 1993.

[234] James W. York. Conformal "thin-sandwich" data for the initial-value problem of general relativity. *Phys. Rev. Lett.*, 82(7):1350–1353, Feb 1999.

[235] Nicolás Yunes and Emanuele Berti. Accuracy of the post-Newtonian approximation: Optimal asymptotic expansion for quasicircular, extreme-mass ratio inspirals. *Phys. Rev. D*, 77(12):124006, 2008.